HIGHLY MOBILE DROPLETS ON SLIPPERY SURFACES

B V ORME

PhD

2019

HIGHLY MOBILE DROPLETS ON SLIPPERY SURFACES

BETHANY VICTORIA ORME

A thesis submitted in partial fulfilment
of the requirements of the
University of Northumbria at Newcastle
for the degree of Doctor of Philosophy

Department of Mathematics, Physics
and Electrical Engineering

October 2019

Abstract

Droplets on slippery surfaces such as Slippery Liquid Infused Porous Surfaces or Liquid - Impregnated Surfaces (SLIPS/LIS) are inherently highly mobile and therefore can be difficult to control in terms of position and motion. This thesis has explored how to return droplet control back to very slippery surfaces via four interconnected studies. The first study investigated how to return droplet control back to these slippery surfaces by adding a simple step structure to the surface. The adhesive force created by this structure has been quantified by measuring the droplet sliding angle as a function of step height and oil thickness. As the step height was increased so did the adhesive force, as the oil thickness was increased the adhesive force decreased. Given the correct conditions the adhesive force can be great enough to hold a droplet upside down. The ability of the structure to produce motion via a repulsive or attractive force has been investigated in the second study by changing where the droplet was placed onto the substrate. The type of force produced was found to not only vary with position but with oil thickness and time. The third study involved a more complex topography onto which the SLIPS coating was applied, creating a mobile surface which also shaped the droplet. As a droplet placed on to this surface evaporated it was shown that the shape of the droplet could be accurately predicted for a given droplet volume. The final study developed a SLIPS coating that could be applied to any structure, even a closed geometry, in one single step, producing sliding angles equivalent to those seen on a standard SLIPS coating. This coating has also been shown to be long lasting with the SLIPS properties remaining more than two years after it was first produced and tested.

Contents

List of Figures

List of Tables

Acknowledgements

Firstly, I would like thank my primary supervisor Dr Gary Wells and co-supervisors Prof. Glen McHale and Dr Rodrigo Ledesma-Aguilar for their guidance as well as their support throughout this project. Their extensive experimental and theoretical knowledge has been invaluable through this project.

I owe the technical staff at Northumbria University, Dr Pietro Maiello, Rebecca Payne and Gavin Warburton, my thanks for their assistance and valuable experience.

I would like to thank the staff, academics and fellow Ph.D students I have had the pleasure of working with at Northumbria University. Every discussion has been valuable and has made each of the three years enjoyable.

I would also like to thank my friends, family and Ph.D students from other institutions for their continuing support and understanding throughout this project.

Lastly, I am very grateful to Northumbria University for the funding of this Ph.D studentship.

Declaration

I declare that the work contained in this thesis has not been submitted for any other award and that it is all my own work. I also confirm that this work fully acknowledges options, ideas and contributions from the work of others.

Any ethical clearance for the research presented in this thesis has been approved. Approval has been sought and granted by the Faculty Ethics Committee on 29/11/2016.

I declare that the Word Count of this Thesis is 44899 words.

Name: Bethany Victoria Orme

Signature:

Date: 18/10/2019

Chapter 1

Introduction

The presence and appearance of liquids on surfaces is a common occurrence in nature and more particularly plant biology[1, 2]. Plants have evolved to suit their environment and in so doing have changed the physical and chemical structure of their surfaces[3]. For Lotus plants the collection of dust and large contaminants on the surface would eventually prevent the plant from performing photosynthesis[4]. Therefore, this plant has developed a structure on the leaves which consists of hairs that are micrometric in height. These hairs act to repel water droplets creating a highly mobile droplet. Thus, when it rains, the water will fall on to the leaf and readily fall off, dragging with it the contaminants and cleaning the leaf. In the case of the Nepenthes Pitcher plant the inverse has been involved[5]. Around the outer perimeter of the plant an interconnected network of overlapping epidermal cells acts not to repel water but instead to attract it and force it to spread into a thin film. Whilst this film will not repel water droplets when it rains it will instead repel other liquids such as oil. This surface acts to assist the plant in much the same was as the Lotus effect, by feeding the plant. Any flies that land on this perimeter (peristome) will be repelled and will slide into the depths of the pitcher where they will be dissolved and absorbed[6]. The fields of plant biology and wetting are inextricably linked therefore, when trying to study wetting phenomena the surfaces seen on plants are replicated in a laboratory setting.

Young and Laplace were among some of the first to study the interaction of (specifically water) droplets with flat, solid surfaces in the early 1800's exploring equilibrium states of contact angles[7, 8]. By adding a structure to a flat surface, it is rendered hy-

drophobic simply via the reduction of the solid-liquid contact creating surfaces, similar to the Lotus leaf. The field of wetting was subsequently driven into the early 1900's by the studies of Wenzel[9, 10], Cassie and Baxter[11] exploring the different interaction types a water droplet can have with a textured substrate. Hydrophobicity can be broken down on structured surfaces by simply applying either pressure or mechanical abrasion to the surface, making it difficult to apply these types of surfaces to many practical applications. The case of hydrophobicity continued to be an area of intense research into the late 1990's and early 2000's with the creation of new chemical coatings that can be applied to the structures to push the hydrophobicity into the regime of superhydrophobicity where the contact between solid and liquid is further reduced. Superhydrophobic surfaces have been used to aid the removal of water droplets for many self-cleaning applications however due to their delicacy the ability to use them on a wider scale was reduced.

The development of Slippery Liquid Infused Porous Surfaces (SLIPS)/Liquid Impregnated Surfaces (LIS) in the early 2010's generated much interest in their ability to not only repel water droplets but to easily transport these droplets across the surfaces[12, 13, 14]. These surfaces consist of a structure imbibed by a lubricating layer, creating a very low hysteresis, highly mobile surface akin to the Nepenthes Pitcher plant. As these surfaces can retain the lubricating layer for extended periods of time the low sliding angle of water droplets on these surfaces ($<1^{\circ}$) can be maintained, making them viable options for applications where contact line pinning has inhibited droplet movement. Whilst these surfaces provide a solution to the problem of contact line pinning, they introduce the new problem of droplet control. Once droplets are deposited onto the surface the ability to control where they will assume a stationary position is lost and slight perturbations to the surface will generate droplet movement. Taking this idea of surface perturbations further, the droplet control can be regained. The Cheerios effect is driven purely by surface deformations, hence coupling this effect with the slippery surfaces may be a way to generate droplet control.

This thesis will report the studies conducted to reintroduce control back to the slippery surfaces using only the surface topography and the deformation to the oil layer

that this creates. Water droplets deposited on such surfaces can either be attracted to or repelled from structures (Chapters 4 and 5) as well as affecting the evaporative behaviour (Chapter 6) generating droplet transport. A new coating method has also been developed (with a patent pending) to be able to coat different geometries and surfaces with the process requiring only a single step as opposed to the multiple steps required for the spray coating method (Chapter 7).

Chapter 2

Background

This chapter introduces the theoretical concepts necessary to understand how liquids interact with other liquids and solids, giving the fundamental background to the phenomenon of wetting. The specific concepts of Slippery Liquid Infused Porous Surfaces (SLIPS)/Lubricant Impregnated Surfaces (LIS) has been explored with emphasis on how a binary liquid system acts with a structured surface. The applications that SLIPS could or have been used for has been outlined in the conclusion of this chapter.

2.1 Wetting Parameters

When a liquid is in contact with a solid it can form differently shaped interfaces depending on many factors, such as the volume of the liquid, capillary length, surface chemistry or texture, surface tension etc. Overall it is perhaps the surface tension of the liquid that is the main factor governing all these effects (especially for droplets that are small), as it is the term universally linking the key governing equations.

2.1.1 Surface Tension

Consider a liquid droplet floating in an environment in contact only with the surrounding vapour, the droplet will form a perfect sphere. The spherical shape is determined by the interaction of the molecules within the liquid and the attractive van der Waals forces they produce. In the bulk of the liquid, a single molecule will have an equal attractive interaction with all of its surrounding molecules. A molecule at the liquid-

vapour interface has fewer molecules of liquid surrounding it on one side, leading to an imbalance of van der Waals forces at this point. This molecule still wants to be in contact with other liquid molecules, therefore the attractive force only acts towards the bulk and not outwards towards the vapour (Figure 2.1.1). The energy of the system (the liquids surface area) must also be minimised. A perfect sphere allows for a give volume of liquid to have minimal surface area and therefore system energy. The shape that the droplet takes is only governed by the interfacial tension between the liquid and vapour, γ_{lv}.

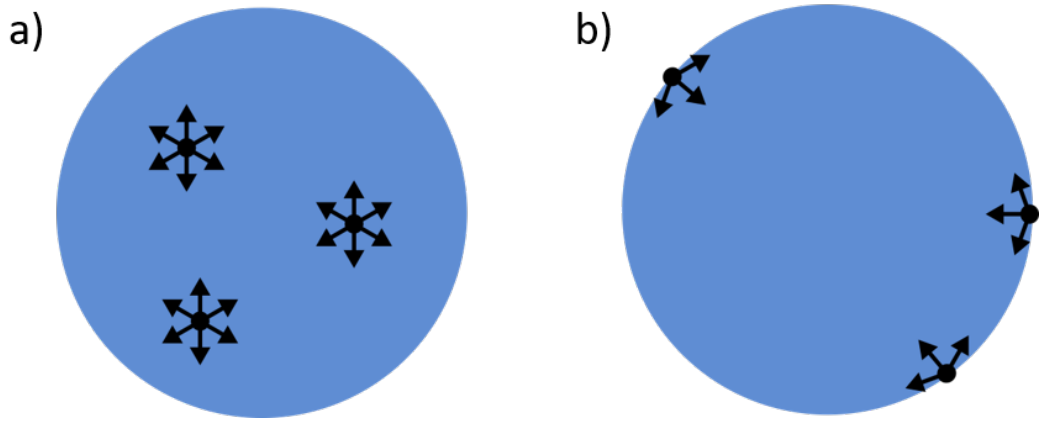

Figure 2.1.1: A perfectly spherical liquid droplet surrounded only by vapour with a) the molecules in the bulk of the liquid with equal interactions and b) molecules at the interface with an imbalance in the forces.

2.1.2 Laplace Pressure

For the spherical droplet suspended in vapour there is a pressure inside the droplet driven by the surface tension, γ_{lv}. The difference in pressure inside the droplet and outside the droplet creates the curvature of the droplet (equation 2.1.1),

$$\Delta P = P_{inside} - P_{outside} = \gamma(\frac{1}{R_1} + \frac{1}{R_2}). \tag{2.1.1}$$

If two droplets of the same liquid but differing sizes are connected together the smaller droplet (with greater pressure) will empty into the larger droplet (with lower pressure) (Figure 2.1.2) due to the pressures inverse dependence on the droplet radius (R) equation 2.1.1. The same will occur in the case of bubbles. Small droplets, or

bubbles, will always empty into bigger droplets or bubbles to form a single, large droplet or bubble.

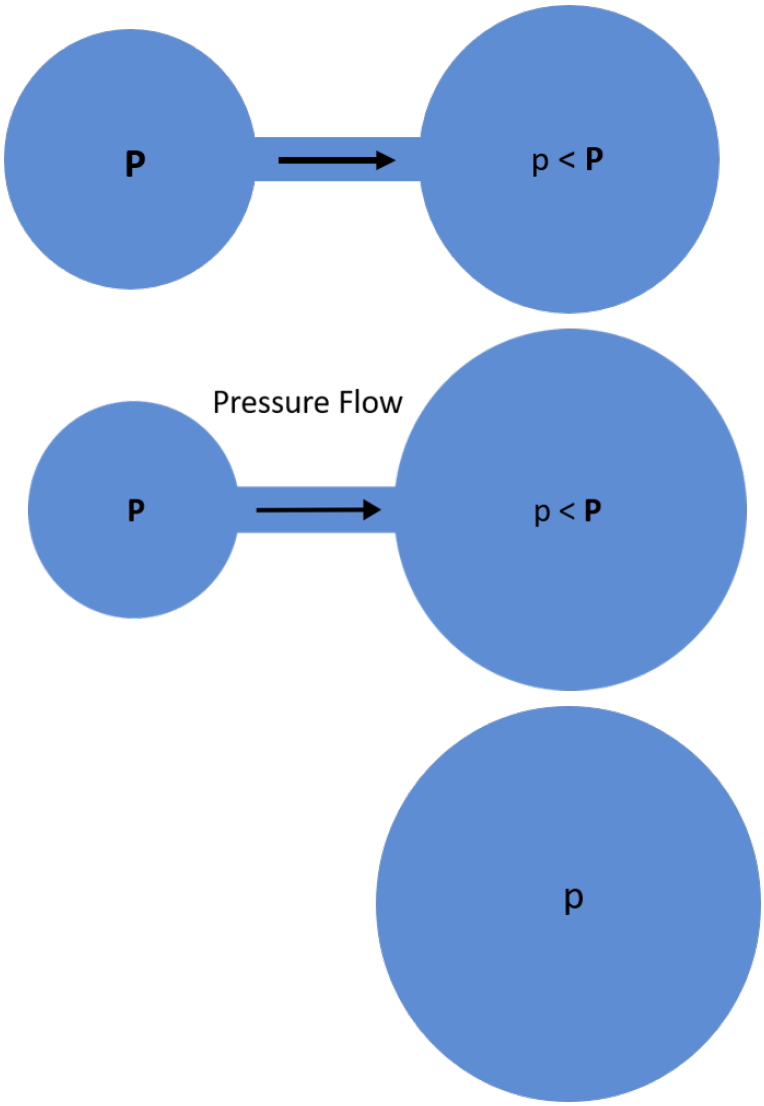

Figure 2.1.2: A small droplet (or bubble) of high pressure emptying into a large droplet (or bubble) of lower pressure connected by a channel.

2.1.3 Spreading Coefficient

If another interface, a solid, is added into the system there will now be two interfaces that form. The liquid-vapour interface, γ_{lv}, from the spherical droplet argument (Section 2.1.1) and the new liquid-solid interface, γ_{ls}, formed by the droplet contacting the solid. The presence of these two interfaces assumes that the liquid has spread into a thin film over the solid (Figure 2.1.3)[15].

Figure 2.1.3: A liquid spread into a thin film over a solid substrate.

For complete spreading to occur, the liquid must have displaced the solid-vapour interface, γ_{sv}. In order for the liquid to spread it must be more energetically favourable for the liquid to be in contact with the solid and vapour, rather than the vapour with the solid. As the interfacial (surface) tensions equate to an interfacial energy per unit area, mN/m, a simple energy balance can be calculated. For the thin film case, the energy of γ_{sv} must be larger than the combination of γ_{lv} and γ_{ls} (equation 2.1.2),

$$\gamma_{sv} > \gamma_{lv} + \gamma_{ls}. \tag{2.1.2}$$

This equation can be converted to a spreading coefficient (S) where

$$S = \gamma_{sv} - (\gamma_{lv} + \gamma_{ls}). \tag{2.1.3}$$

As can be seen from equation 2.1.3, if S is positive ($S \geq 0$) the spreading of the liquid is favourable. In this case it has been assumed that the surface is perfectly smooth, creating a system that is driven purely by the surface or interfacial tensions[2].

2.1.4 Youngs Angle

For $S < 0$ the liquid will not spread into a thin film. $S < 0$ does not create a surface that will necessarily have no contact whatsoever with the liquid, it instead produces a partial wetting case (Figure 2.1.4). The droplet will sit on the surface forming a spherical cap, a situation partially between the spherical droplet and thin film case (Section 2.3.1). For a spherical cap the three interfacial tensions are present in the system and meet at the point of contact with the surface (Figure 2.1.4)[16].

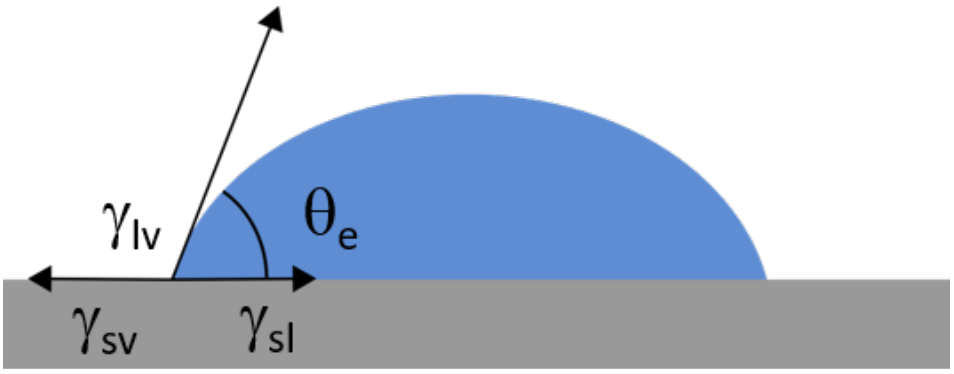

Figure 2.1.4: A spherical cap formed with the surface with the direction the three interfacial tensions operate in.

The interaction between all three interfacial tensions in the x-direction (along the surface) produces a characteristic equilibrium contact angle determined by the Young's equation

$$cos\theta_e = \frac{\gamma_{sv} - \gamma_{ls}}{\gamma_{lv}}. \tag{2.1.4}$$

The vertical force (y-direction) does not contribute to the system as the surface on which the liquid is sitting is non-deformable. Combining this equation (2.1.4 with the spreading coefficient produces the Young-Dupre Law (equation 2.1.5)

$$S = \gamma_{lv}(\cos\theta_e - 1), \tag{2.1.5}$$

showing that the degree of spreading can be determined solely by the equilibrium contact angle and the interfacial tension between liquid and vapour.

As the effect of the interfacial tensions acts on the contact line, only at the contact point, the contact angle is independent of droplet size.

2.1.5 Capillary Length

For small droplets on a surface a spherical cap is formed. Increasing the volume (size) changes the shape of the liquid from a spherical capped droplet to a flat-topped puddle, with the interface curving to the equilibrium contact angle at the solid contact point (Figure 2.1.5). The length at which the transition from droplet to puddle occurs is

known as the capillary length and can be calculated from the equation

$$\kappa^{-1} = (\frac{\gamma}{\rho g})^{1/2}, \tag{2.1.6}$$

where ρ is the liquid density, γ the surface tension between liquid and vapour, g the acceleration due to gravity and κ^{-1} the capillary length. κ^{-1} is derived from the reciprocal of the circles radius where κ=1/R. The capillary length (Equation 3.3.2) is the balance between surface tension, or Laplace pressure ($P = 2(\frac{\gamma}{R})$) and pressure due to gravity ($P_g = 2\rho g R$). At small droplet sizes, $\leq \kappa^{-1}$, surface tension dominates producing a spherical cap (Figure 2.1.5 a). $\kappa^{-1} = r$ is the balance between surface tension and gravity (Figure 2.1.5 b), creating a spherical cap with maximum base radius. For larger sizes, $\geq \kappa^{-1}$, gravity dominates over surface tension, flattening the spherical cap to a puddle (Figure 2.1.5 c).

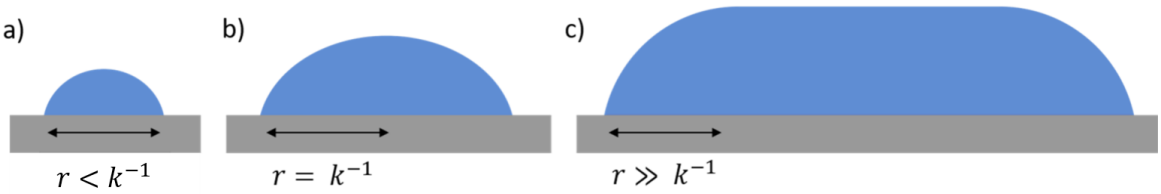

Figure 2.1.5: Shaping of liquid in contact with a solid surface with a) the capillary length equal to the size of the droplet, b) the capillary length equal to the radius of the droplet and c) the capillary length much smaller than the scale of the droplet, producing a puddle.

Using water as the example liquid (g = 9.81 mm/s, γ = 72.8 mN/m, ρ = 997 kg/m^3)[17], $\kappa^{-1} = 2.7$ mm. The easiest experimental way to measure this is to introduce a vertical wall to a bath of the liquid. The liquid should rise from its equilibrium level, up the wall, creating a deformation to the liquid layer extending away from the wall. The distance of this deformation is equal to the capillary length.

2.1.6 Philicity, Phobicity and 90°

As the Young's contact angle cannot be changed by increasing the droplets size the interfacial tensions have to be changed. As has previously been discussed in section 2.1.3 the interfacial tension between the vapour and solid must be greater than γ_{ls} +

γ_{lv} for the liquid to have an affinity with the surface inducing complete wetting into a thin liquid film. If γ_{sv} is less than $\gamma_{ls} + \gamma_{lv}$ the liquid has less affinity with the surface, creating a partial wetting system. The degree to which the liquid wets the surface can be determined from equation 2.1.5. For the phillic case $\cos\theta_e$ must be between 0 and 1, producing contact angles, θ_e, between 0° and 90° (Figure 2.1.6 a). The phobic case requires $\cos\theta_e$ to be between 0 and -1 and contact angles, θ_e, between 90° and 180° (Figure 2.1.6 b)[18].

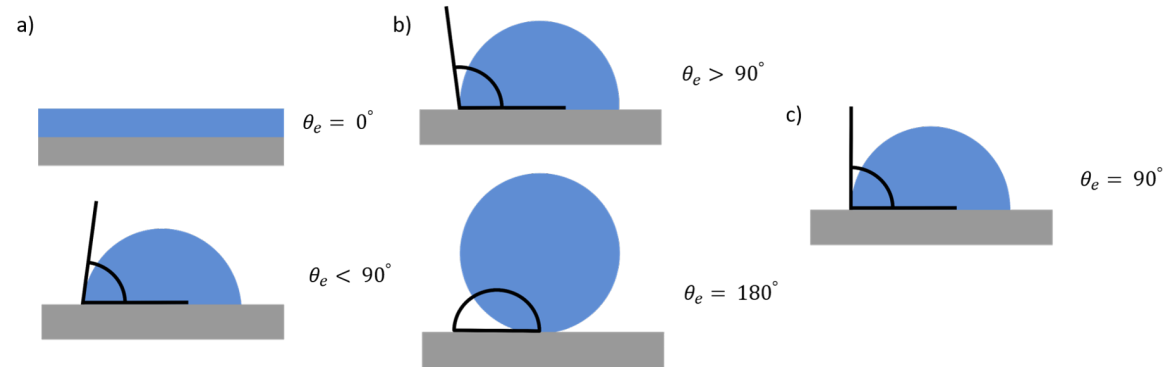

Figure 2.1.6: Philicity and phobicity of the surface with a) the extremes of philicity, b) the extremes of phobicity and c) 90°.

For philicity, θ_e must be less than 90° and phobicity, greater than 90°, meaning that when $\gamma_{ls} = \gamma_{sv}$ the contact angle is 90° and the surface is neither phillic or phobic, creating a perfect hemisphere on the surface (Figure 2.1.6 c)[18].

2.1.7 How to change a surface

To change the interfacial tensions, the type of liquid being used could be changed, creating differences in γ_{ls} and γ_{lv}. In nature it is normally water that is present on the surfaces. Depending on what surface with which the water is in contact, the contact angle will change. On the rim of the Nepenthes pitcher plant the overlapping epidermal cells trap the water in the structure, creating a thin film of water[5]. On rose petals or windows after rain, the water droplets are clearly partially spherical, but are stuck on the substrate with a high adhesion force[19, 20]. On a ducks' back or on the lotus leaf the droplets ball up and have very little contact with the substrate[4, 21].

In order to replicate such surfaces under lab conditions chemical coating and rough-

ness can be added to solid surfaces, changing their affinity with the liquids[22, 23]. By considering a nanometrically flat surface, such as a polished Silicon Wafer or Float Glass (produced via the Pilkington process), the surfaces can be made hydrophilic by changing the surface chemistry and introducing OH- bonds to the interface. Due to the polarisation of water and now the polarisation of the surface a forced wetting state is induced. To hydrophobise the substrate the energy of the substrate must be lowered. There are two chemical based coatings that could be used. The first is based on a fluorinated polymer coating, either Teflon or polytetrafluoroethylene (PTFE), which lowers the surface energy to approximately 21 mN/m[24, 25]. The second is based on silane chains, such as octadecyltrichlorosilane (OTS), which lowers the surface energy even further to 15 mN/m, preventing both high (water) and low (silicone oils) surface tension liquids from spreading[2].

Chemical based coatings however, have a limit. The maximum contact angle that a chemical coating can achieve is 120°[26, 27]. To push the surface towards superhydrophobicity, where the contact angle must be over 150°, another structure must be added to the surface[26, 27]. By adding roughness to the surface along with a chemical hydrophobic coating, the area that the liquid (water) will be in contact with is reduced. There are many ways to add a surface roughness to the substrate. The surface can be roughened by removing some of the surface by using etching techniques which can be based on chemicals that will remove some of the surface[28, 29], or plasma[29, 30, 31], again which will damage the surface and remove microscale fragments. The other standard way to introduce roughness is to add to the surface. Using processes such as lithography (photolithography, soft lithography, electron beam lithography, etc.) a highly structured surface, normally consisting of pillars on the micron scale, can be added to the surface[32, 33, 34]. For nanoscale roughness crystal growth, or nanoparticle deposition, can be implemented[26, 35]. If deposited in a controlled manner using techniques such as layer-by-layer the subsequent surface will appear to be closely packed and highly ordered. The advantage especially of the particle deposition is that not only do the particles create the roughness needed but they can also be pre-coated with a chemical coating fulfilling both criteria for superhydrophobicity[36]. Combining

multiple techniques on the micron scale and nanoscale can produce hierarchical scaled roughness that enhances the hydrophobicity even further[2, 27, 37]. The roughness not only enhances the hydrophobicity of the surface, if the surface has undergone a process to make it hydrophilic, adding roughness will also enhance the philicity, creating a superhydrophillic surface[38, 39].

Whether a surface can ever truly be termed hydrophobic or even superhydrophobic is debateable. According to McHale et al.[40, 41] if this hydrophobic coating is not attached to the surface the water will have enough energy to physically lift the hydrophobic coating and fully envelop the droplet in a way akin to a liquid marble.

2.1.8 Contact Angle Hysteresis

Contact angle hysteresis (CAH) stems from the inherent surface roughness or other heterogenecity present on all surfaces[42, 43, 44, 45]. Even on a silicone wafer, there is still roughness, on the nanoscale, which distort the contact line. For realistic surfaces, there are likely to be defects, either from the fabrication process or the handling of the samples. It is likely to find large (microscale) scratches on what would otherwise be a much smoother surface or even chemical staining, such as oils from skin, if the sample ha not been kept in a clean environment or handled with care. If the surface is constructed from spherical grains, the fabrication process of the surface requires close packing, producing an inherent roughness as there is a limit to close packing.

Therefore, when a droplet is placed onto these surfaces, depending on where the droplet rests, the contact angle may differ between two limits of the advancing and receding contact angles, giving a range of static contact angles producing the hysteresis for the surface.

To measure CAH there are two standard experimental methods. Method one is termed the inflation and deflation method. This involves depositing a droplet onto the surface and instead of removing the needle to measure the static contact angle the needle is left in the droplet. The needle is then used to inflate the surface droplet by pumping in more of the same liquid at a very slow rate. Pumping in the liquid in turn increases the volume of the droplet, in doing so, for a surface with hysteresis, the

contact angle will also increase (Figure 2.1.7 a). At some point during the inflation, a threshold contact angle will be reached and one of the droplets contact lines will appear to jump, increasing its droplet footprint area and base diameter. The angle prior to this increase in base diameter is the advancing contact angle (θ_A)[42, 44].

A similar process is seen for the deflation procedure. Again, with the needle left inside the droplet, the liquid is slowly withdrawn, at the same rate used for the droplet inflation. At a threshold angle, the droplets contact line will undergo a secondary jump, retracting its contact line, reducing its droplet footprint on the surface and therefore base diameter (Figure 2.1.7 b). The contact angle prior to this decrease in droplet footprint is the receding contact angle (θ_R).

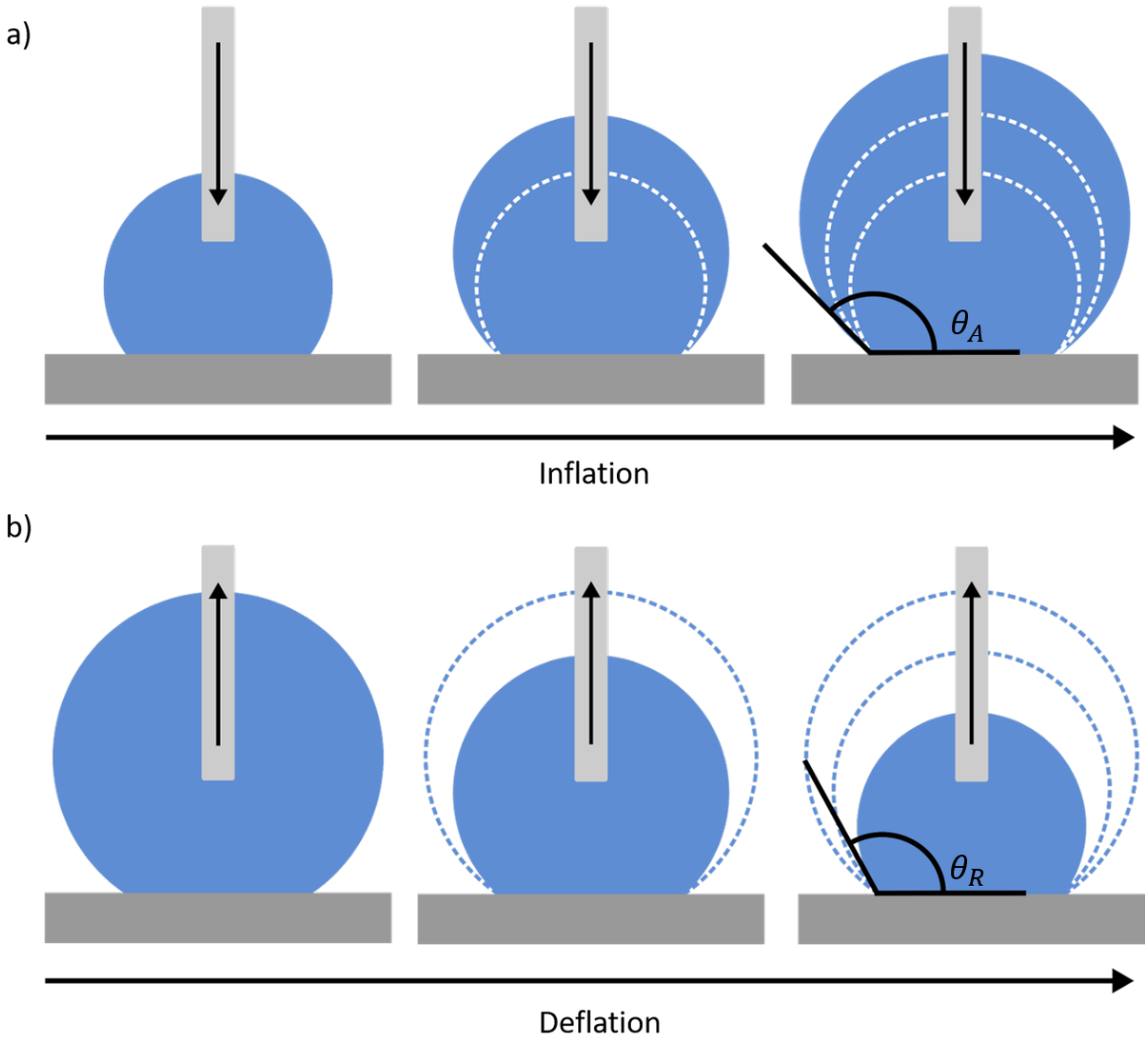

Figure 2.1.7: Contact angle hysteresis measurements conducted using the inflation/deflation method. a) The inflation and advancing angle and b) the deflation and receding angle.

The difference between the advancing angle and receding angle is the contact angle hysteresis.

For this hysteresis measurement technique, the contact lines will always be moving using this method and therefore it is dynamic contact angles that are being measured, this may overestimate the hysteresis seen for the surface in question[46].

The second method is the sample tilting method. This requires a droplet to be placed onto the substrate and the substrate to be subsequently tilted. Through the tilting procedure the droplet will deform from the perfect spherical cap, creating a tear drop shaped droplet. The leading droplet edge will begin to bulge as the droplet tries to keep it's contact line pinned. The trailing edge again has a pinned contact line and will begin to be stretched by the bulk of the droplet being pulled by gravity down the inclined surface. This creates a difference in the interface curvature and therefore generates a Laplace pressure opposing the pull of the gravitational force. Providing the contact lines remained pinned, the Laplace pressure will grow in accordance with the difference in curvatures. At a certain inclination angle, the contact lines will depin and the droplet will slide or roll down the surface. The point just prior to detachment, the leading edge will form the advancing angle with the surface and the trailing edge the receding angle (Figure 2.1.8). The contact angle hysteresis can be calculated by measuring these angles and taking the difference between the two. However, this difference will be equal to the angle of inclination, or siding angle (θ_s).

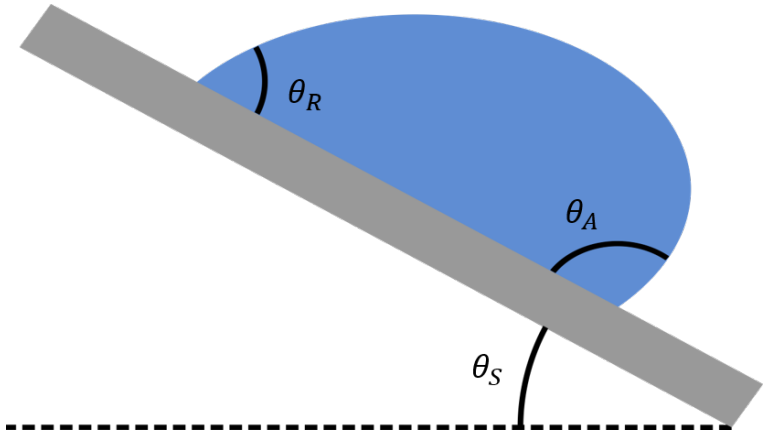

Figure 2.1.8: Contact angle hysteresis measurements using the sample tilting method with the leading edge creating the advancing angle and trailing edge the receding angle.

The volume of the droplet chosen to perform this experiment is the most important

factor to consider. Firstly, the droplet must be below the capillary length defined in section 2.1.5 in order for surface tension to dominate over gravity. If the radius of the droplet is above this value the hysteresis measured will be lower than the hysteresis actually present on the surface. Secondly, even when the droplet is below this value gravity will still act, therefore the droplet needs to be as small as possible to reduce these effects.

Therefore, when a droplet is deposited on to the surface and the static contact angle measured it is not always the equilibrium Youngs angle that is actually being measured, it is merely an angle between the advancing and receding constraints.

2.1.9 Surface Free Energy

In section 2.1.4 Youngs equation has been derived from a simple force balance. This however is not the only approach that can be taken to derive this formula. The forces present on the surfaces are inherently linked to the energies on the surface. Therefore, by taking a surface free energy approach Youngs equation should be reached.

By taking the area next to the contact line and advancing the liquid front by a small area (ΔA) there will be a portion of solid-vapour interface lost and an area of liquid vapour and liquid-solid gained (Figure 2.1.9).

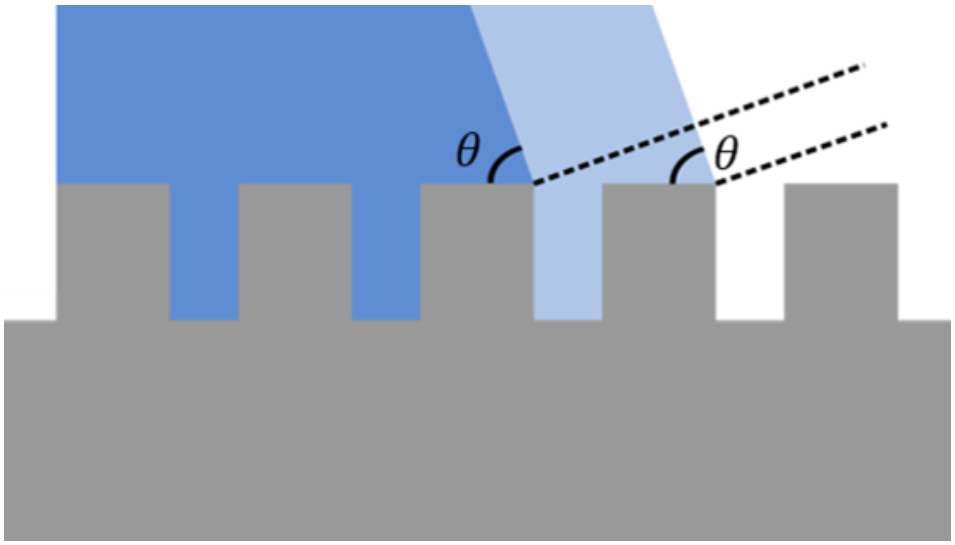

Figure 2.1.9: Small displacement of the contact line showing the interface areas lost and gained.

The area lost is equal to $\Delta A\gamma_{sv}$, the area gained is equal to $\Delta A\gamma_{sl} + \Delta A\cos\theta\gamma_{lv}$.

The combined change in energy is equal to ΔE,

$$\Delta E = \Delta A \gamma_{sl} + \Delta A \cos\theta \gamma_{lv} - \Delta A \gamma_{sv}, \tag{2.1.7}$$

$$\frac{\Delta E}{\Delta A} = \gamma_{sl} + \cos\theta \gamma_{lv} - \gamma_{sv}, \tag{2.1.8}$$

To be in equilibrium the surface free energy should be at a minimum, hence ΔE = 0 at this point. Therefore, by applying this condition to equation 2.1.8 Youngs equation is produced

$$0 = \gamma_{sl} + \cos\theta \gamma_{lv} - \gamma_{sv}, \tag{2.1.9}$$

$$\cos\theta \gamma_{lv} = \gamma_{sl} - \gamma_{sv}, \tag{2.1.10}$$

$$\cos\theta_e = \frac{\gamma_{sl} - \gamma_{sv}}{\gamma_{lv}}. \tag{2.1.11}$$

This relationship only holds true for a small contact line movement on a surface with no roughness or hysteresis.

2.1.10 Controlled Roughness

When considering how liquids interact with surfaces and the possible application of these surfaces it is important to understand all of the characteristics in order to tailor the system components to produce the desired wetting characteristics. As has been discussed in section 2.1.7, photolithography is one possible method to introduce roughness to the surfaces (Figure 2.1.10).

Figure 2.1.10: A typical schematic of a pillared substrate.

The pillared structures develop complex liquid–solid interactions which are not an

issue on an ideal flat substrate used for many models. Taking the static equilibrium contact angle as an example, on a flat surface, the contact angle can be accurately measured from side view images. On a pillared surface the droplets can sit in one of two regimes. If the solid-liquid contact is only with the tops of the pillars, side view images can still be an accurate measure of the contact angle. However, it is also possible for the liquid to fully wet and penetrate the structure, contacting the pillar bases, hence the contact angle will be hidden by the structure when using side view images. The case where the structure is completely wetted was first explored by Wenzel in the 1930's (Figure 2.1.11 a). Cassie and Baxter in the 1940's described the case where the droplet partially wets the surface, only contacting the top of the pillars (Figure 2.1.11 b).

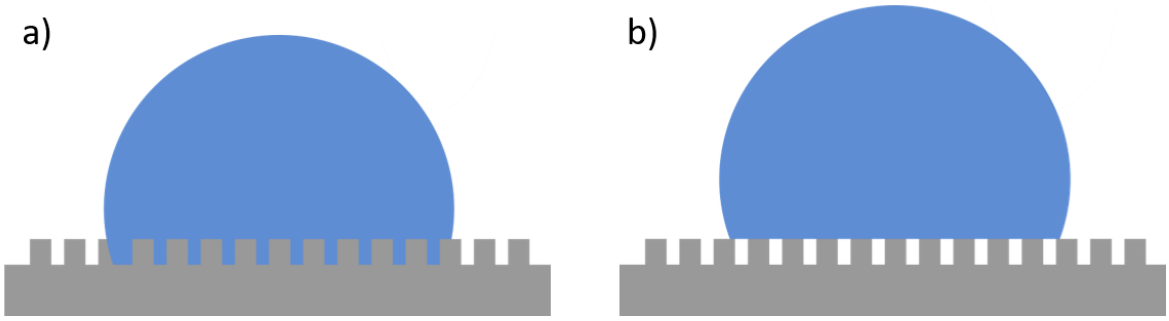

Figure 2.1.11: a) The fully wetted Wenzel case and b) the partially wetted Cassie – Baxter case.

2.1.11 Wenzel

In order for the liquid in a Wenzel state on a pillared surface to advance, the liquid must move from the top of one pillar to the top of the neighbouring pillar, displacing a portion of the solid-vapour interface (Figure 2.1.12)[9, 10, 45].

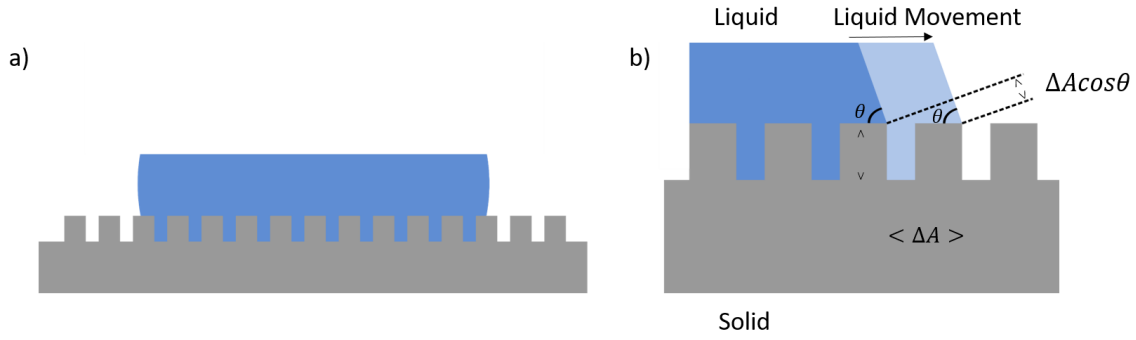

Figure 2.1.12: a) A fully impaled droplet sitting in a Wenzel state. b) The increase in droplet footprint as the contact line is advanced for a Wenzel case.

Thinking of this problem from a surface free energy approach, the displaced interface is equal to ΔA in terms of an apparent area. In real terms the actual surface area displaced is equal to the height of the pillars in addition to the apparent surface area, 2h+ ΔA. This can be thought of in terms of a roughness factor, taking the ratio of the apparent contact area and the actual contact area,

$$r_w = \frac{ActualSurfaceArea}{ApparentSurfaceArea}, \tag{2.1.12}$$

$$r_w = \frac{2h + \Delta A}{\Delta A}, \tag{2.1.13}$$

$$r_w = 1 + \frac{2h}{\Delta A}, \tag{2.1.14}$$

where r_w is the Wenzel roughness.

Advancing the contact line creates a loss in one interface and a gain in another two interfaces. The portion of solid-vapour interface lost is equal to $r_w \Delta A \gamma_{sv}$, the gain of solid-liquid equals $r_w \Delta A \gamma_{sl}$ and the gain of liquid-vapour $\cos\theta_w \Delta A \gamma_{lv}$. Therefore, the change in the surface energy, E, is shown in equation 2.1.15,

$$\Delta E = r_w \Delta A \gamma_{sl} + \Delta A \cos\theta_w \gamma_{lv} - r_w \Delta A \gamma_{sv}. \tag{2.1.15}$$

The change in energy per unit area is therefore,

$$\frac{\Delta E}{\Delta A} = r_w \gamma_{sl} + \cos\theta_w \gamma_{lv} - r_w \gamma_{sv}. \tag{2.1.16}$$

As with the surface free energy argument for a flat surface $\Delta E = 0$,

$$0 = r_w \gamma_{sl} + \cos\theta_w \gamma_{lv} - r_w \gamma_{sv}, \tag{2.1.17}$$

$$\cos\theta_w \gamma_{lv} = r_w(\gamma_{sv} - \gamma_{sl}), \tag{2.1.18}$$

$$\cos\theta_w = r_w(\frac{\gamma_{sv} - \gamma_{sl}}{\gamma_{lv}}). \tag{2.1.19}$$

The equlibrium angle from Youngs equation can be inputted into the brackets from equation 2.1.19 to produce the Wenzel relation (equation 2.1.20),[9, 10, 45, 47, 48]

$$\cos\theta_w = r_w \cos\theta_e. \tag{2.1.20}$$

2.1.12 Cassie - Baxter

In the Cassie – Baxter case a layer of air is trapped in between the liquid and solid texture. In a similar way to the Wenzel model the contact line will advance from the corner of one pillar to the neighbouring pillar displacing some of the interfaces (Figure 2.1.13).

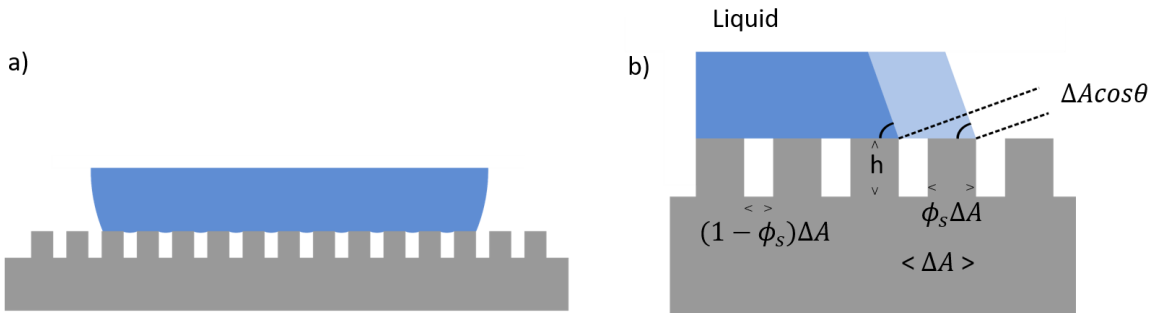

Figure 2.1.13: a) A droplet sitting on top of the pillars in a Cassie – Baxter state. b) The increase in droplet footprint as the contact line is advanced for a Cassie - Baxter case.

For the Cassie – Baxter model the solid-vapour interface that is lost is not the

entirety of the actual surface area, it is only a portion of the area, $\phi_s \Delta A \gamma_{sv}$. The gain in solid-liquid area equals $\phi_s \Delta A \gamma_{sl}$ and the gain in liquid-vapour is $1 - \phi_s \Delta A \gamma_{lv} + \cos\theta_{CB} \Delta A \gamma_{lv}$. The change in surface free energy produces equation 2.1.21,

$$\Delta E = (1 - \phi_s)\Delta A \gamma_{sl} + \phi_s \Delta A \gamma_{sl} + \cos\theta_{CB} \Delta A \gamma_{lv} - \phi_s \Delta A \gamma_{sv}. \tag{2.1.21}$$

The change in energy per unit area equals,

$$\frac{\Delta E}{\Delta A} = (1 - \phi_s)\gamma_{sl} + \phi_s \gamma_{sl} + \cos\theta_{CB} \gamma_{lv} - \phi_s \gamma_{sv}. \tag{2.1.22}$$

Again, at equilibrium, ΔE = 0. Placing the condition into equation 2.1.21 and rearranging produces equation 2.1.23,

$$0 = ((1 - \phi_s) + \cos\theta_{CB})\gamma_{lv} + \phi_s(\gamma_{sl} - \gamma_{sv}), \tag{2.1.23}$$

$$\frac{(\gamma_{sv} - \gamma_{sl})}{\gamma_{lv}}\phi_s = ((1 - \phi_s) + \cos\theta_{CB}). \tag{2.1.24}$$

Substituting in Youngs equation produces

$$\cos\theta_e \phi_s = ((1 - \phi_s) + \cos\theta_{CB}), \tag{2.1.25}$$

$$(\cos\theta_e - (1 - \phi_s))\phi_s = (\cos\theta_{CB}), \tag{2.1.26}$$

Equation 2.1.26 is the Cassie – Baxter equation with the Cassie – Baxter angle.

As the droplets contact line advances in a Cassie Baxter state, the liquid becomes pinned on the corner. In order to transition to the neighbouring pillar, the liquid must form a capillary bridge connecting the two pillars. The liquid front will rotate around the pinning point until reaching a contact angle of ($\theta = \theta_e + \theta_c$) or 180° contacting with the next pillar and again forming the surfaces contact angle (Figure 2.1.14).

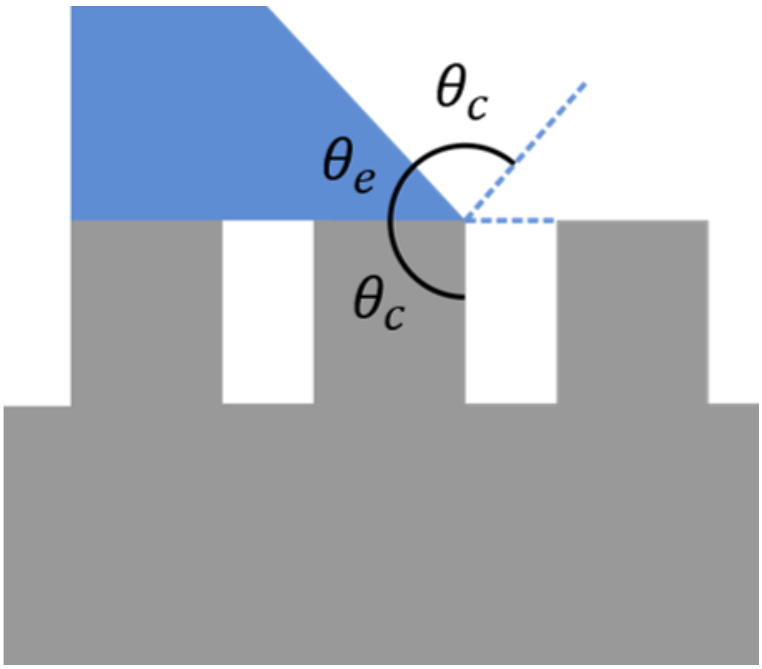

Figure 2.1.14: Advancing liquid front pinned to the corner of the step.

The Youngs angle refers to the static, microscopic, equilibrium contact angle (θ_e) determined by the surface chemistry, corresponding interfacial tensions and is not subject to surface roughness. Both the Wenzel (θ_w) and Cassie - Baxter ($\theta_C B$) angles are modified versions of θ_e, dependent on the surface roughness and measured on the macroscopic scale. As surface roughness is a property inherent of most surfaces and the difficulties associated with the measurement of such an angle on the microscopic scale the static contact angles measured experimentally are almost always macroscopic and roughness modified contact angles, or apparent, static contact angles[47, 48].

2.1.13 Cassie to Wenzel Transition

A droplet in a Cassie - Baxter state can be forced into a Wenzel state by applying pressure to the liquid and forcing the liquid into the structure, contacting the entirety of the surface[49, 50, 51, 52, 53]. From the surface free energy equations, there is a critical contact angle that needs to be reached before the transition can occur. For the droplet to be in a Cassie – Baxter state the energy in the Cassie – Baxter equation must be less than for the Wenzel equation, $\Delta E_w > \Delta E_{CB}$,

$$r_w(\gamma_{sl}-\gamma_{sv})\Delta A+\cos\theta_e\gamma_{lv}\Delta A > \phi_s(\gamma_{sl}-\gamma_{sv})\Delta A+\gamma_{lv}(1-\phi_s)\Delta A+\cos\theta_e\gamma_{lv}\Delta A, \quad (2.1.27)$$

$$r_w(\gamma_{sl}-\gamma_{sv})-\phi_s(\gamma_{sl}-\gamma_{sv}) > \gamma_{lv}(1-\phi_s)+\cos\theta_e\gamma_{lv}-\cos\theta_e\gamma_{lv}, \quad (2.1.28)$$

$$(r_w-\phi_s)(\gamma_{sl}-\gamma_{sv}) > \gamma_{lv}(1-\phi_s), \quad (2.1.29)$$

$$\frac{\gamma_{sv}-\gamma_{sl}}{\gamma_{lv}} < -\frac{(1-\phi_s)}{r_w-\phi_s}, \quad (2.1.30)$$

$$\cos\theta_e < -\frac{(1-\phi_s)}{r_w-\phi_s}. \quad (2.1.31)$$

Therefore, if $\cos\theta_e$ is less than $\cos\theta_c$ (critical contact angle) the condition is satisfied and the droplet will be in a Cassie – Baxter state where,

$$\cos\theta_c = \frac{(1-\phi_s)}{r_w-\phi_s}. \quad (2.1.32)$$

For the droplet to transfer to the Wenzel state $\Delta E_w < \Delta E_{CB}$.

2.1.14 Hemi-Wicking

During the transition from Cassie – Baxter to Wenzel hemi-wicking occurs. As the name suggests this is a wicking liquid front which imbibes into the structure. The surface free energy argument can be used to determine whether it is more favourable for the liquid to be in the Cassie – Baxter or Wenzel state (Figure 2.1.15)[54, 55, 56, 57].

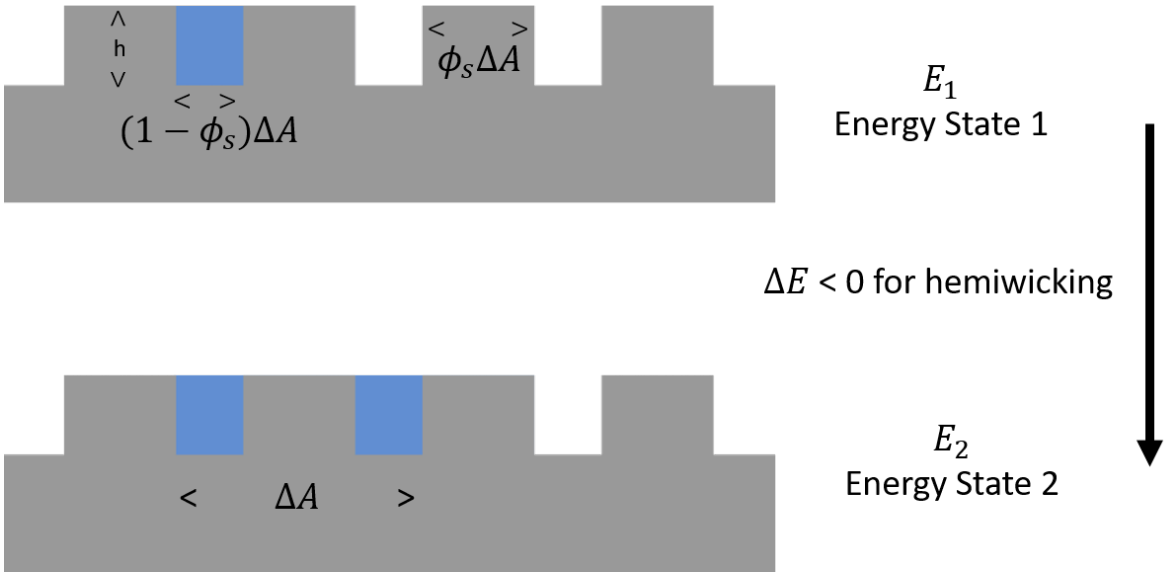

Figure 2.1.15: Hemi-wicking energy states.

The gain in solid-liquid interface equals $(2h+(1-\phi_s)\Delta A)\gamma_{sl}$ and the gain in liquid-vapour interface equals $(1-\phi_s)\Delta A\gamma_{lv}$. The loss therefore in solid-vapour interface is $(2h+(1-\phi_s)\Delta A)\gamma_{sv}$. The change in energy, ΔE, must be less than 0 for E_2 to be favourable,

$$\Delta E = (2h+(1-\phi_s)\Delta A)\gamma_{sl} + (1-\phi_s)\Delta A\gamma_{lv} - (2h+(1-\phi_s)\Delta A)\gamma_{sv}, \tag{2.1.33}$$

$$\frac{\Delta E}{\Delta A} = \frac{2h}{\Delta A}(\gamma_{sl}-\gamma_{sv}) + (1-\phi_s)(\gamma_{sl}-\gamma_{sv}+\gamma_{lv}). \tag{2.1.34}$$

From Wenzels model, the roughness, r_w, equals $2h/\Delta A + 1$, therefore

$$\frac{\Delta E}{\Delta A} = (r_w-1)(\gamma_{sl}-\gamma_{sv}) + (1-\phi_s)(\gamma_{sl}-\gamma_{sv}+\gamma_{lv}), \tag{2.1.35}$$

$$\frac{\Delta E}{\Delta A\gamma_{lv}} = (r_w-1)(\frac{\gamma_{sl}-\gamma_{sv}}{\gamma_{lv}}) + (1-\phi_s)(\frac{\gamma_{sl}-\gamma_{sv}}{\gamma_{lv}}+1). \tag{2.1.36}$$

Replacing $(\frac{\gamma_{sl}-\gamma_{sv}}{\gamma_{lv}})$ with Youngs angle produces

$$\frac{\Delta E}{\Delta A\gamma_{lv}} = (1-r_w)(\cos\theta_e) + (1-\phi_s)(1-\cos\theta_e). \tag{2.1.37}$$

For $\Delta E < 0$ hemi-wicking will occur, therefore

$$0 > ((1 - r_w) - (1 - \phi_s)) \cos\theta_e + (1 - \phi_s), \tag{2.1.38}$$

$$\cos\theta_e > \frac{(1 - \phi_s)}{r_w - \phi_s}. \tag{2.1.39}$$

2.2 Slippery Liquid Infused Porous Surfaces/Liquid Impregnated Surfaces

Superhydrophobic surfaces always suffer from some degree of contact line pinning due to the solid-liquid contact, meaning that hysteresis will always be present. These surfaces are very prone to physical damage and the air plastron can be easily displaced by applying slight pressure to the liquid[26].

The concept of replacing the air plastron with a fluid was first explored by Quere et al. in 2005[12] where it was stated that impregnating a texture with a liquid creates a hemi-solid, hemi-liquid surface. Then, introducing another immiscible liquid into the system, one of two situations ccould occur. Situation one is that the second liquid could sink through the first liquid, contacting the solid. The second possibility is that the second liquid will float on top of the first liquid, this second situation creates a very highly mobile droplet with hysteresis of $< 1°$[12].

This concept is based on the Nepenthes Pitcher plant which imbibes a thin layer of liquid, water, into its overlapping epidermal cells. This water layer then repels any oils on the feet of insects (in particular, flies) creating a slippery interface on which the flies will slide (Figure 2.2.1)[6, 5].

https://www.edenproject.com/learn/for-everyone/plant-profiles/highland-tropical-pitcher-plant

Figure 2.2.1: Image of the Nepenthes Pitcher plant.

In 2011 these surfaces were experimentally tested by the group of Aizenberg[13]. This group produced the surfaces in two different ways, one was to infuse a Teflon mat with a lubricating oil, the second was to structure a surface with photolithographically created pillars and to infuse this structure with an oil. These surfaces are quite literally the opposite of the Nepenthes Pitcher plant, where instead of the surface having been made hydrophilic and oleophobic it has been constructed to be hydrophobic and therefore oleophillic[58, 59, 60]. These surfaces are typically referred to as either Slippery Liquid Infused Porous Surfaces (SLIPS) or Lubricant Impregnated Surfaces (LIS). Whilst the use of these two terms is interchangeable as the surfaces used within this thesis are based only on a porous network, the surfaces will hence be referred to only as SLIPS.

2.2.1 Criteria for SLIPS/LIS

To produce a SLIPS certain criteria must be met[13]:

1. The lubricating liquid and working liquid must be immiscible.
2. The lubricating liquid must fully imbibe into the structure.

3. The working liquid must not preferentially wet the substrate over the lubricating liquid.

4. The contact angle hysteresis or sliding angle must be 5° or below.

2.2.2 Wetting Ridge and Neumann Triangle

A droplet in contact with a solid, forms a spherical cap with the surface (if the radius is below the capillary length) and a contact angle that can be calculated using Youngs equation 2.1.4 (Section 2.1.4). Taking the same size droplet and now placing it onto a soft solid surface, the surface will be deformed by the presence of the droplet[61, 62, 63], therefore the vertical foroce component (y-direction) ignored in Section 2.1.4 is now contibutes to the force balances. The extreme of a droplet on a soft solid is a liquid lens which, in short, is a droplet placed onto a bath of immiscible liquid Figure 2.2.2[64]. The deformation to the bath of liquid and subsequent wetting ridge is determined by the balance three surface tensions at the three phase contact point, producing a Neumann Triangle[65, 66].

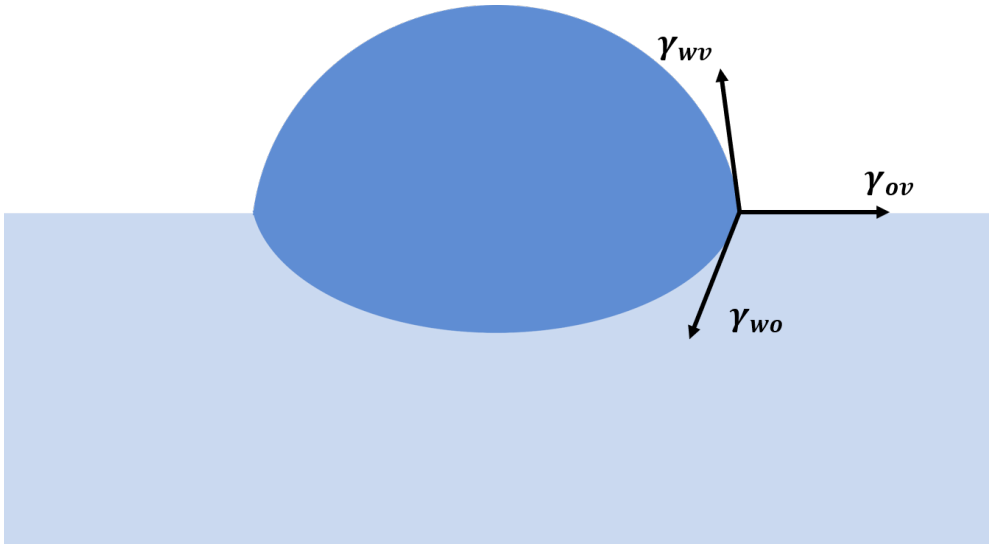

Figure 2.2.2: A schematic of a liquid lens showing the three interfacial tensions acting at the triple point, creating a Neumann triangle.

The same mechanism is seen on SLIPS with the lubricating liquid being deformed by the presence of the immiscible working liquid (droplet). Towards the apex of this droplet the typical spherical cap shape is formed. Closer towards what would be the liquid-solid interface on a dry surface (now the liquid-liquid interface) there is a

deformation to the lubricating liquid in the form of a wetting ridge (Figure 2.2.3).

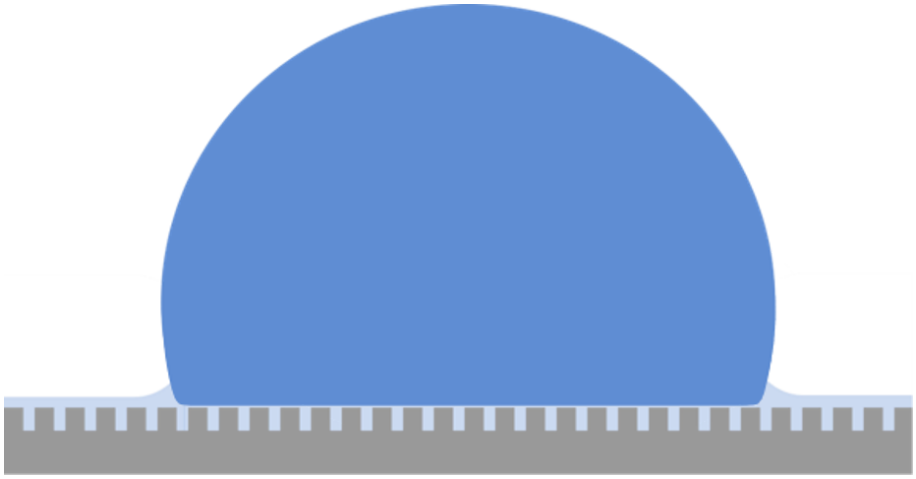

Figure 2.2.3: Schematic of a droplet on a SLIPS with a typical wetting ridge.

The wetting ridge in effect hides the possible droplet contact with the surface, hence Youngs equation can no longer predict the contact angle, but neither can a Neumann triangle, therefore an apparent, SLIPS contact angle is measured. Guan et al.[67] detailed one way to extrapolate the apparent SLIPS contact angle experimentally by fitting a circle to the droplet and identifying where the fitted circle and surface intersect. In addition to this, studies by Semprebon et al.[68] and McHale et al.[41] have shown that a correction to the Young's equation can be implemented, predicting the contact angle on a vanishingly thin lubricant layer to within 0.1° when compared with experimental values[41]. Schellenberger et al.[69] directly measured and observed the wetting ridges dependence on the fluids within the system and the thickness of the lubricating layer used, highlighting the importance of choosing the correct lubricating and working liquids[70].

2.2.3 Spreading Coefficient

Despite the fact that Youngs equation can no longer accurately predict the contact angle with the surface, the spreading calculations derived in section 2.1.3 can still be implemented.

The first criteria that must be met for SLIPS is that the oil has to spread over the solid surface (Figure 2.2.4). Thus, converting equation 2.1.3 to

$$S_{os}^{v} = \gamma_{sv} - \gamma_{os} - \gamma_{ov}. \tag{2.2.1}$$

For $S_{os}^{v} > 0$ the lubricating liquid will spread over the solid.

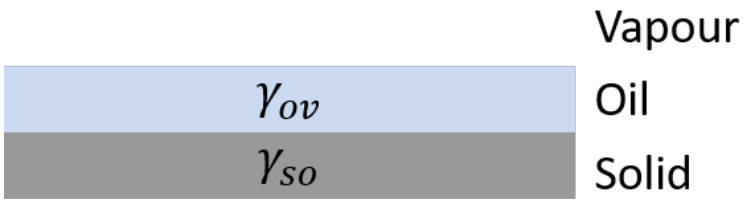

Figure 2.2.4: The spreading of oil over a surface in the presence of vapour.

2.2.4 Droplet Cloaking

The same spreading coefficient arguments can be used to determine the interaction between the two liquids (Figure 2.2.5). For the lubricating liquid (oil) to spread over the working liquid (water), $S_{ol}^{v} > 0$, where

$$S_{ol}^{v} = \gamma_{lv} - \gamma_{lo} - \gamma_{ov}. \tag{2.2.2}$$

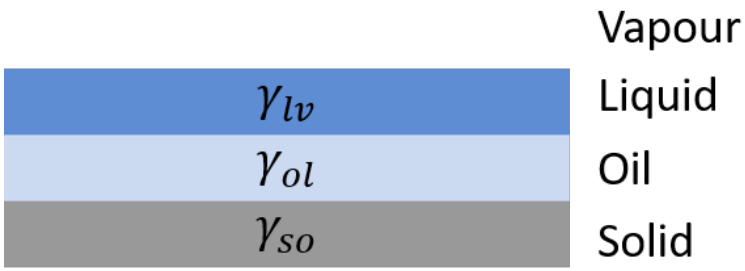

Figure 2.2.5: The spreading of oil over a surface in the presence of vapour.

2.2.5 Energies

Considering only the surface and its interaction with oil it is found in Smith et al. the surface can take 3 states. The first state (A1) (Figure 2.2.6) is the simplest, this is a surface that is dry with no lubricating liquid in contact with any of the structure[71].

If a droplet of water were to be deposited on to this surface it would be either in a Wenzel or Cassie – Baxter state. The energy in this system is dependent only on the surface roughness, r and the solid-vapour interface, γ_{sv},

$$E_{A1} = r\gamma_{sv}. \tag{2.2.3}$$

The second state (A2) is for a surface that has been hemi-wicked by an oil with the tops of the pillars exposed to the vapour. This produces the energy condition,

$$E_{A2} = (r - \phi_s)\gamma_{os} + \phi_s\gamma_{sv} + (1 - \phi_s)\gamma_{ov}. \tag{2.2.4}$$

The third state (A3) is the fully encapsulated and is therefore dependent only on the surface roughness and the oil-vapour, γ_{ov} and oil-solid interfaces γ_{os},

$$E_{A3} = r\gamma_{os} + \gamma_{ov}. \tag{2.2.5}$$

Adding another liquid into the system, such as water, produces another set of energetics. For state W1 the water has replaced the vapour from A1 and has fully encapsulated the surface and structure producing energy state E_{W1}, where

$$E_{W1} = r\gamma_{ws}. \tag{2.2.6}$$

State 2 (W2) takes the hemi-wicked state from A2 and replaces the vapour interface with water, creating the energy criteria,

$$E_{W2} = (r - \phi_s)\gamma_{os} + \phi_s\gamma_{ws} + (1 - \phi_s)\gamma_{ow}. \tag{2.2.7}$$

Taking the fully encapsulated oil state from A3 and again replacing the oil-vapour interface with oil-water interface produces the final energy state, E_{W3}, where

$$E_{W3} = r\gamma_{os} + \gamma_{ow}. \tag{2.2.8}$$

Combining the 3 energies for the system with only oil (A1 to A3) and the 3 energies for the system where water has been added (W1 to W3) produces a set of 6 possible

combinations for the surface and liquid combinations shown in Figure 2.2.6 taken from Smith et al[71].

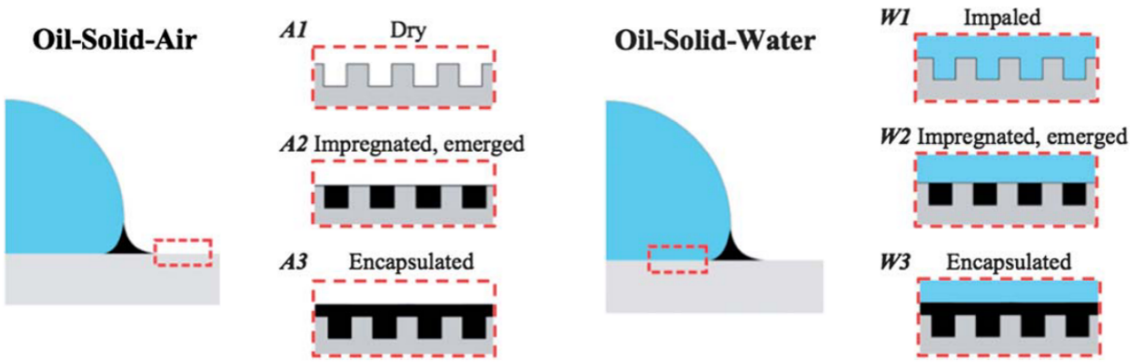

Figure 2.2.6: Six possible energy combinations for a single liquid system (A) and binary liquid system (W) Smith et al.2013.

2.2.6 12 SLIPS States

Figure 2.2.6 details the 6 cases for the energy states with an uncloaked droplet. By adding in the criteria that the droplets could be cloaked with the lubricating oil[70], another 6 states can be identified (Figure 2.2.7).

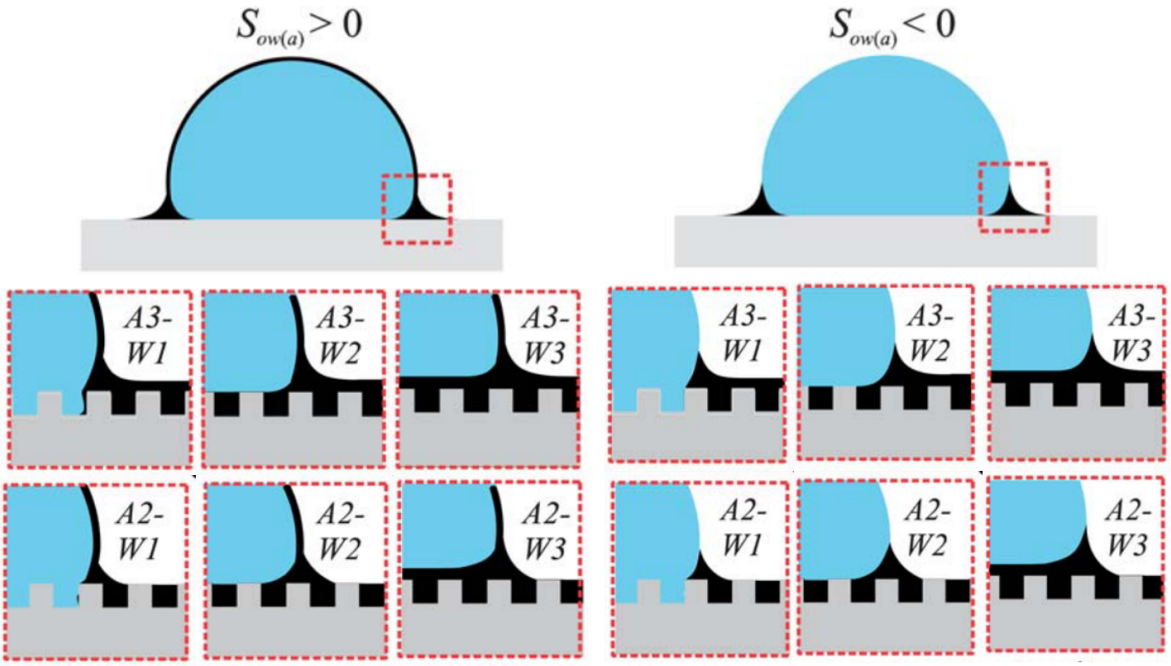

Figure 2.2.7: 12 thermodynamically stable state for oil infused surfaces Smith et al.2013.

The 12 conditions can be split into 3 separate clear sections all determined by the droplet's mobility on these surfaces. The lowest mobility conditions are A2-W1 and A3-W1 for a cloaked and uncloaked droplet. These states have high levels of pinning due to the displacement of the lubricant layer and subsequent impalement of the droplet into the structure. The partially mobile states are those that have direct contact of the droplet with the solid (A2-W2 and A3-W2) and the case where oil is not retained on the top of the pillars in the presence of vapour (A2-W3). The highest mobility case is A3-W3 where the lubricating layer is maintained in the presence of vapour and underneath the droplet.

When wanting to create a surface with optimum mobility A3-W3 is the surface that will provide the least droplet contact with the solid substrate. The other 5 states will produce pinning on a similar scale to that on a hydrophobic surface[71].

2.2.7 Is there a Lubricating Layer?

For conditions A3-W3 to be satisfied a lubricating liquid has to be maintained below the droplet. To prove whether this is the case the energy calculations in Section 2.2.5 can be completed, but the lubricating layer also has to be directly viewed for the equations to be shown to hold true on an experimental level. There have been many studies in to SLIPS and how droplets act on the surfaces but there have been far less conclusively proving or disproving whether there is a lubricant layer present underneath the droplet.

Smith et al. in 2013 performed direct measurements of their predicted states showing that the pillared structures did exhibit the fully encapsulated state with lubricating liquid coating the tops of the pillars, however these measurements were only conducted whilst the surface was in contact with air[71]. Confocal images of the droplets were taken showing the deformation to the oil layer but not how adding a droplet to the system changes the oil layer underneath this droplet.

Schellenberger et al. again used confocal microscopy to image the droplet and oil layer[69]. They showed that on a pillared structured surface the droplet will always contact the tops of the pillars but won't displace the oil from the texture. The opposite is seen for inverse opals (droplets on a flat surface with a lubricating liquid) as there is

a thin layer of oil under the droplet that appears to be stable, with it's thickness being independent from the overall thickness of the lubricating layer.

Daniel et al. performed interference contrast microscopy on the thin film of lubricant underneath the droplet[72]. They showed that with differing combinations of lubricant and working liquid each of the states from A1 to A3 from Figure 2.2.7 can be achieved. When dragging the droplets across the surfaces the liquid layer is equal to the value predicted by the Landau-Levich-Derjaguin equation (LLD) for a flat surface (further discussed in Section 3.3.3). If the surface is constructed of pillars the pillar height changes how the thin film is formed and a correction to the LLD formula needs to be applied to calculate the thin film height[73, 72].

It is unlikely that droplets on SLIP surfaces would exhibit such low hysteresis and sliding angles[13] if the droplet itself was in contact with the underlying solid substrate, such as the pillared structure. Droplet-solid contact would revert the surface from a SLIPS to surface similar to the Cassie-Baxter case, reintroducing the characteristic contact angle hysteresis. Therefore, given the correct selection of liquids (working and lubricating), condition A3-W3 can be achieved to leave a layer of lubricant between the solid structure and droplet.

2.3 Applications

Whilst SLIPS provide an interesting test bed to study droplet dynamics on surfaces with a highly mobile contact line and how this affects phenomena such as evaporation, to be effective they have to have practical applications.

2.3.1 Evaporation and Condensation

Evaporation and condensation are two droplet phenomenoa that are seen both in nature and industrial processes/applications.

When droplets evaporate, if they are contaminated with particles, the particles will be transported to the contact line in the coffee ring effect[74, 75]. This is particularly relevant in inkjet printing applications where a droplet carries the coloured ink particles and when dried creates a specific pattern on a surface. If the droplet is deposited in the

wrong section this will result in a printing error[76]. If a SLIP surface is added into the system it will suppress the transport of the particles to the edge and allow a droplet to be moved after printing if deposited in the wrong section. Particle self-assembly is also normally conducted by suspending the particles within a liquid, by controlling both where the liquid sits on the surface and how it releases particles, more accurate and complex self-assembly can be conducted[77].

Superhydrophobic and SLIP surfaces exhibit similar droplet shedding abilities, however the condensation characteristics are very different. When droplets condense on superhydrophobic surfaces they tend to nucleate within the structure, adding to the surface pinning. As the surface texture for SLIPS has already been filled by the lubricating liquid the nucleation of the droplet happens on the lubricating layer[78]. Nucleation of water droplets has been shown to happen faster on surfaces that have been infused with a lubricating liquid. This coupled with the fact the surfaces are capable of shedding very small droplets provides a system which could easily be applied to fog harvesting devices, replicating the type of behaviour seen on a beetles back[79, 80].

Power plants exploit both the evaporation and condensation of droplets in cooling and steam condensing. As the droplets have a larger footprint with the surface, heat transfer can be accomplished more efficiently[80, 81]. Condensation will also happen quicker as the droplets can be transported from the surface faster creating more space for other droplets to subsequently condense[82].

2.3.2 Anti-Icing

Icing effects are commonplace especially on metallic surfaces. When wind turbines are exposed to extreme weather conditions the blades can form ice layers, impeding their optimum turbine blade design and reducing the amount of energy that can be gained from the surroundings. Aircraft also suffer adverse effects from ice accretion especially in moving mechanisms such as the engines and landing gear, if these key features are impeded the aircraft can no longer operate at it's full capacity[25, 83, 84].

2.3.3 Anti-Biofouling

Anti-biofouling coatings in the past have been created from chemicals that are generally toxic and pollute the environment. Such chemicals have been added to paints before being applied to ships[85]. The anti-biofouling works to kill the biofilms as they attach to the surface however when released into the sea, they are detrimental to other marine life[86]. Such coatings are now prohibited and therefore new systems need to be developed. Whilst anti-drag effects[87] were being investigated for the hulls of ships it was found that the anti-drag effects were also anti-adhesive, preventing the biocides from attaching to the surface before being able to form a biofilm[88, 89, 90, 91, 92]. The issue with current methods is that the anti-adhesive effects are reduced over time as the lubricating layer is depleted[34, 93].

2.3.4 Self-Cleaning

The self-cleaning ability of SLIP surfaces has been mainly focused on the anti-biofouling abilities, however for larger contaminants, such as dust, a droplet rolling across the surface is capable of picking up any contaminants and removing them as the droplet is removed from the surface[94, 95].

2.3.5 Droplet Shaping

The ability to shape droplets is an important factor when considering applications such as sensing. Sensing where a droplet is on a surface requires a large droplets footprint, on SLIPS the droplet have both a large droplet footprint and are mobile enough to be transported to different surface sections[96]. When applying an electric field to a droplet it can spread into a thin film following the lines of the electric field. A similar effect can be replicated by adding magnetic particles to the liquid and then applying a magnetic field, the droplet will again follow the magnetic field[97, 98].

2.3.6 Droplet Transport

Transporting liquids and droplets is used in many applications such as cassettes used for bio-medical devices. These normally exploit effects such as thermal gradients[99, 100, 101], chemical (wettability) gradients[102, 103], physical gradients[104, 105, 106], electric fields[107, 108, 109], magnetic fields[110, 111, 112, 113] or pressure behind liquids travelling through channels. The disadvantage with all of these effects is that there is the possibility for liquids to contaminate the surfaces and require a force to move the liquid. SLIPS coatings reduce the contamination and reduces the amount of force required for transport[114, 115, 116, 117, 118].

2.4 Conclusions

This chapter has demonstrated all the necessary theoretical concepts required to fully understand Slippery Liquid Infused Porous Surfaces and the criteria that must be fulfilled to produce these surfaces experimentally. For each of the results chapters the specific background will be outlined in the chapters introductory paragraphs.

Chapter 3

Methods

This chapter explains the standard techniques used to fabricate the surfaces used almost universally throughout this thesis. Each of the characterisation techniques implemented to provide more information about these surfaces is also outlined. The development, as well as characterisation thereof, for the surfaces explained within this chapter has allowed for the study of the droplet's complex interaction with the surfaces.

3.1 Substrate Cleaning

A sample cleaning method was developed to ensure that each sample would be clean, free from contaminants and that the samples were starting from the same initial conditions before every experiment. Plain glass slides (Fisherbrand) were used as the standard sample substrate for the SLIPS (Slippery Liquid Infused Porous Surfaces). These should have been clean when removed from the wrapping in which they were packed however, dust particles were visible on the surface. To remove the large particles a quick and very simple first step was implemented. This involved washing the samples in warm tap water and washing up liquid. The washing up liquid left a soap film on the surface which was removed by again rinsing the sample under running warm tap water. As the tap water could not be relied upon to be clean and any smaller contaminants that may be on the surface would not have been removed by the first cleaning step, the second cleaning step was implemented. A solution of Decon 90 (between 2% and 5%) was produced in a 500 ml beaker of De-Ionised (DI) water and the samples placed

into the solution. The samples were sonicated for 30 minutes in a slightly warmed bath (approximately 40°C) to agitate the samples and remove any contaminants. To then clean the sample from any remnants of the Decon 90, the samples were placed in a fresh beaker of pure DI water and the 30-minute sonication step repeated. The last cleaning step was a solvent rinse. The two solvents used were Acetone, then IPA (when Acetone dries it can leave streaks on the sample which the IPA removes). The samples were dried immediately after the IPA rinse with compressed air to give a clean, dry sample which could either be stored or used immediately.

3.2 Glaco Coating

Normally SLIPS are created by structuring a surface using a technique such as photolithography to create a pillared structure[13]. This pillared structure accompanied with a chemically hydrophobic coating creates a superhydrophobic surface, where if a droplet is deposited onto the surface it may sit on top of the pillars in a Cassie – Baxter state. Or if large enough, or the pressure on the droplet great enough, the droplet will be in a Wenzel state. To convert the pillared surface from hydrophobic to superhydrophobic a chemical coating, for example OTS (OctadecylTrichloroSilane) or Teflon, must be applied to the entirety of the structure[33, 35]. Once in a superhydrophobic state, droplets are more likely to stay in the Cassie – Baxter state, as the affinity to the surface has been further reduced, however the droplet can still be forced into a Wenzel state[26]. The disadvantage associated with producing a pillared, structured surface is that standard SU-8 Photolithography must be done on a flat substrate, on a small scale, reducing the possibility of the use of the surfaces within industrial or commercial applications. Not only would it be difficult to scale up the process in terms of physical size, it would also be difficult in terms of volume. In addition to this Photolithography is a time-consuming process as well as an expensive one, with the required components and equipment needing a large initial outlay and upkeep costs. Roll-to-roll nanoimprinting is another lithographical technique that can be performed on larger sample sizes and flexible substrates however it still requires access and upkeep of equipment and materials[34].

Another chemical based coating that could be added to the tops of the pillars is a commercial spray coating called Glaco Mirror Coat (Nippon Shine). The Glaco consists of propellants (to assist with the expulsion of the mixture from the can), nanoparticles (constructed from silicone and oxygen to create silica or SiO_2) and IPA to disperse the nanoparticles[35, 36, 119]. The nanoparticles have a chemical coating on them, presumably similar to OTS, however as Glaco is a commercial product the exact composition is unknown. The unique advantage of using Glaco is the nanoparticles themselves. If deposited correctly onto a substrate it is possible that this coating could fulfil the two criteria, structure and chemical modification, required for superhydrophobic surface, removing the need for an underlying, pillar like structure[120, 121].

3.2.1 Coating Method

To ensure that the coating of Glaco would be reproducible and could be repeated by others, a robust coating method had to be developed. Samples that were cleaned using the method outlined in Section 3.1 were placed into the fumehood at an angle (approximately equal to 75°). Glaco was then sprayed onto the sample, starting at the top, from left to right and then further down the sample right to left. This was classed as one coating. The angle of the samples allowed for the Glaco to flow down the sample and fully cloak the whole surface. As the Glaco runs down the sample there is some excess run off that gathers at the bottom, creating an edge bead. The samples were therefore all placed onto an absorbent cloth and the samples tilted from $\approx 75°$ to fully vertical in an attempt to remove this edge bead. After the first coating, the samples were left in the fumehood at the coating angle for 10 minutes to allow for the majority of the solvent to evaporate from the surface. Once the 10 minutes had elapsed there were two different possible methods that could be used to ensure all the solvent had evaporated. Method one involved removing the samples from the fumehood and placing them in an oven set to 250°C for 10 minutes (Figure 3.2.1). This method quickly drove the solvent from the sample. Method two simply required the sample to be left in the fumehood for 1 hour for slower solvent evaporation (Figure 3.2.1). Testing both of these methods by placing a droplet of water onto a selected

sample, produced a droplet that was partially stuck to the surface but did not indicate any significant difference between the two methods[120, 121].

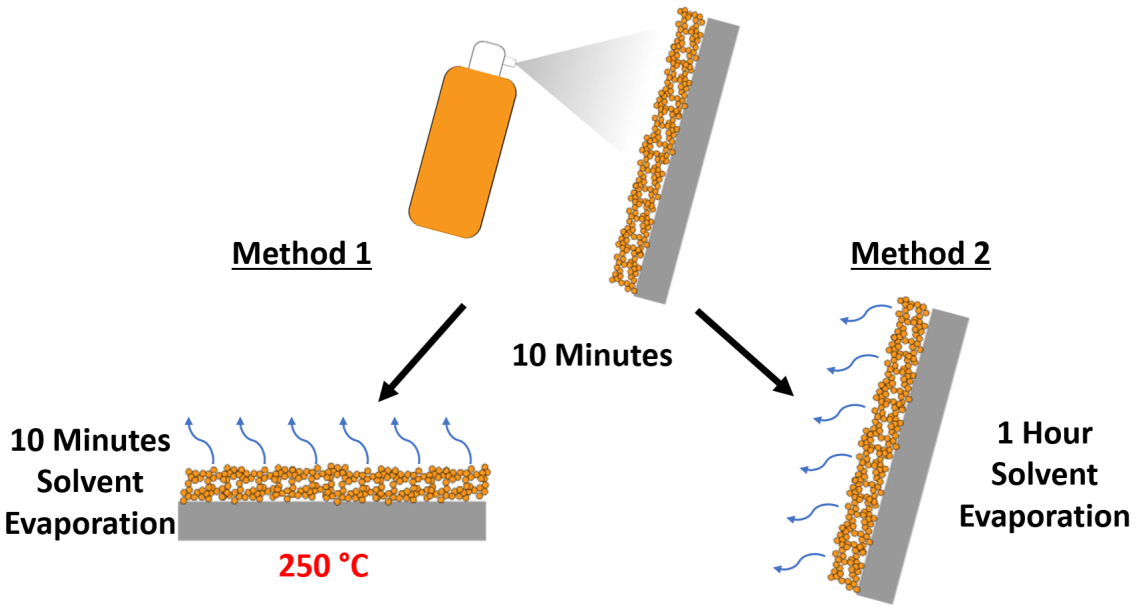

Figure 3.2.1: Coating method from cleaned substrate to Glaco deposition for a) fume-hood drying and b) oven drying.

The quick droplet test indicated that the Glaco surface was patchy and may require refinement or further coating. When considering the different types of substrates that might be used in further applications, not all of these may be resilient to heat, therefore using a method that can be completed at room temperature would be a better universal method. Hence, by taking method 2, the Glaco coating procedure was repeated 7 times, with two samples being removed from the batch after each coating, creating 16 samples in total with 8 different numbers of Glaco coats on the surface ranging from 0 to 7 coats.

According to the safety data sheet for Glaco it takes a total of 3 hours for the solvent to fully evaporate from the coated substrate, however the samples didn't visibly appear to have any solvent left on the substrate before 3 hours had elapsed, placing a droplet onto the sample didn't appear to damage the coating and the enhanced extraction given by the fumehood will have decreased the evaporation time.

3.2.2 Superhydrophobicity Characterisation

To be classed as a superhydrophobic surface, two main criteria must be met. These are, the surface should form a contact angle of 150° or larger with water and the surface must have a contact angle hysteresis of 10° or less[122]. To determine how many coatings of Glaco were required to produce a truly superhydrophobic coating, the samples ranging from 0 to 7 coats had to be characterised. Three different methods were used to characterise the samples, these were: the static contact angle, the contact angle hysteresis (by inflation and deflation) and the sliding angle. Each of these characterisation techniques were performed on a Krüss DSA 30 contact angle meter. Before any measurements were taken, the sample table on the Krüss DSA 30 was levelled using a Level Development Engineering level, which was accurate to 50 μm in the meter. The Krüss DSA 30 was equipped with a calibrated tilting table which was capable of tilting a sample from 0° to 90° in 0.1° increments, however the table had an ultimate accuracy of $\pm$ 0.2°, therefore the entirety of the equipment could only reasonably be levelled to an accuracy of $\pm$ 0.2°. After every five to ten measurements (depending on whether the characterisation technique being used required a sample change or movement of the table, or simple deposition of a droplet onto the sample) the level of the equipment was checked using a less accurate level. If the bubble on the spirit level was centred no adjustments were carried out, if the bubble had moved then the equipment was levelled as before.

To measure the static contact angle on the surface a droplet first had to be generated. The smallest volume droplet that could be produced using a 0.7 mm diameter needle (and to be accurate each time) was 2 μl. Once generated, the needle was bought down in order to allow the droplet to contact the surface. For the droplet to detach from the needle the force of adhesion to the surface needs to be greater than to the needle. For 2 μl droplets and Glaco coated surfaces the droplets did not detach from the needle, therefore the volume of the droplets had to be increased. Given that the capillary length for water is approximately 2.7 mm, the maximum volume for a droplet to be below the capillary length and for the surface tension to dominate over gravity is approximately 10 μl. However, even at this volume there were some areas of the

surface where the droplet would not detach from the needle, therefore the volume had to be increased by another 2 μl to 12 μl. From the images taken of the droplets, the static contact angle can be determined using the DSA4 software. This involves placing the baseline and computing the contact angle on the left and right hand side by fitting a tangent to the edge of the droplet. The software then checks the fitting of the first tangent by fitting a second tangent. The software determines where these tangents should be by looking at the gradient of grey between the background that should be white and the droplet which should be black. However, when zooming in on the contact point, it is clear to see that the software is not fitting to the contact point and edge of the droplet, therefore subsequent fitting is done using ImageJ. In ImageJ, the image is first sharpened and the brightness/contrast adjusted so as to see the baseline and contact line more clearly, but not enough to lose definition on the edge of the droplet. As the sample is reflective, to position the baseline correctly the reflection of the droplet was used. The point at which the reflection and droplet meet was deemed to be the baseline. The angle tool was used to fit a tangent to the edge of the droplet at the contact point with the baseline in a manner similar to the DSA software by looking at the gradient of colour between background and droplet. Table 3.2.1 shows the values for the static contact angles for zero to seven coats of Glaco. The errors reported in Table 3.2.1 are the standard deviations taken from the experimental static contact angles used to produce the Mean CA (Table 3.2.1). However, in reality the error related to the static contact angle measurement is much higher as changing the baseline/tangent position by just one pixel, or adjusting the brightness/contrast by one point can change the static contact angle by approximately $\pm$ 5°. The errors reported throughout the remainder of this thesis will be the standard deviations of the average measurements taken using the same ImageJ analysis technique.

From the static contact angles, Glaco coating numbers three to six show superhydrophobic static contact angles, including errors. However, the static contact angle is not the most accurate measure as the angle determined from the images is not the equilibrium contact angle and could sit anywhere between the advancing and receding contact angles for the surface.

Table 3.2.1: Mean static contact angles for zero to seven Glaco coats with the volume of droplets used.

Coating Number	Mean CA (°)	Error CA (°)	Average Volume (μl)
0	43.0	1.0	2.0
1	148.8	1.5	7.3
2	153.0	3.0	10.7
3	155.2	0.5	11.3
4	153.0	0.9	10.7
5	152.4	0.6	10.0
6	152.4	0.6	10.0
7	149.9	2.2	10.0

To determine what the advancing and receding contact angles were for the surface a 4 μl droplet (still attached to the needle) was bought into contact with the surface. The droplet was left to settle until any vibrations from moving the needle had dissipated. A further 4μl was pumped into the droplet, before again leaving the droplet to settle. The 4 μl that was added to the droplet was subsequently removed by deflating the droplet and drawing the liquid back into the needle. To determine the advancing frame, the inflation frames were scanned through until there was a change in droplet base diameter. The contact angles in the frame prior to the increase was measured for the advancing angle. The same procedure was followed for the deflation frames, except a decrease in base diameter was looked for. Again, the angles in the frame prior to the decrease were measured to give the receding angle. Taking the difference between the advancing and receding angles produces the contact angle hysteresis, seen in Table 3.2.2. Similarly to static contact angle measurements, the error for contact angle hysteresis is larger than the standard deviation in Table 3.2.2. For the static contact angles the error was approximately $\pm$ 5°, measuring the advancing and receding angles for CAH also involves the determination of the baseline and tangent for contact angle measurement so is subject to the same error value, however it also involves determining which video frame contains the advancing and receding angles. This adds to the error, increasing the value to approximately $\pm$ 8°, again the errors reported in subsequent tables will be the standard deviations.

Table 3.2.2: Advancing, receding and contact angle hysteresis values for all 7 coats of Glaco.

Coating Number	Advancing (°)	Receding (°)	CAH (°)	Error CAH (°)
0	52.3	0.0	52.3	0.7
1	155.0	142.0	13.0	5.0
2	158.75	149.90	12.85	0.21
3	163.15	136.25	26.90	0.14
4	162.9	155.0	7.9	1.1
5	166.1	161.0	5.1	1.1
6	163.0	127.2	35.8	2.0
7	163.0	140.0	23.0	13.0

From the values for contact angle hysteresis only four and five Glaco coats fulfils the <10° requirement for superhydrophobicity. As both these samples also had static contact angles above 150°, both requirements for superhydrophobicity have been reached. The static contact angles measured in Table 3.2.1. should be between the advancing and receding angles. For samples with four and five Glaco coats this is not the case. As the volume of water droplet required to detach from the needle is close to the capillary length, the shadow created by the droplet partially hides the exact contact point, decreasing the measured angle. Therefore, as the droplet volume used for the hysteresis is lower, the true static contact angle is between the advancing and receding.

An additional way to measure the contact angle hysteresis is to measure the sliding angle. This is the angle a sample needs to be tilted to before the onset of continuous droplet motion is observed[123, 124]. The leading droplet contact line, pointing down the slope, should form the advancing angle and trailing edge, the receding angle. As with the static contact angle measurements the droplet must fully detach from the needle, therefore the volume on the Glaco substrates must be large. Despite the fact that the droplets are below the capillary length and surface tension dominates, gravity still affects the droplet and will help to pull the droplet away from the surface. The maximum angle that the table was taken to was 20°, as 10° is the superhydrophobic limit, taking the table to double this value should release the droplet if it is caught on a pinning point. If the droplet is in fact being affected by the surface as a whole it

shouldn't slide at 20°. As evaporation is an issue for droplets in ambient conditions, for the first droplet deposited onto the surface the table was tilted quickly until the droplet slid. This sliding angle was recorded and for the subsequent droplets the table was tilted quickly to approximately this value and then the table's angle increased in increments of 0.1° until the droplet slid, providing a more accurate value for the sliding angle. Table 3.2.3 shows the sliding angles for each number of Glaco coats.

Table 3.2.3: Sliding angle measurements with the accompanying errors for each number of Glaco coatings.

Coating Number	Average Volume (μl)	Sliding Angle (°)	Error SA (°)
0	2.0	>20	
1	7.3	18.4	2.7
2	10.7	12.0	7.0
3	11.3	15.0	4.0
4	10.7	9.7	2.7
5	10.0	7.6	0.5
6	10.0	17.8	3.8
7	10.0	>20	

Again, samples with four and five Glaco coats have a hysteresis value of less than 10°, but when considering the errors only the sample with five coats had a sliding angle <10°. Therefore, as the sample with five coats fulfilled the criteria using all three characterisation techniques, this sample and coating method was used on all subsequent samples.

3.2.3 SEM

In order to understand the physical structure of the Glaco coated samples and how the superhydrophobicity, characterised by the DSA measurements, relates to the nanoparticulate structure. Apart from being an interesting aspect of the surface, the physical structure can provide information on the surface roughness, porosity, coverage and height. To view this structure, a Scanning Electron Microscope, SEM (Tescan MIRA3), is used to take micron scale images. As Glaco is a highly insulating material a thin layer of Platinum has to be applied to the surface to dissipate the charge from the elec-

trons. In order to avoid smothering the nanoparticles and hide the surface structure, 4 nm of Platinum was deposited. Taking top view images of this surface, Figure 3.2.2, at a view field of 31.5 μm provides a general overview of how well the surface is coated. Figure 3.2.2 a shows that the entirety of the surface area is coated with darker and brighter areas designating troughs and peaks in the Glaco, giving some roughness to the surface. Selecting an area on the sample and increasing the magnification to decrease the view field to 5 μm provides a more detailed picture of the particle structure with the porosity and roughness of the smaller aggregates evident (Figure 3.2.2 b). From both images in Figure 3.2.2 it is clear that the Glaco has covered the entirety of the substrate producing a fairly even overall coating, with a significant porous network into which the oil can imbibe.

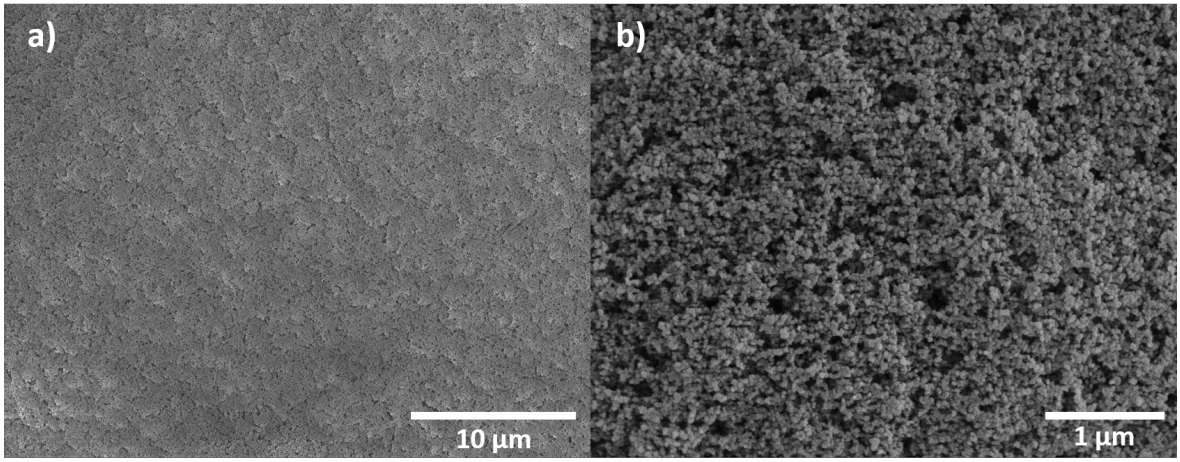

Figure 3.2.2: Top view image of a sample coated 5 times with Glaco for a view field of a 35.7 μm and b 5 μm.

The slight roughness apparent in the Glaco may account for the presence of some pinning on the surface and the sliding angles of $7.6° \pm 0.5°$ as well as the hysteresis of $5.1° \pm 1.1°$. However, it is expected that either a lack of particles or agglomerations of particles are causing larger hysteresis values on the surface with more and less numbers of Glaco coats.

The height of the coating cannot be measured from the top view images as the substrate – Glaco interface cannot be seen and the depth of the sample can also not be measured. Therefore, to measure the height of the coating, cross-sectional images through the sample have to be taken. To do this the samples have to be snapped.

Typically, to snap a sample, such as a glass slide, the surface would be scored with a diamond scribe before snapping the sample along this line. However, for the Glaco there are a few issues with this method. If the surface were to be scored before the application of the Glaco, when spraying the particles onto the surface the defect may create a pinning point, affecting the surface coating at the point, meaning any images taken would not be a true representation of the surface. Scoring the surface after coating would damage and potentially remove some of the Glaco, again producing inaccurate surface images. The other issue with both of these methods is that the scored line creates a position to induce a forced break in the surface and coating. This risks having parts of the coating possibly break off around the edge, again giving an incorrect picture of the particle height and structure. To produce a natural break in the substrate the sample can be placed over a Tungsten wire and pressure applied to either side of the sample. The wire does not force the sample to break where it is positioned but it enables a small gap to be formed under the sample meaning that when the pressure is applied the sample will break at its weakest point. The subsequent sample was prepared as before with a thin platinum coating but instead of the flat area of the sample being in line of the electrons, the sample is rotated 90° for the snapped edge to now be visible. Figure 3.2.3 shows a typical example of a cross – section with the height of the coating measured using the SEM. From this image the porous network can be clearly seen to extend from the upper, flat surface (Figure 3.2.2 b) to the substrate – Glaco interface. The roughness that was evident in the top view figures also does not appear to affect the uniformity of the height to a large degree, with the average height of the Glaco measuring 1.93 μm $\pm$ 0.16 μm.

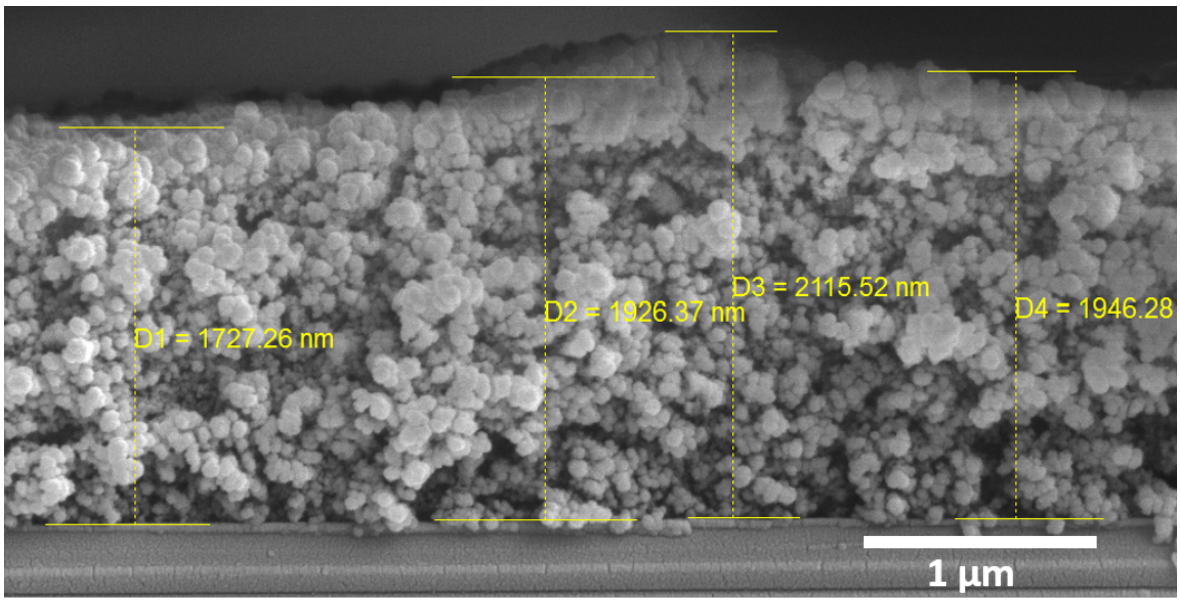

Figure 3.2.3: Cross – sectional image of a sample coated 5 times with Glaco, with the heights of the layer overlaid on the image.

From Figure 3.2.2 b) and Figure 3.2.3 it is possible, using ImageJ and the SEM scale bar, to determine a rough estimate of the particle size. There appears to be a significant variation in particle sizes in both images but given the particles are so small it is difficult to separate one particle from another. By performing some measurements on Figure 3.2.2 b) the smallest particle size was approximately 40 nm and the largest approximately 60 nm in diameter. Performing similar measurements on Figure 3.2.3 gives slightly larger particles, with the smallest diameter approximately equalling 80 nm and the largest 100 nm. Comparing the two figures visually is difficult as the working distance and view field are slightly different, however the particle size should be consistent for different coatings. Despite the disparity between the particle diameter measurements there is a difference of 20 nm in particle diameter within each sample, contributing to some of the roughness but also to the porosity.

Once all of the superhydrophobic characterisation techniques have been carried out, the surface is ready to be converted into a SLIPS via the addition of oil.

3.3 Oil Thickness

3.3.1 Different Methods for Oil Imbibition

To change the sample from a superhydrophobic surface to a SLIP surface the air gaps have to be imbibed with an oil[11]. There are many ways to introduce oil to the surface, one of which could be to simply pipette a certain volume of oil onto the sample and allow the oil to wick into the structure however this is a slow process. Another way would be to increase the spreading time by spinning oil onto the sample with increasing spin speeds giving thinner layers of oil. The final way is to immerse the sample into an oil bath and then withdraw the sample at a given speed with high speeds producing thicker oil layers (according to Landau - Levich - Dejaguan - LLD theory). The disadvantage with the first method is the oil thickness can only be calculated by a volume calculation. This causes problems when considering the porosity of the nanoparticles, as Glaco is a commercial product, the exact composition of the SiO_2 particles is unknown meaning they may be hollow, creating a further pore for the oil to imbibe into and therefore lowering the oil thickness. When spinning the oil, a spin curve has to be created , meaning that the thickness of the oil layer has to be directly measured which is difficult to do as the oil and substrate are index matched. The spinning of the oil is also a messy method of introducing oil to the surface as the excess oil is difficult to clean from equipment and can cause cross contamination. The final method, oil dipping, is the easiest experimental method to produce SLIPS and is the method used for the subsequent SLIPS production.

3.3.2 Experimental Method

A dipping robot, Fisnar 4200N, was used to immerse and withdraw the Glaco coated sample from a bath of Silicone oil (Figure 3.3.1). The Fisnar was capable of a 50 mm distance of travel and a smallest withdrawal speed of 0.1 mm/s, meaning a full run time of 500 seconds. The Silicone oil was stored in a dipping pot 80 mm in length to allow for a full glass slide (25 mm by 75 mm) to be fully immersed and withdrawn in one dip. The withdrawal speed that the Fisnar operates at could be changed by altering the

operating code, for example, from 0.1 mm/s to 2.5 mm/s. Each sample was immersed in the Silicone oil for 10 seconds before withdrawal. As the dipping robot produces a thin film on the surface of the sample, it is possible to re-dip a previously imbibed surface to produce a thinner or thicker layer than had previously been present on the surface.

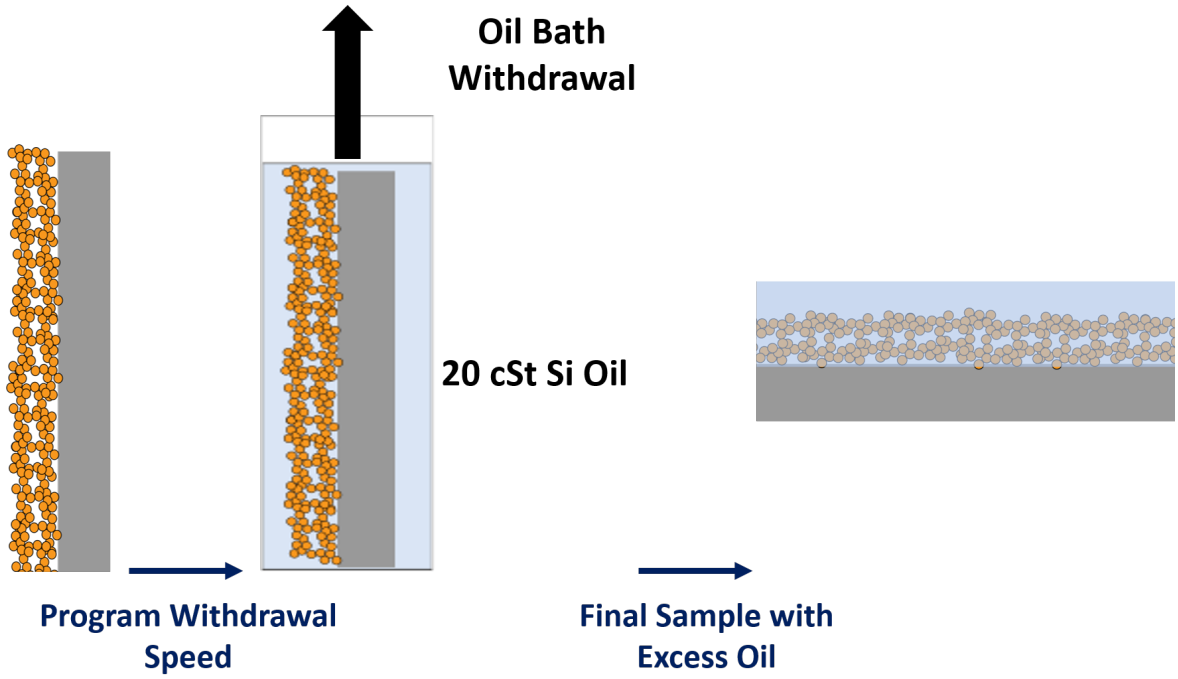

Figure 3.3.1: Schematic depicting the Glaco surface dipping procedure.

3.3.3 LLD

By changing and increasing the withdrawal speed, the thickness of the oil layer will increase as the thin layer of oil left on the surface does not have time for the bulk of the liquid, in the oil bath, to pull and remove the liquid from the surface. The thickness of this oil film will be dependent on the viscosity of the oil, gravitational effects and the oils surface tension. By balancing these forces the thickness can be theoretically calculated using the Landau – Levich – Derjaguin (LLD) formula,[73, 125, 126]

$$h_o \approx 0.94 \alpha Ca^{2/3}. \tag{3.3.1}$$

Where the height of the oil, h_o, is dependent on the capillary length,

$$\alpha = (\gamma/\rho g)^{1/2}, \tag{3.3.2}$$

and capillary number,

$$Ca = \frac{\eta V}{\gamma}. \tag{3.3.3}$$

The surface tension (γ), density (ρ) and viscosity (η) can all be taken from the data sheet for the oil used. The withdrawal speed (V) is the speed set experimentally and g, the acceleration due to gravity. The LLD applies to surfaces that are flat and requires a correction factor for structured surfaces. As the Glaco layer has been built on the surface via multiple spray coatings until resembling a flat topped layer, with a porous network the standard LLD (Equation 3.3.1) can be applied.

The oil chosen for the experiments was 20 cSt Silicone oil. This silicone oil has little to no evaporation from the surface, so should remain there for an extended period of time and the viscosity of the oil can easily be changed without changing the surface tension, or significantly changing the density.

For the LLD equation to accurately predict the physical height of the oil layer the capillary number (Ca) must be below 0.01, otherwise the layer will, in reality, be thinner than predicted. In the following experiments the withdrawal speed (V) was increased from the thinnest oil layer (0.1 mm/s) to a very thick oil layer at 2.5 mm/s where the capillary number should vary from 0.000096 to 0.0024, which fulfils the small capillary number criteria[73]. Putting these values into Equation 3.3.1 produces the theoretical graph plotted in Figure 3.3.2, with the withdrawal speed (in mm/s) plotted as a function of oil layer thickness, so the thickness of the oil layers in μm can be directly determined from the graph. From the LLD equation the overall oil thickness should vary from 2.87 μm to 24.55 μm.

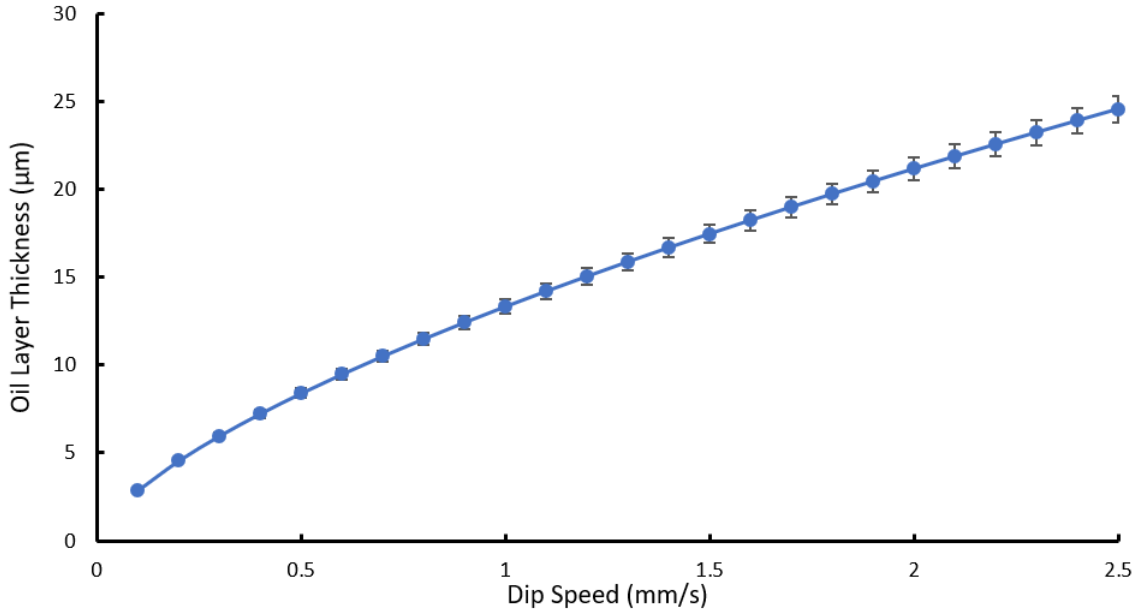

Figure 3.3.2: LLD equation plotted for 20 cSt Silicone Oil.

3.3.4 Confocal Microscopy

To verify that the LLD was producing oil thickness values that were reasonable for the SLIP surfaces, the oil thickness had to be directly measured. As has previously been stated, measuring the thickness of the oil layer is difficult to do. Using physical instruments such as SEM, AFM or stylus profilometry cause abrasion to the surface which can damage or remove the fragile underlying Glaco coating and as Silicone oil has a low contact angle on most surfaces it will spread and coat the instruments. Therefore, a non-destructive method had to be used to measure the thickness.

Confocal microscopy was one method that had been previously used to measure the thickness of the oil[115]. This involves dying the oil with a lyophilic fluorescent dye that could possibly change some of the oil's properties (such as viscosity or surface tension) and therefore the height of the oil layer. A 40 x lens was used on a Nikon A1R, producing a resolution or z-step of 0.38 μm. Scans through certain samples were taken with Figure 3.3.3 depicting two scans from samples dyed with fluorescin with a withdrawal speed of 0.1 mm/s (Figure 3.3.3 a) and 1.0 mm/s (Figure 3.3.3 b). Figure 3.3.3 a) is a scan of the thinnest oil layer, predicted by the LLD to equal 2.87 μm, with the bright green in the image indicating the oil layer itself. Determining the bottom of the sample, by scanning through the confocal slices until the was a

brightness change, places the interface between glass and oil at a z-position of 5.25 μm. Scanning up through the slices to the air – oil interface gives a z-position of 9.75 μm. Subtracting these values produces a film thickness of 4.50 μm, which is much larger than expected given the value from the LLD. For Figure 3.3.3 b), the scan of the 1.0 mm/s withdrawal speed sample (13.33 μm from the LLD) was performed in the opposite direction to Figure 3.3.3 a. The bottom of the oil layer was positioned at 7.88 μm and the top of the sample at 19.88 μm, meaning a total film thickness of 12.00 μm, which is slightly lower than the theoretical value (13.33 μm).

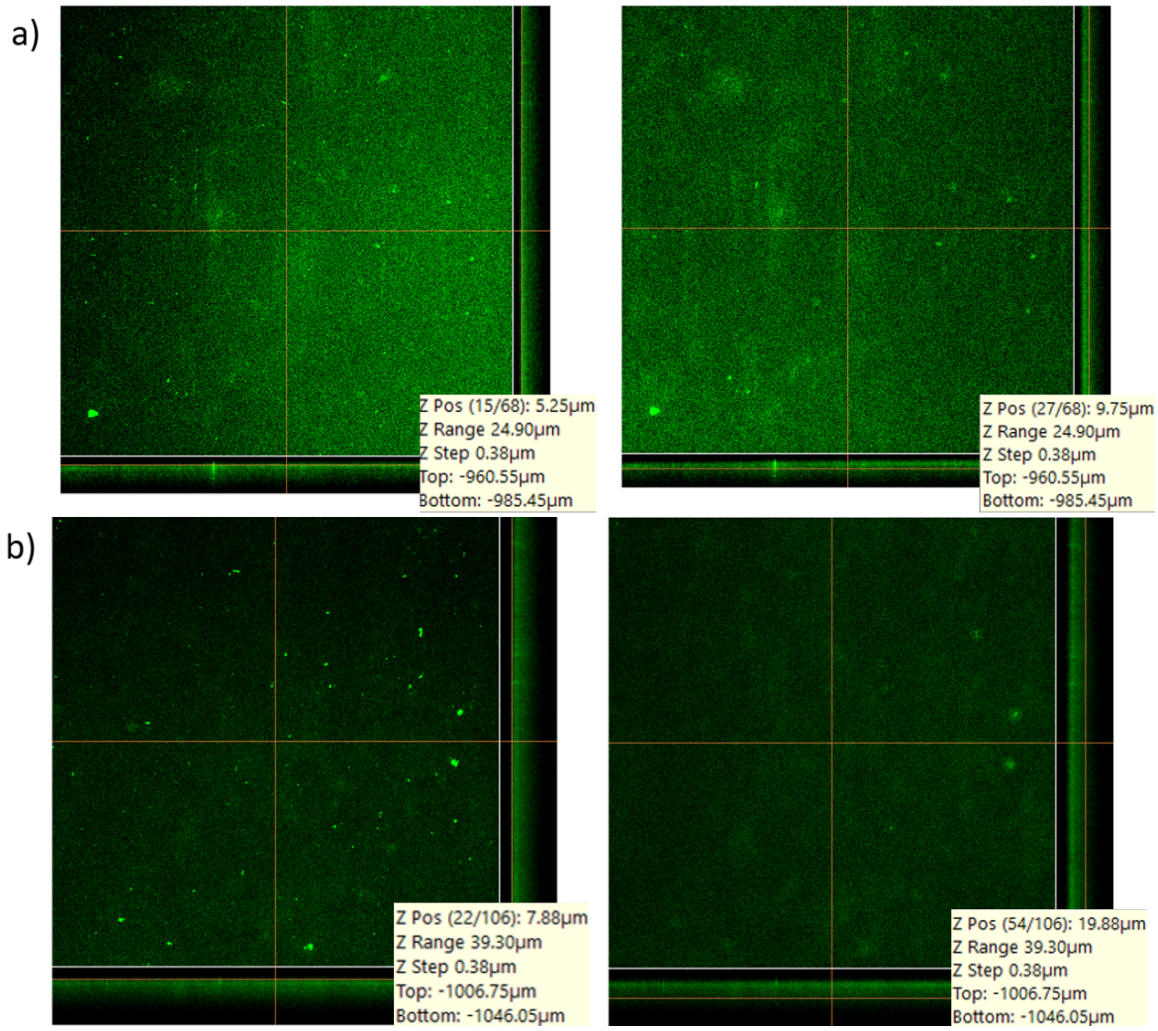

Figure 3.3.3: Two confocal scans of the silicone oil imbibed surfaces with a the surface withdrawn at a) speed of 0.1 mm/s and b) withdrawn at 1.0 mm/s.

The interfaces of the oil layer were difficult to determine due to the amount of noise in the sample, possibly caused by the lack of fluorescent dye in the oil. This uncertainty in determining which z position in the image stack corresponds to either of the two

interfaces increases the error in the measurement from the z resolution to a maximum of three times the z resolution (1.14 μm). Therefore, the error in the measurements taken via confocal microscopy is large when considering the size of the film heights being measured. There appears to be no distinguishing feature representing the separation between the nanoparticle layer and the silicone oil. This would indicate that the silicone oil had fully imbibed into the particle layer and coated all of the particles.

3.3.5 Reflectometry

Changing the sample base from a glass slide to a silicon wafer not only provides a fully flat sample (when compared with glass) but it is a highly reflective sample, allowing a reflectometer to be used on the sample. A reflectometer transmits white light from an optical fibre into the sample and monitors how much light is returned over a 3 mm diameter area, converting the amount of light into a thickness given a certain refractive index.

As the height of the Glaco layer, measured via SEM cross sections, equals 1.93 μm and the predicted height of the oil layer, calculated using the LLD, is 2.87 μm, then there must be a bi-layer on the surface, meaning that two refractive indices may have to be used for the reflectometer. The refractive index of the Glaco was unknown but could be inversely calculated given the knowledge of the height provided by the SEM. A sample of Glaco, without oil, on a silicon wafer was placed under the reflectometer and the refractive index changed until giving the value of the thickness of Glaco that would be expected. As the area the reflectometer focused on was 3 mm in diameter any non-uniformities would be smoothed. By performing this experiment the refractive index was found to be 1.1 for an approximate thickness of 2.0 μm.

After the addition of the oil, the Glaco sample changes from a slightly opaque, white surface to fully optically transparent, indicating that the Glaco has become index matched with the silicone oil. Therefore, the reflectometer was used without inputting a value for the refractive index and it was instead asked to calculate a value for the refractive index using a Fourier transform. By doing this a peak was seen at 1.45 (close to the refractive index value for pure silicone oil of 1.403 taken from the

Sigma website) but there was no indication of two layers, Glaco and silicone oil, present on the surface. Given this information only one refractive was used (1.403) to measure the oil layer thickness for the withdrawal speeds used from 0.1 mm/s to 2.5 mm/s. At low withdrawal speeds the theoretical curve generated by the reflectometry software struggled to fit the data for the measured thickness at the full range of wavelengths (approximately 300 nm to 800 nm). Reducing the wavelength range to the central region of the visible spectrum (approximately 450 nm to 650 nm) improves the fitting of the data. Repeating the reflectometry measurement for the thinnest oil layer (withdrawal speed of 0.1 mm/s) in 3 different sections of the sample gave an average thickness of 3.09 μm $\pm$ 0.35 μm. The reflectometry was repeated for all five remaining oil thicknesses for the reduced range of wavelengths producing the data plotted in Figure 3.3.4.

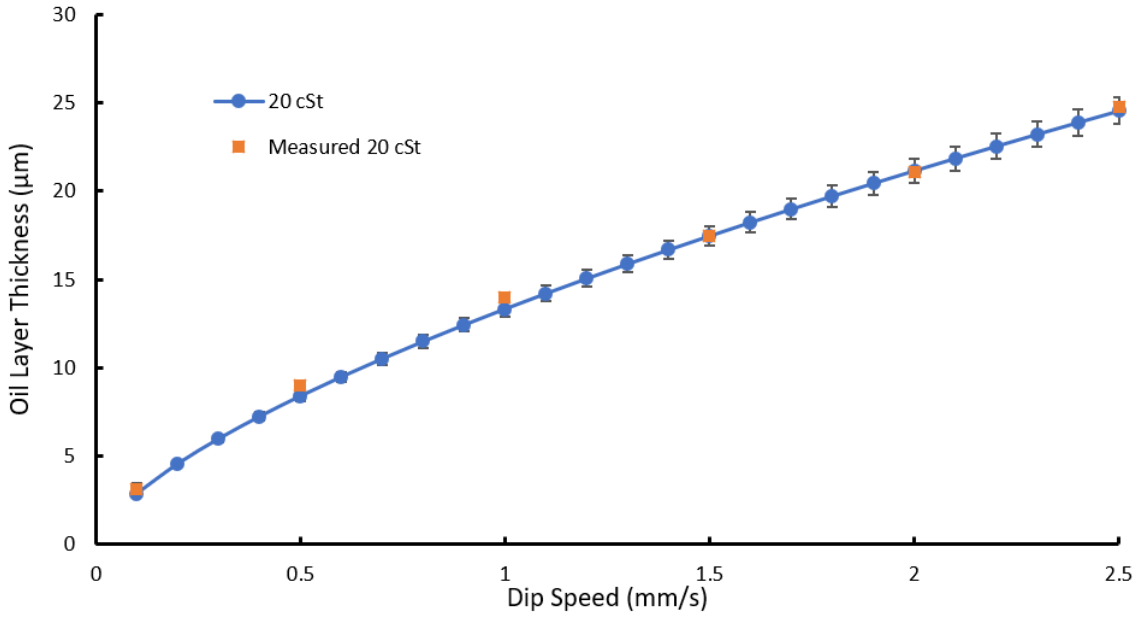

Figure 3.3.4: Experimental reflectometry data (orange coloured squares) overlaid on the 20 cSt LLD data (blue circles) showing the agreement between the two data sets.

As there does not appear to be a separation between the imbibed Glaco and what would be the mobile silicone oil layer (the layer on top of the oil that is locked into the porous structure) then the values measured experimentally and by the LLD is a combination of the two. To extract the values for the mobile oil layer the height of the Glaco has to be subtracted from the experimental values measured from the reflectometer, giving the values plotted in Figure 3.3.5.

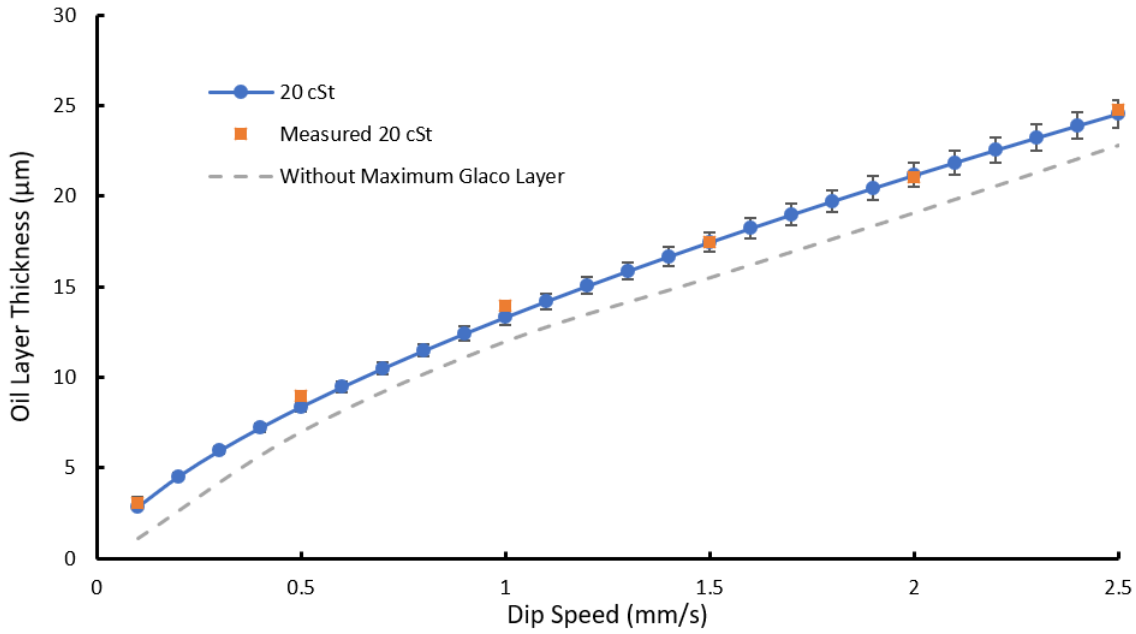

Figure 3.3.5: Mobile oil layer thickness calculated for each of the six withdrawal speeds (grey dashed line) compared with the LLD and experimental values.

3.4 Spreading Criteria

To calculate whether it is more energetically favourable for the oil to fully cloak the droplet or to only form a wetting ridge (Smith et al.)[71] a spreading coefficient calculation can be performed. Given the knowledge of the interfacial tensions between water and vapour, $\gamma_{w,v}$, water and oil, $\gamma_{w,o}$, and oil and vapour, $\gamma_{o,v}$, a spreading coefficient calculation can be calculated from the difference between these values

$$S^{v}_{w,o} = \gamma_{w,v} - \gamma_{w,o} - \gamma_{o,v}. \tag{3.4.1}$$

If the combination of water-oil and oil-vapour interfacial tensions is greater than water-vapour then the spreading coefficient will be less than zero and the oil will not spread and replace the water-vapour interface with water-oil and oil-vapour, leaving the droplet uncloaked. If the interfacial tension of water-vapour is greater than or equal to the combination of water-oil and oil-vapour then the spreading coefficient will be positive (or zero), meaning that there will be a thin layer of the lubricating liquid to cloak the droplet.

For the combination of liquids used to make SLIPS the interfacial tensions are as

follows: $\gamma_{w,v} = 72.8$ mN/m, $\gamma_{w,o} = 38.0$ mN/m [127], $\gamma_{o,v} = 19.8$ mN/m. Entering these values into Equation 3.4.1 produces a spreading coefficient of 15.8 mN/m therefore, for SLIPS using 20 cSt silicone oil as the lubricating liquid and water as the working liquid, any droplets on the surface will be cloaked[128]. The thickness of the cloaking layer is expected to vary over the droplet/vapour, now droplet/oil, interface. Towards the contact line the layer thickness is large, exhibited by the thick wetting ridge. However, at the point where the wetting ridge ends and the spherical cap of the droplet begins the layer is expected to be nanometrically thin as previous studies have found that this layer has a nominal effect on evaporative effects[67]. Therefore, this cloaking layer is expected to have no effect on subsequent contact angle measurements so long as they are taken above the wetting ridge.

3.5 SLIPS Characterisation

To ensure that every sample produced had the same qualities the characteristics had to be measured. For superhydrophobic surfaces this involved taking measurements of the contact angle, the contact angle hysteresis and the sliding angle. For SLIPS the same procedure was followed.

Unlike with a dry, superhydrophobic surface, a SLIP Surface, on first inspection, does not appear to have a clear, well defined contact line. It has in the past been defined as the point of intersection with the surface baseline, where if a circle were to be fitted to the spherical cap section and extrapolated through the wetting ridge these two points would cross (Guan et al.)[67]. As what is happening with the droplets at the surface is unclear, it is perhaps not correct to assume that the droplet is making any contact whatsoever with the surface. The other way to define the contact angle is to fit the baseline to the top of the wetting ridge at the point where the positive wetting ridge curvature changes into a negative droplet curvature (Figure 3.5.1). At this point calling this measured angle a contact angle is slightly incorrect as the droplet is not truly contacting a solid substrate. Therefore, to differentiate between an angle measured for a droplet contacting a solid and a droplet on a SLIPS, this angle will be termed an apparent SLIPS contact angle (θ_{app}).

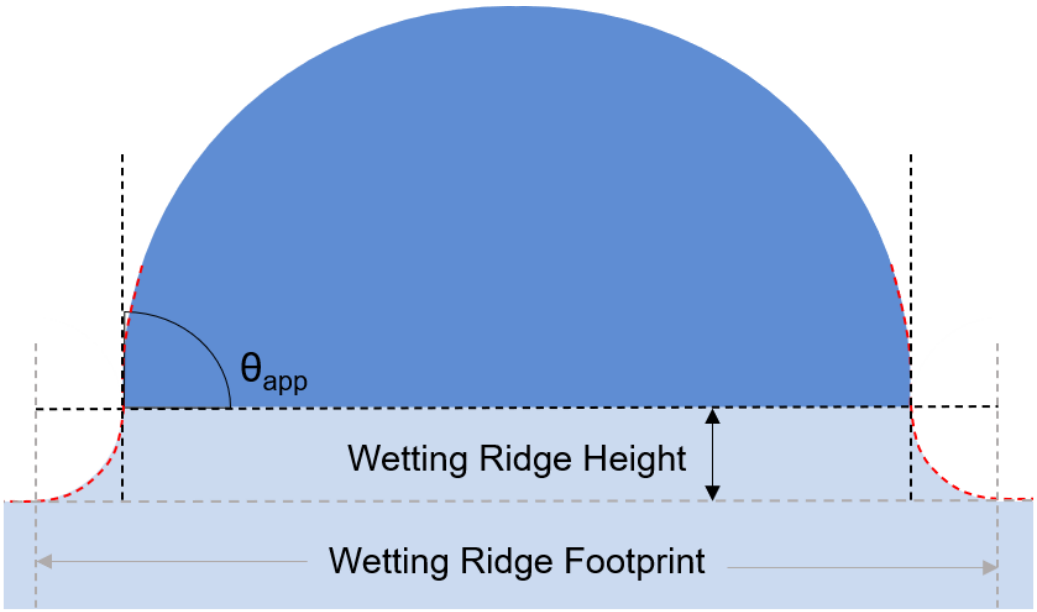

Figure 3.5.1: A droplet schematic to show the procedure used to measure wetting ridge height, footprint and apparent SLIPS contact angle on a SLIP Surface.

One disadvantage of this method is that the wetting ridge height changes with oil thickness on the surface. Figure 3.5.2 shows two experimental images of a droplet on a surface dipped at the smallest controllable withdrawal speed (0.1 mm/s) and (2.0 mm/s) with the corresponding apparent contact angles displayed on the images.

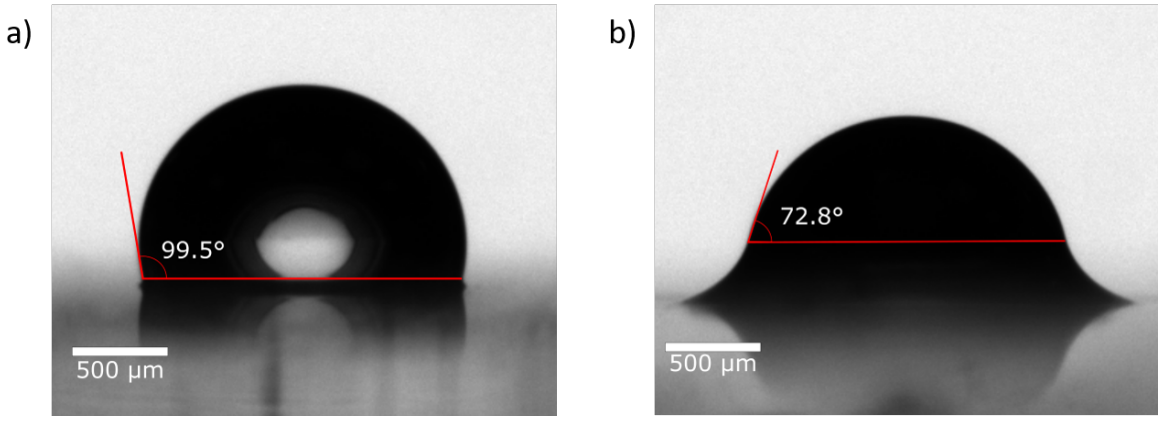

Figure 3.5.2: Typical experimental images of a droplet sitting on a) a surface withdrawn at 0.1 mm/s and b) a surface withdrawn at 2.0 mm/s with the corresponding experimental contact angles.

The contact angles on SLIP Surfaces withdrawn at a range of speeds from 0.1 mm/s to 2.5 mm/s is displayed in Table 3.5.1.

Table 3.5.1: Contact angles for 2 μl droplets deposited onto SLIPS withdrawn from an oil bath at speeds ranging from 0.1 mm/s to 2.5 mm/s.

Withdrawal Speed (mm/s)	Oil Thickness (μm)	CAL (°)	CAR (°)	Mean CA (°)	Error (°)
	1.93	108.6	108.2	108.4	0.2
0.1	3.09	97.3	101.7	99.5	2.2
0.5	8.98	88.3	94.3	91.3	3.0
1.0	13.97	85.7	82.2	84.0	1.8
1.5	17.48	74.4	76.1	75.3	0.9
2.0	21.07	77.1	68.5	72.8	4.3
2.5	24.79	68.7	68.5	68.6	0.1

By simply changing the withdrawal speed, the apparent contact angle changes from 100° to 70° causing a change of 30° turning the surface (when considering standard contact angles) from a hydrophobic too hydrophilic surface. Even when withdrawn at the slowest controllable speed, there was still a small layer (mobile oil layer) left on top of the nanoparticulate structure, contributing to the height of the wetting ridge and effecting the contact angle.

To achieve an apparent contact angle that is the closest measurable to what a contact angle would be on a SLIP Surface the oil layer needs to be thinned down to the smallest possible value, creating a conformal SLIPS coating. To do this the surface was rinsed with DI water along with a compressed air run across the surface until there was no oil accumulation at the sample edges. Any oil that was not held on the surface by van der Waals forces was removed by this method. Once the oil thickness had been thinned down to this level the height becomes comparable, within error, to the nanoparticle thickness of 1.93 μm $\pm$ 0.16 μm which has been confirmed with further reflectometry measurements. Placing a droplet on this surface further confirms the removal of the mobile oil layer with the wetting ridge becoming barely visible (Figure 3.5.3). The value for the apparent contact angle measured for a 2 μl droplet on the surface is 108.4° (Figure 3.5.3).

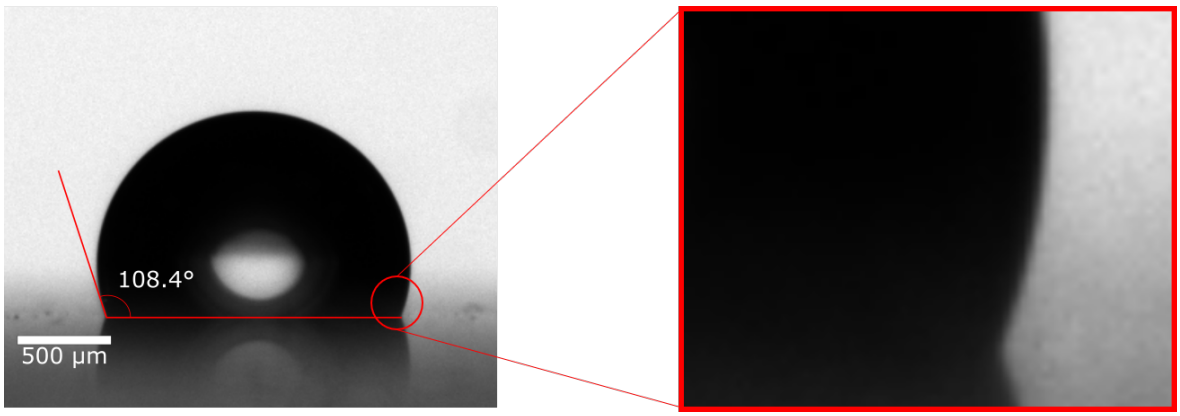

Figure 3.5.3: A 2 μl droplet on top of a conformal SLIPS, with the wetting ridge no longer visible on the surface.

To theoretically predict this value, a slight alteration to the Young equation (Equation 3.5.1) can be performed to include and effective surface tension, which compensates for the replacement of the water – vapour interface with oil – vapour and water – oil, given a positive spreading coefficient [41].

$$cos\theta_{app} = \frac{\gamma_{ov} - \gamma_{wo}}{\gamma_{eff}}, \tag{3.5.1}$$

$$\gamma_{eff} = \gamma_{ov} + \gamma_{wo}. \tag{3.5.2}$$

Performing this calculation for the values of γ_{ov} = 19.8 mN/m and γ_{wo} = 38.0 mN/m (Banpurkar et al.[127]) produces the value of

$$cos\theta_{app} = \frac{19.8 - 38.0}{19.8 + 38.0} = -0.31488. \tag{3.5.3}$$

$$\theta_{app} = 108.4°. \tag{3.5.4}$$

The theoretical value of 108.4° and the experimental on conformal SLIPS (108.4° ± 0.2°) are in good agreement with each other, indicating that the surface produced experimentally is truly conformal.

The hysteresis measurements were conducted in much the same way as previously seen in Section 3.2.2 with the position of the baseline adjusted to be situated at the

top of the wetting ridge. As the droplet is inflated and deflated the droplet not only changes in volume but it spends more time on the surface, allowing the wetting ridge to increase in height. This means that between the advancing and receding frames the baseline needed to be moved further up the droplet which has the effect of increasing the hysteresis value measured. Figure 3.5.4 shows an example of hysteresis measurements performed on SLIPS withdrawn at 0.1 mm/s with the baseline and apparent contact angles measured for the advancing and receding frames.

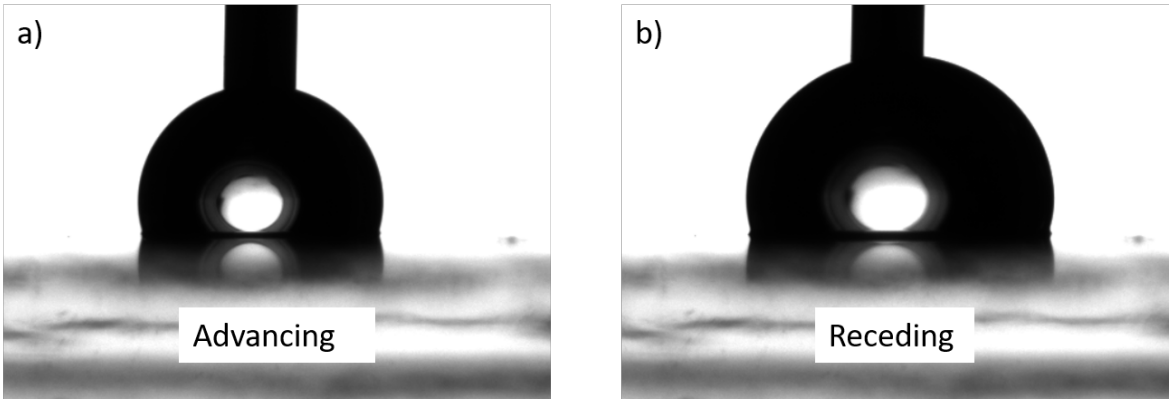

Figure 3.5.4: Hysteresis measurements performed on a SLIPS with an oil thickness of 3.09 μm with a) the advancing frame and b) the receding frame.

The value for the apparent contact angle hysteresis on this surface was 4.30°.

For the measurements of the sliding angle on SLIPS, 2 μl droplets were deposited onto the substrate and the sample tilted until continuous droplet motion was observed. This process was repeated for the six withdrawal speeds between 0.1 mm/s and 2.5 mm/s along with the conformal SLIPS sample. On the conformal SLIPS the sliding angle, for the droplet in Figure 3.5.3, was 3.4° ± 0.2° which over halved the siding angle of 7.6° ± 0.5°, indicating that the addition of oil led to the decrease of hysteresis. Increasing the oil thickness to 3.09 μm decreases the sliding angle by almost 3° to 0.5° ± 0.2° demonstrating that the droplet was no longer in contact with the solid substrate. After each droplet was deposited onto the surface the SLIPS were re-imbibed with oil to replenish any that was lost by cloaking the previous droplet. By increasing the oil thickness further, some droplets struggle to remain stationary and will move on the surface without the table being tilted (0.0°) making it difficult to take a reading of the vanishingly small sliding angle at large oil thicknesses. In an attempt to settle the

droplet, the surface was re-levelled and the sliding angle experiments were repeated. After droplet deposition, on the thickest oil layers, the droplets still moved on the surface without the table being tilted. Therefore, at larger oil thicknesses the sliding angle is taken to be $0.0° \pm 0.2°$. The error reported for the sliding angles in comparison to the error on the contact hysteresis values is much smaller and far less subjective.

Table 3.5.2: Sliding angles on SLIPS surfaces with varying oil bath withdrawal speeds.

Withdrawal Speed (mm/s)	Oil Thickness (μm)	Sliding Angle (°)	Error (°)
	1.93	3.4	0.2
0.1	3.09	0.5	0.2
0.5	8.98	0.2	0.2
1.0	13.97	0.2	0.2
1.5	17.48	0.1	0.2
2.0	21.07	0.1	0.2
2.5	24.79	0.0	0.2

Therefore, despite the fact that the inflation and deflation method is the best determinant for hysteresis on a dry surface, on SLIPS the apparent contact point is difficult to determine and is some what subjective (dependent on the person doing the measurement). Hence, the sliding angle has been chosen as the preferred measure of hysteresis, ensuring that the volume of droplet used is as small as possible and consistent for all measurements.

3.6 Conclusion

The methods used within this chapter have developed a surface that is both uniform and reproducible with characteristics that fulfil superhydrophobic and SLIPS criteria. These surfaces have been used to study the wetting ridge meniscus effects as well as how water droplets interact with solid objects.

Chapter 4

Droplets on Steps

This chapter will discuss an experimental process conducted to return the type of droplet control seen on a surface with hysteresis to a surface absent of hysteresis. A step has been used to deform the liquid surface to create a pinning point. The attractive force that the pinning point adds to the surface, driven by a capillary force towards the step, is characterised by the detachment angle for 2 μl water droplets[129]. Changing the initial positioning of the droplet, step height, oil thickness and tilting direction are parameters that govern the force of attraction and can be tailored for specific applications explored in the chapter summary. The work presented has recently been published in Langmuir as a journal article[130].

4.1 Introduction

One of the main issues that inhibits the wider use of SLIPS in industry is the inability to control a droplet on this very low hysteresis surface[131]. As previously discussed, a droplet on a flat solid surface and even a droplet placed onto a superhydrophobic surface experiences a certain amount of contact line pinning. Hence creating a little droplet control which may not be optimised but will still trap the droplet in a stationary position on the surface. Taking this idea of a pinning point on a surface and applying this to SLIP surfaces will return some control to the surface but the effect on the slippery properties is unknown. What is known is that when applying the coating (multiple coating method in Chapter 3) it needs to have a very flat layer to obtain

the lowest sliding angles as any particle agglomerations can cause a pinning point, a similar effect being able to be replicated on the macro scale by dust particles on the surface. Introducing a droplet to a SLIPS deforms the liquid surface as do pinning points, therefore by exploiting this deformation with an effect, such as the Cheerios Effect, may provide droplet control[132]. The effect of adding a designed pinning point instead of an accidental point (dust) to a SLIPS has been investigated in the following chapter.

4.2 The Cheerios Effect

The standard Cheerios effect[132] is considered to be the aggregation of particles placed onto a liquid surface and stems from the observation of breakfast cereal placed into a bowl of liquid, such as milk and the collection of Cheerios either at the solid/liquid interface at the edge of the bowl or with each other (Figure 4.2.1 a). Such effects are very easy to reproduce in a 'kitchen experiment' and can even be seen in nature with water boatmen floating on a pond[133, 134] or a drawing pin, buoyant on a bath of liquid, held in place by the surface tension of the liquid (Figure 4.2.1 b and c).

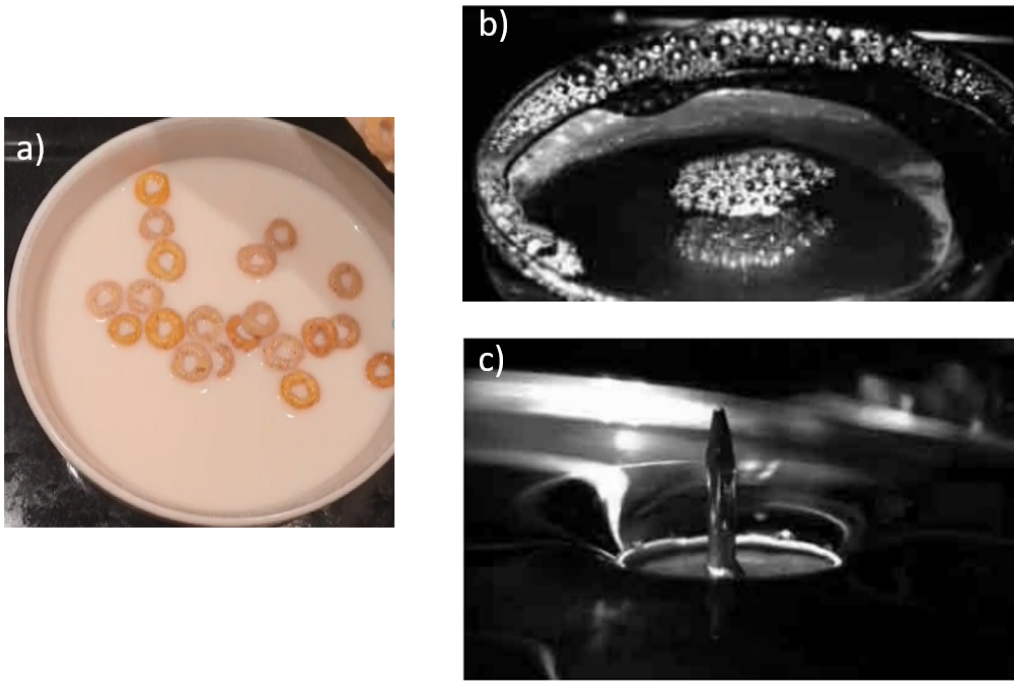

Figure 4.2.1: The Cheerios effect in nature. a) Cheerios in a cereal bowl, b) water boatman on a pond and c) a drawing pin on a bath of liquid (Vella et al. 2004).

When the solids are in contact with the liquid the interface between the two is deformed, with two possibilities of the deformation configuration. In this case if the object is heavy (or hydrophobic) it will sink slightly into the surface creating a negative curvature into the liquid, with the surface tension preventing the object from sinking completely (Figure 4.2.2).

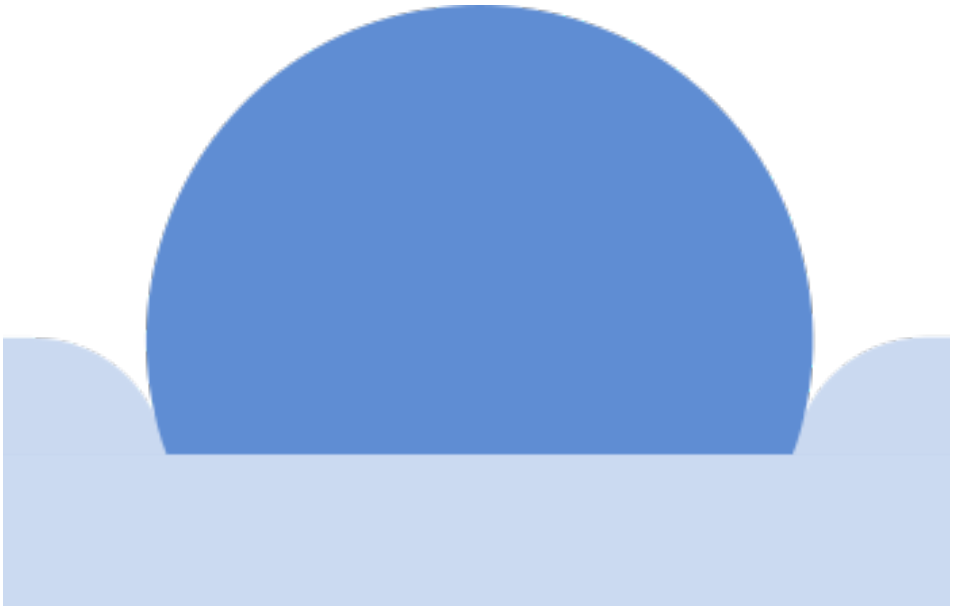

Figure 4.2.2: Schematic of a heavy droplet on a surface causing a negative interface curvature.

The other case is for a light object, or hydrophilic, a positive curvature is formed with the liquid creeping up the interface, rising above the equilibrium level (Figure 4.2.3). This is applicable for objects such as Cheerios or the water boatman, which appear to float on the liquid surface. Similar effects can be seen with air bubbles (formed from the base liquid layer itself) moving towards the edge and towards each other in the centre of the liquid bath. An example of this can be seen with bubbles on a freshly poured cup of tea.

Figure 4.2.3: Schematic of a buoyant droplet on a surface causing a positive interface curvature.

It is unlikely that there will be only a singular particle, bubble or droplet on a surface at any one time, therefore the objects will have some sort of interaction with surrounding objects. For the surface to assume its minimum energy state, the liquid/gas interface should be flat, the addition of an object changes the level of the liquid layer. Bringing two objects into interaction range with each other will cause further deviation of the liquid/gas interface from the horizontal. In order to minimise the energy on a surface where a negative curvature object and positive curvature object have been bought into interaction range (Figure 4.2.4 a) the two objects are compelled to move away from each other until the interface between the two objects has returned to horizontal. Bringing two objects into interaction range with like curvatures, be that negative (Figure 4.2.4 b) or positive (Figure 4.2.4 c) the two objects are attracted together, pushing out the liquid from in-between them, removing the liquid/gas interface, in turn minimising the energy. Therefore, in this case (unlike magnetism) opposites don't attract (Figure 4.2.4).

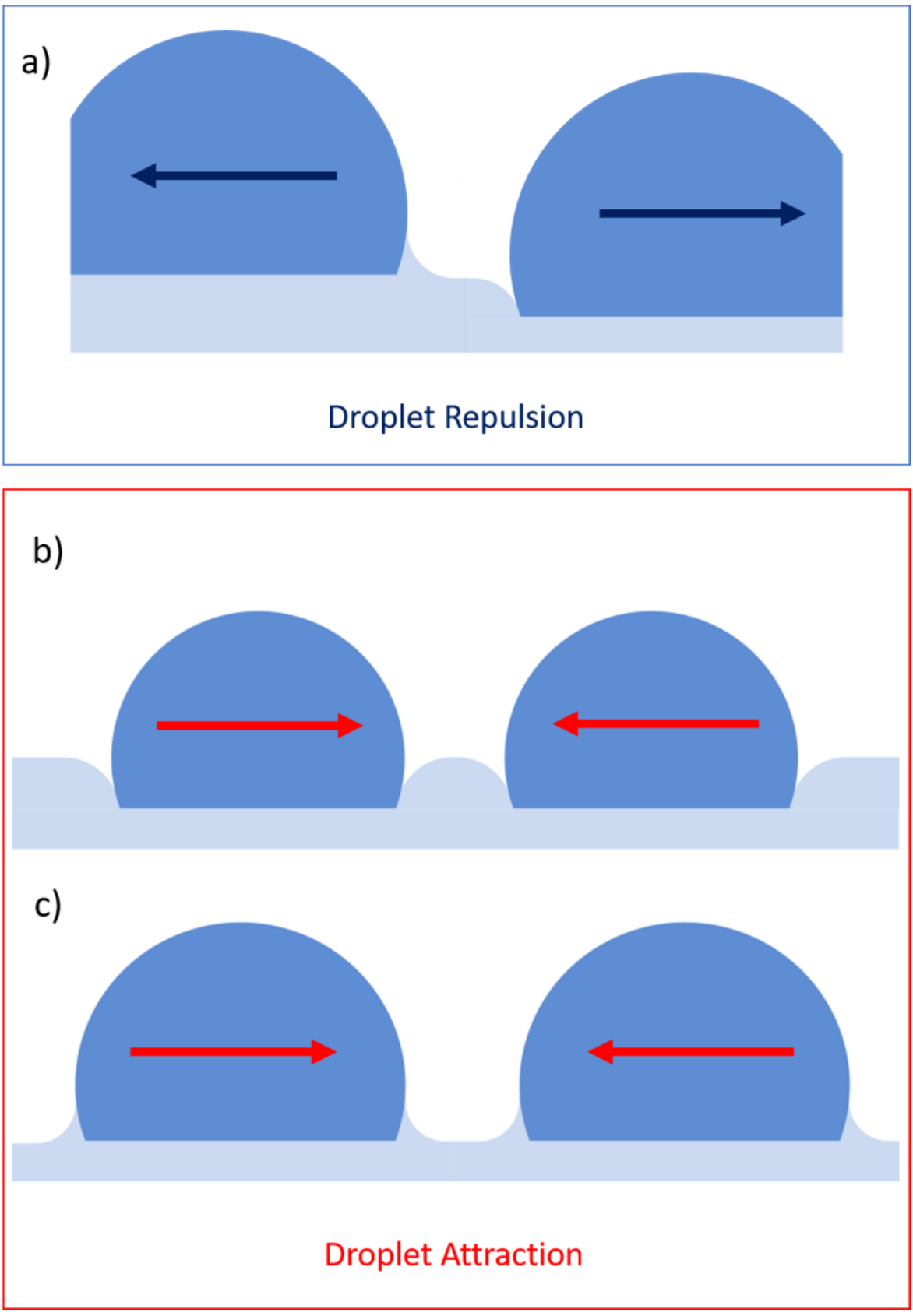

Figure 4.2.4: Schematics of a) opposing curvatures, leading to droplet-droplet repulsion and like curvatures (b) negative and c) positive), leading to droplet attraction.

The first question to answer is, can the Cheerios effect be seen on SLIPS? To show that in fact it is possible to see an effect, the simple Cheerios in a breakfast bowl or bubbles on a petri dish (Vella et al.) can be recreated[132]. To do this, a glass petri dish was coated in the nanoparticle structure and infused with an excess of oil, multiple water droplets of volume 2 μl were then placed into the dish and left to interact with each other and the sides of the dish. As can be seen from the sequence of images in Figure 4.2.5 the droplets are not only drawn to the side, they are drawn to each other as well, the interaction lengths seem to be on the length scale of the wetting ridge, with the larger droplets attracting the smaller droplets. If left for long enough, the droplets cloaking oil layer is displaced, allowing the two droplets to merge (Figure 4.2.5).

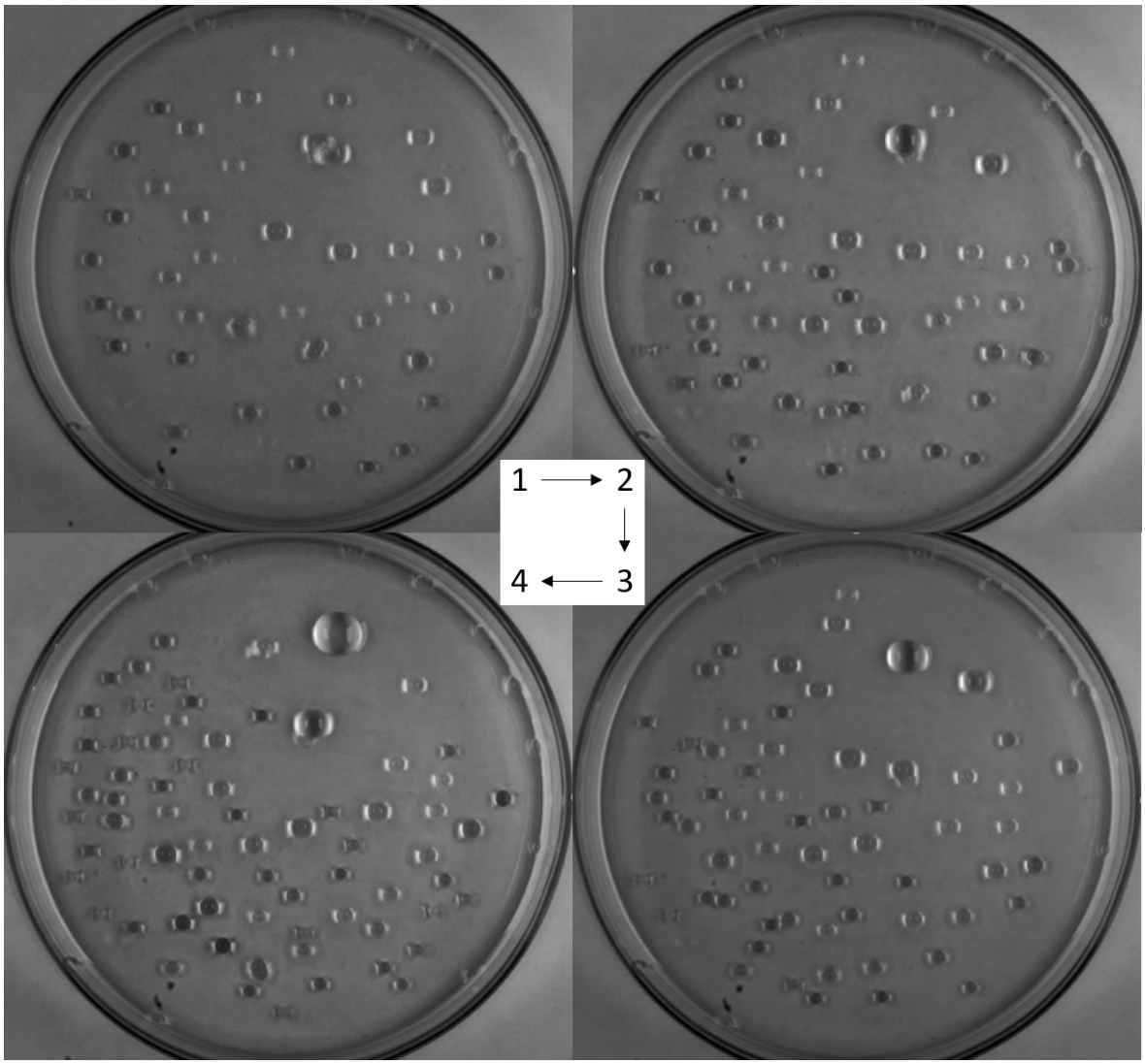

Figure 4.2.5: Image sequence of 2 μl droplets placed into a SLIPS coated petri dish showing the droplet movement towards the walls of the dish and towards other droplets.

To further prove that this effect was only governed by the Cheerios force and not by any sloping seen in the dish itself a 3D printed confinement ring was attached to a Glaco coated slide and the sample infused with Silicone oil. Droplets of volume 2 μl were again deposited onto the sample which had been infused with an oil layer approximately equal to 21.07 μm. As seen previously (Figure 4.2.5) the droplets were both attracted to the walls of the 3D printed ring and to each other but on a slightly shorter time scale as the area of the ring was smaller than the petri dish. From Figure 4.2.6 it can be seen that the droplets seem to prefer to attract other droplets and coalesce. This is due to the ability of the droplets to move freely; this means it is more likely that two droplets will be attracted to each other than for a single droplet to move towards an immovable object. As the droplets coalesce the corresponding wetting ridge footprint grows, increasing the interaction distances, whereas the wetting ridge present on the wall is constant in length.

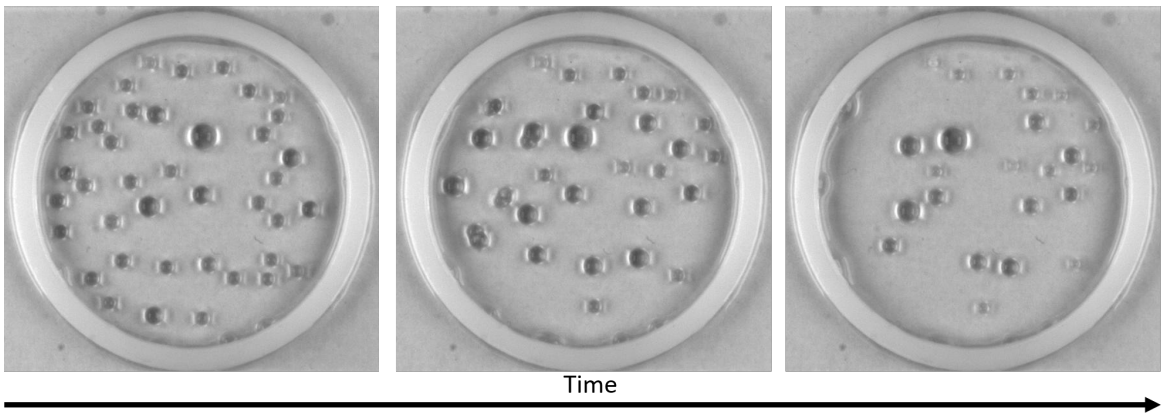

Figure 4.2.6: Image sequence of 2 μl droplets placed into 3D printed ring with an approximate oil thickness of 21.07 μm, showing the droplet movement.

Increasing the oil thickness to approximately 33.59 μm does not appear to have any effect on the speed of the interaction or the mobility of the droplets The 2 μl droplets still seem to prefer to move towards each other, however if placed in close enough proximity to the wall they will be attracted to and spread along the curvature as can be seen on the bottom left hand edge of the ring in Figure 4.2.7.

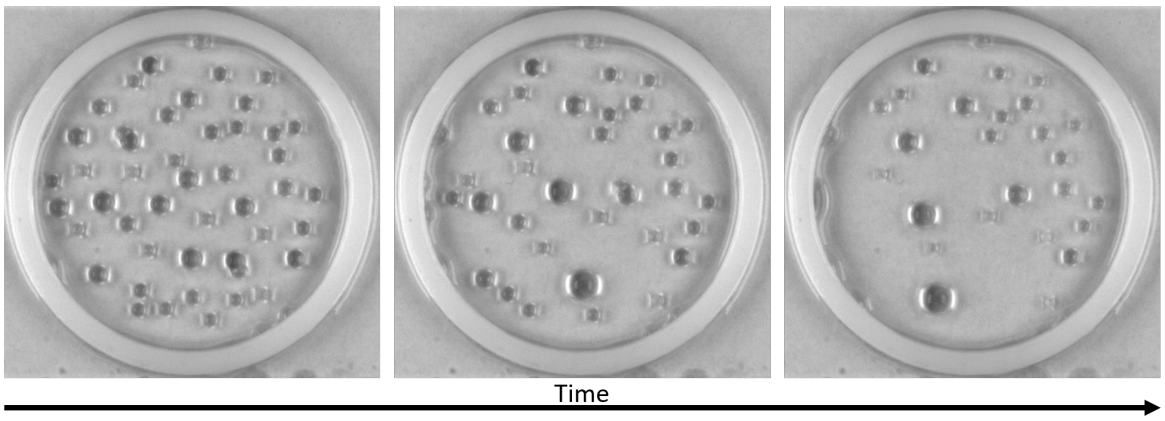

Figure 4.2.7: Image sequence of 2 μl droplets placed into 3D printed ring with an approximate oil thickness of 33.59 μm, showing the droplet movement.

Whilst the Cheerios effect on SLIPS produces a viable method for passive droplet movement, there is still very little control over where the droplets will first be attracted to or where they may assume a stationary position. To use the Cheerios effect to its full potential a controlled pinning point, to deform the liquid layer, can be added to the surface to produce a similar effect to that of other droplets or the wall of the petri dish.

4.3 Creation of the Step

The simplest structure to produce that will act as a specifically tailored pinning point is a step. In this case the term step refers to a discontinuity that can be added to a surface to induce a structure that the droplet will experience and will also create a deformation to the imbibed liquid layer. For the following experiments the step has been created by two methods. Method one involved attaching a glass cover slip, of thickness 140 μm, to a standard glass microscope slide using an epoxy adhesive. This method creates a sharp, vertical step however, the height is fixed. For method two, a negative photoresist (SU-8) and simple photolithography was used to create the step. By changing the viscosity and spin speed the height of the layer could be accurately varied.

As the glass cover slip step samples (Method One) were all produced from standard cover slips with a given height, a micrometer was used to confirm that the thickness

of the cover slips transferred to the final step height. However, as the SU-8 steps were produced by varying more than one factor, this height might in turn be more variable across the samples produced, therefore a reproducible technique to measure the height in multiple positions and across multiple samples had to be implemented. Stylus profilometry was not an appropriate technique to use for these samples as the step should be sharp and may not provide an accurate picture of the shape. Therefore, white light optical profilometry was chosen as the preferred measurement technique as it provides an accurate, non-destructive way to measure the height of the SU-8 steps. An example of a typical image from the optical profilometer (Bruker ContourGT-K) can be seen in Figure 4.3.1.

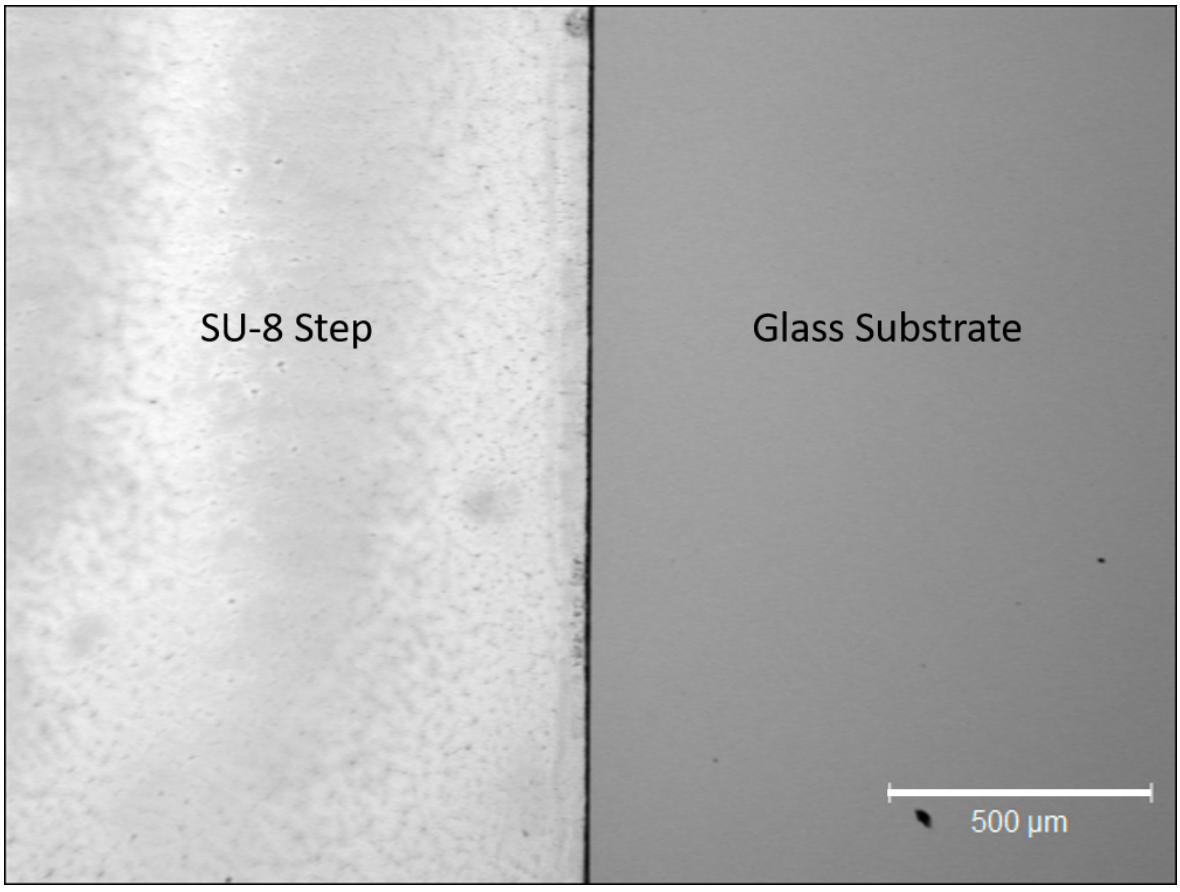

Figure 4.3.1: An example profile taken by the optical profilometer.

The other advantage of this technique is that it can also provide information on whether there was any under/over exposure during the photolithography by measuring how vertical the steps are. When plotting the data taken by the profilometer the fewer the points between the first plateau and the second plateau (highlighted in Figure 4.3.2)

the more vertical the step is. As can be seen for all of the plots of step height data, each sample produced has a very clear vertical step with the maximum number of points between plateaus (2 points) appearing for the 10 μm step height. The greatest variation in step height appears for the 150 μm sample. This is due to the fact the SU-8 was spun at a lower speed than recommended by MicroChem, leading to a surface that wasn't completely flat at the time of curing and therefore a large error bar in subsequent data plots. However, as it appears that the main source of error was caused by one area in particular of a sample, when conducting experiments, the droplets were placed away from this point.

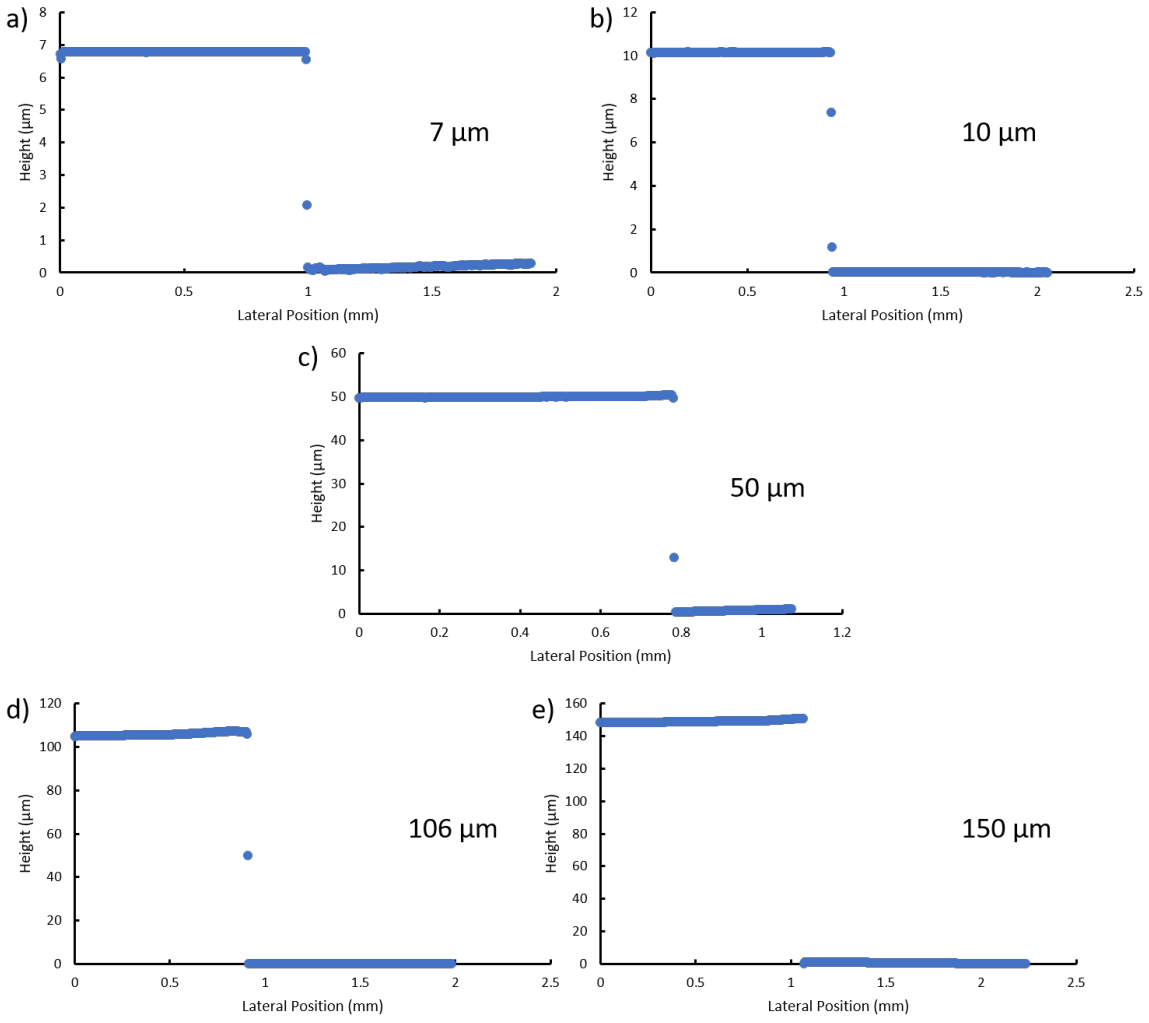

Figure 4.3.2: Step heights for each sample plotted as an average. a) 7 μm, b) 10 μm, c) 50 μm, d) 106 μm, e) 150 μm.

The data for the spin speeds, SU-8 product and final step height for the SU-8 is shown in Table 4.3.1.

Table 4.3.1: SU-8 product, spin speed, exposure time, developing time and final step height.

SU-8 Product	Exposure Time (s)	Developing Time (min)	Final Spin Speed (rpm)	Step Height (μm)
20-10	4	3	3000	10.11
20-10	6	4	3000	6.79
20-50	7.5	6	3000	49.67
20-100	10.4	10	3000	105.94
20-100	13	17	1250	150.08

To show that a SLIPS is still produced on this stepped structure a 2 μl droplet was placed on the step, with an oil thickness of 3.09 μm and the sample tilted in a direction parallel to the step. This produces a sliding angle of $0.56° \pm 0.20°$, this is slightly higher than the angle measured for a completely flat surface but is still well below 1° and again within the SLIPS angle criteria. The exact positioning of the step in relation to the droplet is difficult to see from experimental images and the step position can only be determined from the sample images before the droplet was added. A schematic in Figure 4.3.3 roughly depicts where the droplet sits in relation to the step when the sample is horizontal. The exact shaping of the droplet caused by the step and the proportion of the droplet on top of the step has been assumed, as it cannot be directly imaged, however the proportion does seem to vary depending on the step height and imbibed oil layer thickness. It is the Cheerios effect and the non uniformity in oil layer thicknesses, specifically in the wetting ridges that draws droplets together (Figure 4.2.5) and droplets to the step. Figure 4.3.3 is only a simple 2 dimensional representation of the droplet in relation to the step, the true system is 3 dimensional.

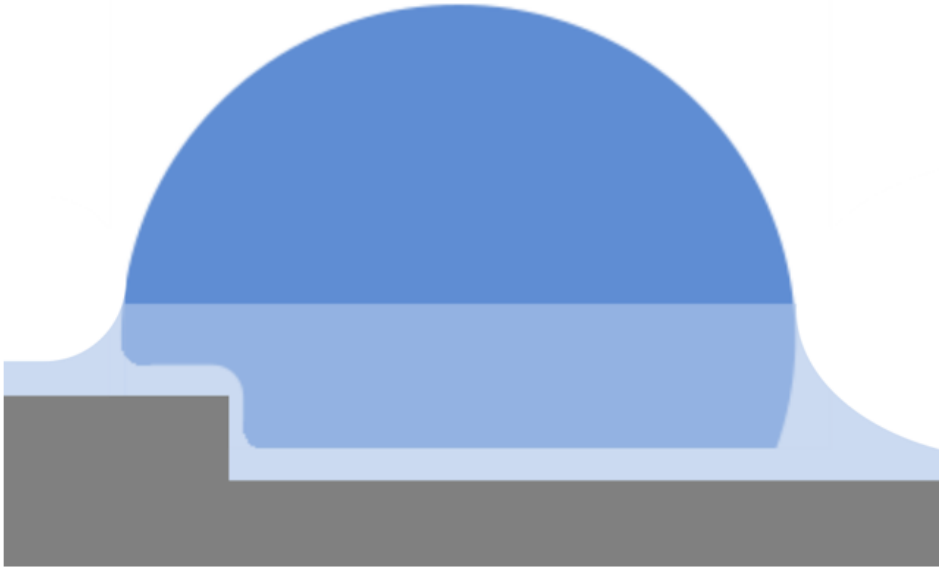

Figure 4.3.3: Schematic of the droplet position in relation to the step.

When coating the step with Glaco it is important to ensure that there is an even coating of Glaco on the entirety of the structure. This involved choosing the correct orientation for the sample to prevent Glaco build-up in the step corner and to also ensure Glaco would coat the riser of the step. To check this SEM images were taken after 5 coats of the Glaco had been applied. In order to view the Glaco without charging a larger than ideal layer of platinum had to be applied to the sample. For Figure 4.3.4 an 8 nm layer of platinum has been applied but appears to have aggregated more in the corner and on the riser of the step than on the flat sections. The Glaco does appear to have adhered to the step but the total layer is partially concave and has created large Glaco clumps. This means that the accumulation of particles in this area was not fully prevented but during experiments it did not seem to affect the SLIPS properties of the sample.

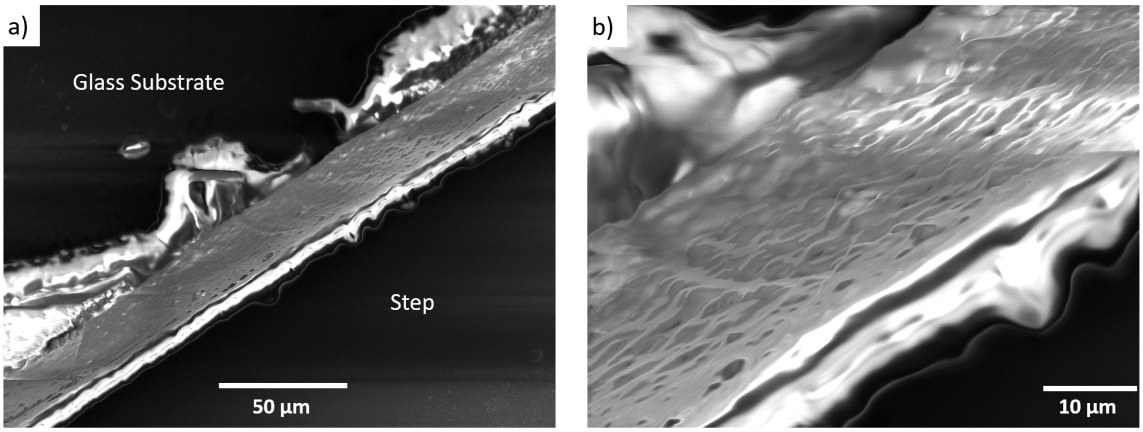

Figure 4.3.4: SEM images of the Glaco coating the riser of the step.

4.4 Attraction Force

As the purpose of adding the step is to create a pinning point where a droplet will be highly mobile in one direction and not the other. The force of attraction to the step and therefore the immobility of the droplet in the pinned, direction needs to be quantified[135].

When placing a droplet very close to the bottom of the step, the droplet is immediately drawn towards the step due to an attraction between equal wetting ridge curvatures and a need for the surface to minimise the energy. To quantify this force of attraction to the step, the amount of tilt required to remove the droplet was used as a measure. In previous experiments, this angle has been termed as the sliding angle (angle required for the onset of motion). However, in this instance the onset of motion on these samples occurs at $0.56° \pm 0.20°$, therefore the angle required for detachment from the step will be termed as the detachment angle.

To initially test this attractive force, a droplet of volume 2 μl was placed at the bottom of the thinnest sample, in terms of both h_s (7 μm) and h_o (3.09 μm), in order to ensure attraction to the step. The sample was then tilted in a clockwise direction, perpendicular to the step, in increments of 0.20° until the droplet detached, this occurred at an average angle of $7.18° \pm 0.31°$. The height of the step is approximately 3 orders of magnitude smaller than the height of the droplet itself, however it gives rise to a siding angle 10 times larger than on a flat surface. To investigate how the step height influences the detachment angle the height of the step was increased from 7 μm.

The step heights chosen varied from 3 orders of magnitude smaller than the droplet height to just 1 order of magnitude smaller. As a side view camera has been used to record the droplets on these surfaces, neither of the two step height images in Figure 4.4.1 can be in focus on the droplet and the edge of the step simultaneously, therefore the images shown are an example of what would be seen in an experiment prior to droplet deposition. As can be seen from the comparison between the side profile of the 7 μm step height image and the 150 μm step height image (Figure 4.4.1) the larger step can be identified from the image but not clearly and the shape of the wetting ridge is almost impossible to measure. As for the smallest step nothing can be seen from the image. The position of the steps in these cases have be determined by top view images.

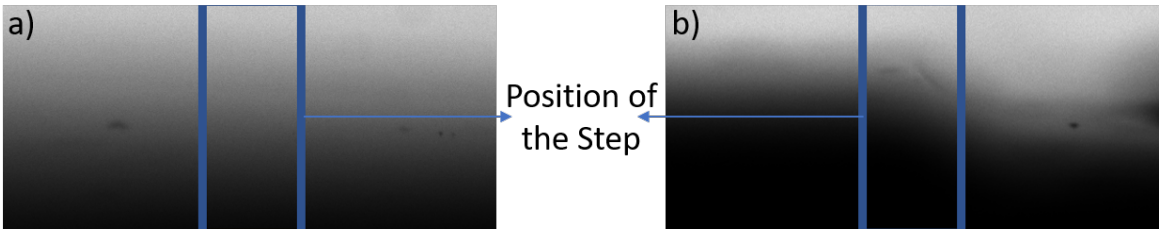

Figure 4.4.1: Comparison between the a) smallest and b) largest step heights prior to droplet deposition.

By changing the height of the step, the vertical area for the droplet to adhere to is also increased, therefore it is expected that the adhesive force will also increase with this height as the contact area has increased. The same experimental procedure was followed with a 2 μl droplet used to test the adhesive force and the oil thickness kept constant. With an increase in step height there was an increase in detachment angle. Plotting this in Figure 4.4.2 it can be seen that the increase in detachment angle is linear, with the angles increasing from 7.18° ± 0.31° to 46.2° ± 1.6°.

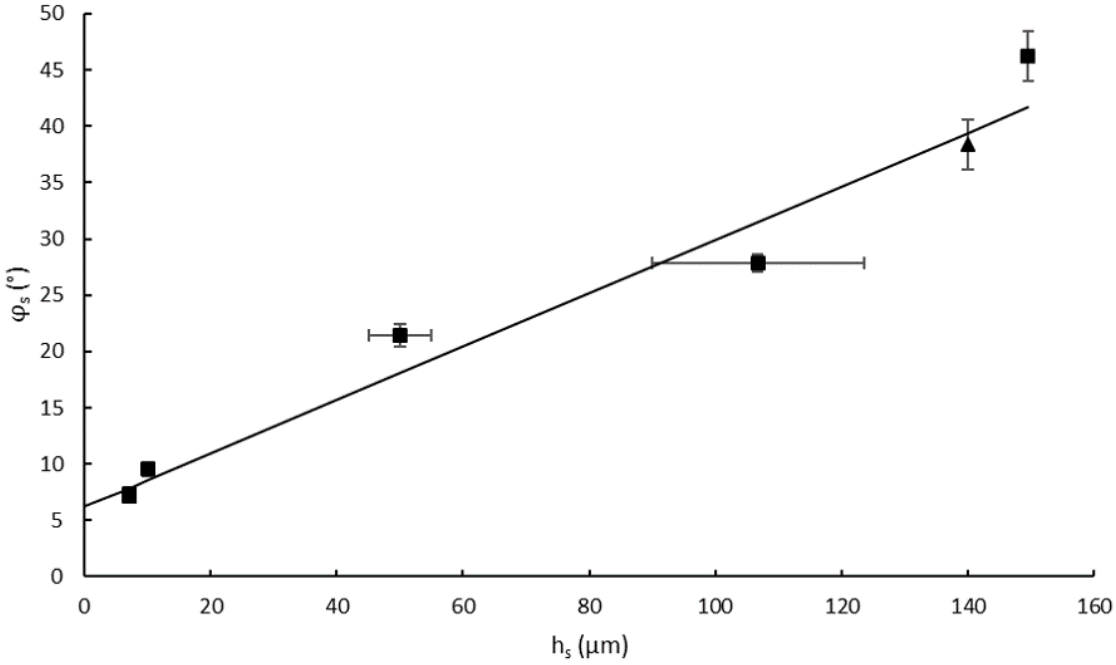

Figure 4.4.2: Detachment angle data for a change in step height for an oil thickness of 3.09 μm. A guideline has been fitted to the data

Increasing the step height not only increases the adhesion force, it also appears to change the overall shape of the droplet. As can be seen from the image sequence depicted in Figure 4.4.3, the droplets in both the h_s = 7 μm and h_s = 150 μm have a spherical cap however the size of the wetting ridge is significantly different. The droplet wetting ridge on the 7 μm step droplet is barely visible, in contrast to the 150 μm step where the wetting ridge is large for both the trailing and leading edge of the wetting ridges. As the withdrawal speed of the samples has not be changed, h_o must also remain the same, hence the droplet was most likely not increasing its wetting ridge by drawing oil from the thin film. As was seen in Figure 4.4.1 the appearance of the filed step corner changes from the smallest to the largest h_s, therefore it can be reliably assumed that the droplet must be drawing oil into its ridge from the oil filled corner.

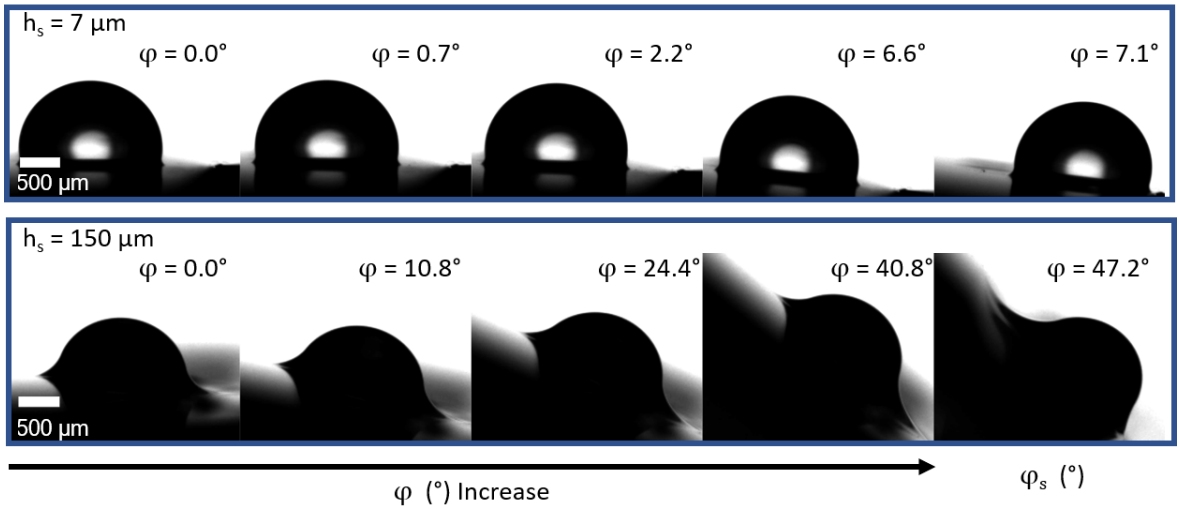

Figure 4.4.3: Image sequence showing the evolution of droplet shape through sample tilting, comparing the smallest and largest step height for $h_o = 3.09$ μm.

The other way to change the wetting ridge size is to increase the oil bath withdrawal speed and therefore increase the film thickness, h_o. Guan et. al. 2017[115] experimentally produced a similar structure with the step in this instance with the geometry of a v-shaped channel, or the equivalent of two converging walls. The length of the wetting ridges were then measured optically and the withdrawal speed increased. The result of this showed that an increase in withdrawal speed equates to an increase in wetting ridge length, meaning that the amount of oil trapped within the constraints of the corner increases with oil thickness. It can be assumed that despite the fact there is only one wall used within this study, the increase in step height still leads to an increase in wetting ridge length.

The oil thickness increase was performed for just one step height, the 140 μm sample. For the thinnest oil layer, the detachment angle on this step height is fairly high, $38.4° \pm 2.2°$. As it is predicted that the detachment angle will decrease with increasing oil thickness (on a flat surface the sliding angle of a droplet decreases with increasing h_o, Table 3.5.2) the large initial detachment angle gives an opportunity to analyse how a large range of oil thicknesses influences the attraction force. By plotting the detachment angle as a function of oil thickness, instead of step height, the detachment angle switches from a linear increase (Figure 4.4.2) to an almost exponential decrease (Figure 4.4.4).

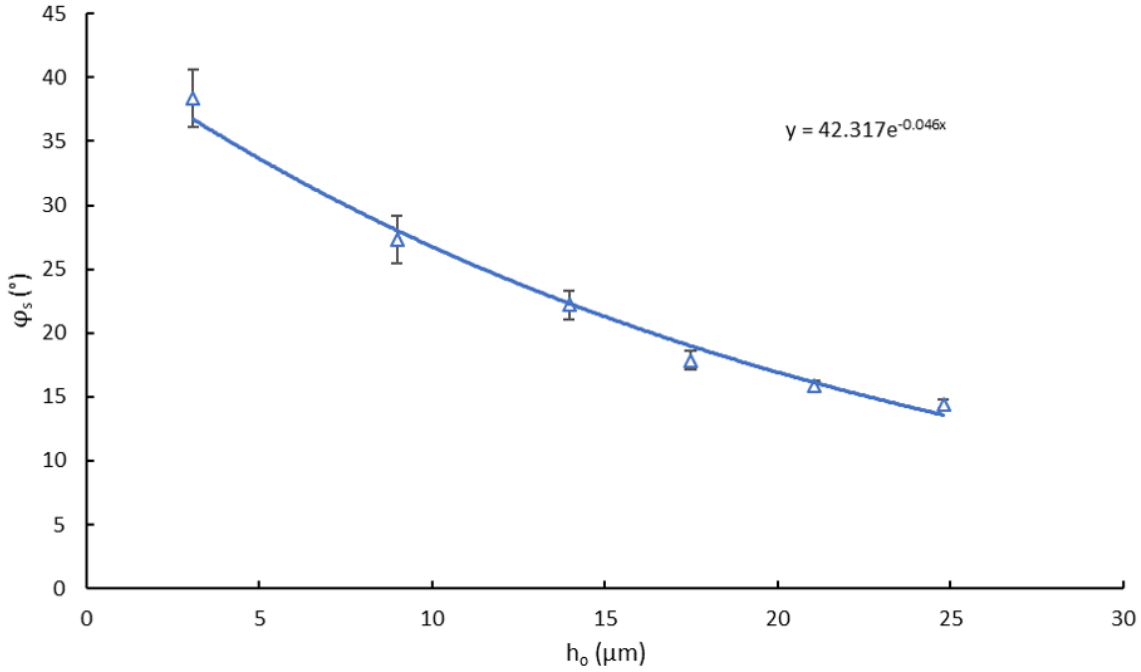

Figure 4.4.4: Detachment angle data for a change in oil thickness, keeping the step height constant (140 μm). An exponential fit has been fitted to the data.

The reason for this decrease being exponential and not linear can be determined from the images of the droplets just before they detach from the step. As can be seen in Figure 4.4.5 the difference between the shapes of the droplets and the size of the wetting ridges a) ($h_o = 3.09$ μm) and f) ($h_o = 24.79$ μm) is very clear, with the smaller oil thickness having the smallest wetting ridge. However, when comparing e) and f) or even d) and f) the difference between wetting ridge size is less clear. This can be attributed to the fact that whilst the droplet and wetting ridge will never be in an equilibrium state there has to be a limit to how much oil a particular sized droplet can be cloaked in and draw into its ridge. Therefore, at the thicker oil layers the wetting ridge is almost at capacity, hence increasing the withdrawal speed will begin to have less of an effect on the droplet adhesion force. The origins of this phenomena start to present themselves on a flat surface with the increase in the width of the wetting ridges decreasing with large oil thicknesses however, there is an extra source of oil stored in the filled corner of the stepped sample which ultimately equates to a much larger dip speed than had been tested on flat samples. This indicates that at a certain level, changing the step height will have more of an effect on the detachment angle than

changing the oil thickness. Increasing the withdrawal speed not only increases the size (height and length) of the wetting ridges but this also adds to the weight of the droplet. By adding to the weight of the droplet, the force pulling the droplet away from the step should also increase.

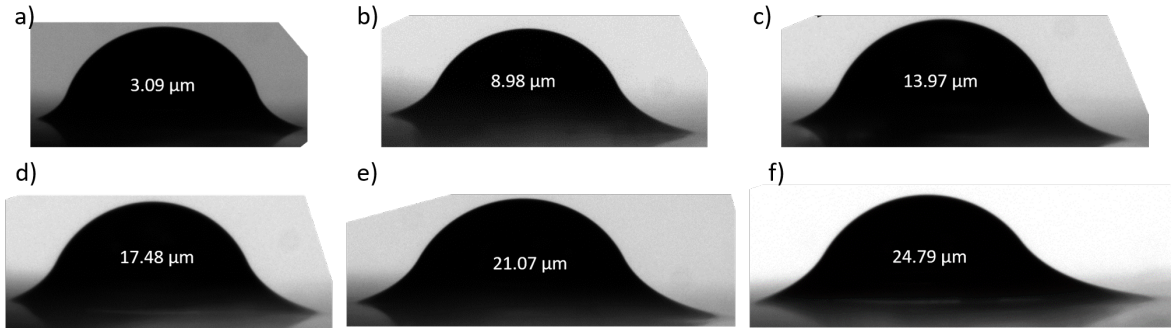

Figure 4.4.5: Image sequence showing the shape of droplet and wetting ridge just prior to step detachment for a) 3.09 μm, b) 8.98 μm, c) 13.97 μm, d) 17.48μm, e) 21.07 μm and f) 24.79 μm on a 140 μm high step. Each of the images have been rotated by their detachment angle to appear horizontal.

To confirm that the decrease in detachment angle as a function of step height was consistent across all the step heights the withdrawal speed was increased from 0.1 mm/s to 0.5 mm/s, increasing the oil thickness from 3.09 μm to 8.98 μm and the experiment repeated on 5 different step heights from 7 μm to 140 μm (Figure 4.4.6). The detachment angles, when plotted as a function of step height, show the same linear increase as was seen in Figure 4.4.2.

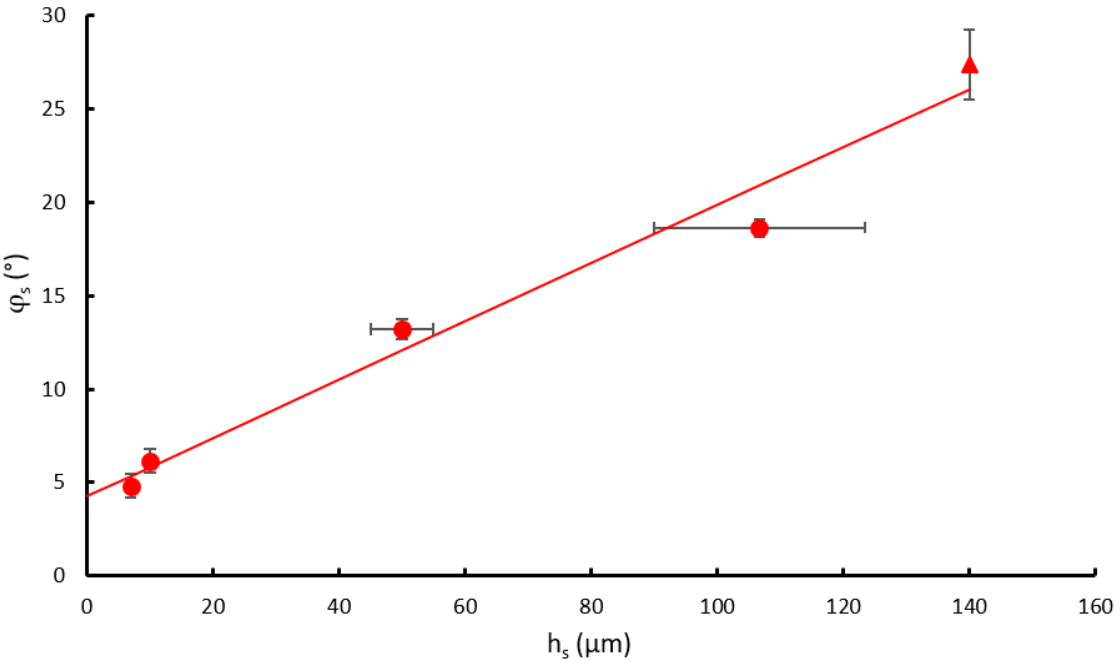

Figure 4.4.6: Detachment angle data for a change in step height for an oil thickness of 8.98 μm. A guideline has been fitted to the data.

By combining the detachment angle data for the increase in step heights and oil thicknesses the full range of interactions can be analysed.

The first noticeable difference between the data for the 0.1 mm/s (Figure 4.4.5) to 0.5 mm/s (Figure 4.4.6) withdrawal speed is a reduction in the gradient for the linear increase. This difference in gradient is due to the fact the detachment angles for smaller step heights begin to plateau at a value of h_o smaller than that required for larger step heights, as can be seen in the data for 140 μm. By looking at both sets of data (3.09 μm and 8.98 μm) it can also be seen that the substrate type (SU-8 or Glass) has very little to no effect on the detachment angles (Figure 4.4.7).

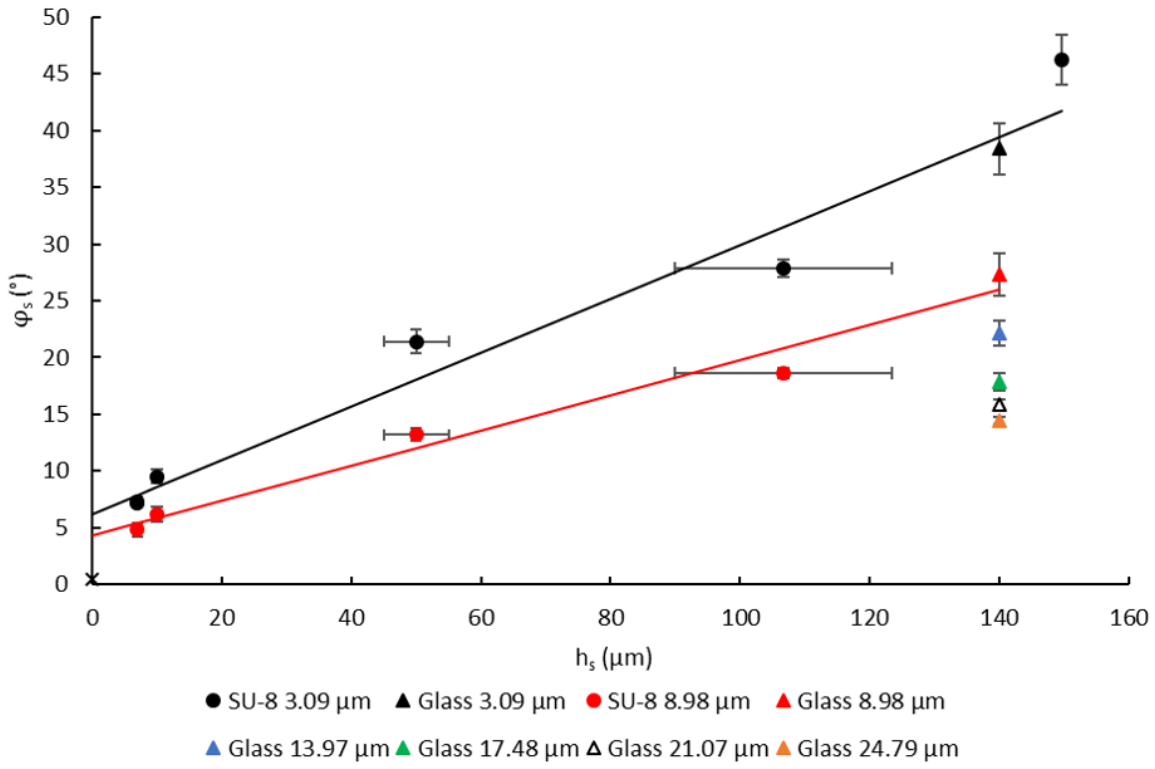

Figure 4.4.7: Combination of data from Figure 4.4.2, Figure 4.4.4 and Figure 4.4.6

When increasing h_o there is little difference between the detachment angles for the smallest step heights, this is because the oil thickness is almost equivalent to the step height (Figure 4.4.7). When the oil thickness becomes greater than the step height the oil stored within the step corner makes little difference to the droplets wetting ridge, making the surface again almost equivalent to a flat surface and in effect begins to hide the stepped structure from the droplet. There is also little difference between the detachment angles for the 140 μm sample at the largest oil thicknesses. In both cases there is a reduction in curvature difference between leading and trailing wetting ridges. This reduction in difference is likely to be caused by a restriction to the wetting ridge shape due to the oil layer thickness, therefore reducing the adhesion force. This idea has been examined by Semprebon et al. for the case where the pressure in the wetting ridge is increased, deforming the wetting ridge, this is equivalent in this experimental case to decreasing the oil layer thickness[68].

As h_s is the control parameter for the geometry of the step and h_o the control for the oil meniscus length (oil filled corner), then it is reasonable to assume the adhesion force is dependent on the ratio of step height to oil thickness (h_s/h_o). By replotting

the data from Figure 4.4.7 on to a log-log scale of the sin of the detachment angle as a function of the ratio of step height to oil thickness, the data, with error bars, all collapses on to one straight line (Figure 4.4.8). The line the data follows appears to fit a one-half power law.

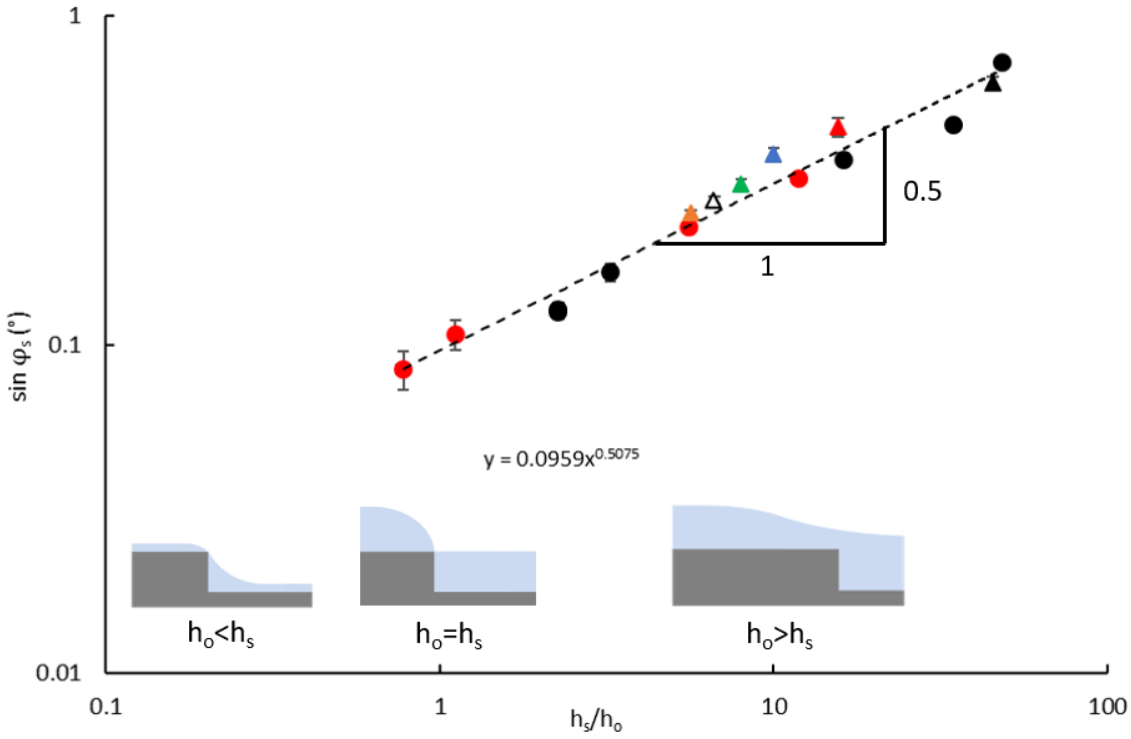

Figure 4.4.8: Replotting of Figure 4.4.7 data on to a log-log scale, showing a linear trend accompanied by the oil layer schematics.

As with flat SLIPS, on a stepped sample, an increase in oil thickness leads to an increase in wetting ridge radius and height. However, as the droplet sits partially on the step there is an asymmetry between the leading and trailing wetting ridges, with the leading edge appearing to have a larger radius of curvature. Whilst tilting the sample both ridges grow, but the leading wetting ridge appears to grow at a faster rate, extending down the surface and pulling away from the step. At the onset of detachment motion, the droplet removes itself from the step and the trailing ridge then slowly increases in radius until it is of a similar size to the leading wetting ridge before full droplet and wetting ridge detachment. During the wetting ridge detachment process the height of the wetting ridge does not appear to change significantly, this is because the wetting ridge and droplet are in 3 dimensions with the wetting ridge

wrapping around the droplet, therefore the leading and trailing ridges are connected and reach the same height around the droplet (Figure 4.4.9). The asymmetry between wetting ridge curvatures can also provide an explanation for why the droplets remain attached to the step.

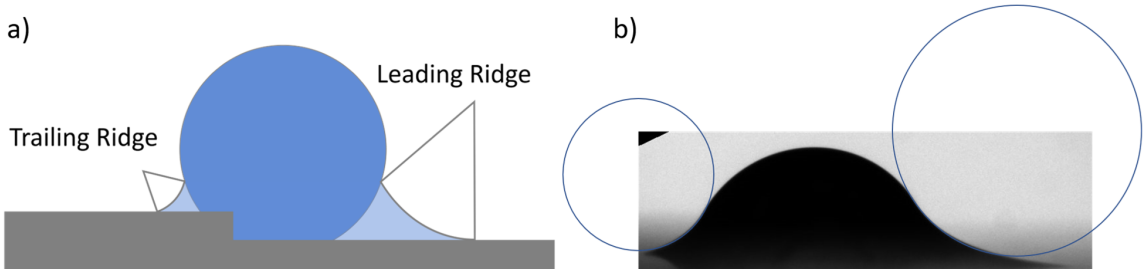

Figure 4.4.9: The asymmetry between leading and trailing wetting ridges depicted by a) a schematic of the droplet position in relation to the step and subsequent wetting ridges and b) a typical droplet image with $h_s = 140$ μm step and $h_o = 8.98$ μm with 2 circles overlaid on the wetting ridges to indicate the asymmetry.

Taking the droplet with wetting ridge on the step as a 1-dimensional system, with the pressure in the wetting ridge calculated by the Laplace pressure

$$\Delta P = P_L - P_G, \tag{4.4.1}$$

where P_L is the pressure in the liquid and P_G the pressure in the gas. The pressure in the gas is higher than that in the liquid, creating a negative curvature in the liquid, which we have termed a positive wetting ridge curvature in terms of the Cheerios effect (Figure 4.2.3). The radii of the curvatures at the liquid gas interface produces a pressure difference,

$$\Delta P = (\frac{1}{R_1} + \frac{1}{R_2}). \tag{4.4.2}$$

As the system is in 1 dimension the first radii term (what would be equivalent to parallel to the step) will have an infinite curvature, making this term equal to zero. The second radii term can simply be calculated from the wetting ridge curvature which will have a negative value if calculating the pressure in the liquid, rather than the gas. Therefore, with a higher value for the radius, the smaller the pressure in the liquid. This means that for a droplet on the step, seen in Figure 4.4.9, the pressure in the liquid

on the lower portion of the step is smaller than the pressure on the upper portion of the step. Therefore, this asymmetry produces a Laplace pressure in a direction towards the step (leading to trailing wetting ridge) in effect pulling the droplet towards the step[2].

Thinking about the detachment angle from a force perspective, at the point of detachment the gravitational force (F_g) pulling the droplet away from the step must be balanced by the force attracting the droplet created by the Laplace pressure, the capillary force (F_{cap}), therefore $F_g = F_{cap}$. Considering very simply that $F_g = mg\sin(\phi_s)$ and assuming mg remains constant from deposition to detachment, then $F_g \approx \sin(\phi_s)$ and $F_{cap} \approx \sin(\phi_s)$. It was determined from Figure 4.4.8 that h_s and h_o are the two factors that determine the force of adhesion and that the ratio of these fits a one half power law, therefore $F_{cap} \approx (h_s/h_o)^{(1/2)}$. Whilst in reality this is a much more complex, 3-dimensional problem, with the wetting ridge curvature evolving around the perimeter of the droplet footprint, this simple force balance gives a good idea of what parameters can be changed to achieve the desired detachment angle. As the droplet is stationary at the point of detachment any viscous drag effects can be neglected within the force balance.

When converting the detachment angles measured into the adhesion force the mass term is taken to be the mass of a 2 μl water droplet alone. As with the detachment angles, the larger the step height and the smaller the oil thickness the larger the adhesion force. The magnitude of this force is measured to be on the order of μN (Figure 4.4.10).

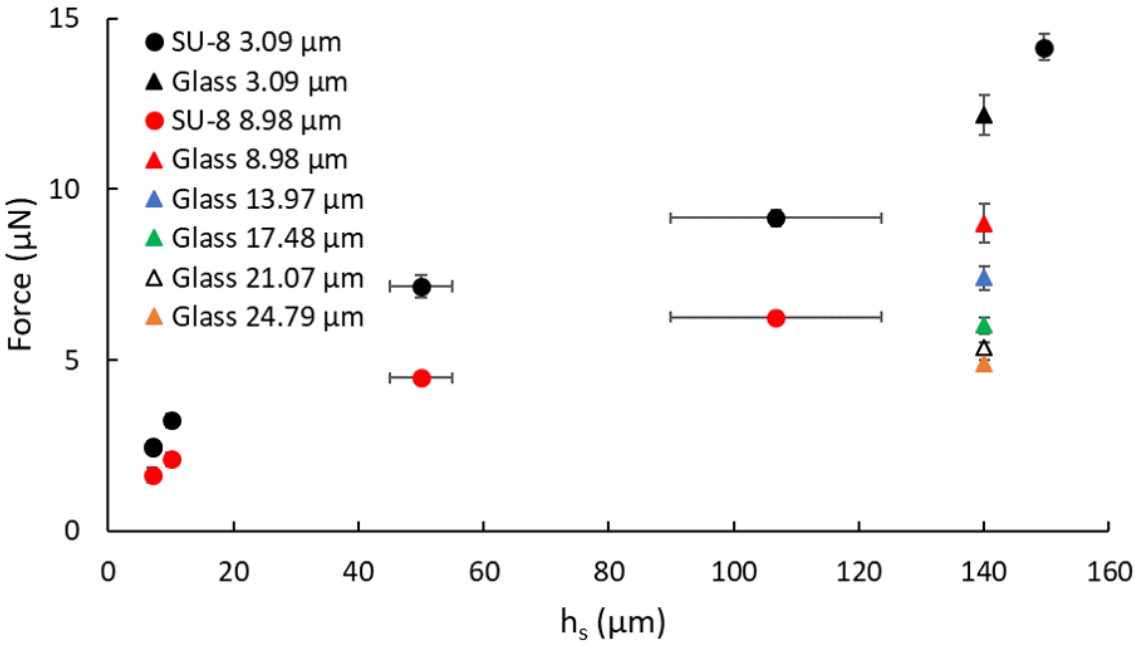

Figure 4.4.10: Force plot of the detachment angle data.

It is expected that over the course of the experiment there will be some oil loss from the sample. The scale of this oil loss determines whether there will be any significant impact on the adhesion force. To test how much oil might be lost over the course of an experiment the weight of a 140 μm stepped sample dipped at a withdrawal speed of 2.5 mm/s was measured over 30 minutes. At this withdrawal speed the maximum oil loss is expected as this sample has the largest layer of unimbibed excess oil that is not held on the surface by the porous nanostructure and associated van der Waals forces. Over 30 minutes the average excess oil weight loss was 0.00367 g $\pm$ 0.00181 g which as a percentage of the excess oil weight was 7.29%. As the experiments do not take 30 minutes to conduct it is really the experimental window where the amount of excess oil weight loss is crucial. The experimental window for these experiments was between 1 and 6 minutes after the sample was dipped. It took 1 minute from sample dipping to mount the sample onto the Krüss tilting table and to start the experiment. As the experiment takes a maximum of 5 minutes to conduct the maximum limit on the experimental window was set to 6 minutes. The average excess oil weight loss was measured as 1.4×10^{-3} g $\pm$ 1.3×10^{-3} g, which as a percentage of the maximum excess oil weight is 2.72%.

4.5 Configurations

As the stepped sample is a 3-dimensional structure, there is more than one direction the sample can be tilted in to aid droplet removal. The first is in the direction parallel to the step, where there should be the minimal capillary force adhering the droplet to the step and should be equivalent to a flat SLIP surface. This angle has been previously measured in Section 4.3 and is found to be $0.56° \pm 0.20°$.

The other possible directions are normal to the step. Configuration 1 is the same as seen in section 4.4, Attraction Force, where the droplet is attracted to the step and the sample tilted clockwise (Figure 4.5.1 a), with the data for these detachment angles plotted in Figures 4.4.7 and 4.4.8. Placing the droplet in the same lower position and tilting anticlockwise to push the droplet up and over the step gives Configuration 2 (Figure 4.5.1 b).

By going even further and splitting the sample into 2 sections (Figure 4.5.1 c) there is an additional initial position the droplet can take – which we will term the upper section – and hence, a further 2 droplet detachment configurations again with the tilting direction normal to the step. Configuration 3 starts with the droplet on top of the step. The droplet is immediately repelled due to the opposing curvatures created by the droplet wetting ridge and the step corner (Figure 4.5.1 d). This configuration is equivalent to placing the droplet in this initial position and then tilting anticlockwise. Starting again at the upper section but this time tilting in the opposite direction, clockwise, sees the droplet overcome the step repulsive force and drop down into the lower section, the same stationary position as seen in Configuration 1. This gives the final combination of initial position and tilting direction, Configuration 4 (Figure 4.5.1 e).

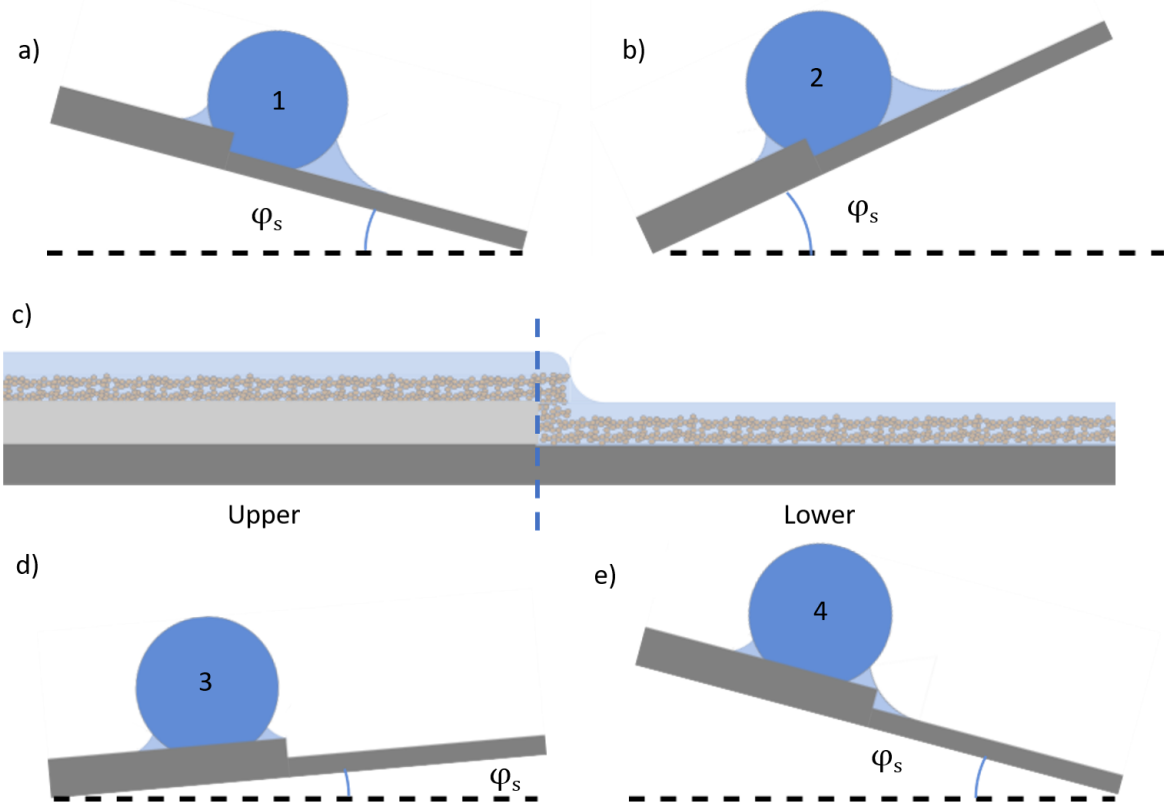

Figure 4.5.1: Schematics showing the droplet position and direction of sample tilting for a) Configuration 1 and b) Configuration 2. c) Side view schematic image of the sample split into 2 sections, upper and lower. Schematics showing the droplet positions and direction of sample tilting for d) Configuration 3 and e) Configuration 4.

To investigate the full range of interactions, the detachment angles for each Configuration need to be measured. Taking just one step height ($h_s = 140$ μm) and performing the same experiment as conducted on Configuration 1, on the 3 new configurations, with the range of oil thicknesses from 3.09 μm to 24.79 μm, gives three different sets of data to that for Configuration 1. Configuration 3 (Table 4.5.1) is the easiest to interpret as it does not require an angle for the droplet to move, the repulsion created by the difference in curvatures creates a strong enough force to initialise droplet movement. The droplet will then settle to a position away from the influence of the negative oil curvature created by the corner, this distance is determined by the oil layer thickness. To transport the droplet further the sample has to be tilted to the angle measured for the droplet placed onto and then tilted parallel to the step ($0.56° \pm 0.20°$). The data presented in Table 4.5.1 relates to the initial detachment angle, therefore for all oil thicknesses this value is $0.00° \pm 0.20°$.

Table 4.5.1: Depletion region distances away from with step and length of the depletion region with changes in oil thickness.

Oil Thickness (μm)	Detachment Angle (°)	Error (°)
3.09	0.0	0.2
8.98	0.0	0.2
13.97	0.0	0.2
17.48	0.0	0.2
21.07	0.0	0.2
24.79	0.0	0.2

Droplets in Configuration 4 have the same final stationary position as those in Configuration 1, therefore the droplets first have to overcome the step repulsive force to assume the position on the lower portion of the step. As the table is tilted the droplet first approaches the top of the step where it remains stationary. As the table is tilted further the wetting ridges of the droplet (leading and trailing) grow until the point where the leading wetting ridge begins to join with wetting ridge held in the corner of the step. Once these two wetting ridges have joined the droplet is pulled over the step into the lower stationary position. Figure 4.5.2 (blue triangles) show the angle that needs to be achieved for each value of h_o for the droplet to assume the final stationary position along with the data for the detachment angle (black triangles). For each oil thickness the angle required for the droplet to transition from the upper to the lower surface decreases, following the same reduction curve as the detachment angles. Towards the thickest oil layer used (24.79 μm) the difference between the transition angle, $11.80° \pm 0.28°$, and detachment angle, $12.64° \pm 0.30°$, decreases from $\approx 2.4°$ at the thinnest oil layer to to less than 1°, appearing to converge to $\approx 12°$.

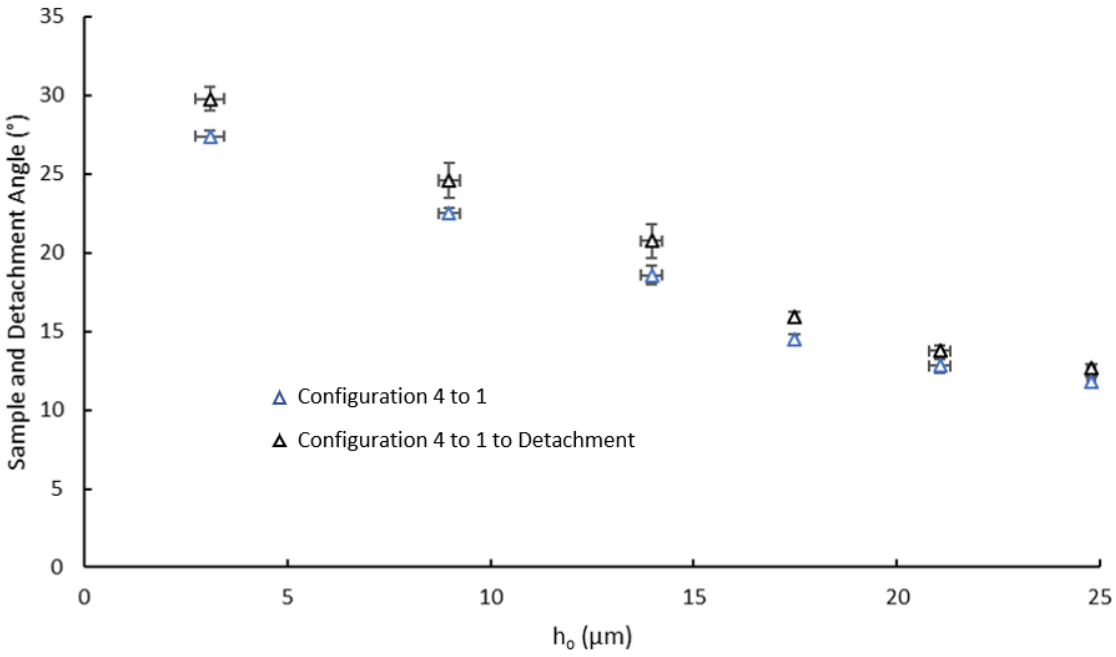

Figure 4.5.2: Detachment angle data for Configuration 4 (black triangles) accompanied by the step-down transition angles (blue triangles).

Figure 4.5.3 shows the detachment angle data for Configuration 2, with the detachment angles decreasing with increasing oil thickness. For the two thinnest oil layers (3.09 μm and 8.98 μm) even when the table is tilted to 90° the droplet is not removed from the surface, therefore the detachment angle could be anywhere between 90° and upside down (180°). In order to determine what this angle is and tilt the sample beyond 90° some modifications to the Krüss tilting table were required. A custom-built sample holder which could be fixed to the stage allowed for the sample to start at 90°, meaning that the sample can be tilted a further 90° to a full 180°. By repeating the experiment for the thinnest oil layers and using the sample holder, the droplet remains attached to the surface through all the angles, finally leaving the droplet hanging upside down from the surface. Beyond 180° the configuration in effect switches from Configuration 2 to Configuration 1.

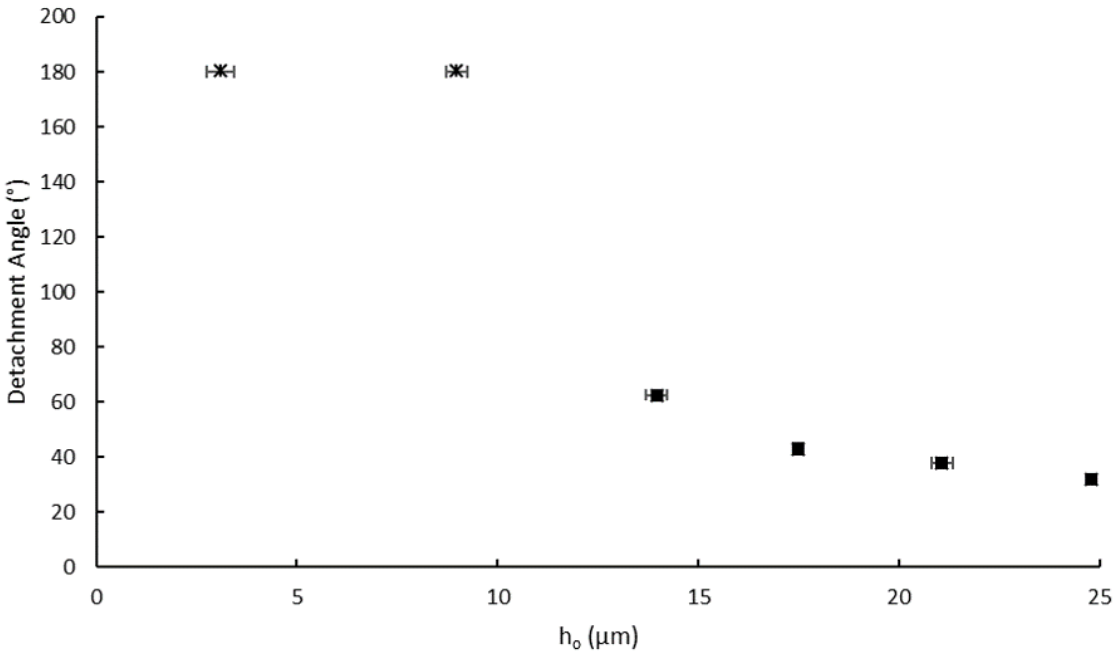

Figure 4.5.3: Detachment angle data for Configuration 2.

Throughout sample tilting, the droplet does not appear to undergo a significant shape change, maintaining its spherical cap. As with all other configurations the leading and trailing wetting ridges grow with increasing time spent on the surface and the droplet does appear to move away slightly from the step but still remains firmly attached.

The detachment angle data for Configuration 1, 4 and 2 (after hanging droplets h_o = 3.09 μm and 8.98 μm) all appear to follow an almost exponential decrease with increasing h_o, possibly meaning that the interactions are similar, independent of the initial positioning (Figure 4.5.4 a, b, d). The detachment angle data for Configurations 1 and 4 appear to have almost exactly the same shape and very similar values, which intuitively makes sense given that the droplets in the 2 different configurations have the same final stationary position.

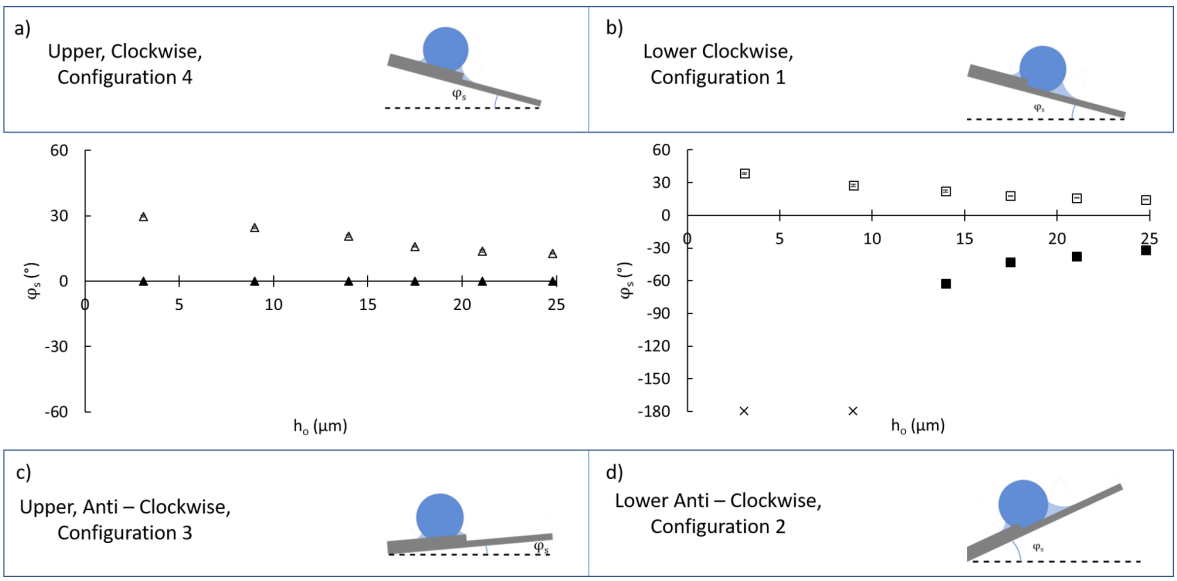

Figure 4.5.4: Comparison between detachment angles for all 4 droplet configurations. a) Configuration 4, b) Configuration 1, c) Configuration 3 and d) Configuration 2.

For the different step heights, that have not been experimentally tested, for the 4 configurations it is reasonable to assume that each configuration will have the same effect on the droplets but the detachment angle data will be shifted. Therefore, with smaller step heights the detachment angle data for each oil thickness will reduce with reducing step height and the points with no detachment would decrease, shifting the graph to the left. As the step height increases the detachment angles would still shift to the right, increasing the values. For Configuration 2, the effect of increasing h_s might be to increase the number of parameter combinations where the droplet will hang upside down. The only configuration where it can be assumed there will be no change in data would be for Configuration 3 (Figure 4.5.4 c). The repulsive force should still be large enough to move the droplet away from the step, the aspect that may change could be the distance the droplet will be repelled from the step.

Placing the droplets in differing initial positions changes the detachment angles as well as how the droplets interact with the surfaces with two instances of the droplet remaining attached to the surface. Despite this the droplets detachment angles, when they are initially attached to the step and then are removed, appear to follow a similar decrease in detachment angle for increasing oil layer thicknesses. Implying that the process of detachment is similar for the differing oil thicknesses and configurations.

4.6 Initial Positioning

As is very evident from the side profile schematics in Figures 4.5.1 a and 4.5.1 e, droplets that start on the upper section of the surface and are tilted clockwise (Configuration 4) have the same final stationary position as those that start of the lower surface and are attracted to the step (Configuration 1). However, when the detachment angle data graphs for both of these configurations are plotted on the same set of axes (Figure 4.6.1) the data sets do not match, indicating that there is some inherent difference between the two configurations that may not be immediately obvious.

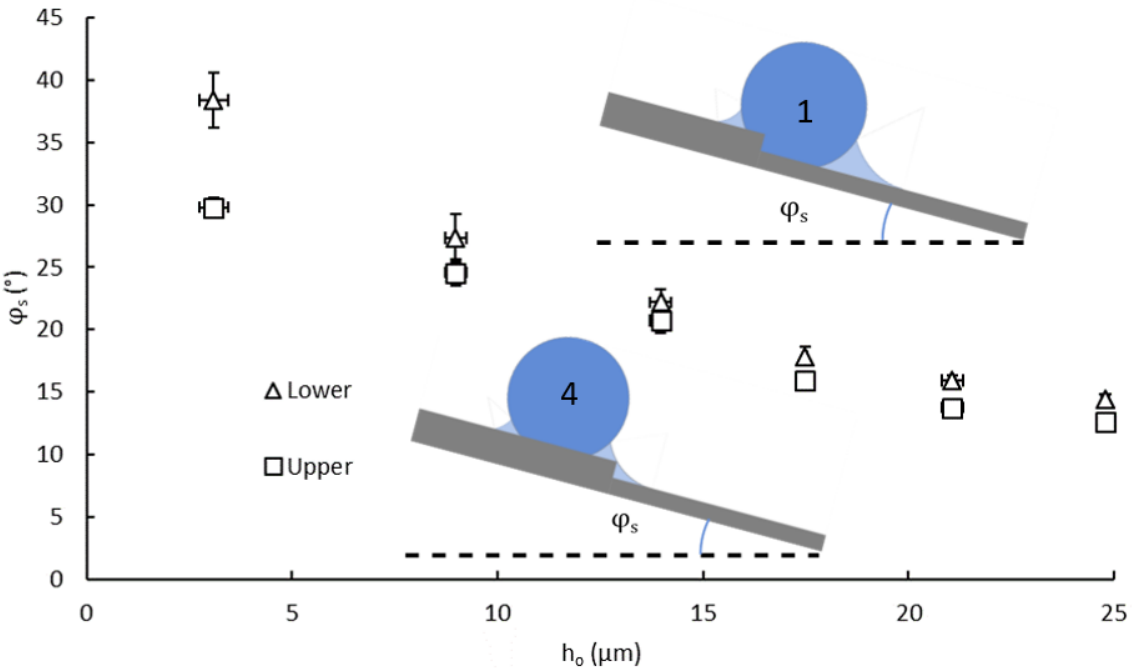

Figure 4.6.1: Detachment angle data for Configuration 1 (triangles) and Configuration 4 (squares) plotted on the same axes to show the discrepancy between the angles.

By taking the final side view frame before the droplet detachment for both cases, the differences in droplet position or shape to cause the differences in detachment angles should be evident. An example of a typical comparison between Configuration 1 and 4 with the wetting ridges appearing to be very evident (oil thickness of 17.48 μm) is shown in Figure 4.6.2. As the angles for detachment are different, the two images have been rotated to appear horizontal (Figure 4.6.2 a, b). Overlaying these two images gives an accurate comparison between the two configurations. From this image it can be seen that on the macro scale there is very little difference between the two configurations

(Figure 4.6.2 c). Both have a very large wetting ridge accompanied by a droplet with a spherical cap. Therefore, the difference between these two configurations cannot be due to the shape of the droplet and wetting ridge and must be governed by another factor.

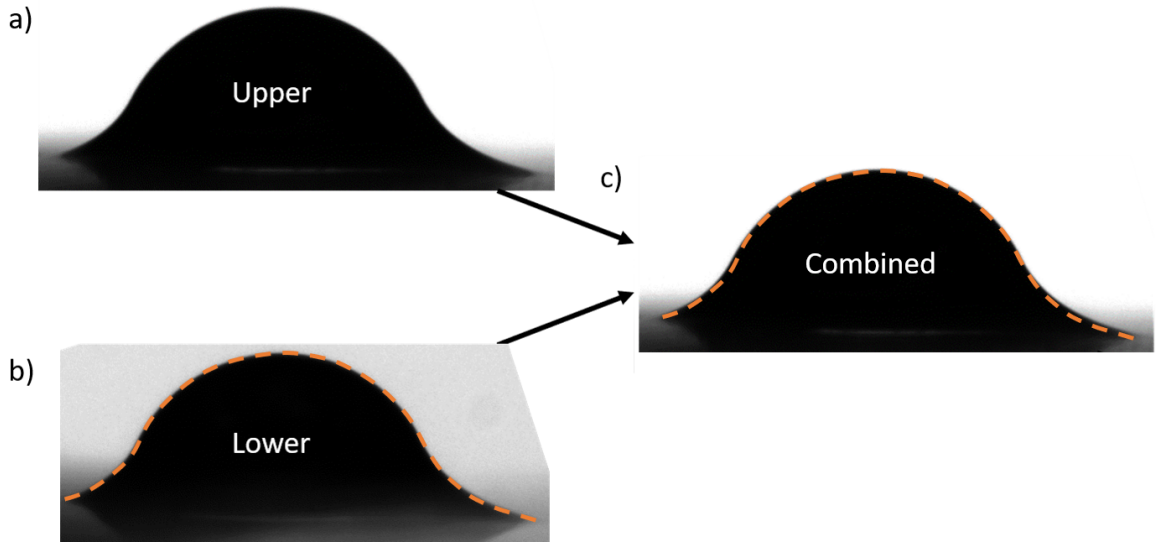

Figure 4.6.2: Side view images of the droplets before step detachment. a) Configuration 4 with a detachment angle of 15.96° rotated to be horizontal. b) Configuration 1 with a detachment angle of 17.86° rotated to be horizontal. c) Overlaid images from a) and b) showing the similarities between be 2 configurations.

It has already been observed in Chapter 3 that the size of the wetting ridge grows over time, therefore it is reasonable to consider that the effect may in fact be time dependent. As the sliding angle for the droplet on the lower section is higher than that on the upper section, it would be reasonable to assume that the lower droplet has spent more time on the surface than the upper droplet. However, as the droplet on the upper section first must travel to the lower position the tilting operation of the stage is stopped whilst the droplet moves to this position, therefore it is in fact the upper droplet that has spent the longest time on the surface. On a surface oil thickness of 3.09 μm there is the largest difference between the two detachment angles. For a droplet that starts on the Upper section the typical time a droplet will spend on this surface before detachment is approximately 186 seconds. For a Lower droplet the typical time is approximately 180 seconds. The difference between the two times is small at 6 seconds but may still have a significant effect. To test whether time was an

influential factor in the detachment angles, a sample of step height 140 μm was infused with an oil layer of 3.09 μm. For this combination of h_s and h_o the sliding angle for the upper droplet is equal to 29.8° ± 0.7°. Hence, the same volume (2 μl) droplet is placed on the lower section and the sample tilted to 30.0° ± 0.2° (Figure 4.6.3 a). The droplet is then left in this position for a total of 5 minutes to allow for the accumulation of oil into the ridge. At 5 minutes the droplet has already begun to noticeably evaporate and as the detachment angle is related to the mass of the droplet $F_g = mg\sin\theta$ once the droplet has begun to reduce in weight the likelihood of detachment is also reduced (Figure 4.6.3 b). After repeating this experiment 5 times the droplet remains attached to the step on every occasion, ruling out the possibility that, in this case, the effect is purely time dependent.

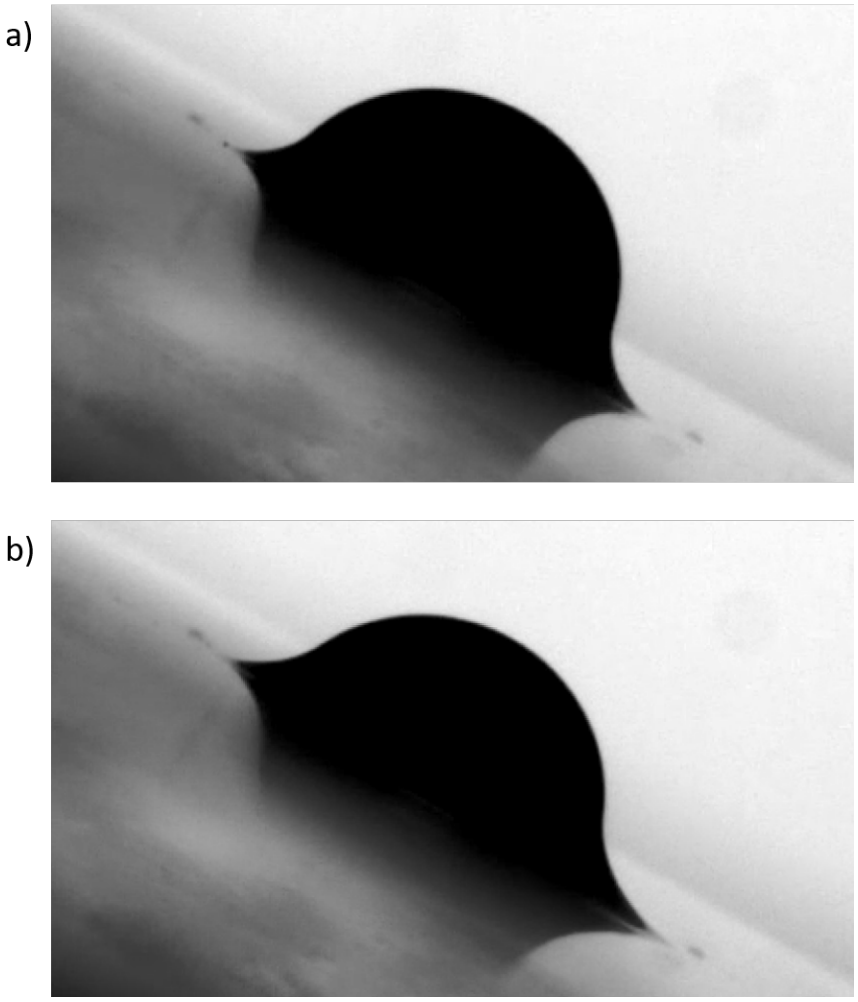

Figure 4.6.3: A 2 μl droplet placed below the step and a) the droplet tilted to 30° and b) at the end of 5 minutes when the droplet (still at 30°) has started to evaporate.

The final possible cause of sliding angle discrepancy to check is the position of the

droplet itself (not the droplet in addition to the wetting ridge) in relation to the step. Viewing the droplet from above allows for the entirety of the droplet and wetting ridge footprint to be seen independently, hence providing information about the two that side profile images can't deliver. By placing a grid underneath the sample, when the droplet is deposited onto the surface the grid is deformed by the wetting ridge and droplet curvatures. Therefore, the extent to which the wetting ridge expands around the droplet footprint can be viewed. By using the same h_o and h_s as seen in the side profile images (Figure 4.6.2) the two sets of images can be directly compared. Again, by taking the final image in the sequence before droplet detachment the configuration of the droplet in relation to the step can be ascertained. By simply viewing these two images (Figure 4.6.4 a, b) as taken by the camera, on the macro-scale it appears that the two droplets are in the same position.

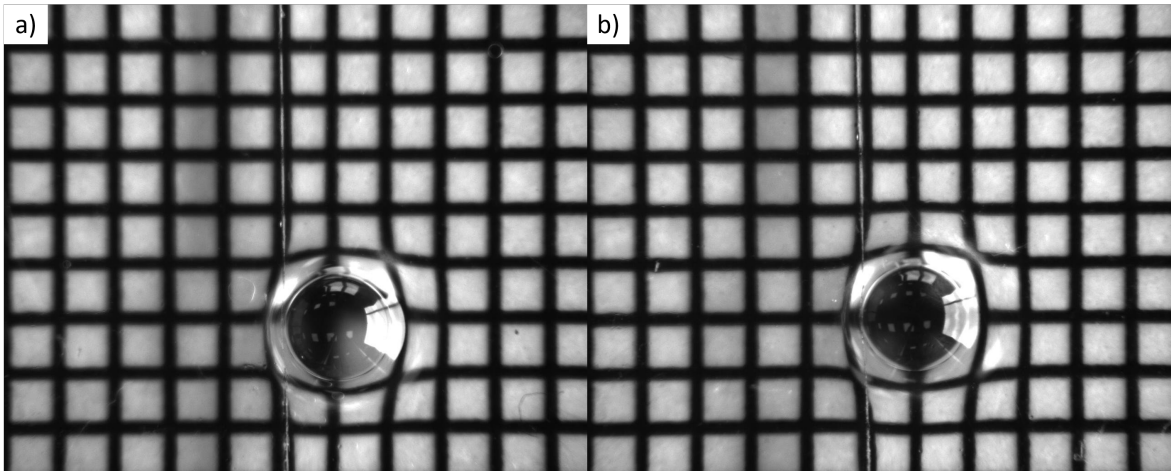

Figure 4.6.4: 2 μl droplets with differing initial positions, a) upper and b) lower, prior to step detachment with each square of the grid equalling 1 mm.

When focusing in on the line of the step in Figure 4.6.5 a) and b) there appears to be a separation between the droplet whose initial position was on the upper portion of the sample and the step. Measuring this gives an average separation of 54.5 μm $\pm$ 11.3 μm. Therefore, it is only the wetting ridge that is holding the droplet in this stationary position. The step still has a small effect on the droplet, flattening the trailing edge slightly. Performing the same analysis for the droplet whose initial position was on the lower section Figure 4.6.5 c) and d), the droplet – step separation cannot be seen, there is in fact an overlap of the droplet on the step. Measuring this distance gives

an average overlap of 88.3 μm $\pm$ 1.7 μm. Therefore, the observed difference between detachment angles can be rationalised by the difference in position relative to the step. As the upper (Configuration 4) droplet is only being retained in its stationary position by the wetting ridge, less force is required to remove the droplet from the step. In contrast to this the lower (Configuration 1) droplet must detach both the droplet and wetting ridge, hence the higher detachment angle. This indicates that the droplets detachment angle is not only affected by step height and oil thickness, but it has a memory of the initial deposition position.

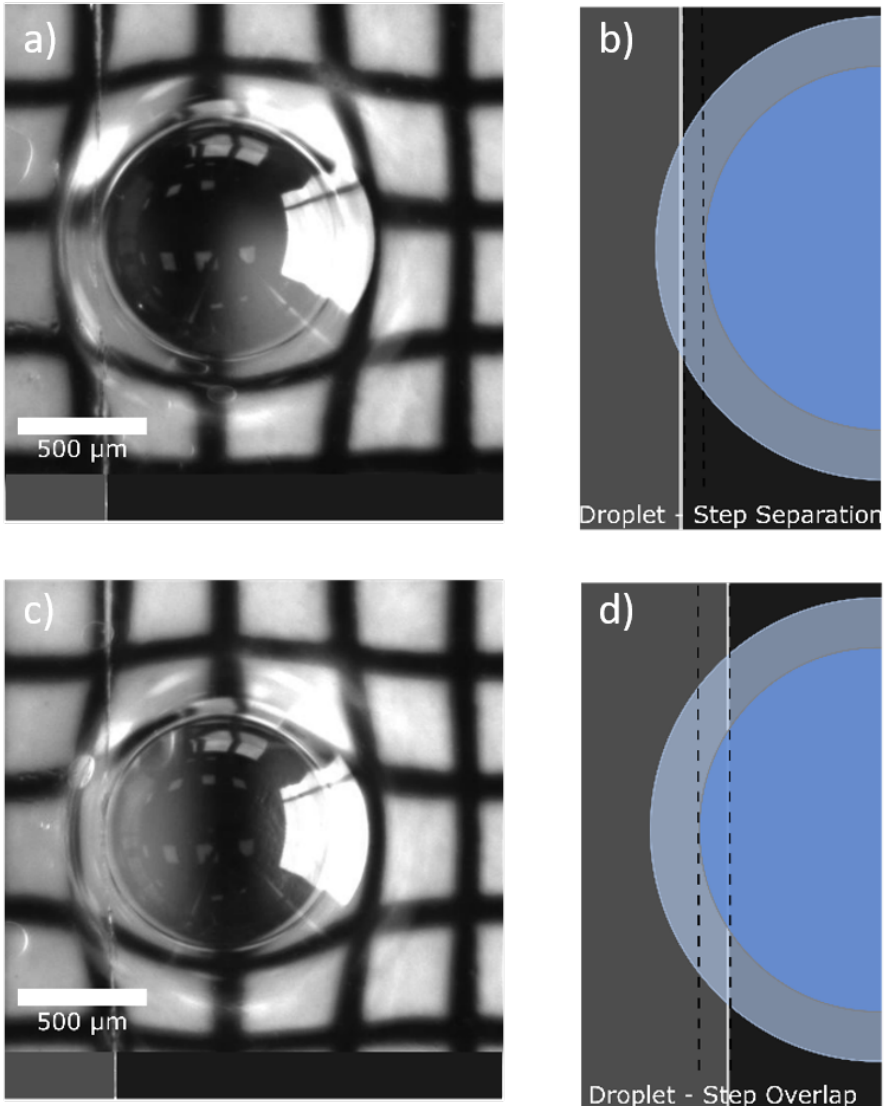

Figure 4.6.5: Position of a 2 μl droplet relative to the step with differing initial positions. a) Top view of a 2 μl close to step detachment droplet showing the exact position the droplet that initially started on the upper portion of the step and b) a schematic indicating the droplet – step separation. c) A 2μl droplet with its initial position having been on the lower portion of the sample with d) indicating the droplet – step overlap.

As the oil thickness increases to its maximum value, 24.79 μm, the lower and upper detachment angles begin to converge to $\approx 12°$. This convergence can be attributed to the contact area of the droplet and wetting ridge with the step. At small oil thicknesses, ≈ 3.09 μm, the difference between having just the wetting ridge, or the droplet plus the wetting ridge in contact with the step is large as the size of the wetting ridge is small, hence the need for more force to remove the droplet and wetting ridge configuration. As the size of the wetting ridge increases with oil thickness the wetting ridge becomes comparable to the size of the droplet, therefore the difference between the two attachment areas does not change significantly when the presence of the droplet is added (the lower droplet configuration). Hence the amount of force required for detachment also becomes comparable, leading to the convergence of detachment angles.

4.7 Conclusion

Droplet control can be returned to a highly slippery surface by adding a very simple structure, such as a step. Adding this pinning point does not affect the surfaces sliding angle when tilting the sample in a direction parallel to the step. Tilting the sample normal to the step increases the sliding angle to a detachment angle by two orders of magnitude with certain parameter combinations where the droplet does not detach from the surface at all. By tailoring the height of the step along with the amount of oil added to the sample the mobility of the droplet can be altered in the parallel direction. By producing a log-log plot of $\sin(\theta_s)$ as a function of step height/oil thickness, the adhesive force is found to depend on the ratio of step height to oil thickness to the power of a half $F_{cap} \approx (h_s/h_o)^{(1/2)}$. The exact reason for this dependency is still unknown as the force balance problem has only been conducted in 2 dimensions, whereas the droplet and wetting ridge are in fact in 3 dimensions.

The initial positioning of the droplet has a significant effect on the droplet's detachment angle even if the final stationary position is the same, which is an effect that is time independent. The negative curvature at the top of the step is strong enough to transport the droplet away from the step due to the repulsive force. Adding pinning points to the surfaces would have uses in a wide range of applications:

• Droplet selection – depending on where the droplets are deposited , or land on the surface a well as their volume could determine whether they remain on the surface or not when tilted.

• Fog harvesting – the step creates a pinning point for water to collect on before reaching a volume (determined by the step height and oil thickness) and then detaching from the surface.

• Microfluidics – a droplet may need to be held in a certain position for a period of time to perform a chemical reaction before being removed from the surface completely or just to the nest section without leaving any contaminants, making the surface multi use.

Chapter 5

Interaction Length Scales

This chapter discusses ways in which droplets can be passively transported without the requirement to add any external force to the system. The attractive and repulsive interaction between two droplets and a droplet and a fixed object is be explored. The interaction effects are also shown to be heavily dependent on the time a droplet spends on the surface before being released from a needle. The work presented in this chapter is currently in preparation for a journal article.

5.1 Introduction

The ability of a structure to generate a repulsive force has been briefly explored in Chapter 4 but the distance a droplet can travel only using the inherent surface features has not been explored. The ability to transport droplets without requiring any external forces, such as gravity that acts on a tilted substrate, would be ideal for applications that require passive droplet control. Extending the idea of the adhesive force between a droplet and a fixed object to a multi-droplet system better replicates the types of interactions droplets will experience in practical applications as it is very rare that a single droplet will be used in an application-based situation.

5.2 Wetting Ridge Growth

When a droplet is placed onto a SLIP surface a wetting ridge immediately develops on a rapid time scale and begins to grow with increasing time spent on the surface. This long-time effect is very easy to study experimentally on the SLIP surfaces by simply placing a droplet on to a surface and attempting to hold it in place until the ridge grows and droplet begins to evaporate[136].

Generally, when a droplet is released from a needle on a SLIP surface, the droplet moves until it has found a position to settle in (this is indicated by the low sliding angles from Table 3.5.2). Therefore, the droplet must be held in place to take measurements of the wetting ridge growth. To do this a thin wire (0.143 mm) was fed through a 0.7 mm needle. The droplets were then deposited through the needle, down the wire and onto the surface. The needle was not used to hold the droplet to remove the possibility of liquid being drawn back into the syringe or for the oil to coat the needle, affecting further droplets deposited. Once the droplets had been deposited onto the surface, they were left to interact with the oil layer for a total of 5 minutes. It is known that at this point the 2 μl droplets will have begun to noticeably evaporate and decrease in size. Therefore, to make all the data comparable but to also give enough time for the wetting ridge to develop a time frame of 5 minutes was chosen. In an attempt to suppress the evaporation but to have the droplet in an environment as close to application conditions as possible, the experiments were conducted in a humidity-controlled environment at 72%, set to room temperature (22°). The height of the wetting ridge (Figure 3.5.1) was tracked over the 5-minute experimental window producing the graph in Figure 5.2.1. As the oil thickness increases so does the growth in the wetting ridge. The wetting ridge growth seems to start to plateau for the smaller oil thicknesses but within the experimental window the increase is still significant.

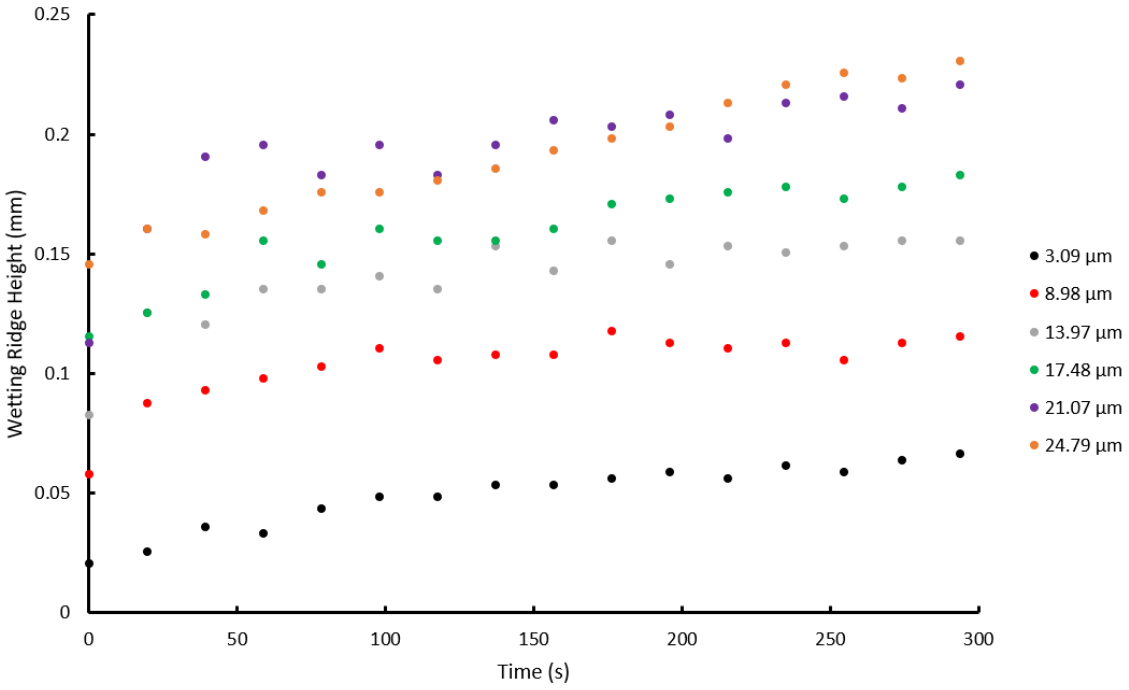

Figure 5.2.1: Wetting ridge height growth data for 5 μl droplets place into a controlled humidity environment set to 72%.

The wetting ridge footprint growth (Figure 3.5.1) was also tracked over the experimental time window as it is the length of the wetting ridges that determines the interaction distance. The wetting ridge footprint will eventually determine how droplets will interact with other droplets or objects on the SLIPS. From Figure 5.2.2 it can be seen that the wetting ridge footprint growth matches the data trends in Figure 5.2.1 with an increase in oil thickness producing larger wetting ridges that continue to grow past the experimental time window.

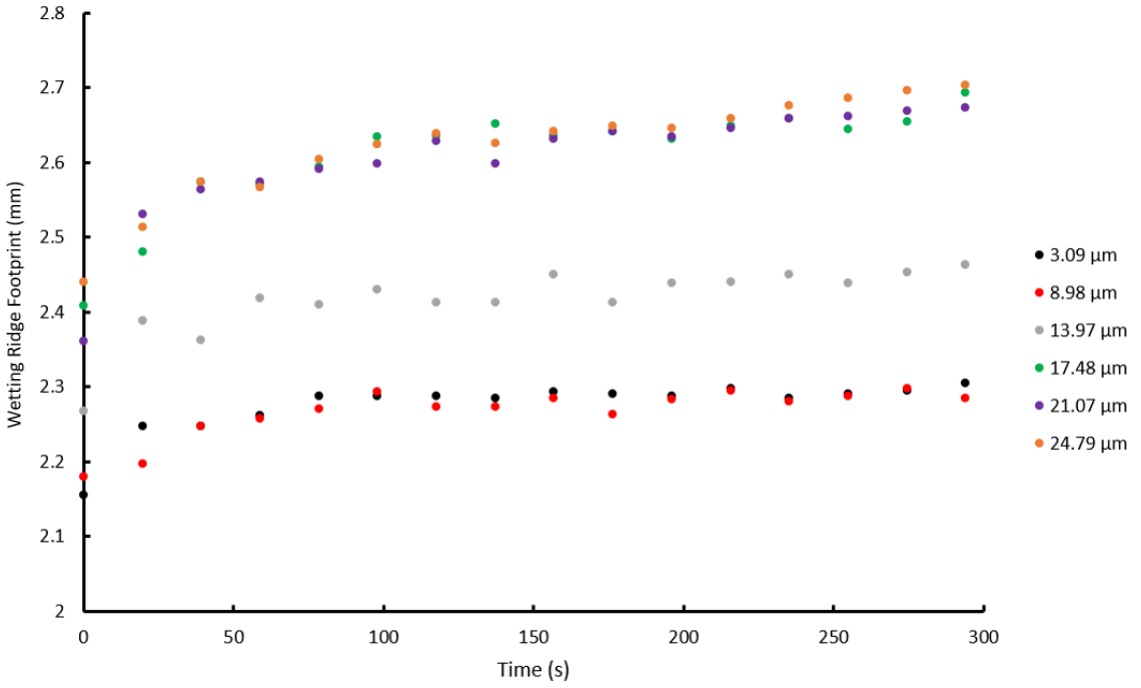

Figure 5.2.2: Wetting ridge footprint growth for 5 μl droplets placed into a controlled humidity environment set to 72%.

The droplets used in previous experiments were not conducted in a controlled environment and there was no intention to do so in subsequent experiments therefore, the above experiments were repeated for a typical droplet size (2 μl) and in typical ambient lab conditions (temperature between 20° and 25° and humidity between 25% and 35%). The droplets were deposited using a 0.7 mm needle on to the SLIPS surfaces which had been imbibed with increasing oil thicknesses and again left for a total of 5 minutes. As there was no controlled chamber to suppress evaporation, at 5 minutes the droplet had begun to noticeably decrease in volume. The decrease in volume, however, did not, at this point, appear to have much of an effect on the wetting ridge for large oil thicknesses. The footprint of the ridge still grew, albeit at a very slow rate and the height almost reached a constant level. Measuring the height of the oil ridge proved to be difficult as the droplets were not held in place by the needle hence the droplet appeared in different positions in each frame Figure 5.2.3.

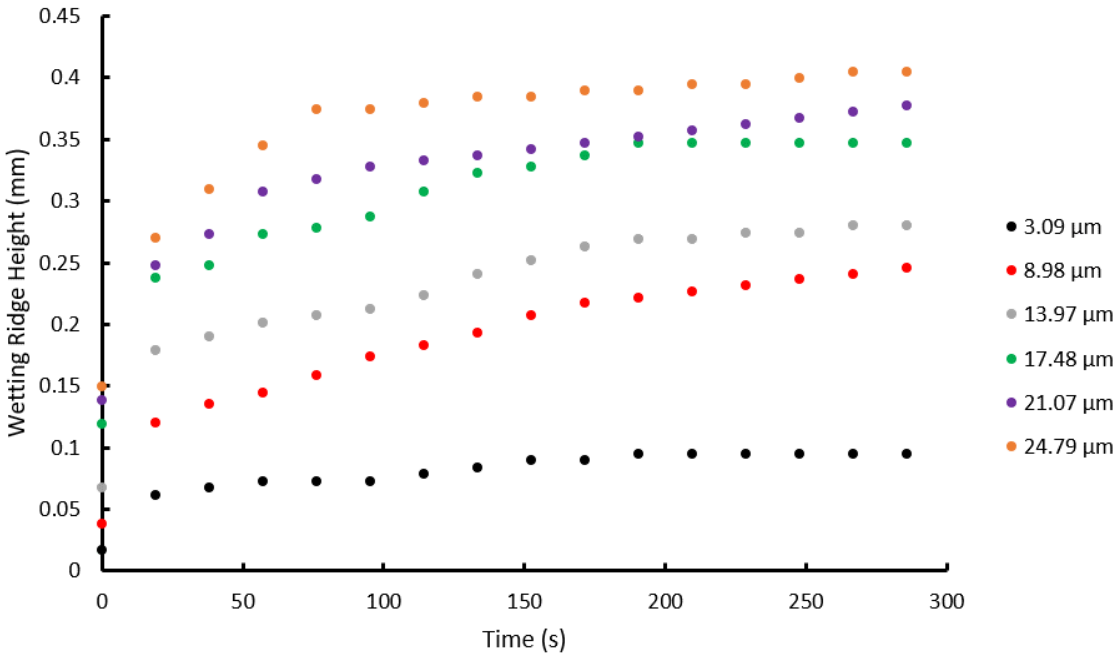

Figure 5.2.3: Wetting ridge height growth for 2 μl droplets placed in ambient conditions with a temperature range of 20° - 25° and humidity range of 25% - 35%, resembling typical experimental conditions.

The influence of the oil thickness is quite significant and appears to change depending on whether the height or footprint is being measured (Figure 5.2.3 and 5.2.4). In Figure 5.2.4 the footprint of the wetting ridge at an oil thickness of 3.09 μm appears to peak at 10 seconds and at approximately 225 seconds the footprint of the droplet and wetting ridge has decreased to less than 1.6 mm (less than the starting value). For oil thicknesses of 13.97 μm to 24.79 μm the wetting ridge footprint continues to increase past the 300 second time window, indicating at this thickness the effects of droplet evaporation are negligible.

For the thinner oil layers the footprint and height both begin to decrease or plateau meaning that for certain conditions the oil ridge appears to spend a period of time in equilibrium with the surface. This period is short lived as the droplet evaporation changes the droplet volume and therefore the height and footprint of the wetting ridge.

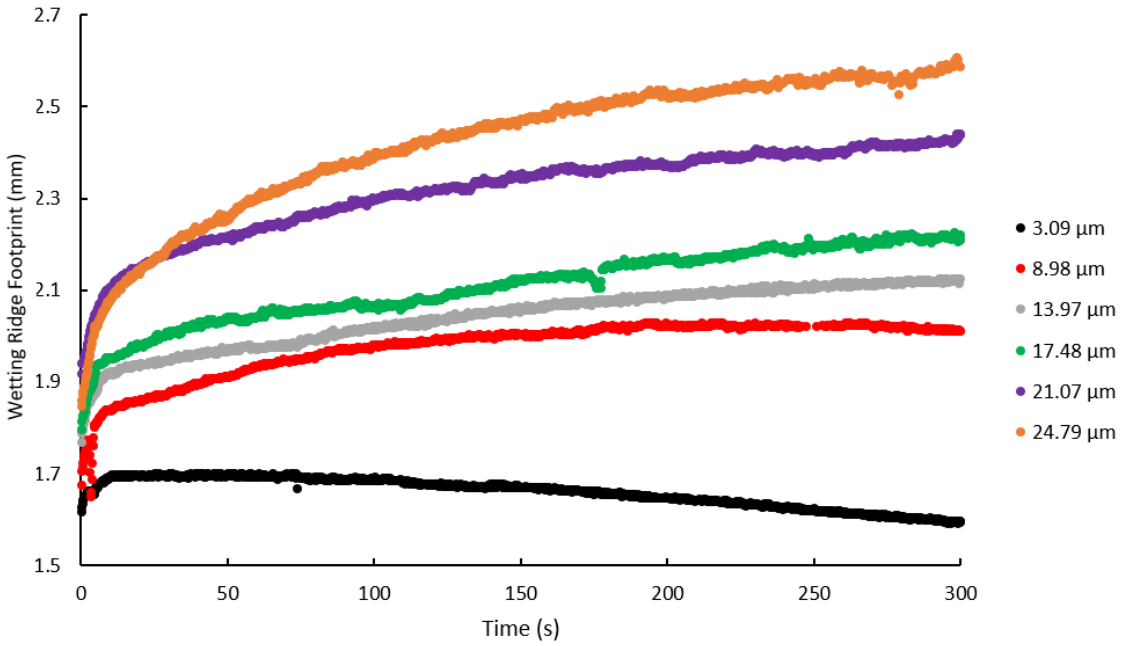

Figure 5.2.4: Wetting ridge footprint growth for 2 μl droplets placed in ambient conditions with a temperature range of 20° - 25° and humidity range of 25% - 35%, resembling typical experimental conditions.

As can be seen for both sets of data, controlled environment and ambient conditions, the droplet will never truly reach an equilibrium with a SLIP surface and any plateau to the data (pseudo-equilibrium) is driven by the evaporation of the droplet and will only be a temporary effect.

Increasing the droplet volume to 4 μl should have very little effect on the droplet diameter and hence the wetting ridge footprint, as the radius of the droplet scales as the cube root of the volume. Therefore, when performing the same experiment used to produce the data for Figure 5.2.3 it is not unexpected that the data in Figure 5.2.5 looks much the same. The only difference that can be identified for the two figures is that the data for 21.07 μm and 24.79 μm switches for 100 seconds, but the start and end of the wetting ridge height data follows the expected trends with the thicker oil layers having larger wetting ridges.

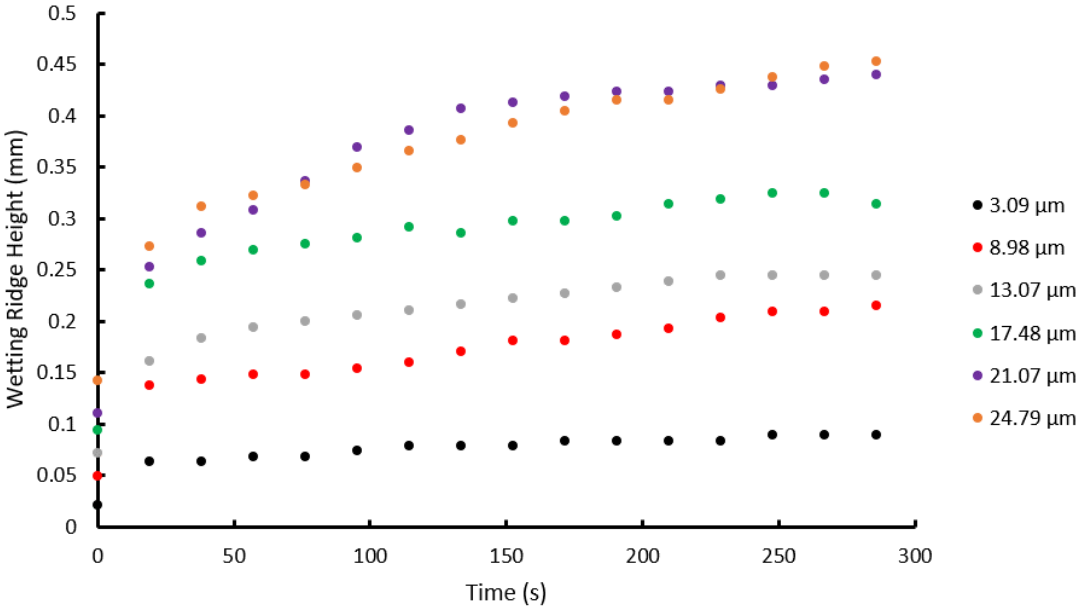

Figure 5.2.5: Wetting ridge height growth for 4 μl droplets placed in ambient conditions with a temperature range of 20° - 25° and humidity range of 25% - 35%, resembling typical experimental conditions.

Comparing the wetting ridge footprint data in Figure 5.2.4 and 5.2.6 again shows the same trends however, the data for the 8.98 μm oil layer appears to plateau and remain constant for the 4 μl water droplet.

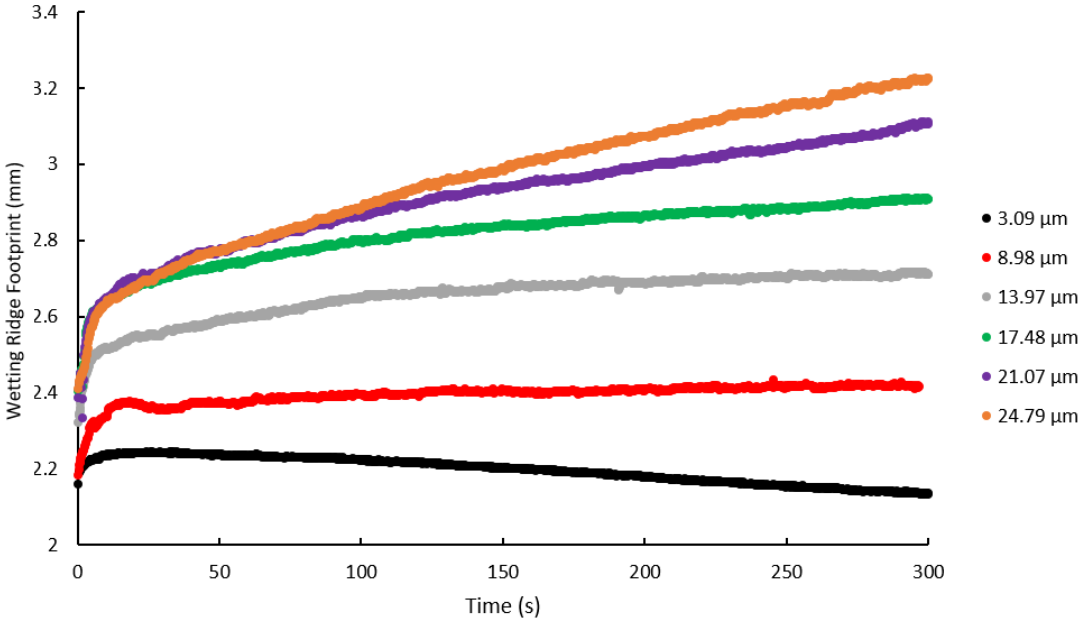

Figure 5.2.6: Wetting ridge diameter growth for 4 μl droplets placed in ambient conditions with a temperature range of 20° - 25° and humidity range of 25% - 35%, resembling typical experimental conditions.

There is little discrepancy between the wetting ridge footprint growth for the 2 μl and 4 μl droplets, so normalising the data from Figure 5.2.4 and 5.2.6 should produce data that follows the same path. For the thinnest oil layer (Figure 5.2.7 a) the first 75 seconds of the data does follow the same path however at later times the two data sets begin to diverge. This indicates that the decrease in droplets footprint for the 2 μl droplet happens faster than for the 4 μl droplet, but the decrease is still present. For the thickest oil layer, a similar effect is seen but this time with footprint growth rather than reduction. For the 4 μl droplet there is a steep continuous increase in the wetting ridge footprint but for the 2 μl droplet the increase is a lot slower, beginning to plateau towards 300 seconds (Figure 5.2.7 b).

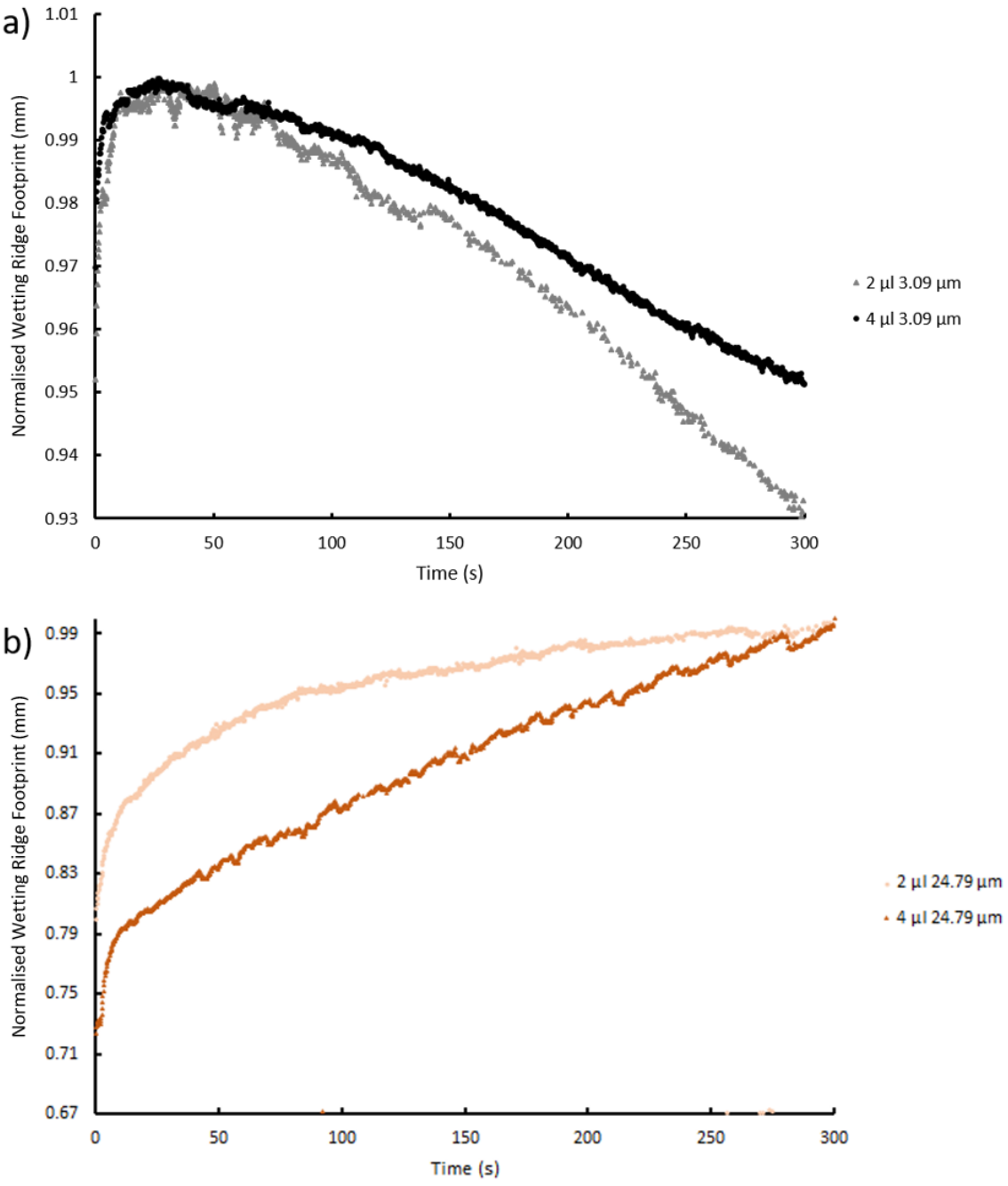

Figure 5.2.7: Normalised diameter position data for the 2 μl and 4 μl droplets at oil thicknesses of a) 3.09 μm and b) 24.79 μm showing the data similarity.

5.3 Distance of Interaction

For two objects to interact on such surfaces the growth of the wetting ridge is a significant factor to consider when it comes to determining exactly what position to deposit an object in order for it be influenced by another object. In the case of two 2 μl droplets the deposition positions should occur between the orange and blue data in order to produce an attractive force (Figure 5.3.1).

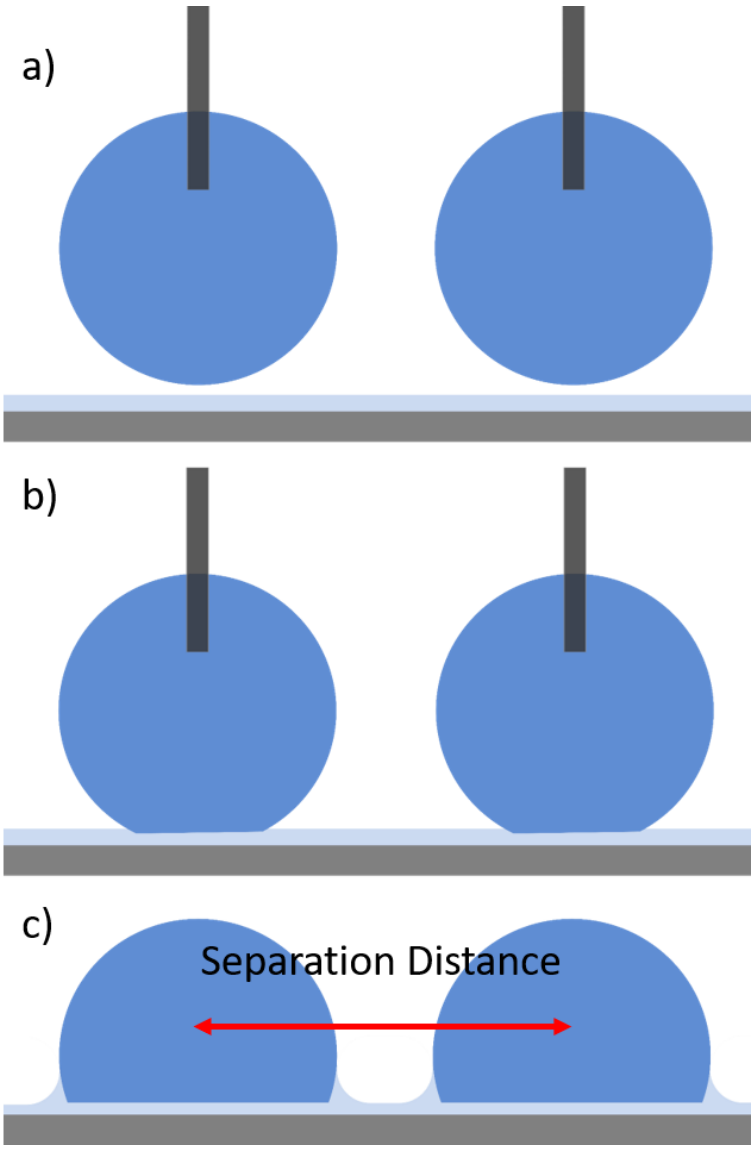

Figure 5.3.1: Experimental set up schematic, a) two droplets on needles prior to surface deposition, b) shortly after droplet deposition and c) just after needle removal where the initial droplet separation distance is measured.

The distance of interaction increases with increasing oil thickness as the size of the wetting ridge the droplets can develop also increases. As the droplet on the oil layer of thickness 3.09 μm starts to evaporate the possible distance of interaction is small and will be more time dependent than the other data sets (Figure 5.3.2).

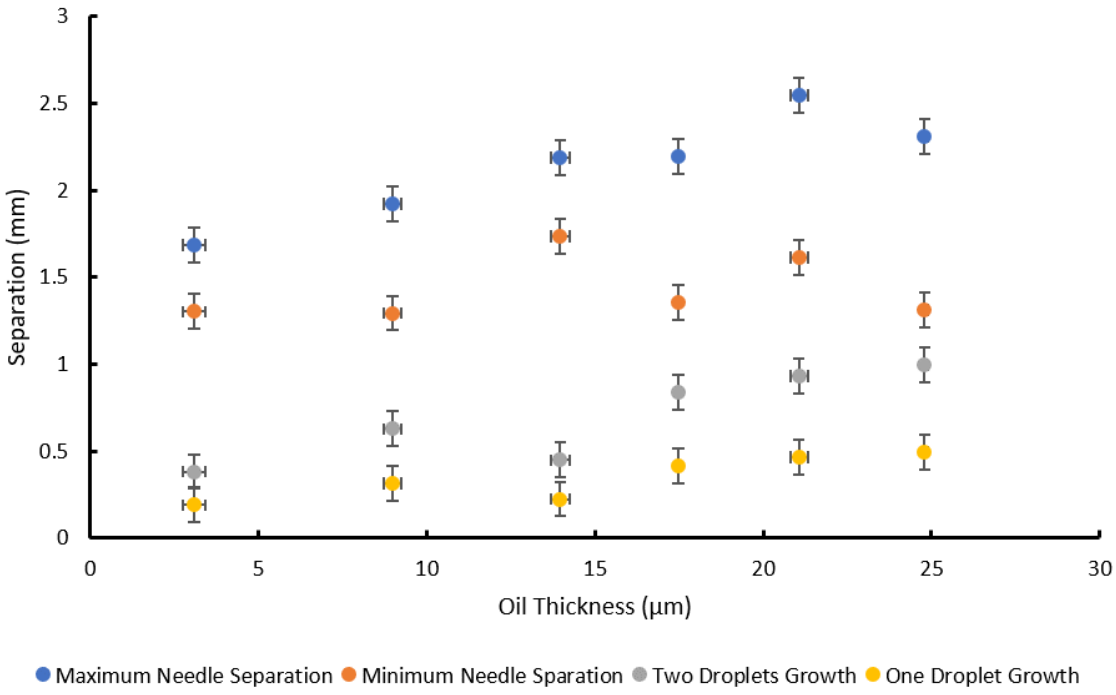

Figure 5.3.2: Expected interaction distance for a 2 μl droplet on each oil thickness including the wetting ridge growth.

For a 4 μl droplet the distance of interaction again increases with increasing oil layer thickness. The droplet on the 3.09 μm oil layer evaporates slower for a 4 μl droplet than a 2 μl droplet therefore, the attractive interaction should be stable for a longer period of time (Figure 5.3.3).

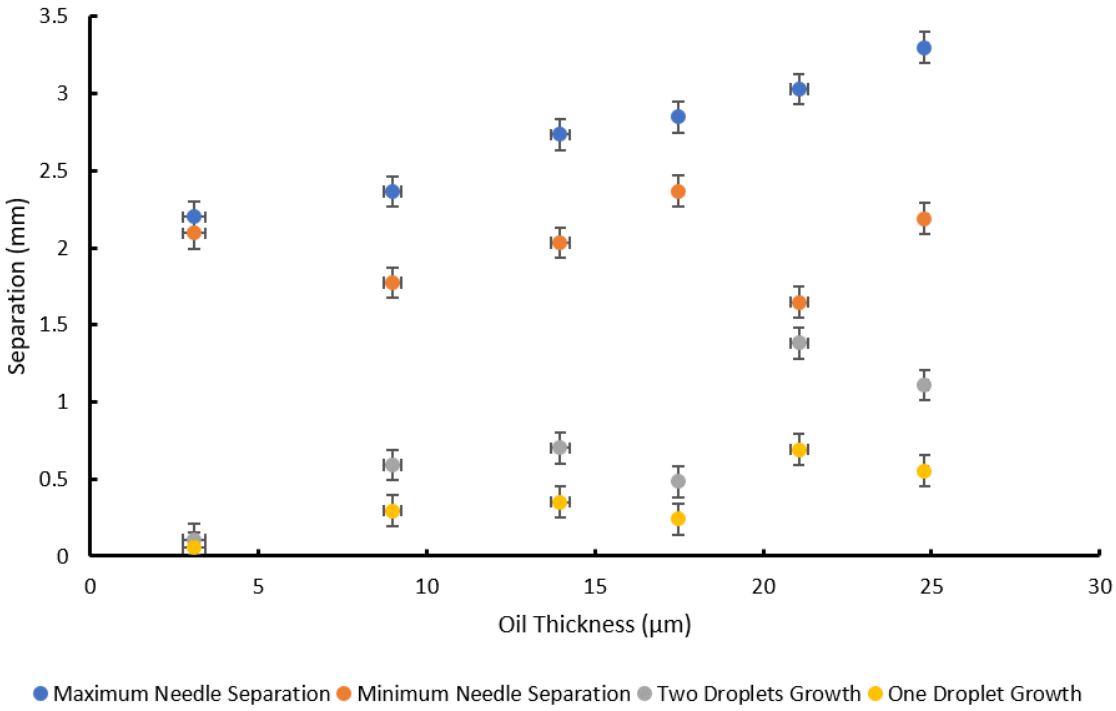

Figure 5.3.3: Expected interaction distance for a 4 μl droplet on each oil thickness including the wetting ridge growth.

From the wetting ridge diameter growth data, Figure 5.2.2, the possible interaction lengths can be extracted for each of the six oil thicknesses for a system undergoing little evaporation. The orange dots in Figure 5.3.4 correspond to the diameter of the droplet plus wetting ridge at time zero (just after deposition) and the smallest diameter that the droplet will adopt. The blue dots are the final droplet diameter (after 5 minutes) and should correspond to the largest droplet size that will be seen through experiments. The grey data points have been extracted from the difference between the blue and orange data points at each oil thickness. These values correspond to the amount of growth one droplet undergoes on each surface however in the case of droplet-droplet or droplet-object interactions it is only one edge of the droplet that will interact with another, hence why the grey data corresponds to a two-droplet system. The yellow data is simply half of the grey data to give the wetting ridge growth of one droplet, or the single interacting edge of one droplet. If the interaction between two droplets is governed by the wetting ridges then initially placing the two droplets close enough together (between the blue and orange data) should lead to an interaction.

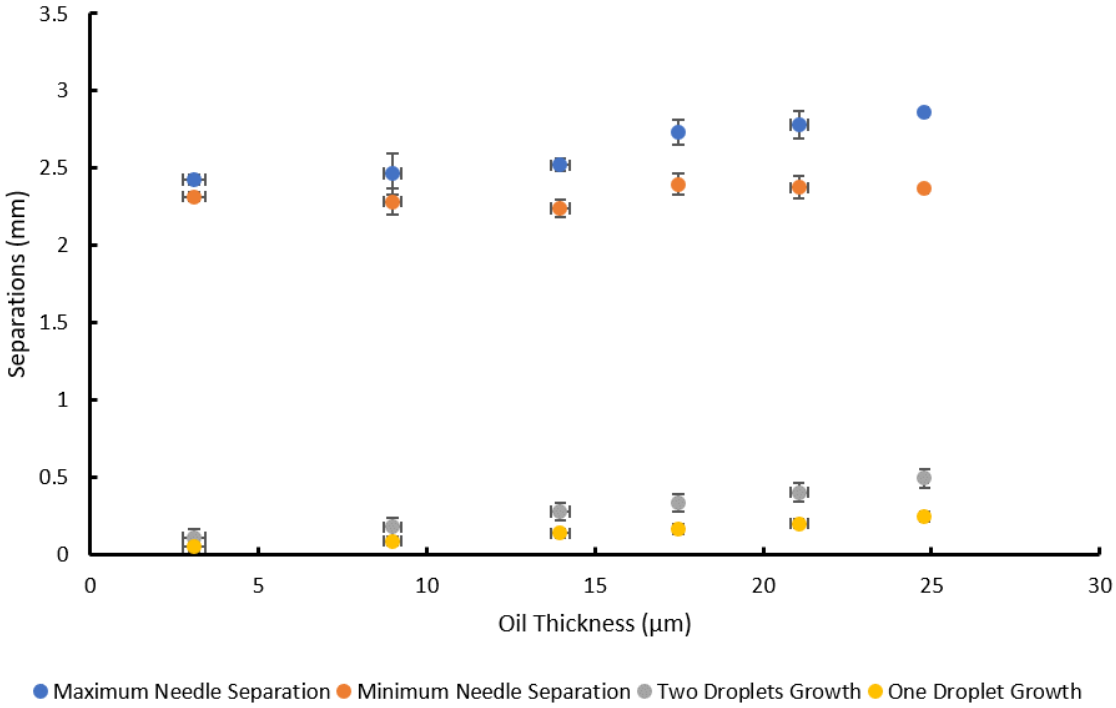

Figure 5.3.4: Expected interaction distance for a 5 μl droplet on each oil thickness including the wetting ridge growth.

5.4 Droplet - Droplet Interactions

To experimentally test the predicted interaction lengths from Figures 5.3.2, 5.3.3 and 5.3.4 droplets of equal size were deposited onto the surface simultaneously. To do this the Krüss DSA 30, with a 0.70 mm outer diameter needle, was used in a fixed position to deposit droplet one. The second, equal volume, droplet was deposited by hand using an auto pipette, again with an 0.70 mm needle, held on a moveable rail, allowing the distance between droplets to be varied easily. The separation distance between the centre of two droplets was measured once the two droplets had been deposited onto the surface rather than using needle separation or droplet separation whilst still attached to the needles.

The interaction between the droplets should be almost instantaneous, meaning that there is very little time available for the droplets to develop their wetting ridges. Therefore, to conduct the initial test, an oil layer thickness of 17.48 μm was chosen to produce a large enough wetting ridge to induce an interaction without having to place the droplets almost on top of each other. According to Figure 5.3.4, for a 5 μl droplet

there should be a fairly large interaction range of 0.34 mm between the blue and orange data points. Instead of tracking the droplets central position as a function of time, it is how the droplets interact together that is measured to produce the additional data for Figure 5.4.1.

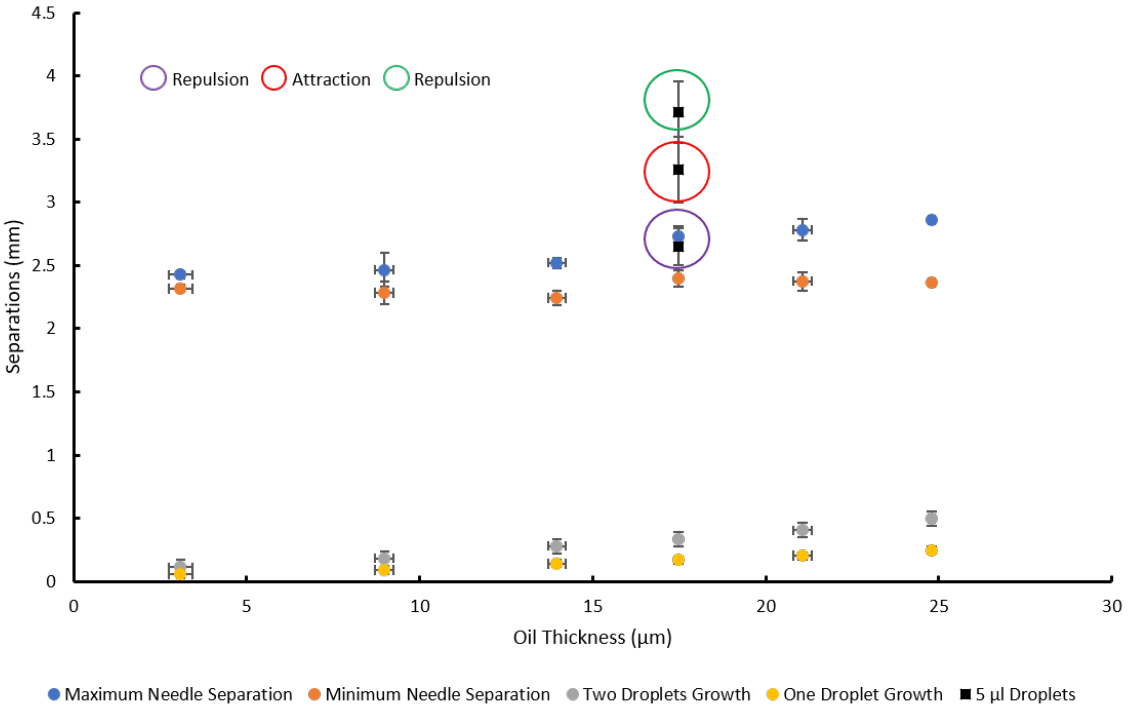

Figure 5.4.1: Expected interaction distance for a 5 μl droplet on each oil thickness including the wetting ridge growth with the measured droplets interactions for an oil thickness of 17.48 μm.

The interaction that is seen between the two 5 μl droplets placed close to each other (between the blue and orange data) is not as expected. As the two droplets form the same wetting ridge curvatures, it is expected that this will produce an attractive force, according to the Cheerios effect. What is instead seen is a repulsive force where the two droplets move away from each other rather than towards (purple circled square in Figure 5.4.1).

From the wetting ridge diameter growth data there should be little effect on separating the droplets further to a separation distance of approximately 3.25 mm as the wetting ridges should no longer be in contact. However, increasing the separation distance leads to a change in interaction (red circled square in Figure 5.4.1), switching from a repulsive force to an attractive force. As the two droplets are placed on to the

surface the wetting ridge develops slightly and then immediately feels the force from the neighbouring droplet. The droplets are then pulled towards each other eventually pushing the oil cloaking layer between the droplets out of the way allowing them to coalesce.

At the separation distance of approximately 3.75 mm (green circled square in Figure 5.4.1) the droplets undergo another switch from an attractive behaviour to a repulsive behaviour. However, this repulsive behaviour differs slightly from the behaviour seen when the droplets are close together. In the first repulsive regime the two droplets always push each other away in the same plane. In the second repulsive regime the direction the two droplets travel in changes. The normal behaviour at this distance is for the two droplets to be pushed away from each other but at the same time to rotate and move out of the cameras plane. The other behaviour sometimes observed is for the droplets to repel each other but in the opposite plane to the camera.

By decreasing the withdrawal speed and reducing the oil layer thickness the types of interactions identified in Figure 5.4.1 are unchanged. Figure 5.4.2 shows the similarity between the two oil thicknesses and the interactions that two 2 μl droplets undergo.

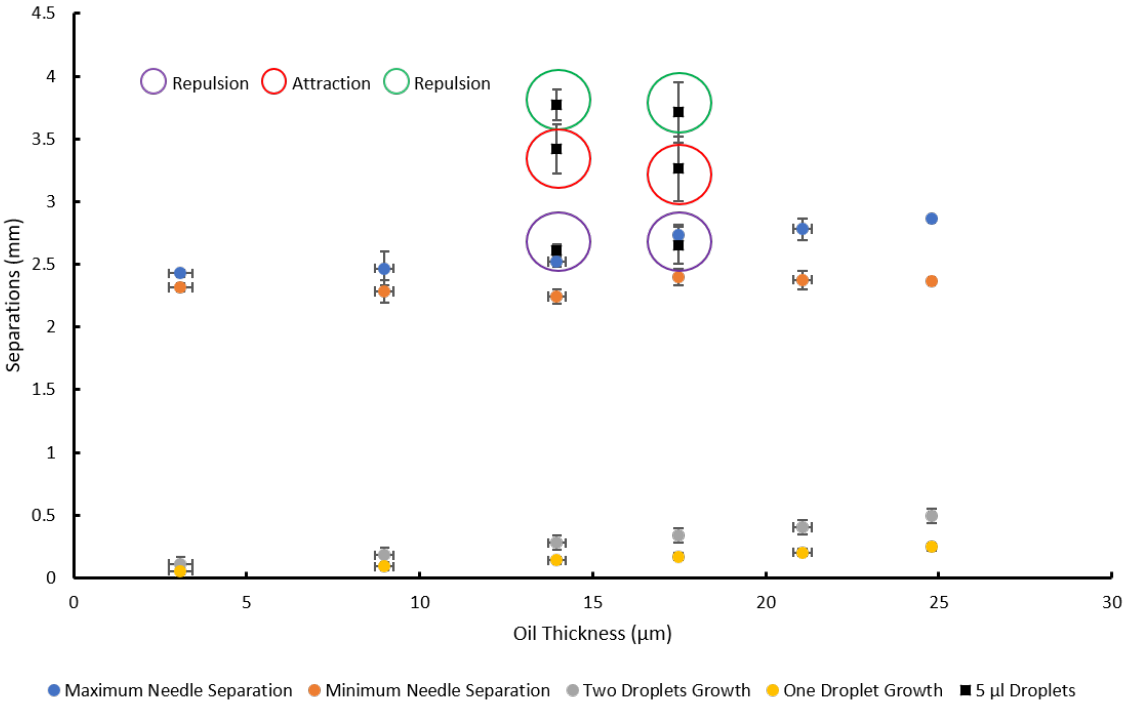

Figure 5.4.2: Expected interaction distance for a 5 μl droplet on each oil thickness including the wetting ridge growth with the measured droplets interactions for oil thicknesses of 13.97 μm and 17.48 μm.

As both droplets are capable of movement, in this instance it is very difficult to study the complexities involved in this problem. Therefore, to understand what is driving the differing interactions the experiments will be conducted again with the fixed object in the form of a step used previously in Chapter 4.

5.5 Attraction to Fixed Object

The length of the wetting ridge, or droplet footprint, should determine the length scale of the droplet interactions with another object that produces a wetting ridge. As has been seen in section 5.2.3 the length of the wetting ridge that can be measured by eye is smaller than the interaction length scale, therefore the droplet and wetting ridge must be inducing more changes to the surface than are immediately apparent. Again, looking at the stepped structure from the previous Chapter 4, it is easy to see that the wetting ridge length is determined by the oil thickness. Therefore, by changing the oil thickness this should change the position where the interactions occur.

As the ability of the stepped structure to retain a droplet has been fully explored

in Chapter 4 it is now the ability of this surface to produce this retention (attraction) force over a distance that will be explored.

5.6 Soft Solid

The inverted Cheerios effect has similar characteristics to the Cheerios effect and is quite literally the opposite of the Cheerios effect with the liquid base being replaced by a soft solid and the solid or bubble replaced by a droplet[137, 62]. The overall effect, however, is very similar to that previously seen, the droplet deforms the underlying substrate, pulling up the solid, creating a solid version of a wetting ridge with a positive curvature. The thickness of the solid is what ultimately determines how large the solid wetting ridge will be and governs the type of interaction, attractive or repulsive, that will be exhibited. The case with the soft solid however is slightly different to what is seen on a liquid. As the soft solid has been pulled up from the horizontal plane to wrap around the droplet there will in turn be a depletion created in the solid itself next to the wetting ridge. Without having a liquid reservoir to draw from to refill this depletion the depletion will remain until the droplet has been removed from the surface[61, 63]. As the level of the depleted area will be lower than that of the surroundings a negative interface curvature must be created. The negative curvature of the depletion region and the positive curvature of the wetting ridge (created by the droplet) will create a repulsive interaction as the droplet will try to move up the interface to balance the gravitational and (for a liquid interface) surface tension forces[132].

It is possible that the SLIP surfaces used within this study are subject to this depletion region seen on soft solids as when the wetting ridge is formed it depletes the oil layer[138]. Flow through the porous media is slow hence the time to refill the depleted region is longer than the interaction time scale. This depletive effect can be seen on these substrates. When sliding a droplet down the surface an area, approximately the diameter of the droplet and length equalling the distance travelled, appears to be slightly less reflective than the surrounding surface, resembling a trail similar to the wake a boat or even one a microbial swimmer would leave behind it.

One possible method to view the potential depletion region, without directly imag-

ing the sample, would be to use the Cheerios effect. If there is in fact a depletion region near to the step corner, caused by the step oil meniscus and proximity of a droplet, there should be distinct areas near to the step where there is droplet attraction and droplet repulsion, in effect providing a surface map of the oil layer thickness.

These can be split into three distinct categories[135] (Figure 5.6.1):

• Attraction – the droplet is drawn towards the step and eventually ends up in Configuration 1, described in Chapter 4 Section 4.

• Repulsion – the droplet is pushed away from the step and settles at a point away from the step (thin oil layers) or continues to move (large oil thicknesses).

• Normal Movement – the movement of the droplet without the influence of the step leading to a general settling of the droplet where it may be slightly attracted, repelled, or could even move out of plane of the camera creating a zero-net movement.

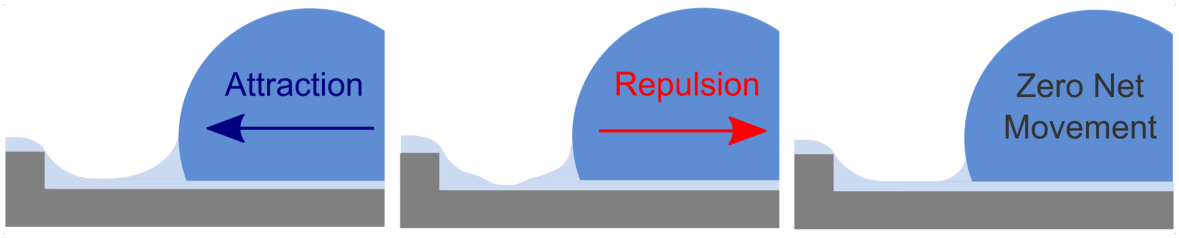

Figure 5.6.1: Schematics showing the three possible types of droplet interaction with the step.

A single step height of 140 μm was used to conduct the experiment with the sample infused with oil layers ranging from 3.09 μm to 24.79 μm. By varying both the oil thickness and the distance away from the step that the droplets are initially deposited the interaction type is changed. The attractive interaction can be seen on all samples but does not extend to 1.5 mm away from the step for the majority of the oil thicknesses. The attractive force can be seen for the 2 thickest oil layers at a distance of 1.5 mm away from the step but does not extend beyond this value meaning that it is the repulsive force that dominates the interaction types. The oil thicknesses from 8.98 μm to 17.48 μm all exhibit the same behaviour for all distances tested away from the step, with the oil thickness having to be increased to 21.07 μm in order to shift the data one data point to the right converting a repulsive force to attractive and zero movement to repulsion. The thickest oil layer exhibits the greatest range of interaction types with

the repulsive force stopping after 3.5 mm (two times the droplet radius) away from the step (Figure 5.6.2).

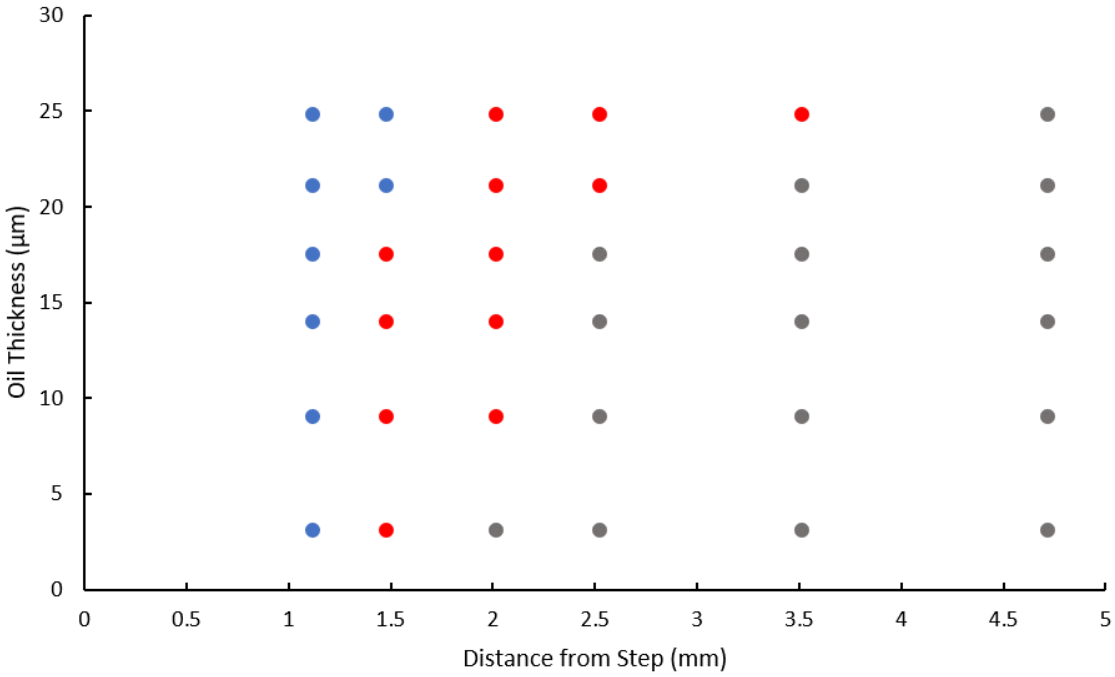

Figure 5.6.2: Attraction (Blue), Repulsion (Red) and Normal Movement (Grey) for a 2 μl droplet deposited onto the lower section of a 140 μm step sample.

Again, as has previously been discussed there is a time related element to SLIPS, which determines how the droplets will act with the surfaces oil layer and any objects on such a surface. This time factor specifically influences the wetting ridge growth, which has been fully explored in Section 5.2. Therefore, it is expected that the time dependence factor will also be applicable in the case of interaction distances. Hence, by placing a droplet onto the surface and holding it in position, using the needle, until the wetting ridge has developed before releasing should change how the droplet interacts with the step. It is expected that as the time on the surface increases and the wetting ridge develops the interaction at a given distance will change in a way equivalent to increasing the oil layer thickness. The first distance tested in Figure 5.6.2 already exhibits attractive behaviour for all oil thicknesses, therefore this distance is not tested for time dependence. The last distance, approximately 4.75 mm, is also not tested, as for a 2 μl droplet the position is too far away from the influence of the steps wetting ridge for any interaction to be noticed.

By selecting the droplet deposition distance of approximately 2.0 mm away from the step there is the opportunity to change all of the interactions depending on the length of time the droplet spends on the surface. From the wetting ridge growth data, a 2 μl droplet will either have minimal growth for the thinnest oil or a maximal 0.6 mm growth at 2 minutes. This is the same at 3 minutes, however the wetting ridge diameter is larger with a maximum growth of 0.9 mm, past 3 minutes the wetting ridge will begin to decrease for the thinnest oil layer but will continue to increase for the thicket oil layer. For the thinnest oil layer (3.09 μm) the wetting ridge diameter starts to decrease at 2 minutes and 3 minutes due to evaporative effects. However, in this case the needle was left in the droplet which slightly changes how the droplet evaporates but it is not only the droplet which has a growing wetting ridge, the depletion region also has a longer period of time to refill.

Two minutes on the surface at an initial distance of 2 mm away from the step is a sufficient period of time for the droplet behaviour on the thickest oil layer to switch from Repulsion to Attraction (Figure 5.6.3). 3 minutes on the surface creates further changes in the behaviour, switching the point of Normal Movement to Repulsion for the thinnest oil layer (Figure 5.6.3).

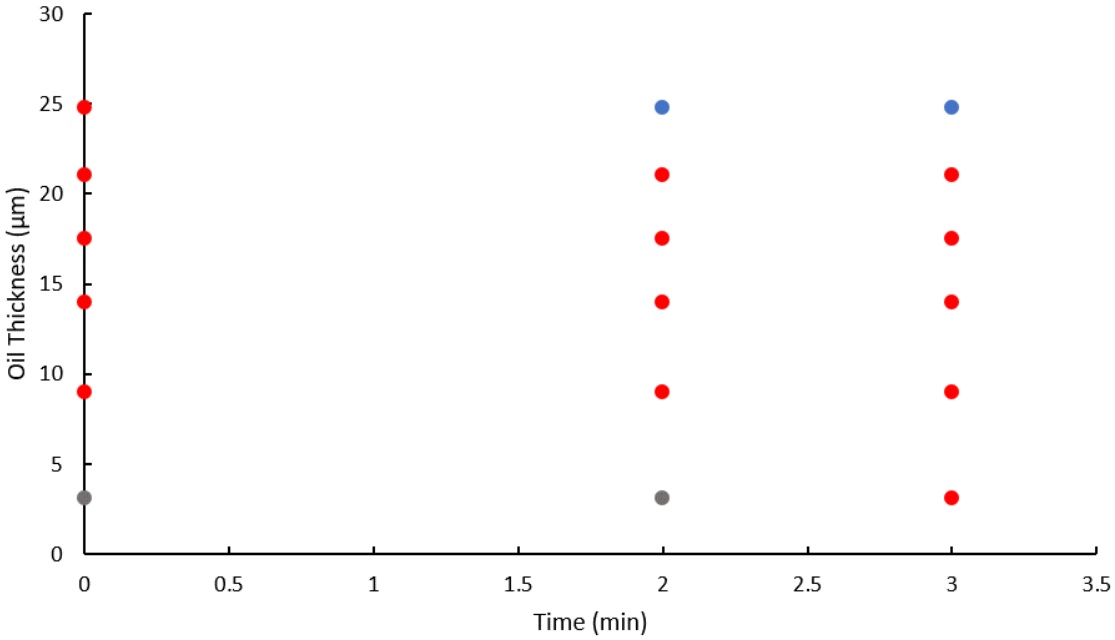

Figure 5.6.3: Attraction (Blue), Repulsion (Red) and Normal Movement (Grey) for a 2 μl droplet 2 and 3 minutes after deposition onto the lower section, approximately 2.0 mm away from a 140 μm step sample showing a shift in behaviour.

Selecting a distance further away from the step to repeat the time experiment, (approximately 2.5 mm away) where there are more data points showing Normal Movement, opens up more possibilities for a change in interaction behaviour. At 2 minutes the wetting ridge has grown sufficiently enough to convert Normal Movement at oil thicknesses of 13.97 μm and 17.48 μm to a Repulsive behaviour. Leaving the droplets for a further minute converts a droplets behaviour on an 8.98 μm thick oil layer from Normal Movement to Repulsion. At three minutes the wetting ridge interactions have not developed enough to produce any attractive behaviour even on the thickest of oil layers (Figure 5.6.4).

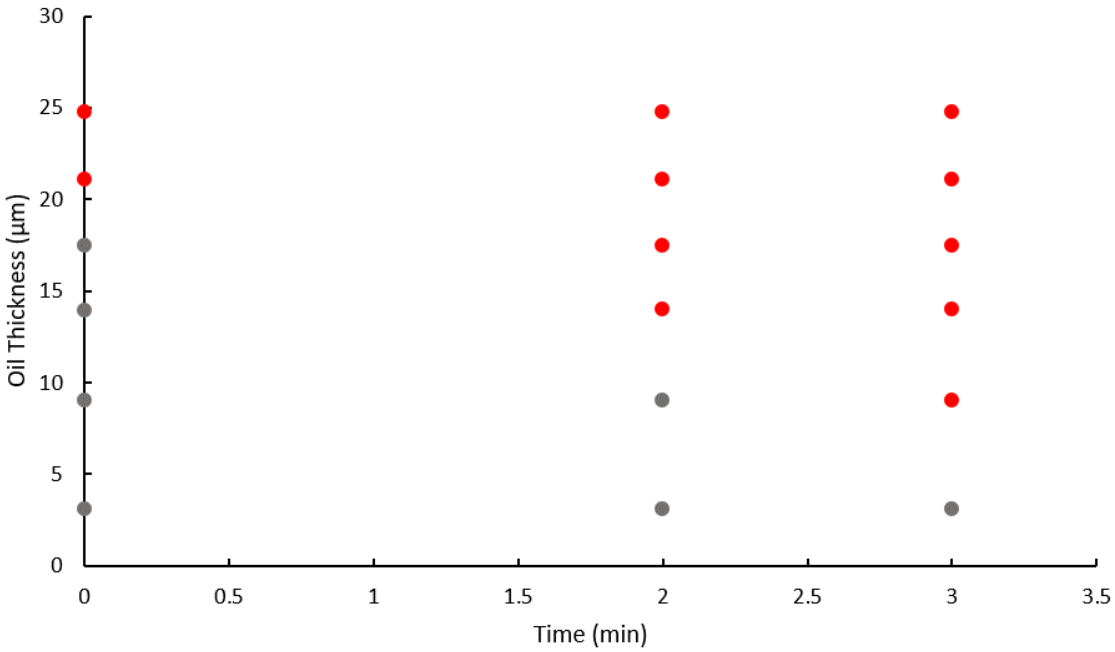

Figure 5.6.4: Attraction (Blue), Repulsion (Red) and Normal Movement (Grey) for a 2 μl droplet 2 and 3 minutes after deposition onto the lower section, approximately 2.5 mm away from a 140 μm step sample showing a shift in behaviour.

Plotting the time data in a similar manner to that seen in Figure 5.6.1 shows that for 2 minutes and 3 minutes (Figure 5.6.5 b and c) the transition between regimes is shifted towards the right from the data in Figure 5.6.5 a. Performing the same experiment on the other distances should switch the behaviour on all bar the distance closest to the step (1.1 mm) which already produces purely Attractive behaviour.

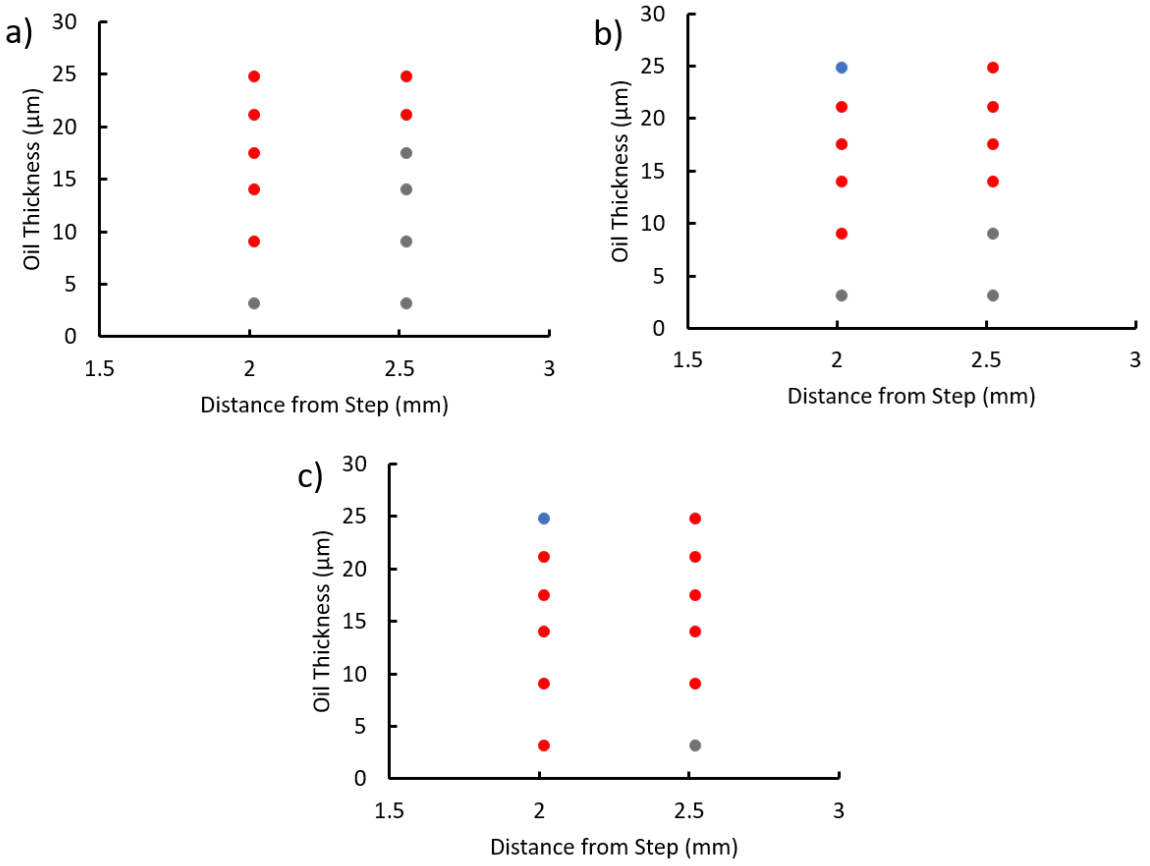

Figure 5.6.5: Interaction types shifted by changing the length of time the droplets spend on the surface before release from the needle. a) The original data at zero minutes, b) the experiments from the distances in a conducted after two minutes on the surface and c) the experiments from the distances in a conducted after three minutes on the surface.

What is yet to be accomplished is a full switch from Zero Net Movement straight to an Attractive interaction. It is expected that if the parameters were changed and a droplet could be left on the surface for a longer period of time without evaporation this shift could be achieved.

5.7 Velocity Towards a Fixed Object

To further prove that the extra, unexpected, repulsive force seen for certain conditions in Figure 5.6.2 is caused by a depletion region and therefore a deformation to the liquid layer, producing a negative curvature, this region needs to be viewed. Again, the method of reflectometry was implemented in the same manner as described within the methods section (Chapter 3) with the light now directed on the area next to the step.

For a depletion region to be present, the thickness measured by the reflectometer should have a lower value in relation to the surrounding lubricant layer. When attempting to measure this value on all six oil thicknesses (particularly the thickest layer as this is where the depletion region should cover the largest area) it is difficult to position the fibre optic light in the correct region. Too close to the step, the thickness measured is greater than the overall layer thickness, too far away and none of the steps influence on the lubricant layer is detected. Placing the fibre so that the light is on the very edge of the positive curvature should capture the full area of the depletion region, however the value measured is still found to be equal to the overall thickness away from the step. The reason for this is due to the resolution limit of the fibre light and the area it covers. For the system used the minimum diameter of the light source is 3 mm with the reflectometer averaging the thickness measured over this area, therefore the area of depletion is too small to have a significant effect on this value. Thus, reflectometry cannot image this region.

If the depletion region cannot be directly measured it has to be indirectly measured. From Chapter 4, the repulsive force has been overcome by tilting the substrate and using the gravitational force to pull on the droplet, overcoming the repulsive force before the droplet interacts with the step (Figure 4.5.2). Therefore, by applying an angle to the substrate, propelling droplets towards the step and repulsive region both the exact positioning of this region and the effect of the depletion region should be seen. The idea behind this experiment was to tilt the surface and place a droplet far away from the step, then to allow the droplet to slide towards the step whilst monitoring the transportation of the droplet and in particular the interactions close to the step (the droplet velocity) (Figure 5.7.1). If the depletion region is present it should have an effect on the droplet's velocity, possibly reducing some of its momentum as overcoming the repulsive force will require energy from the droplet.

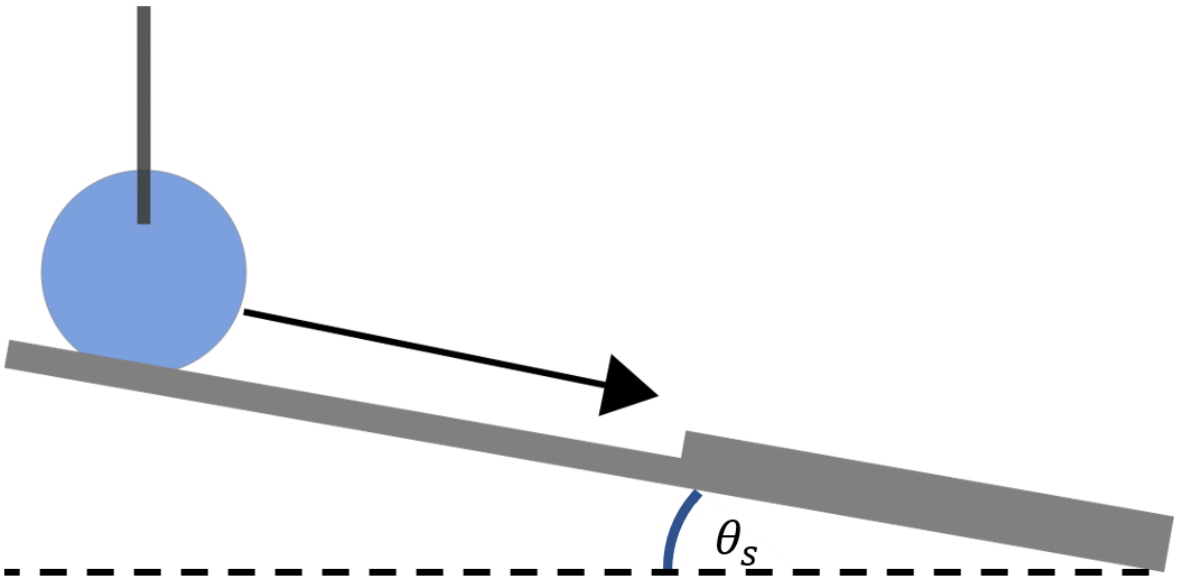

Figure 5.7.1: Schematic of the proposed experimental set up.

The angle the substrate was tilted to was chosen to be 1°. As this angle was above the threshold angle (0.56° ± 0.20°)if the droplet encountered any small, non-visible, pinning points on the path towards the step, the angle should give the droplet enough momentum to overcome these and reduce the possibility of pinning point inhibiting the droplet motion rather than the depletion region. If the angle of the substrate was set too high, the droplet may be travelling too fast when it approaches the step for any depletion effects to be visible.

The experiment was conducted on samples with h_s = 140 μm and h_o = 3.09 μm to 24.79 μm. Starting at the thinnest oil layer (3.09 μm), the depletion region should have the smallest area, given the data from Figure 5.6.1 From the videos of the droplet it can be seen on release from the needle there is an initial fast movement of the droplet towards the step as the wetting ridge develops, similar to the fast regime from Figure 5.2.4. Once the wetting ridge has developed the droplet continues to move towards the step at what visually appears to be a constant velocity. When this droplet nears the step, it slows until the leading wetting ridge has had enough time to develop further and grow towards the steps wetting ridge. As soon as the droplet leading wetting ridge and step wetting ridge 'see' each other the droplet is pulled towards the step creating the same snapping motion as seen for the attractive interactions. By tracking the droplets central position as a function of time, the graph seen in Figure 5.7.2 is produced.

The four regions of droplet interaction with the surface which were identified from the video can also be identified in the graph. Region 1 is the fast development of the ridge, region 2 the constant velocity section, region 3 is the position plateau/slowing down of the droplet area and region 4 the quick snap to the step before assuming a stationary position attached to the step (Figure 5.7.2).

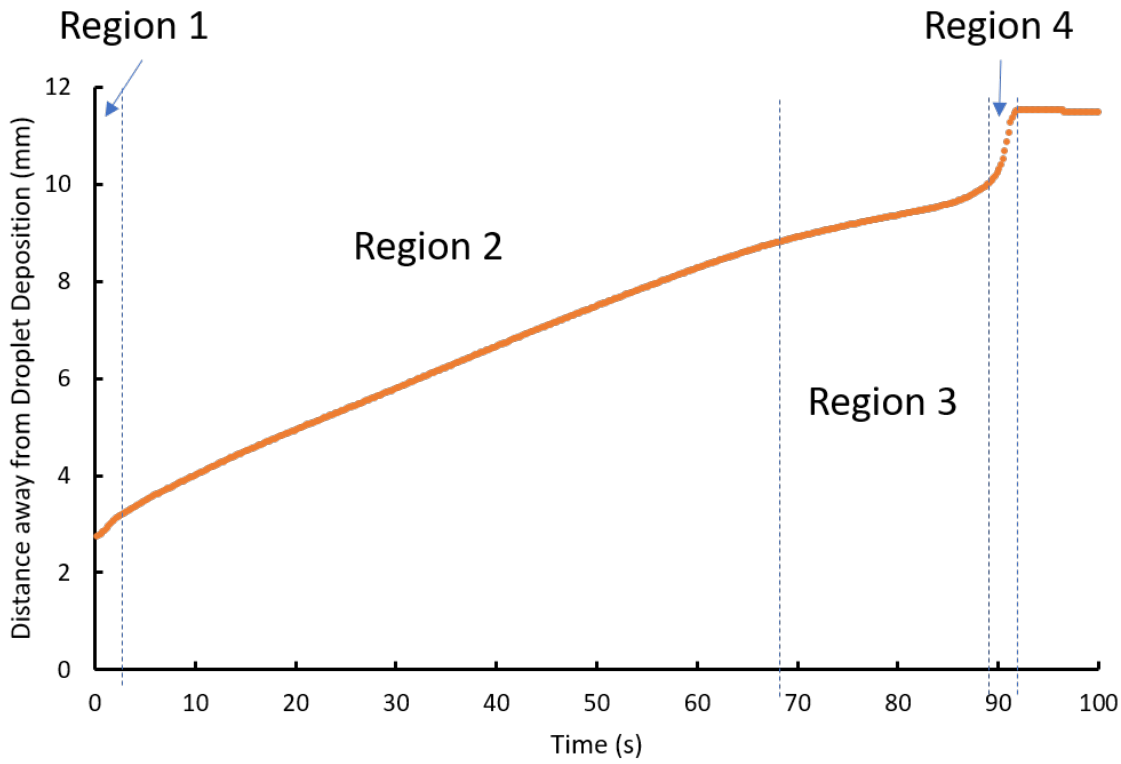

Figure 5.7.2: An example of position versus time data for the thickest oil layer at 24.79 μm.

Region 3 is the area that corresponds to the surface depletion region. Increasing the oil thickness should increase the size of the depletion region but should also move this region further away from the step. As the oil flow through the layer should be easier for thicker layers, the depletion regions should refill faster. Figure 5.7.3 is the position versus time data for each value of h_o, showing that the interaction regions identified in Figure 5.7.2 are universal, independently of the oil thickness value. The data for the position and time has been normalised around the corner of the step, therefore in Figure 5.7.3 position zero is the corner of the step. The data has also been cropped to only display regions 2, 3 and 4.

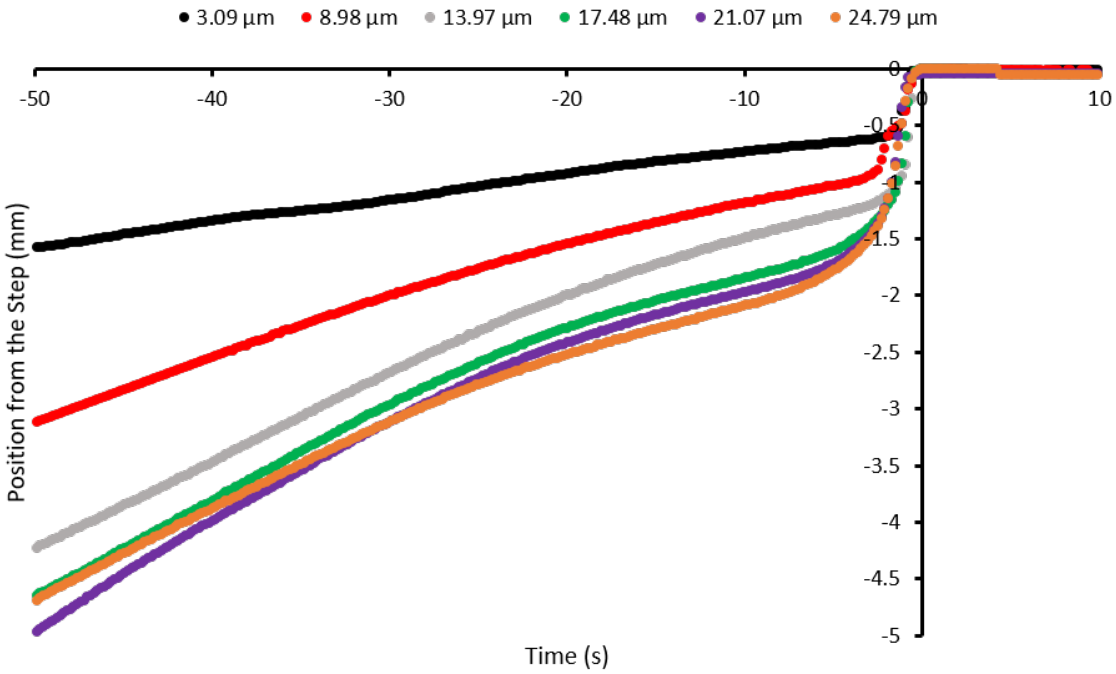

Figure 5.7.3: Combination of position versus time data for each of the six oil thicknesses used on the surfaces with the later times of interaction highlighted.

By cropping the data from Figure 5.7.3 to show only the plateau region and fast attractive snap towards the step and plotting all of this data on the same set of axes provides information on the size of the depletion region and the wetting ridge length (position of the region away from the step) as the oil thickness changes (Figure 5.7.4).

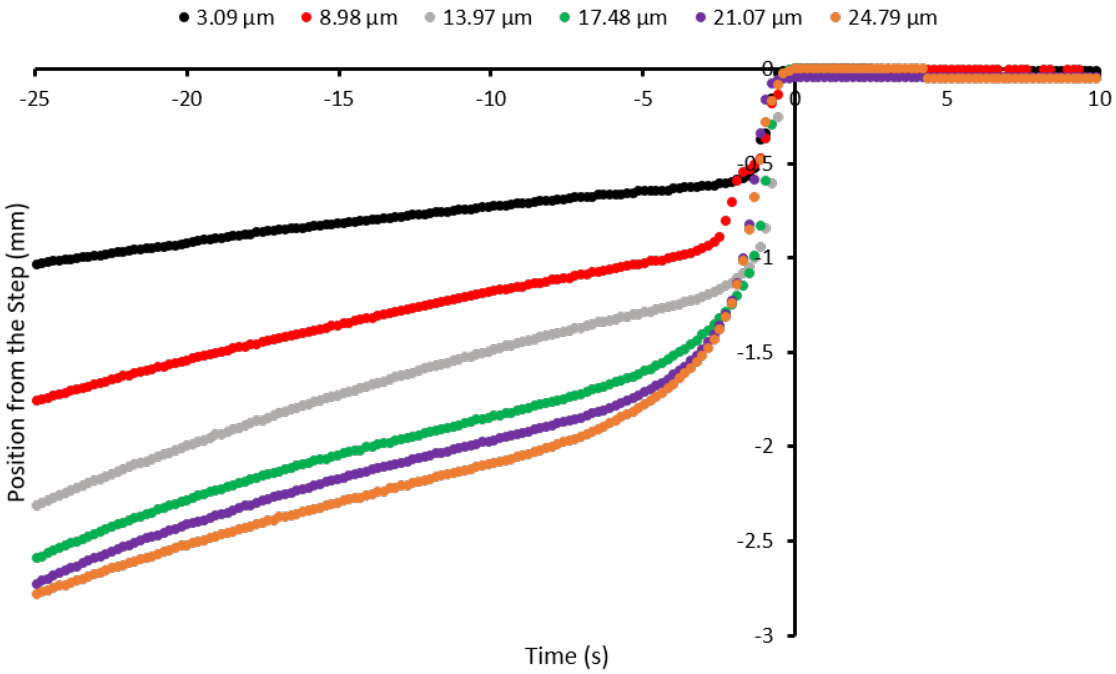

Figure 5.7.4: Cropped data for each oil thickness showing only the depletion and attractive data sections, comparing the difference in depletion region size and distance away from the step (region 3 and 4 from Figure 5.7.3).

The results from cropping the data in Figure 5.7.4 and comparing the results of this to each of the oil layer thicknesses produces the expected behaviour with the largest depletion region and furthest distance away from the step occurring in the data for the largest oil thickness. To determine the position of the area from the step, the distance at time zero (position of the step corner) simply has to be subtracted from the turning point where the slow motion in the depletion region suddenly switches to fast motion (limit of the depletion area). For the length of the area the turning point needs be subtracted from the secondary turning point where the steady increase in position (constant velocity region) switches to the slow creeping motion. Table 5.7.1 displays that average length of the depletion region and distance away from the step for each oil thickness.

Table 5.7.1: Depletion region distances away from with step and length of the depletion region with changes in oil thickness.

Oil Thickness (μm)	Depletion Region Length (mm)	Depletion Region Distance (mm)
3.09	0.05	0.58
8.98	0.13	0.95
13.97	0.15	1.22
17.48	0.40	1.65
21.07	0.56	1.81
24.79	0.66	1.95

The distance versus time plots for the data in Figure 5.7.4 can be converted into velocity plots, providing information on the speed of the droplets as they approach the step to further prove the observation seen from the velocity videos. Figure 5.7.5 displays the velocity versus position away from the step data for the thinnest oil layer.

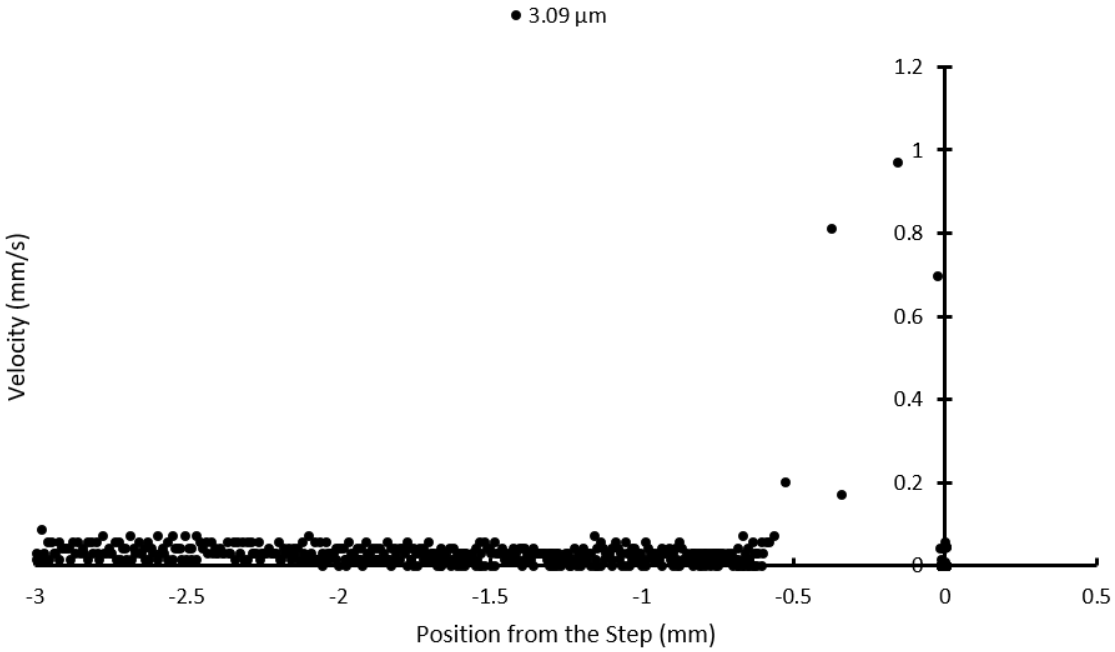

Figure 5.7.5: Velocity as a function of position away from the step data for the thinnest oil layer (3.09 μm).

This velocity shows good agreement with the observations with the slow then fast movement particularly highlighted. Comparing the thinnest oil layer with the thickest oil layer (24.79 μm) in Figure 5.7.6 again shows expected behaviour with the fast move-

ment occurring at a distance of approximately 2.25 mm away from the step indicating that the depletion region starts further away from the step for 24.79 μm oil thickness. The velocity slows again as it approaches the step (0.5 mm away) as the droplet has to adjust it's shape to conform to the step corner. The thinnest oil layer at 0.1 mm/s withdrawal speed exhibits the same behaviour but over a shorter distance, reinforcing the evidence for the depletion region occurring in different areas for different oil thicknesses.

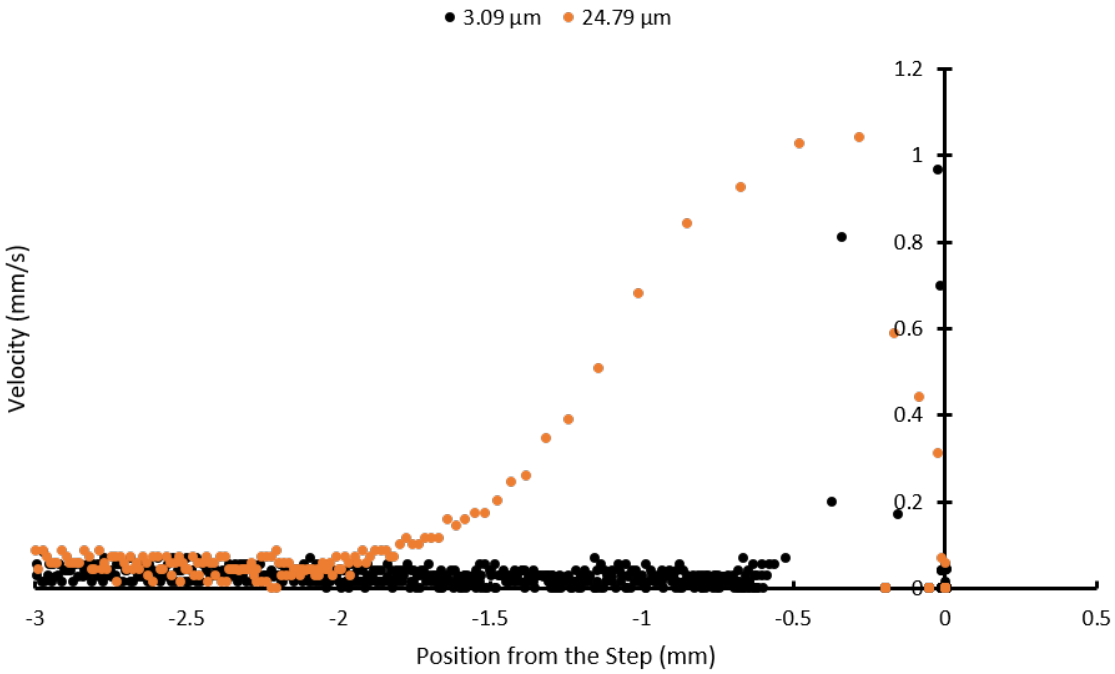

Figure 5.7.6: Comparison velocity data between the thinnest and thickest oil layers.

The start of the depletion regions for all the overlaid data in Figure 5.7.7 agrees with the position data from Figure 5.7.4 with the velocity beginning to increase at the start of the depletion region (end of the wetting ridge created by the step). The depletion region area and position from the step increases with increasing oil layer thickness. What is unexpected is that the reduction in velocity close to the step is seen for the oil thicknesses corresponding to 1.0 mm/s and 1.5 mm/s withdrawal speeds but at a much larger values (1.3 mm/s to 1.6 mm/s) than the thickest oil layers.

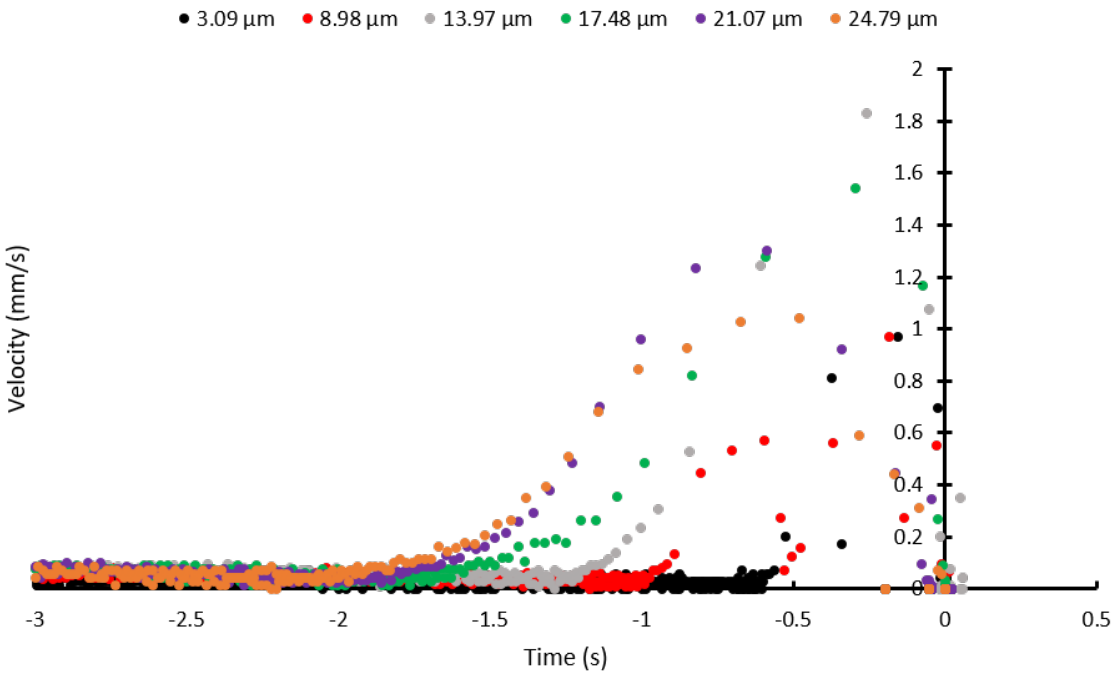

Figure 5.7.7: Overlaid data of the droplet velocity for all oil thicknesses with the start of the fast movement and velocity increase occurring at increasing distances away from the step.

5.8 Repulsion from a Fixed Object

The ability of the stepped structure to produce a repulsive force strong enough to move a 2 μl has been briefly explored in Chapter 4, Section 5. The curvature created by the top of the wetting ridge repels the positive curvature of the droplet, pushing the droplet away from the corner until the wetting ridges have been separated enough to avoid feeling each other's influence. As has been stated in Chapter 4, on certain oil thicknesses the droplet will come to a stop through the recording window, however droplets on thicker oil layers will continue to move due to the wetting ridges for larger oil layers being larger. The recording window was set to 30 seconds to observe the initial repulsive movement and a 2 μl droplet placed near to the edge of the upper section of a 140 μm step and the needle removed. The droplet immediately feels the repulsive force and is subject to motion in a direction perpendicular to the step. Five repeats of the experiment were carried out on each oil thickness and an average taken of the central droplet position to be plotted as a function of time in Figure 5.8.1. The central position was measured by tracking the base diameter, as the wetting ridge

develops evenly all around the droplet half the base diameter gives the central position.

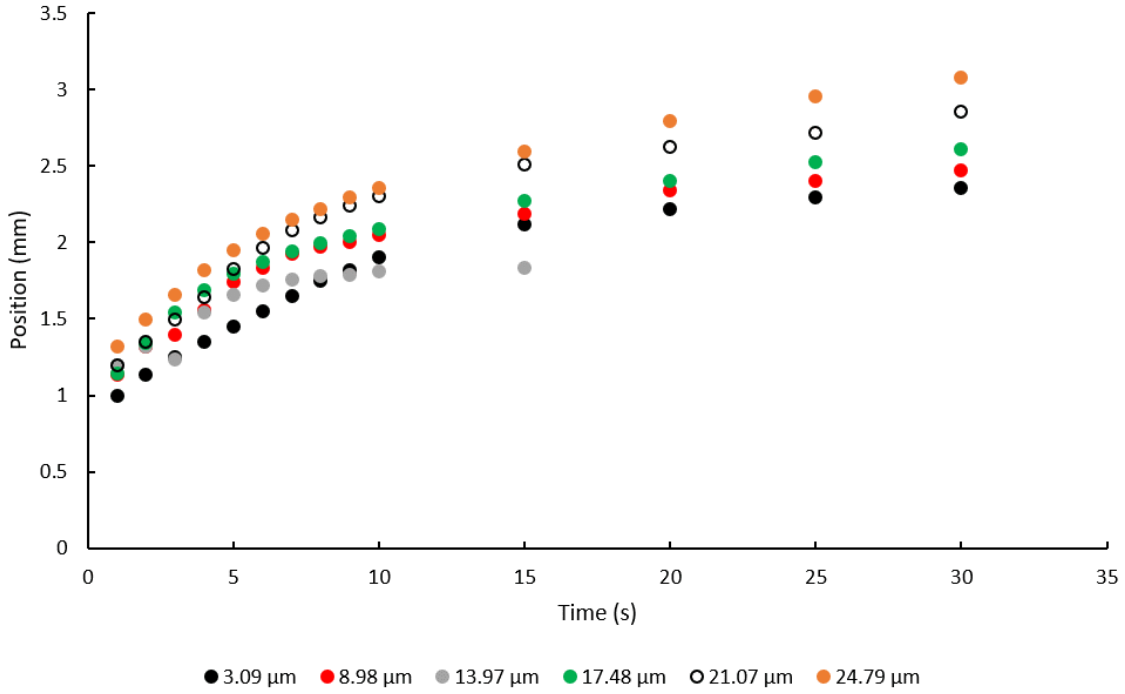

Figure 5.8.1: Average change in central droplet position in relation to the step for each of the six oil thicknesses.

By removing the position data for 13.97 μm from the position versus time plot (Figure 5.8.2) the remaining droplets follow the general trend of distance away from the step increasing with oil thickness.

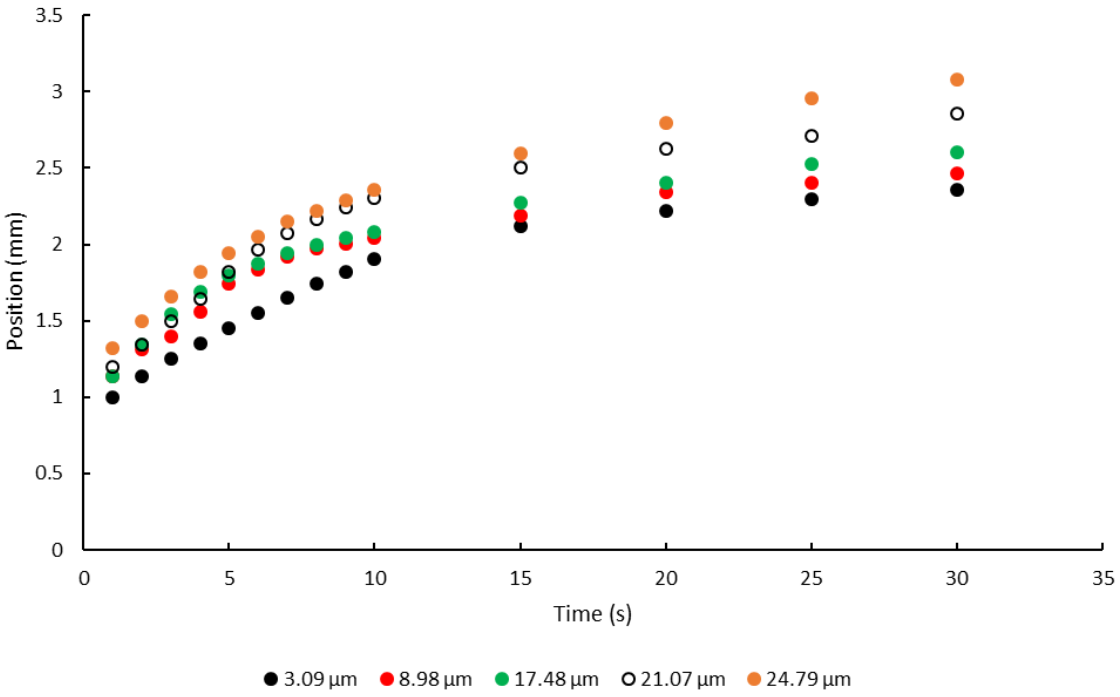

Figure 5.8.2: Average change in central droplet position in relation to the step for each oil thickness (omitting the 13.97 μm oil thickness data).

By separating out the raw droplet position data for 13.97 μm it can be seen that the data does not extend beyond 15 seconds, due to the fact the droplet remains stationary after this point throughout each of the videos and therefore the recording was stopped early. By examining the data further, Figure 5.8.3 shows that none of the 5 experimental repeats follow the data curves of any of the other repeats, meaning that the data taken was unrepeatable leading to the requirement of more experiments.

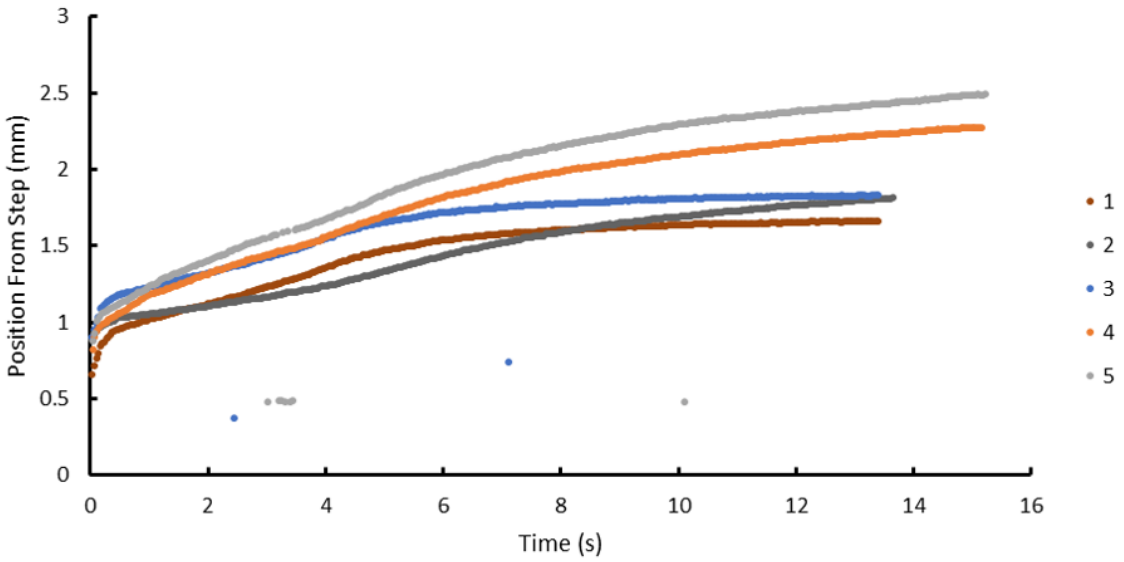

Figure 5.8.3: Raw position data for the 13.97 μm oil thickness.

16 more repeats of the experiment were carried out on 2 different sets of equipment to eliminate the possibility of any equipment irregularities influencing the final experimental result. Before each experimental run the sample bed was levelled to ensure that the droplet was only subject to the influence of the wetting ridge curvatures and not gravity. The sample was also infused with oil prior to each experiment to ensure the droplet was starting from the same experimental conditions.

Despite all of these precautions, none of the 21 experimental repeats follow each other, with the final position spread over 2 mm.

Taking a closer look at all the unaveraged data (Figure 5.8.4), not only do the droplets not follow the same position versus time data curves but they do not all exhibit the same behaviour. Some of the droplets appear to have the initial acceleration expected on such surfaces but then slow down and return towards the step, following the same path (data sets 20 and 21). Other droplets do not appear to move at all and appear to be stuck on the step remaining stationary for the entire recording window with only the wetting ridge growing (data sets 6 and 14). Further droplets have the initial acceleration but then appear to be stuck on an indiscernible pinning point. The wetting ridges grow further before the droplet depins itself and then accelerates again away from the step (data sets 8 and 9). There are a few droplets that follow the expected data path with the initial fast acceleration and then the slow movement

(data sets 15 and 17), however none of the droplets have the same velocity and therefore position, meaning that the experiments conducted on the 13.97 μm oil thickness are unrepeatable.

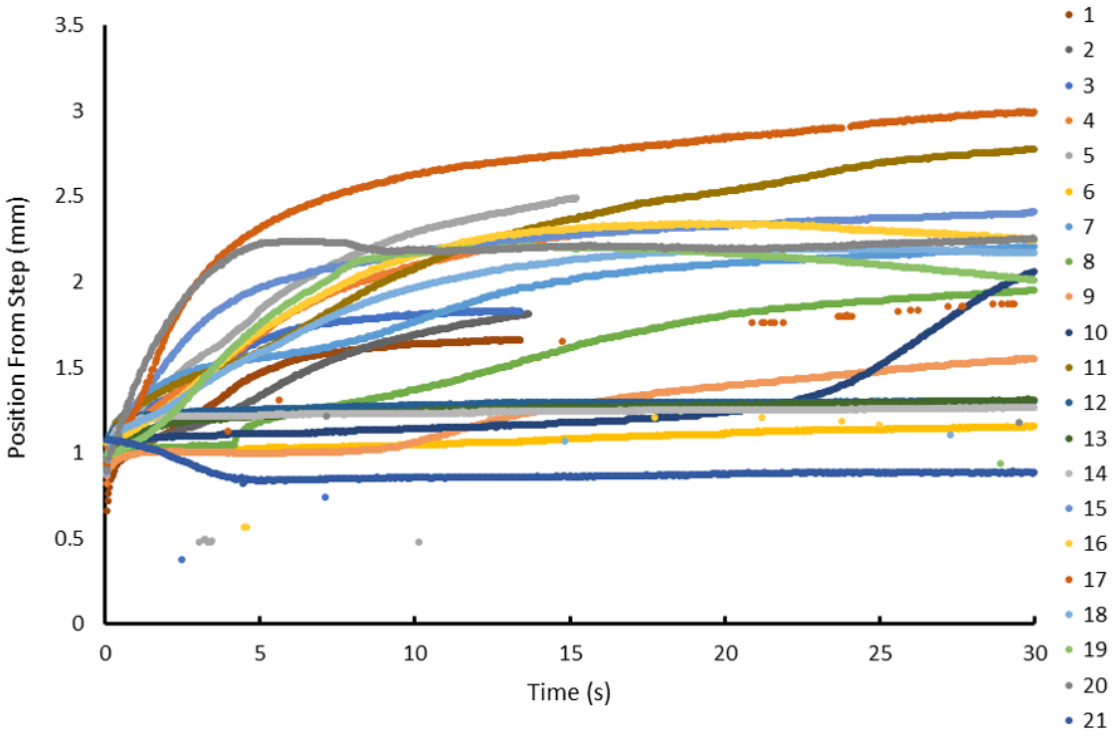

Figure 5.8.4: Repulsion data for all 21 repeats of the 13.97 μm thick oil layer.

To investigate this further the average was taken of the entire data set and plotted with the other five oil thicknesses to give a comparison between the new data and the first data sets. By repeating the data the error has increased slightly as the spread of the data has also increased but the general trend set by the previous experiments is still followed.

Figure 5.8.5 shows the averaged movement of droplets away from the step on each of the six oil thicknesses. Over the first 7 seconds of movement each data set has an overlapping data point with at least one other data set, making the separate data sets difficult to distiguish from one another. After 7 seconds the data set corresponding to 13.97 μm tends away from the other five oil thicknesses. Droplets on oil thicknesses of 8.98 μm and 17.48 μm take the longest to separate, only after 20 seconds do the positions become separately distinguishable. The overall trend is for the droplets to move further on the larger oil thicknesses with the 2 μl droplet on 24.79 μm settling at

3.08 mm at 30 seconds and the droplet on the thinnest layer at 2.36 mm. However, on the oil thickness of 13.97 μm (1 mm/s dip speed) the general trend does not appear to be followed. At 3 seconds the position data stops growing at the expected rate (data points between 8.98 μm and 17.48 μm) and begins to maintain its position around 1.8 mm from 15 seconds onwards.

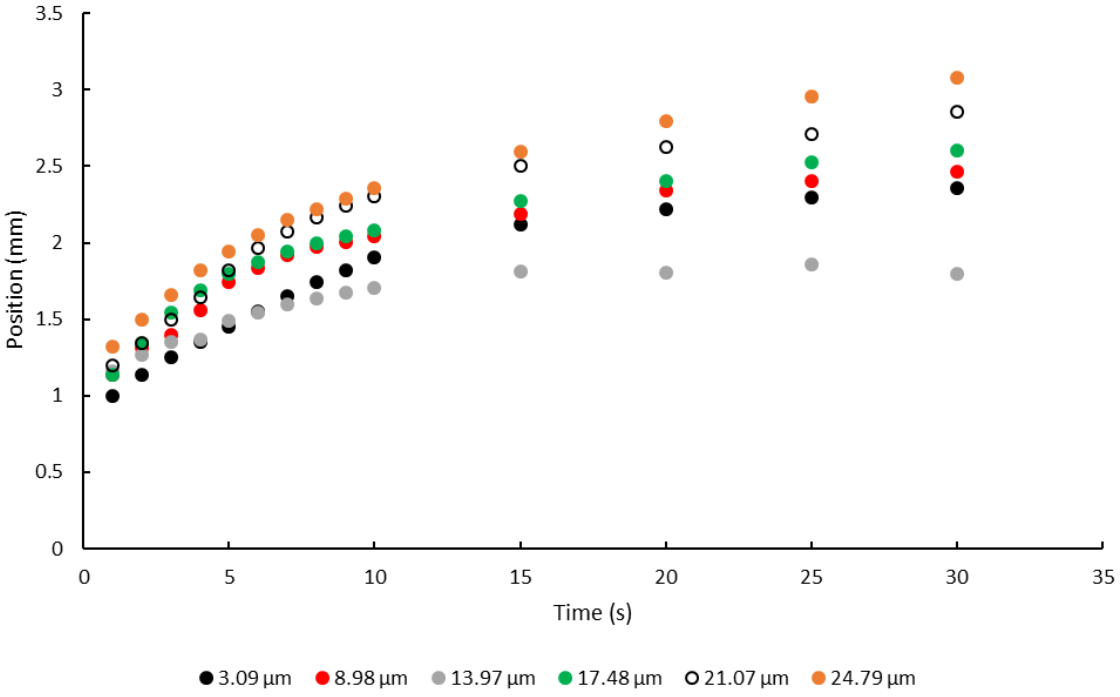

Figure 5.8.5: Average change in central droplet position in relation to the step including the averaged data for 21 repeats of dip speed, 1 mm/s.

The central position of the droplet was taken from the data in Figure 5.8.5 at given time intervals of 1, 5, 10, 20, 30 seconds, to give a better understanding of the evolution of the droplet position as a function of oil thickness. The gradient of the trend lines increases as time progresses indicating that the droplets on the thicker oil layers not only move a greater distance but are moving at a greater velocity than those on the thinner layers. At 30 seconds none of the droplets positions have begun to plateau, indicating that all of the droplets are still in motion away from the step despite the fact the two opposing menisci have moved away from each other's influence, meaning the momentum is still able to propel the droplets.

Separating the data in this manner (Figure 5.8.6) further emphasises the departure of 13.97 μm from the general trend with only the data for 1 second following the other

linear trend lines. When including the error bars, the data points for 10, 20 and 30 seconds all fit onto the trend line for 5 seconds with the data points for 20 and 30 seconds appearing to be overlaid.

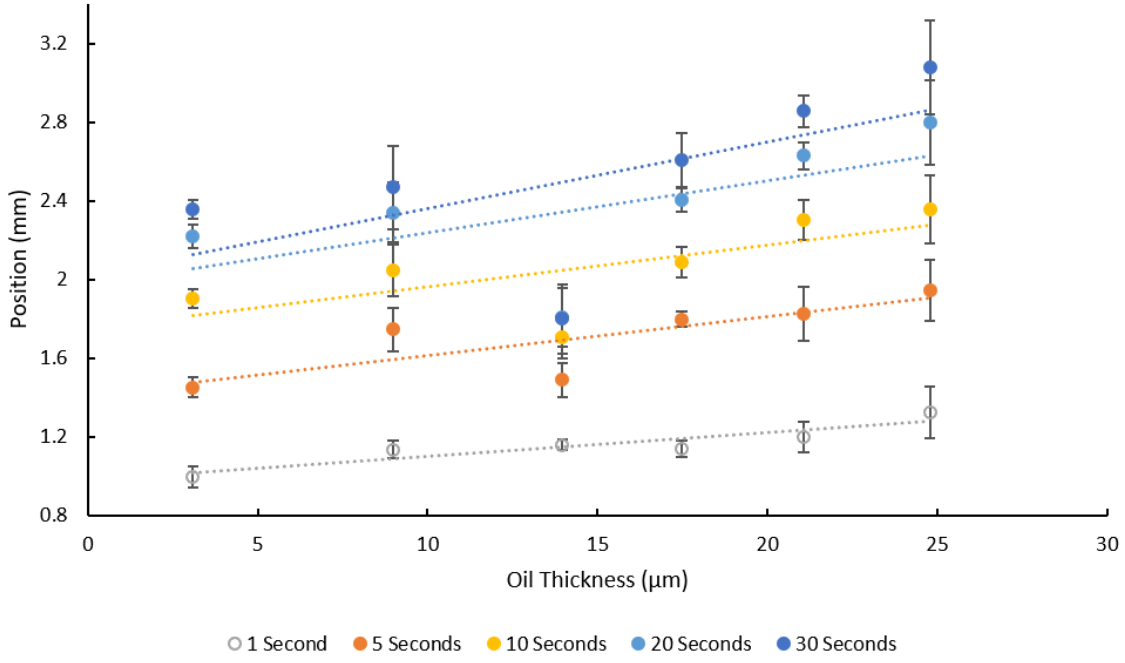

Figure 5.8.6: Time sections through the data with the averaged data from 21 repeats of 1 mm/s dip speed.

To understand whether the anomaly in the data is only linked to the 13.79 μm oil thickness further experiments were carried out on oil thicknesses around this value. The oil bath withdrawal speeds that were used were 0.8 mm/s, 0.9 mm/s, 1.1 mm/s and 1.2 mm/s which correspond to oil thicknesses of 11.48 μm, 12.43 μm, 14.20 μm and 15.05 μm respectively.

The position versus time data for the 11.48 μm oil thickness, Figure 5.8.7 a, exhibits the expected behaviour with regards to the initial acceleration and then constant movement for each of the 9 data sets but with a large spread of data and therefore error. Increasing the oil thickness to 12.43 μm, Figure 5.8.7 b, the droplet begins to act similarly to the 13.97 μm data with 4 of the 10 data sets following the initial movement away from the step and then returning to the original position. The other 6 data sets follow the expected trend with the overall final position finishing between 1 mm and 3 mm. Increasing the withdrawal speed again to give an oil thickness of

14.20 μm, Figure 5.8.7 c, once again gives droplet behaviours similar to that of both the 12.43 μm and 13.97 μm oil layer. However, the final positions of the droplets have decreased by 0.5 mm from what is seen in Figure 5.8.6, varying between 0.5 mm and 2.5 mm. The final withdrawal speed tested produces an oil thickness of 15.05 μm, Figure 5.8.7 d, which in turn produces droplet motion very similar to that seen for the 11.48 μm however, approximately half the data sets have the stationary but then normal acceleration characteristics.

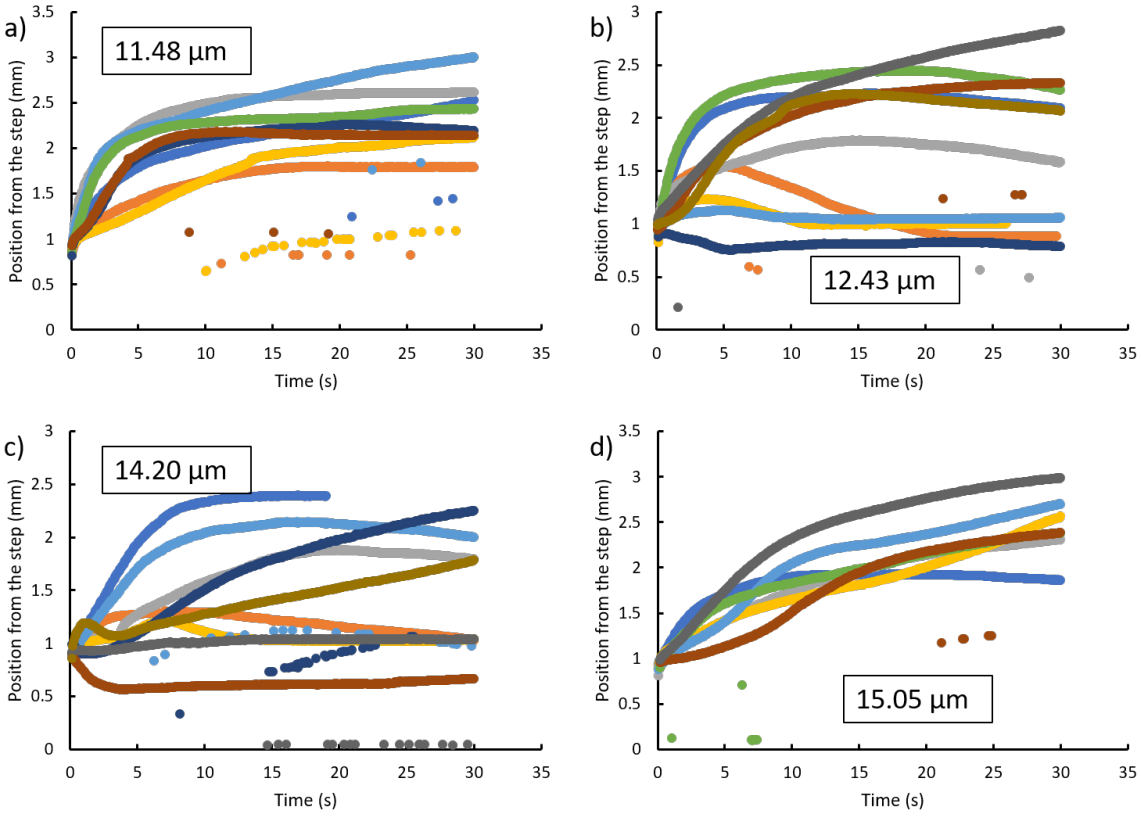

Figure 5.8.7: Raw data for the four new dip speeds a) 0.8 mm/s, b) 0.9 mm/s, c) 1.1 mm/s and d) 1.2 mm/s.

Plotting this data as before with time sections extracted for each oil thickness further highlights the dip in the data at and around the 13.97 μm oil thickness (Figure 5.8.8 a). The oil thickness of 13.97 μm does not in fact show the greatest dip away from the linear trend lines, increasing the withdrawal speed by 0.1 mm/s increases the oil thickness by 0.23 μm to 14.20 μm with all of the data points for this thickness appearing below their corresponding trend lines (Figure 5.8.8 b). Both the 15.05 μm and 11.48 μm oil layers appear to fit the majority of the surrounding data's linear trend

lines with the thickest oil layer (15.05 μm) fitting the trend lines most closely (Figure 5.8.8 b). The position data for the 12.43 μm oil layer is plotted just above the data for 13.97 μm with both the 1 second and 5 second data points fitting the trend lines (Figure 5.8.8 b).

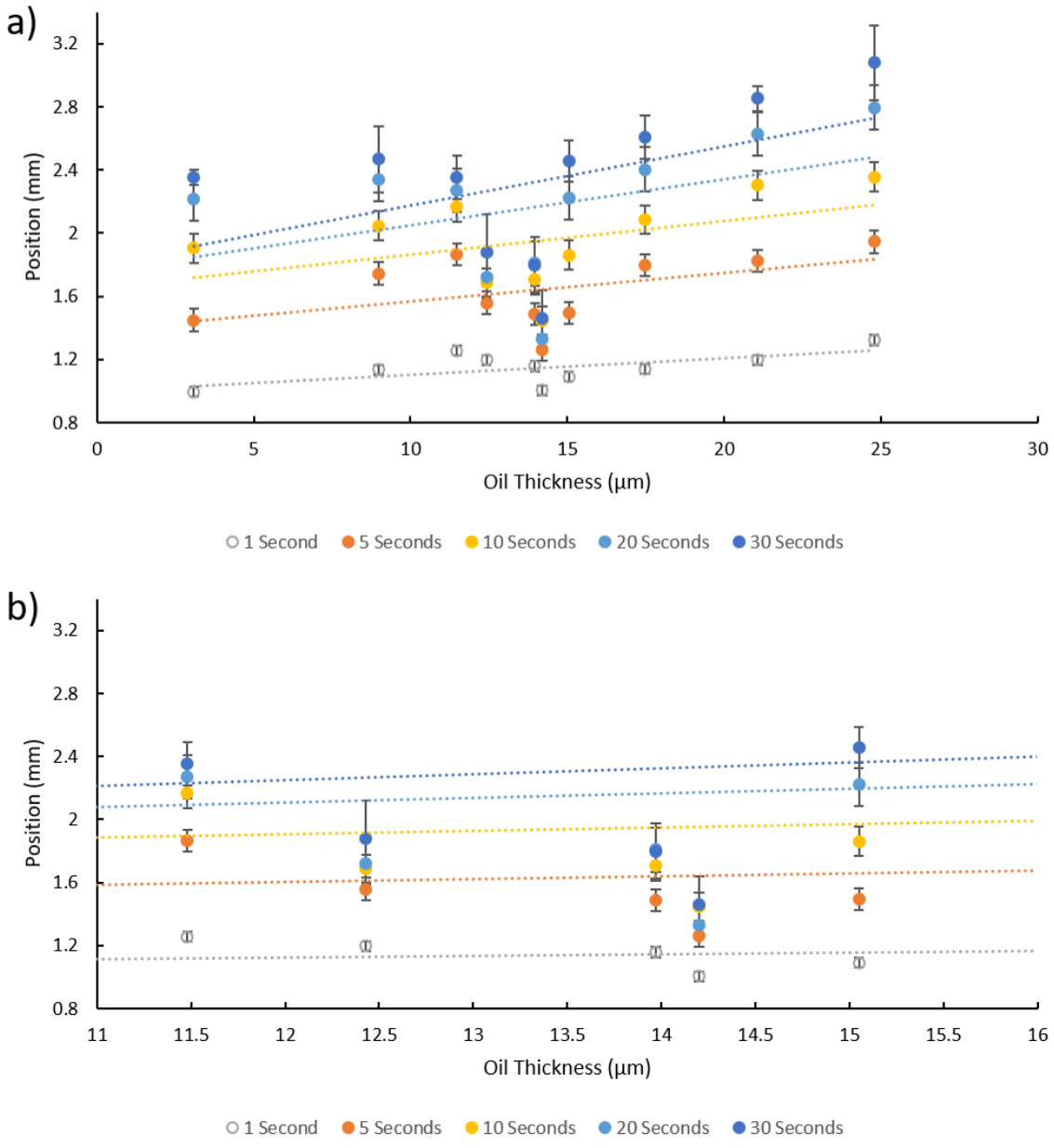

Figure 5.8.8: Time sections through the data showing the central position as a) a function of all combined oil thicknesses with a central data dip and b) dip speeds from 0.8 mm/s to 1.2 mm/s, focusing in on the dip in data.

By replotting the data in Figure 5.8.6 but replacing the oil thickness data at 13.97 μm for the 11.48 μm and 15.05 μm thicknesses. These data sets appear to follow the linear trend lines fitted to each of the data time slices to a greater degree of accuracy

meaning that the dip in data is limited to a maximum range of oil thicknesses spanning 3.57 μm between 15.05 μm and 11.48 μm.

The trend lines from Figure 5.8.8 to Figure 5.8.9 have been shifted due to the elimination of the ill-fitting data meaning that now the data for the 15.05 μm oil layer fits to these lines within errors however for an oil layer of 11.48 μm it is only towards late times that the fits apply to the data.

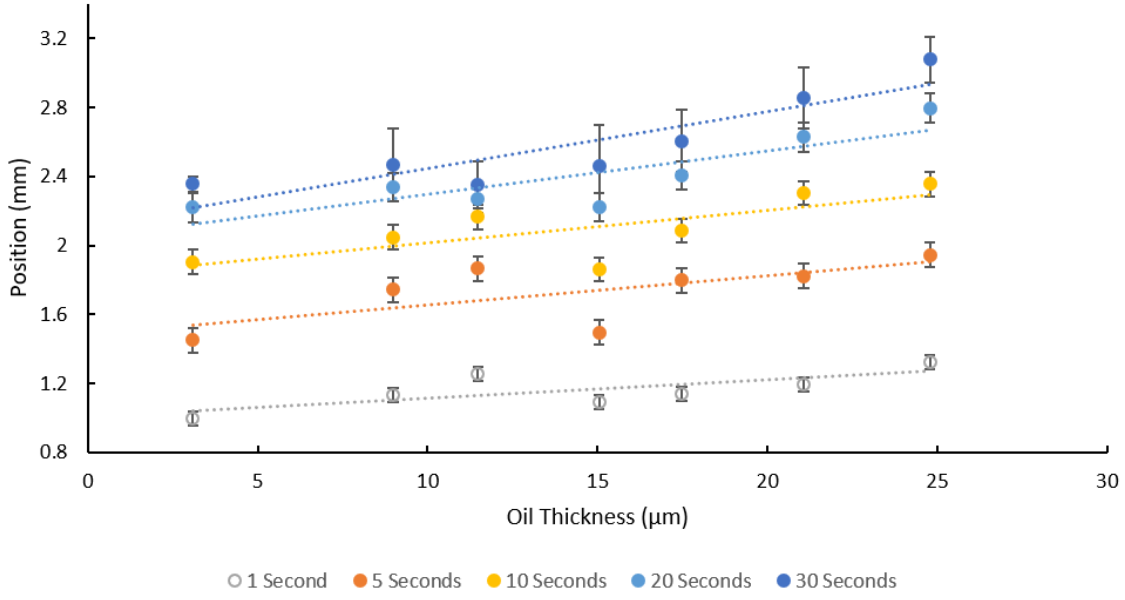

Figure 5.8.9: Time sections through that data showing the central position as a function of oil thicknesses, including 0.8 mm/s and 1.2 mm/s and omitting the data dip.

The reason for this dip in data is currently unknown as is whether this dip is universal across all parameters, however it is reasonable to assume that at this point there maybe an imbalance in forces that the droplet struggles to overcome. As has been stated in Section 4.5, the repulsive force is driven purely by the two curvatures (negative and positive on the surface) producing a capillary force strong enough to push the droplet away from the step. But the forces preventing the movement are yet to be identified. As the surface is imbibed by a viscous oil there will be viscous forces affecting the droplet and attempting to prevent its movement. Intuitively, the more viscous the oil, the more difficult it will be for the droplet to either pull this lubricating liquid into it's wetting ridge or to push the oil out of the way. The droplet will also be subject to some frictional force which will ultimately be determined by the area the

droplet covers on the surface (the droplet footprint), however as the droplet has little to no direct contact with the solid it is assumed that this effect will be minimal and it is in fact the viscous effects that dominate in this case. The Ohnesorge number (Equation 5.8.1) is a good measure of the balance between the viscous dominated effects and the inertial effects (determined by the droplet footprint),

$$Oh = \frac{\mu}{\sqrt{\rho\gamma L}}. \tag{5.8.1}$$

As μ equals the dynamic viscosity, ρ the density and L the droplet diameter, from this equation it can be seen that by simply varying the viscosity or the droplet volume the preventative motion forces could be altered. By inputting the values used for this experiment into the Ohnesorge number equation it is found that the viscous effects are indeed dominating the forces preventing movement. Therefore, to determine whether the data dip can be shifted by changing one parameter the viscosity of the oil would not only be the easiest thing to change but it should also produce the largest effect on the droplet on the surface.

Whilst changing the lubricating oil viscosity would appear to be the most sensible option for controlling the droplet motion and contributing to the dip in data seen in Figure 5.8.9 it is a subject for further study and therefore cannot be said to undoubtedly be the controlling parameter. As has been explored in Chapter 4, the droplet and step system, coupled with the wetting ridge is a complex 3 dimensional system that is most likely controlled by many physical parameters, including the step height.

5.9 Conclusion

In this chapter droplet propulsion has been shown to be generated by simply placing a droplet on to the stop of a stepped structure and allowing the difference in curvature to move the droplet with the distance the droplet travels determined by the oil layer thickness. The attractive (retention) force from Chapter 4 has been shown to act over a large distance away from the step at thick oil layers. However, this interaction switches to a repulsive force with decreasing oil thickness or increasing distance away

from the step. This interaction has indicated that there is a depletion region present on the surface. The switching of interactions has also been shown to be time dependent, further supporting the idea that the surface acts in a way akin to a soft solid. By sliding the droplets towards the step there is shown to first be a decrease in droplet velocity followed by a sharp increase very close to the step, with the decrease being the depletion region and increase the joining of the two wetting ridges. Condensing and nucleating droplets on the surface may also provide physical information on the presence of a depletion region as the droplets will preferentially nucleate in areas of depleted oil[138].

Chapter 6

Snap Evaporation - Droplet Control

This chapter will discuss an innovative method for precise droplet positioning and the possibility for transport, which has recently been published as a journal article[96]. By applying the nanoparticle SLIPS coating to a topographical macrostructure, the shape and local position of a droplet can be accurately predicted and modelled. Changing this macrostructure, changes the predicted position of the droplet but not the underlying mechanism for droplet movement or the presence of negligible contact angle hysteresis[139]. The possible applications for the combination between the macrostructure and nanoparticle SLIPS coating will be briefly explored in Section 6.6.

6.1 Introduction

Controlling droplets, whilst evaporating has many applications as evaporation is a natural process which requires no external energy input into the system. To passively control the position of these droplets via evaporative transport would assist with microfluidic applications where it is important to reduce the amount of contamination sources, leading to more accurate measurements and a reduction of the sample size needed. Conversely, the condensation of droplets is also a natural phenomenon (but currently slightly less common in industrial applications) seen particularly with beetles in the desert gathering the morning dew on their backs[131]. By studying the evaporation of a droplet, the interaction and transport of condensing droplets can be inversely extrapolated[78].

6.2 Evaporation

Evaporation is a process that occurs naturally for all volatile liquids. It can be suppressed by leaving the liquid in an atmosphere saturated by the liquids vapour but ultimately the liquid will evaporate. This process is seen in nature, which is more specifically relevant in the case of the Nepenthes pitcher plant which relies on living in the rain forest where there is a humid environment and rainfall each day to maintain and replenish its water layer[4].

In a non-saturated environment (low relative humidity) a perfectly spherical droplet (a droplet on a spider's web or on a fibre) will evaporate evenly in each direction[140, 141]. As the droplet evaporates it will begin to saturate the environment close to the interface, slightly reducing the evaporation rate. For a droplet sitting on a surface, the contact angle can be either hydrophilic (less than 90°) or hydrophobic (90°). At an angle of 90° or below there will be a non-uniform evaporation gradient along the liquid-vapour interface. At the contact line (near the surface) the rate of evaporation will be greater than at the apex of the droplet[142]. This will in turn create a temperature gradient in the droplet, driving a Marangoni flow within the droplet. For a particle laden fluid, the Marangoni flow will transport the particles towards the pinned contact line, leading to the coffee ring effect and the origin of water marks[74, 75]. On a surface with a contact angle above 90° the evaporation rate near the contact line is suppressed. The vapour between the droplet and surface (anywhere on the droplet above 90°) will quickly become saturated with water vapour as there is little area between the solid surface and droplet for the saturated vapour to diffuse into the surrounding atmosphere. For a puddle with a low contact angle or a thin film the liquid/vapour interface is larger than for a spherical droplet, increasing the evaporation rate for the same volume of liquid.

When a droplet evaporates on a surface it can follow two perfect evaporative configurations, constant contact radius and constant contact angle[140]. For constant contact radius (CCR) evaporation (Figure 6.2.1) the contact line of the droplet is pinned to the surface. As the volume decreases, due to evaporation, the droplet footprint and therefore radius does not change but the contact angle systematically decreases[143].

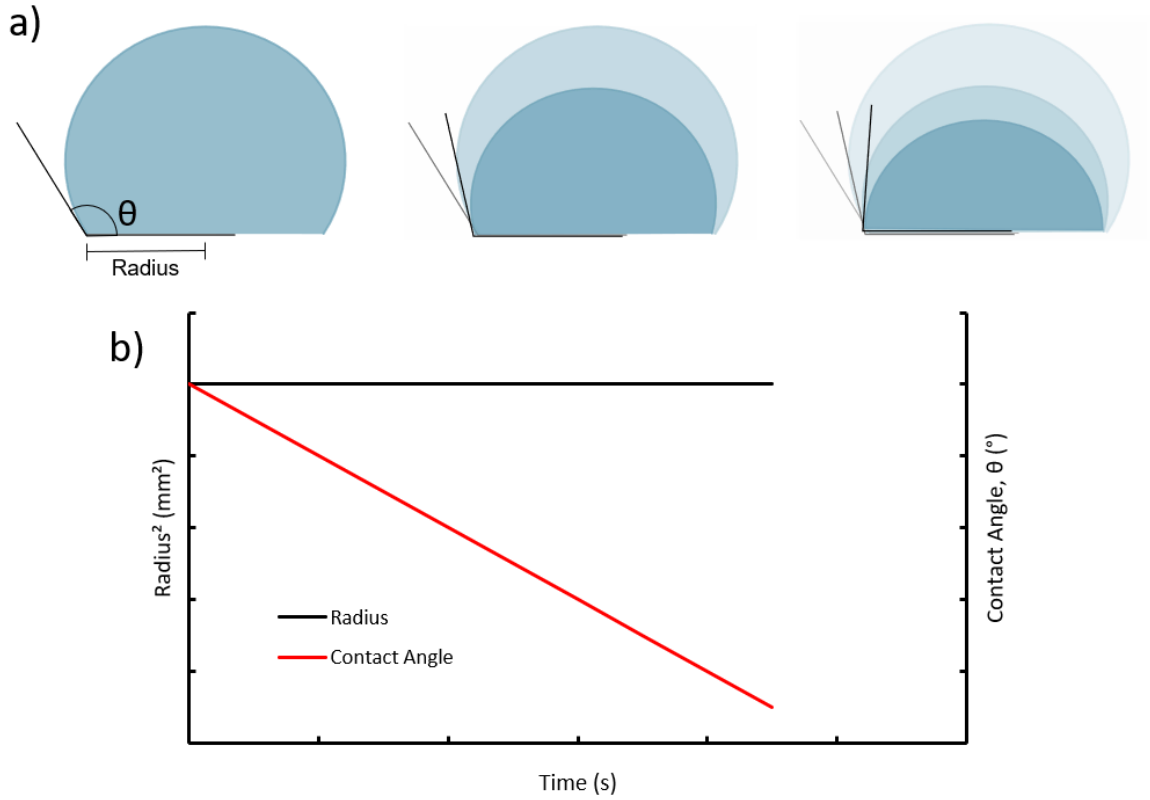

Figure 6.2.1: Constant contact radius evaporation. a) Sequence of schematic images showing CCR. b) Evolution of droplet base radius and contact angle of a droplet undergoing CCR evaporation.

The second is constant contact angle (CCA), where the droplet's contact lines retract with the decrease in droplet volume (Figure 6.2.2). This method is very difficult to achieve as most surfaces, even those that are superhydrophobic, exhibit some form of pinning due to heterogenicities which could be physical or chemical[143].

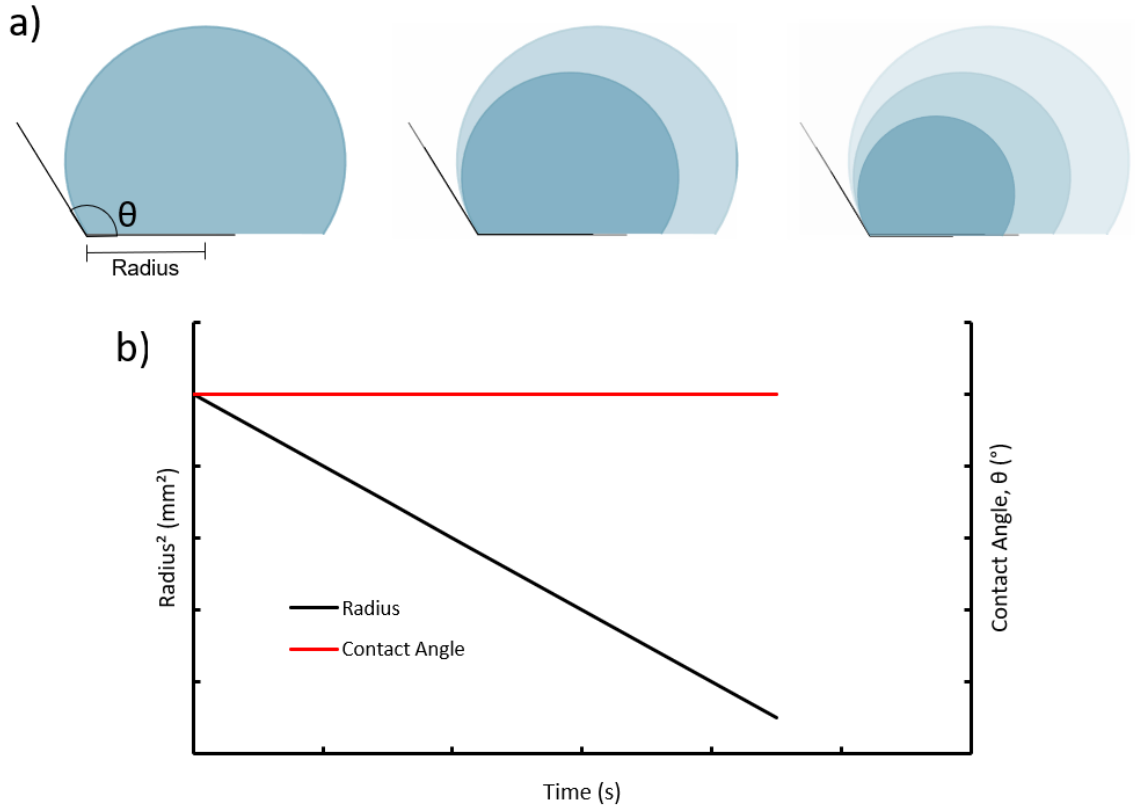

Figure 6.2.2: Constant contact angle evaporation. a) Sequence of schematic images showing CCA. b) Evolution of droplet base radius and contact angle of a droplet undergoing CCA evaporation.

The most commonly seen evaporative path is called Stick – Slip evaporation which is a combination of CCR and CCA. Before the droplet begins to evaporate it forms a contact angle with the surface. Once the droplet has started to evaporate the contact lines will be pinned, reducing the contact angle. When the droplet has reached a threshold point the contact lines will depin and the droplet's base radius will decrease and the contact angle will return to its former value (Figure 6.2.3)[144].

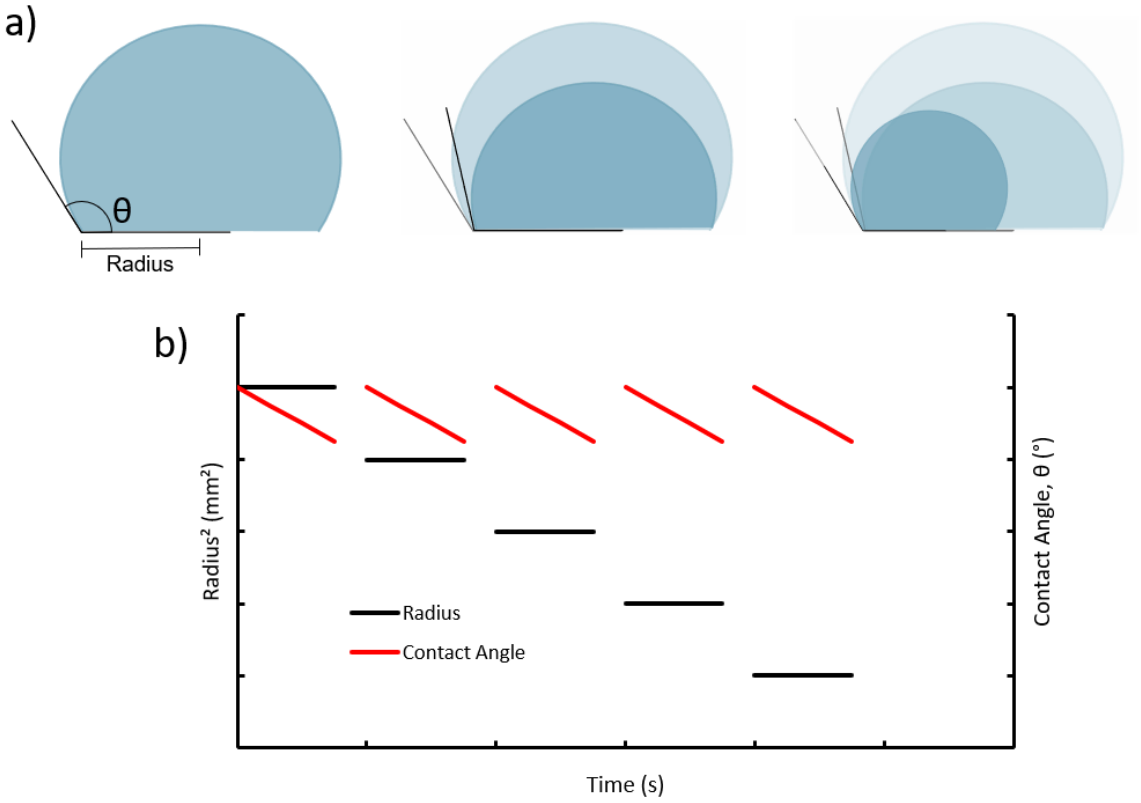

Figure 6.2.3: Stick - Slip evaporation. a) Sequence of schematic images showing Stick - Slip. b) Evolution of droplet base radius and contact angle of a droplet undergoing Stick - Slip evaporation.

Of the two perfect evaporation modes, CCR is the easiest to achieve as most surfaces suffer from inherent contact line pinning, however there have been previous experimental studies completed on CCA. Surfaces that are superhydrophobic (such as PTFE) have been said to produce CCA and are the closest, fully solid substrate to achieve this almost hysteresis free evaporation[145]. However, the hysteresis is still present causing slight variations to the measured contact angles. The choice of volatile liquid used can also produce constant contact angle evaporation. For binary liquid mixtures, such as water ethanol, constant contact angle evaporation has been found to dominate for the majority of the evaporation time, however at early in the process the contact line is pinned with constant contact radius dominating[146].

SLIP Surfaces have very little hysteresis which would indicate that the mode of evaporation for a droplet on this type of surface should be in constant contact angle evaporation mode[67]. As has been previously stated, the presence of the wetting ridge

hides the true droplet solid contact point, therefore it is only an apparent contact angle that is measured. Further to this, the droplet radius (without wetting ridge) can also not be seen, therefore an apparent droplet radius is also being measured. Performing the measurements of apparent contact angle and radius on a SLIP Surface shows an almost perfect linear decrease in the square of the droplet base radius accompanied by smooth apparent contact angle decrease (which is expected for a growing wetting ridge, Chapter 5 and reducing contact angles, Table 3.5.1) as seen in Figure 6.2.4 a (Wells et al.)[96]. Instead of taking the measurements of the apparent contact angles and radius from the top of the wetting ridge and alternatively taking these values from an extrapolation to the surface still produces a linear decrease in droplet radius and constant contact angle (Figure 6.2.4 b Guan et al.[67]). This data shows that SLIP Surfaces have a perfect constant apparent contact angle evaporation mode for the majority of the evaporation time, independent of the measurement technique used.

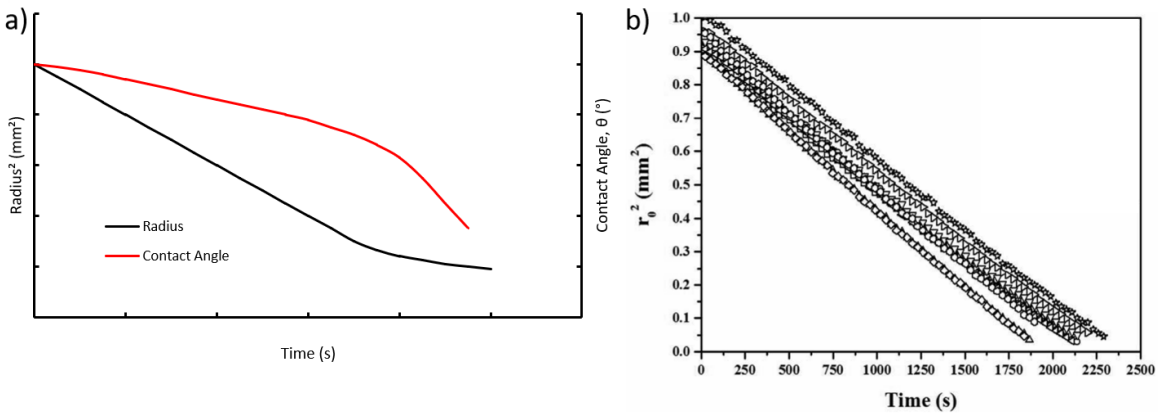

Figure 6.2.4: Constant apparent contact angle evaporation on SLIPS surfaces for the majority of the evaporation time, independent of the measurement manner. a) Linear square radius reduction for contact angles measured from the top of the wetting ridge(Wells et al. 2018) and b) linear square radius reduction for contact angles measured from an extrapolation of the droplet through the wetting ridge to the surface (Guan et al. 2015.)

More recently a liquid like surface (Slippery Omniphobic Covalently Attached Liquid - SOCAL)[147] has been shown to exhibit constant contact angle evaporation without the need for correction due to the wetting ridge, with full droplet contact with the solid surface. These types of surfaces may provide further insights into the possibilities of droplet transport on low hysteresis surfaces, however the slow moving contact line

may inhibit the practical ability to move the droplets[148].

6.3 Flat Surface

In order to ensure that the SLIPS properties of the nanoparticle SLIPS coating would not be affected by the change in underlying substrate (from glass to 3D printed substrate) an initial sliding angle test has to be conducted. A flat sample was printed using an Objet 3D printer (28 μm resolution) from a resin (VeroWhite Plus RGD835), coated with the nanoparticle SLIPS and infused with a 3.09 μm thick oil layer. The Krüss DSA30 was used as previously described to deposit droplets of DI water with volume 2 μl. The previously levelled tilt stage was then tilted in increments of 0.20° and the motion of the droplet recorded (Figure 6.3.1). When continuous motion was observed the angle was taken as the sliding angle. After 10 repeats of the experiment the siding angle on a flat 3D printed sample was measured to be 0.46° ± 0.25° where the error is the standard deviation of the repeats.

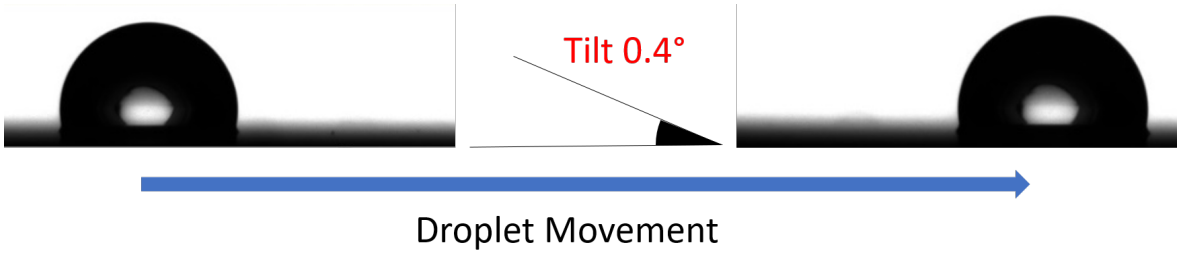

Figure 6.3.1: Images showing a 2 μl droplet deposited onto a flat sample, the tilting procedure and the droplet siding at an angle of 0.40°.

The sliding angle measured on the 3D printed substrate is comparable to that measured on a glass substrate (3.5.2), therefore the SLIPS properties have not been affected by the change in substrate or the presence of micron scale roughness generated at the printing stage. As a result of this, no post printing smoothing has been performed on the 3D printed substrates to ensure that any topographical features added at later stages were altered.

The contact angle hysteresis of the sample was also measured, whilst this method provides the most accurate measure of surface hysteresis, on SLIPS it is difficult to

obtain accurate values due to the wetting ridge. Water droplets of volume 4 μl were deposited onto the sample (Figure 6.3.2 a) and a further 4 μl pumped in to give the advancing angle. 4 μl were then pumped out to give the receding angle. For each of the 10 experimental repeats both the left and right angles were measured for θ_A (Figure 6.3.2 b) and θ_R (Figure 6.3.2 c) with a mean value calculated. All of the angles were measured using ImageJ as the Krüss DSA30 software struggles to take an accurate measurement due to the presence of the wetting ridge. The contact angle hysteresis for the flat 3D printed sample is measured as 2.1° ± 0.7°.

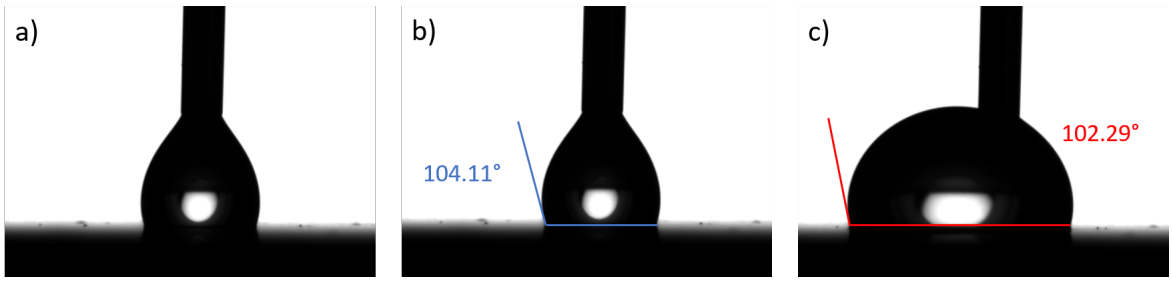

Figure 6.3.2: Contact angle hysteresis measurements on a flat sample. a) Static 4 μl droplet. b) Advancing angle. c) Receding angle.

The large difference between the contact angle hysteresis and sliding angle is expected. Despite the fact that the droplet used for sliding angles is small enough that surface tension is dominant (2 μl), gravity still acts to pull the droplet down the surface, therefore slightly reducing the hysteresis measured via this method. In addition to this, the position of the top of the wetting ridge moves throughout the increase and decrease in droplet volume, meaning the baseline has to move between the measurement of θ_A and θ_R, again increasing the hysteresis.

6.4 Egg-Box Surface

To create the topologically structured surface, a CAD (Computer Aided Design) software, Solidworks, was used to produce the egg–box structure. Connecting a series of splines together allowed for an almost cosine wave to be produced in the horizontal and vertical sample directions and enabled certain parameters to be changed in accordance with the desired application. The total sample size produced for a 500 μl

droplet to evaporate on the egg-box structure was 10 wavelengths horizontally and vertically. The key measurements of this surface and what the droplet will conform to when placed on top of the structure are as follows: horizontal/vertical wavelength (λ) is 4 mm, amplitude (ϵ) is 0.5 mm and the diagonal wavelength ($\lambda/\sqrt{2}$) is 2.87 mm (Figure 6.4.1).

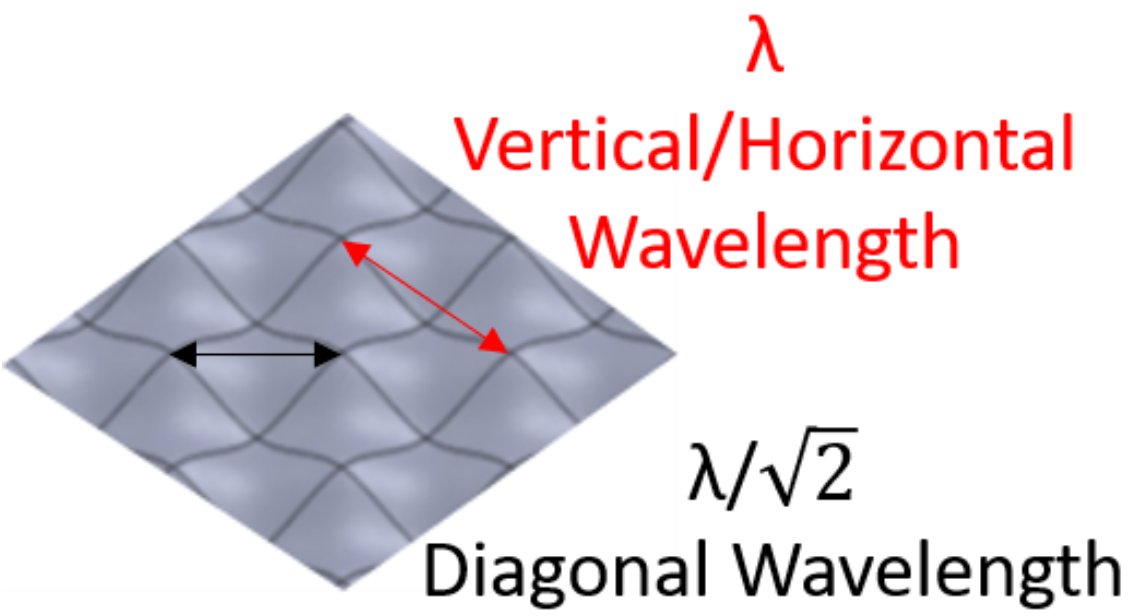

Figure 6.4.1: Solidworks image of the Egg-Box structure showing the diagonal wavelength and horizontal/vertical wavelength.

The combination of SLIPS coating and 3D printed surface topography creates a Liquid Infused Rough Surface (LIRS).

A bespoke LabVIEW program was created specifically to operate an Allied Vision Mako U130B camera, which was positioned to look down at the top surface of the sample (Figure 6.4.2) Time-lapse images were taken at a frame rate of one image every 5 minutes to record the evaporation of the droplet under ambient conditions (humidity 25% - 40%, temperature 20°C – 26°C). Before each experiment the sample's oil layer was replenished by redipping the sample at a withdrawal speed of 0.1 mm/s and the stage levelled with a Level Development Engineering Level with an accuracy of 50 μm per m.

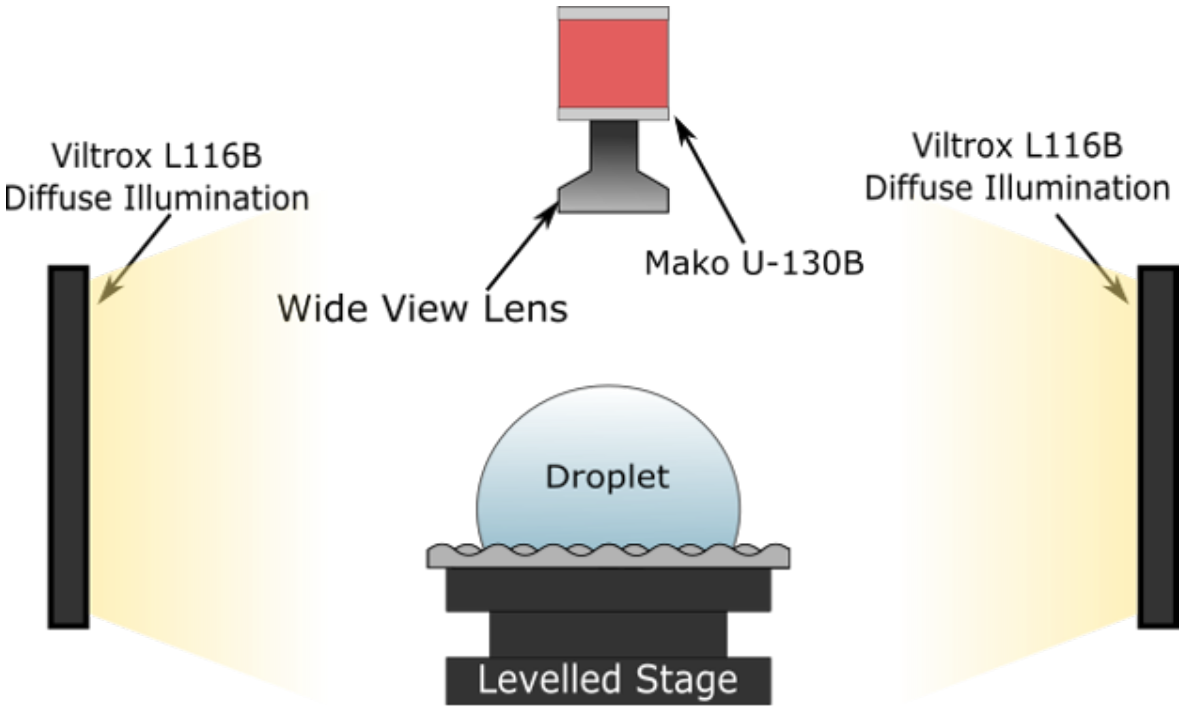

Figure 6.4.2: Schematic of the experimental set up with the Allied Vision Mako U130B camera, 2 diffuse Viltrox light panels and sample positioning.

A DI water droplet of volume 500 μl was placed onto the egg-box structure using a micro-syringe, covering an area of 5 troughs by 5 troughs (black areas underneath the droplet in Figure 6.4.3), forming a diamond structure. As can be seen from the images in Figure 6.4.3 the droplet changes its overall shape from a diamond to a rectangle, with the change in shape being caused by a snap event. Each time the experiment is repeated the droplet will follow a systematic decrease in footprint area following the pattern of diamond, rectangle, diamond, rectangle, until a singular droplet remains in one of the troughs that were initially covered by the 500 μl droplet.

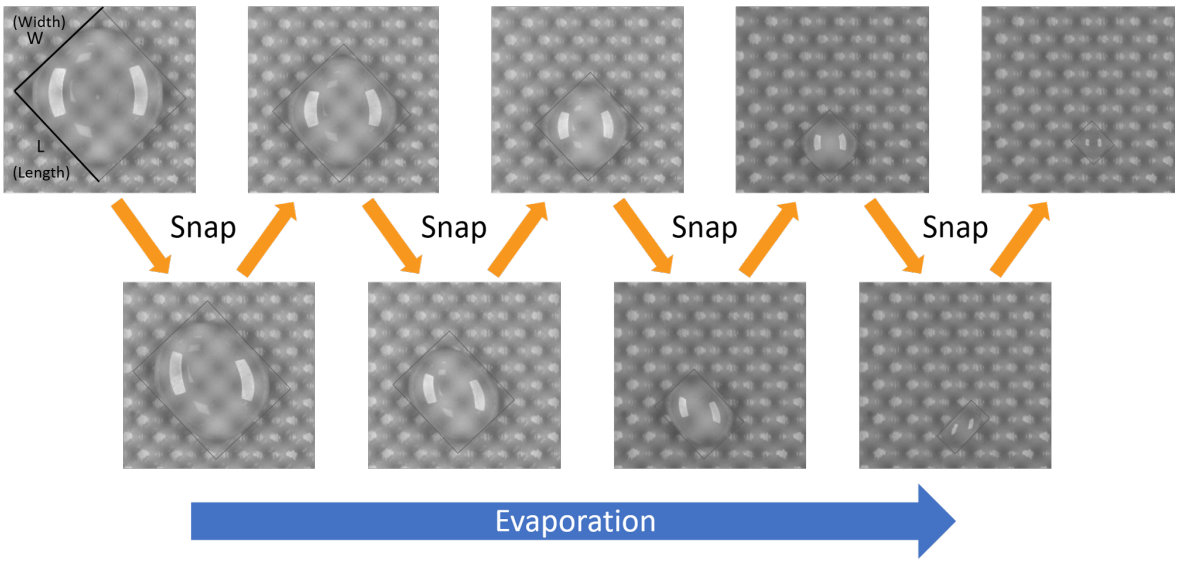

Figure 6.4.3: A sequence of images taken of a 500 μl droplet evaporating on an egg-box surface undergoing a series of snap events to form each stable droplet structure.

From every experiment the images were collated to form a video. For each stable droplet shape i.e. 5x5, 5x4, 4x4 ... 1x1, a sequence of frames were taken from the videos for analysis. The image processing software, ImageJ, was used to fit an ellipse to the droplet and from this measure the semi-major axis and semi-minor axis, which in this case have been termed as the length and width of the droplet respectively (Figure 6.4.4). These values were then used to calculate the droplet's apparent contact area and aspect ratio. For the symmetric droplet structures (diamond) the aspect ratio is 1. For the asymmetric droplet structure, the aspect ratio depends on the size of the droplet and how many troughs are covered. As the droplet reduces in volume, the aspect ratio decreases for the asymmetric, rectangular droplets. When the droplet undergoes its first snap, from 5x5 to 5x4, the aspect ratio only slightly varies from the symmetric 5x5 droplet. As the difference between the two edges of the asymmetric droplet starts to increase the aspect ratio decreases until reaching the final configuration with the smallest edge (width) being approximately half that of the droplets length.

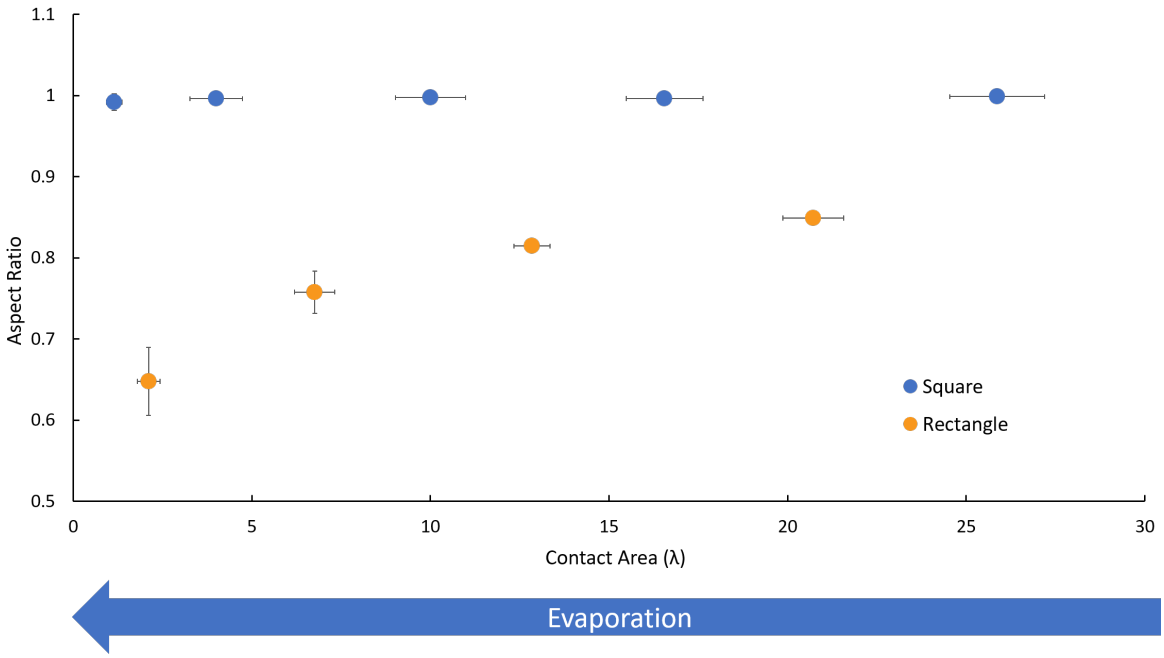

Figure 6.4.4: Droplet aspect ratio (width/length) as a function of apparent contact area(width/(length x wavelength^2)) with the blue dots indicating the symmetric diamond structure and orange dots the asymmetric rectangular structure. The error bars indicate the standard deviation between all 5 experiments.

When taking top view images, the true droplet footprint is hidden and can only be estimated as an apparent footprint as the droplet slightly overhangs the constraints of the troughs and peaks, bulging along the droplet edges. On these samples it is also impossible to take accurate side view images as the underlying topography hides the majority or the droplets base. Because of this, the data (Figure 6.4.4) shows that the droplet does not exactly follow the 5x5, 5x4, 4x4 ... 1x1 reduction in apparent contact area and aspect ratio. For the symmetric, diamond droplet this overhang is even around the entire droplet, therefore when measuring the aspect ratio, the extra area on the length and width cancel each other, giving an approximate aspect ratio of 1 for each droplet. However, when measuring the apparent area, this overhang adds a small factor to the overall value of the apparent area measured, thus overestimating the value.

In the case of the asymmetric droplet, the shape deviates from the perfect, rectangular geometry more than the deviation of the symmetric droplet from the diamond structure. This is because the droplet experiences pinching along the longer sides at the edges of the droplet and bulging in the middle (the droplet always wants to form

as perfect a circular shape as possible to minimise its energy), therefore the shape as a whole appears more ellipsoidal than rectangular. As the droplet reduces in size the droplet pinching and bulging becomes more pronounced at low aspect ratios, further skewing the shape and adding an additional amount to the apparent area. For example, the largest asymmetric droplet (5x4) should have an aspect ratio, in terms of wavelength, of 0.8. When measured, this is found to be 0.849 ± 0.006, which is 0.049 larger than the predicted value, confirming the increase in predicted apparent droplet area. In contrast to this, the smallest asymmetric droplet (2x1), in terms of wavelength, should have an aspect ratio of 1 half (0.5) in fact has a much larger apparent aspect ratio measured to be 0.648 ± 0.042 again confirming that the droplet deforms more as the volume decreases.

Whilst the exact shape of the droplet (square or rectangular) can be accurately predicted, after performing multiple repeats of the above experiment, it is found that the droplet does not follow the same evaporative path each time, with the prediction of the snapping edge impossible to accurately determine. If the sample is placed at a slight angle it is more likely that the edges of the droplet at the top of the slope will be the first to move due to the addition of a gravitational pull. However, if the droplet is oriented in the same direction as that seen in Figure 6.4.3, assuming there are no heterogenicities along the contact lines, it is impossible to predict whether the left or right contact line will be the first to snap (Figure 6.4.5 a). Even though on the face of it is just as likely that the left line will snap as the right line, in experiments the incidence of both lines snapping is never observed. This is because despite the assumption that there are no heterogeneities to force a snapping event, there is an underlying structure that is not homogeneous accompanied with an accumulation of oil in the troughs, leading to a preferential direction for the droplet to snap in. If a macroscopic heterogeneity is introduced to the surface the preferential snapping is clearer. As with the flat standard SLIPS all droplets are drawn and attracted towards the imperfection, therefore the droplets edges will remain pinned on this defect and the lines that are free to move will snap towards the imperfection (Figure 6.4.5 b).

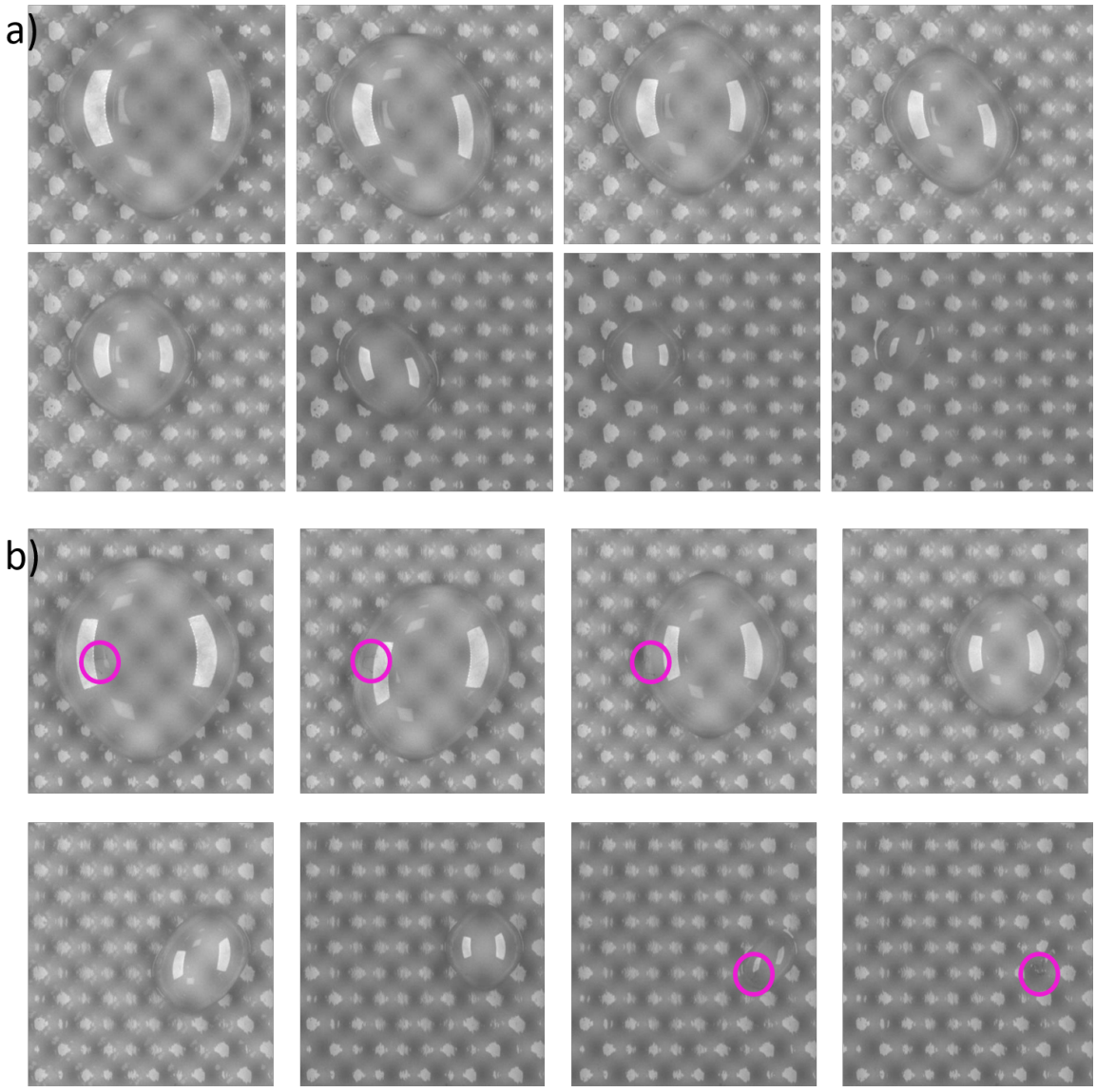

Figure 6.4.5: Imperfect droplet snapping events on the egg-box structure. a) Preferential directional droplet snapping due to the sample being placed at an angle. b) Preferential directional droplet snapping towards a surface defect highlighted by the pink circles.

The factor that was not considered through these experiments was the possibility of oil loss from the tops of the structure whilst the droplet evaporated[149]. Before each experiment, the LIRS was reimbibed with a 3.09 μm thick layer of Silicone oil, meaning that each droplet repeat begins with the same distribution of oil over the surface, hence each repeat is consistent. However, the effect of not reimbibing the surface between droplets has not been investigated.

6.5 A 2D Geometry

Simplifying this structure further to a 2D geometry, with a sine wave passing through only one plane of the substrate, the droplet appears to undergo stick slip evaporation similar to the snap events seen on the egg-box structure. In reality, this is not the case due to the lack of surface pinning and hysteresis.

The apparent stick is where the droplet's contact line moves very slowly over a peak on the surface, creating a small change the droplet base radius, with the contact line appearing to be almost stationary. Throughout the stick period the contact line forms a constant apparent contact angle with the horizontal, indicating constant contact angle evaporation despite being on a structured surface.

The observed slip motion is the snap events, which ultimately govern the mechanism of droplet footprint reduction. This is not a true snap or slip event, with a sudden jump of the contact line due to a depinning event, but it is in fact a very fast, but smooth, retraction of the contact line through the trough. The timescale of the snap event is not on that of the time-lapse image photography (1 frame every 5 minutes) used for the egg-box structure but occurs on the timescale of seconds.

To trigger a snap event the volume and base radius must reach an imbalance where the droplet can no longer decrease in volume and form a constant apparent contact angle. For the droplet to maintain a constant contact angle the contact lines would have to remain in the same position, which would mean the droplet would have to increase in volume contrary to the evaporation. Therefore, for the droplet to remain in a stable, low energy, equilibrium state on the surface the contact lines must move.

6.6 Conclusion

This chapter has explored the ability of a droplet to be transported and accurately positioned as it evaporates on a surface. Combining a topographically structured substrate with the innovative nanoparticle-based SLIPS coating provides a minimal hysteresis test bed for the study of droplet positioning. Droplets on these surfaces conform to the constraints imposed by the underlying substrate without the need for direct contact

with the solid. However, none of the SLIPS properties of the coating have been lost by applying this coating to a new substrate (3D printed plastic sample). Creating an egg-box topography changes the shape of a sessile droplet from circular to square or rectangular without the requirement of any external energy or force. For a given amplitude and wavelength of the substrate, the shaping of the droplet is governed purely by the volume[150, 96].

The combination of the topography and SLIPS coating could reasonably be used to study the phenomena of particle deposition, which has many practical applications especially in areas such as microfluidics. Traditionally, a pinned contact line is required to induce a Marangoni flow within a droplet, pushing suspended particles to the contact line where they are subsequently deposited. Therefore, it is reasonable to assume that a pseudo-pinned contact line(seen with the snapping events) might give much the same effect. Creating a particle laden liquid and applying droplets to the structure, the particles may be deposited evenly into wells or could be held in the liquid and transported to another section of the sample before settling out of the droplet towards the solid surface[151]. However, for the coating to be useful for microfluidic applications the coating will have to fully coat small surface areas and surfaces that often consist of closed geometries.

Chapter 7

Single Coating

This chapter describes the process of producing a SLIPS coating in a single step method, this coating now has a patent pending. It then goes on to discuss the optimum coating that can withstand an extended period of sample storage as well as continuous usage. Finishing with a brief overview of possible applications for which the coating would be ideal.

7.1 Introduction

Having the ability to apply a SLIPS coating in a single step would open up a wide range of applications from immersing a large ship in the solution to improve drag reduction and antibiofouling, to, on the very small scale, applying SLIP coatings to microchannels where it is difficult to uniformly apply the coating[152]. Or even closed geometries, such as sealed lab-on-chip cassettes, where it is impossible to spray directly onto the surface itself and an antibiofouling aspect to the coating is required[153].

The idea was to create a solution containing both the suspended particles in their solvent (IPA) and 20 cSt Silicone Oil, which would replicate the multiple step method in both sliding angle and reproducibility. This solution could then either be poured onto a sample, or the sample dipped into the solution, leaving behind a stable, uniform SLIPS coating on the surface of the substrate[154, 155].

The other benefit of the single coating is the entirety of the sample can be used. During the multiple step spray coating method an edge bead is formed, creating a

build-up of SiO_2 particles at the bottom of the sample creating an area that is not a SLIPS, rendering this section of the sample unusable. The potential to use all of the sample would mean that there were no pinning points, creating a truly uniform sample.

7.2 Ratios

Single coating mixtures were first made in terms of ratios of Glaco to 20 cSt Silicone oil by weight, starting at 4 : 10 and going all the way up to a 20 : 10 mixture. The first component to be weighed out was the Silicone oil, the Glaco was then added to the Silicone oil in order to reduce the amount of IPA evaporation that may occur before sample preparation. When the components of a mixture had been added to the container, to ensure a well-mixed solution the mixture was shaken by hand continuously for 5 minutes. Each of the specific ratio solutions were then used in exactly the same way as follows: 2 ml of the solution was deposited via a syringe onto a standard borosilicate glass microscope slide of dimensions 25 mm by 75 mm which had been cleaned using the procedure detailed in Chapter 3, Section 1. This was the ideal quantity of liquid for the surface tension of the solution to hold all the liquid on the slide without emptying into the container below. The ideal amount of liquid was found not to differ with the changing ratios of components in the mixture. Using less than 2 ml gave a patchy coating that didn't fully spread over and coat the glass slide. After applying the coating to one sample the mixture was shaken again for 30 seconds before applying the coating to the second sample and so on to ensure there was no change in the initial mixture structure between samples.

It is very clear from the sample images seen in Figure 7.2.1 there are distinct differences between each of the single coating side profiles. In Figure 7.2.1 c the particles in the 20 : 10 mixture have aggregated to form large clumps, which act as pinning points and already indicate a non-uniformity in the mixture's coating abilities. However, on the other end of the spectrum at ratio 4 : 10 (Figure 7.2.1 a), the water droplets are more prone to sinking into the oil layer as there are not enough particles in the mixture to form a supportive underlying structure to give the droplet buoyancy. At the 10 : 10 ratio the particle structures are fairly obvious and are again creating pinning points,

however the droplets seem to quite comfortably sit on top of the surface rather than sinking below (Figure 7.2.1 b).

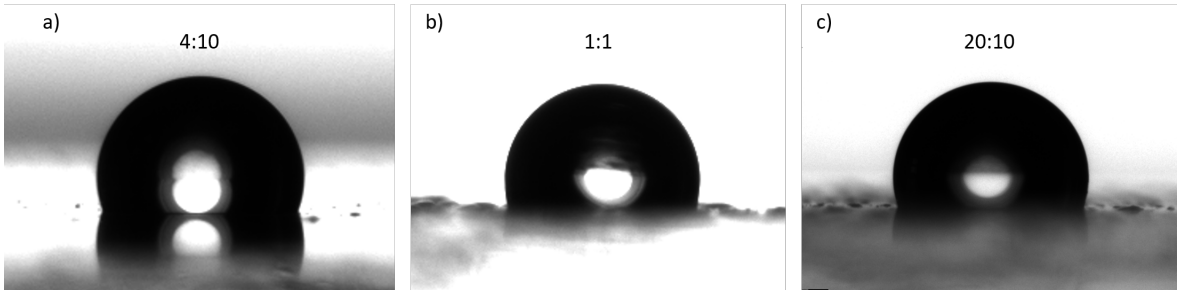

Figure 7.2.1: Droplets on samples with mixture variations, a) 4:10, b) 1:1, c) 20:10, showing the evolution of particle structure on top of the glass substrates.

As seen previously, the siding angles are taken as a measure of the samples slipperiness and to quantify the surface hysteresis. 2 μl DI water droplets were deposited onto each slide and the sample then tilted, until continuous droplet motion was observed. This procedure was repeated 8 times on each individual sample and across 3 samples in total, per ratio. The ratios were converted into Glaco weight percentages to ensure an accurate reproduction of the single coating recipe for any sample size (Figure 7.2.2). From Figure 7.2.2 it can be seen that for the majority of Glaco percentages the sliding angle is above the 5° limit. However, there is a dip between 30% and 40%, with the sliding angles and errors both being at a 5° upper limit or below. The sliding angle appears to begin to dip again at 50% but, as can be seen in Figure 7.2.1, the amount of particles in the mixture seems to be too large with large aggregations appearing on the surface, indicating that increasing the Glaco percentage more will not decrease the sliding angle below 5° again. For every sample the error on the sliding angle appears to be quite high, this is attributed to the non-uniformity of the coating which occurs at the mixing and evaporative stages. The particles could either start out in a non-homogenous mixture or they may aggregate as they begin to settle during the particle percolation step.

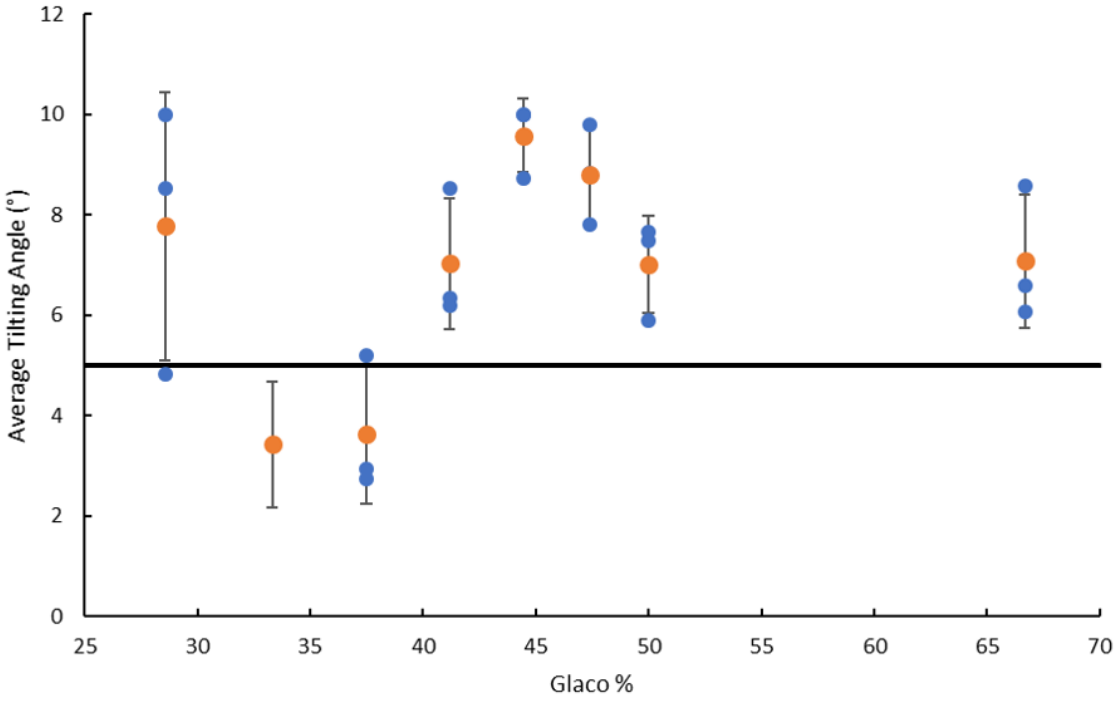

Figure 7.2.2: The blue dots designate the sliding angles measured on each of the samples and the orange, is the averaged sliding angles. The black line indicates the 5° value for SLIPS.

It is noticeable that there is only one data point for the 5 : 10 ratio mixture (Figure 7.2.2) as the remaining 2 samples did not survive the production stage, with the liquid breaking the surface tension before the 24-hour mark. In this case the error is determined by multiple repeat measurements (15 droplets instead of the 8 used on the different ratio samples) in different areas of the sample. This gives us an idea of the coating uniformity across the sample but not the reproducibility.

7.3 Rinse Test for 5:10 and 6:10

As the production step requires a large amount of liquid to create the surface tension required to pull the particles down to the liquid solid interface the excess oil has to be removed at the end of the 24 hour production period. To remove the excess oil from the ratio samples a simple rinse was performed, this involved flowing 50 ml of DI water from a syringe across the sample. Initially the force of the water appears to be displacing a large amount of the oil and in turn removing it from the sample. When

approaching the end of the rinse, ≈ 50 ml, the flowing water appears to stop removing the oil and simply passes over the surface without much interaction, therefore it was determined at this point the surface is assumed to have formed a thermodynamically stable layer.

To see whether this was in fact the case, a more controlled rinse test was conducted on the best single coating samples (5:10 and 6:10). This method consisted of 100 ml of DI water in total being flowed over the surface, again from a syringe, this was spilt into 10 ml aliquots where after each rinse the sliding angle was measured and plotted in Figure 7.3.1. Splitting into 10 ml aliquots not only allowed for the measurement of the sliding angle at given intervals but it also helped with controlling the pressure at which the water left the syringe, allowing for more control of the force of the water flowing over the surface. The sliding angle data for the two ratios appear to follow the same trend with the $6:10$ samples having a lower sliding angle up to the 4th rinse, at this point the $5:10$ ratio drops below the $5:10$ until reaching the 9th and 10th rinse where the two ratios switch again. Both sliding angles for the 1st to 5th rinse are below the 5° limit and the 7th to 9th rinse above the 5° limit, at the 10th rinse the sliding angles again drop below the SLIPS value line. After the 6th rinse the data point for the $6:10$ ratio has risen over the SLIPS value line whist the $5:10$ sliding angle is still below the limit. Therefore, until the 6th rinse both ratios fulfil the SLIPS criteria.

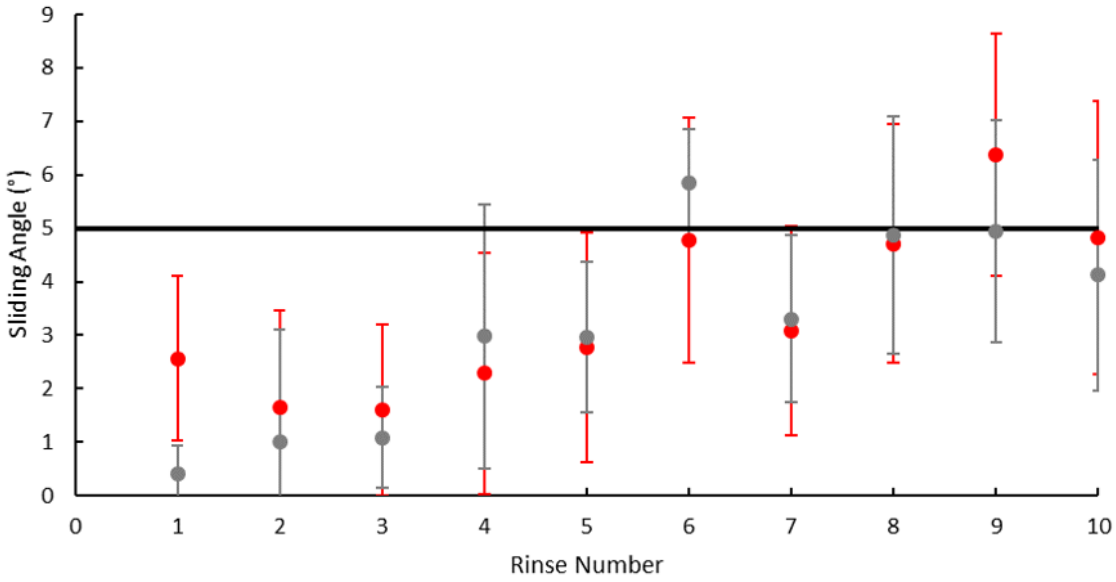

Figure 7.3.1: Sliding angles of 2 μl water droplets as a function of sample rinse number, with the black line signifying the 5° SLIPS criteria, red dots the 5 : 10 mixture and grey dots the 6 : 10 mixture, both with their accompanying errors.

At the 5th rinse, the total amount of water passed over the surface has reached 50 ml (same amount as used in previous experiments, Figure 7.2.2), however the sliding angles appear to be lower than that seen with a full 50 ml rinse (Figure 7.3.2). This difference can be attributed to the better regulation of flow rate in the second method (10 ml aliquots). With an irregular flow rate the force of the water is inconsistent through the sample rinse and between different samples, meaning that more oil may have been removed from one sample than another. If the flow rate is too fast the force of the water may even cause damage to the underlying particle layer, again affecting the sliding angles.

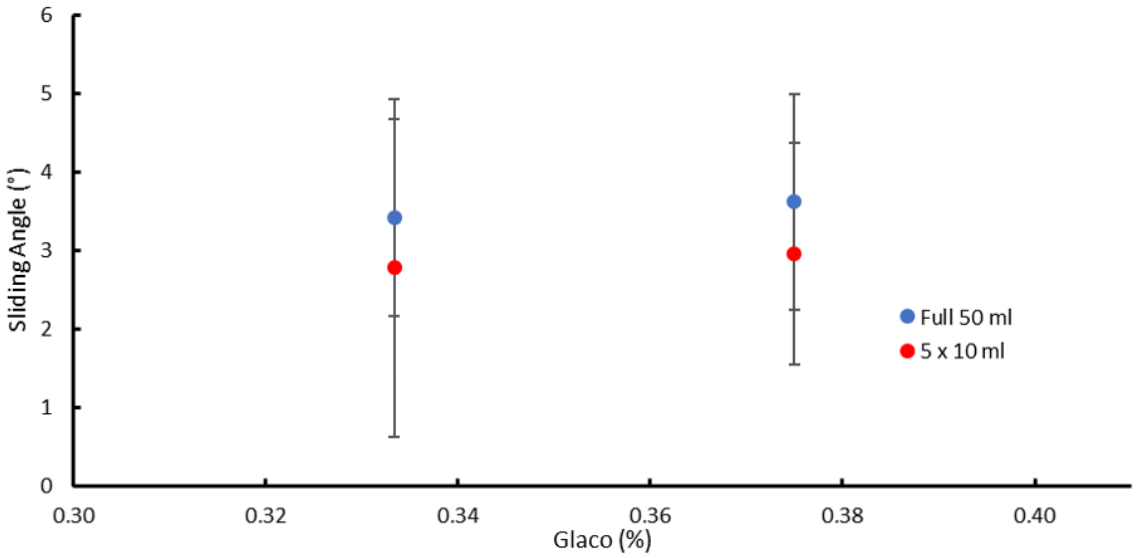

Figure 7.3.2: Comparison between the sliding angle data for the 5 : 10 and 6 : 10 ratios for a full 50 ml water rinse (blue data) and the 5th rinse using 10 ml segments (red data).

The large error bars in Figure 7.3.1 and 7.3.2 highlight the surfaces heterogeneities and emphasise the need for a more controlled recipe, component mixing and excess oil removal method coupled with a more detailed look at the surface composition.

7.4 Glaco Weight

To produce an accurate single coating recipe the exact amount, by weight, of particles in the Glaco needs to be known. From the SDS, the proportion of particles is quoted to be somewhere between 0.1 % and 3.0 %, however this value is not accurate enough for the single coating recipe as the number or particles determines the final porous layer. The SDS also states that Glaco consists of 10 % to 15 % LPG (Liquified Petroleum Gas) however we assume the majority of the propellants are released during the spray process from the can and will not be present in the glass vial and therefore the final mixture. To calculate this, half of two separate Glaco cans were emptied via spraying into two separate glass vials and from there approximately 5 ml of particles and solvent were pipetted into five different pre-weighed watch glasses. The weight of each watch glass was taken once the Glaco (solvent + particles) had been added. Then the final weight of watch glasses and remaining Glaco (particles)was taken after a 3 hour evaporation

time had elapsed. From these values the total weight of the Glaco and its constituent elements can be calculated, therefore the particle weight percentage can be extracted from the data (Table 7.4.1).

Table 7.4.1: Weights of Glaco placed into watch glasses and the remaining particle weight after complete IPA evaporation.

Watch Glass Weight (g)	Glaco (g)	IPA (g)	Particles (g)	Particles (%)
12.5558	4.7465	4.7242	0.0223	0.469820
12.1591	4.8773	4.8542	0.0231	0.473623
12.3336	5.0164	4.9921	0.0243	0.487091
12.1386	4.9888	4.9921	0.0244	0.486405
12.3982	5.0819	5.0581	0.0238	0.468329

Taking an average of this data gives a final particle percentage in Glaco of 0.477 % $\pm$ 0.009% which equates to the weight percentages presented in Table 7.4.2 for the mixtures already tested.

Table 7.4.2: Single coating ratio mixtures in terms of percentage weights.

Ratio - Glaco : Silicone Oil	Silicone Oil (%)	Glaco	
		Solvent (%)	Particles (%)
4:10	71.429	28.435	0.136
5:10	66.667	33.174	0.159
6:10	62.500	37.321	0.179
7:10	58.824	40.980	0.196
8:10	55.556	44.232	0.212
9:10	52.632	47.142	0.226
10:10	50.000	49.762	0.239
20:10	33.333	66.349	0.318

7.5 Percentages

As can be seen from Figure 7.2.2 the two mixtures that give the lowest sliding angle are the 5 : 10 and 6 : 10 ratios, however there is a wide range of percentage mixtures around and between these two values that may produce a lower sliding angle than 3.42°, which

is still far above the multiple coating methods sliding angle. By splitting the mixtures around these values into single percentages, varying from 32% to 38%, the optimum proportion of Glaco to Silicone Oil can be narrowed and the entire recipe refined. The following table (Table 7.5.1) shows the corresponding component percentages for this range of percentage weights of Glaco.

Table 7.5.1: Percentage weight single coating solutions from 32% to 38% with their corresponding particle percentage components.

Glaco Percentage (%)	Silicone Oil (%)	Glaco	
		Solvent (%)	Particles (%)
32	68.000	31.847	0.153
33	67.000	32.843	0.157
34	66.000	33.838	0.162
35	65.000	34.833	0.167
36	64.000	35.828	0.172
37	63.000	36.824	0.177
38	62.000	37.819	0.181

The samples were produced in the way previously described with 10 g of mixture being produced for each percentage. As the density of Glaco and 20 cSt Silicone oil is slightly below that of water, 10 g worth of mixture produces a little over 10 ml, this means that by using 2 ml of mixture per sample, a total of 5 samples can be produced from each batch of single coating mixture.

Again, 2 μl DI water droplets were placed onto the surfaces and the sliding angles measured to provide information on the hysteresis of the surface and therefore how suitable the coating composition is. For these new samples the excess oil was removed by using a total of 50 ml of DI water which was flowed over the surface in 10 ml increments, which is in line with the data plotted in Figure 7.3.1. From the sliding angle data gathered, a graph similar to that previously seen in Figure 7.2.2, with the sliding angles plotted as a function of percentage Glaco weight can be plotted.

In Figure 7.5.1 there are a lot of percentage mixtures that have an average sliding angle above the 5° SLIPS limit. From the 7 percentage mixtures tested only the 34% and 35% mixtures have averages and error bars below the 5° limit. The percentage

mixtures of 32%, 33%, 36% and 38% all have average sliding angles above the SLIPS limit, with the 32% and 33% mixtures containing too few particles to produce a SLIPS and 36% and 38% having too many particles. In addition to this the 37% mixture has an average sliding angle on top of the 5° line, however the error bar extends above this line and is therefore ruled out as a potential viable mixture for SLIPS. The error bars on all of the percentage mixtures appears to reduce as the number of particles in the mixture increases, however the data points with the smallest error have sliding angles too high to be considered as SLIPS.

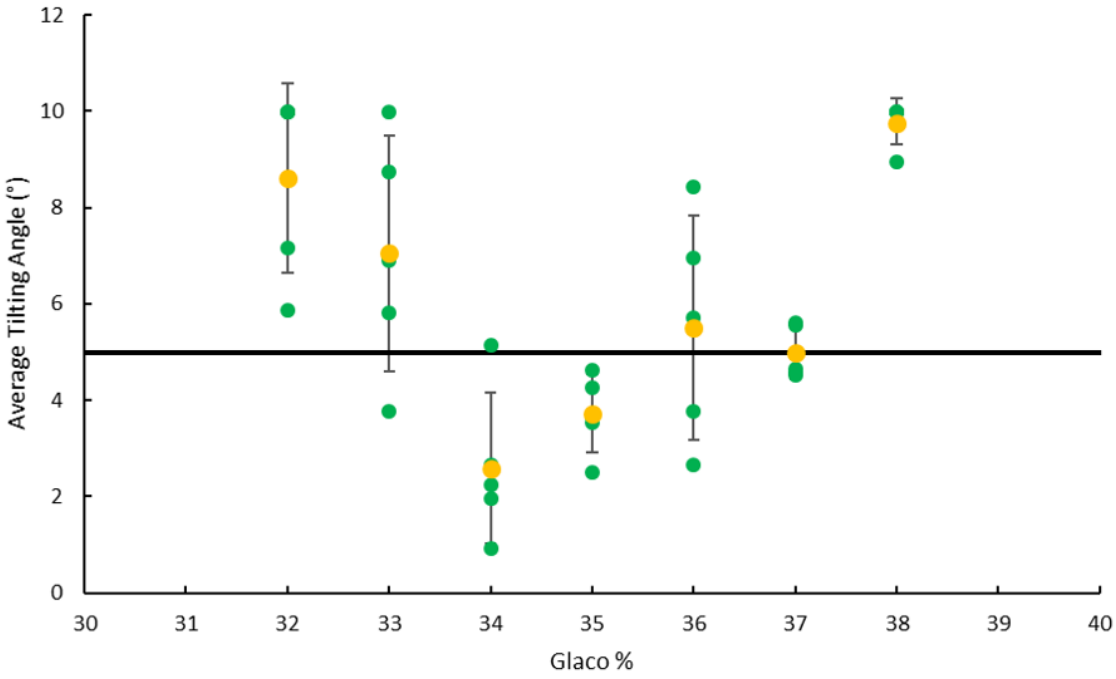

Figure 7.5.1: Measurements of sliding angle (green circles) with accompanying averages (yellow circles) on single coating samples made from different percentages of Glaco, varying from 32% to 38% by weight.

From all the percentage mixtures tested it is only the 34% and 35% mixtures that could be used for further study. However, as the aim of producing a single coating method is to try to match the sliding angles produced by the multiple step method the mixture with the lowest sliding angle (34% = 2.6° ± 1.6°) will be used for further experiments with the aim of reducing the error in the data.

Overlaying the ratio data (Figure 7.2.2) and the percentage data (Figure 7.5.1) it can be seen that the general trends match with the lowest sliding angles (34% and

35%) occurring between the 5 : 10 and 6 : 10 mixtures, any recipe below or above these limits has sliding angles above the 5° limit with only one error bar (33%) dipping below this criteria (Figure 7.5.2). From this it is easy to spot that there is a distinct region that produces a low enough angle to be classed as a SLIPS surface using either the percentage mixing method or the ratio. Both weighing methods still have very large errors but have the potential, if the errors were reduced, to produce a reliable and reproducible single coating method.

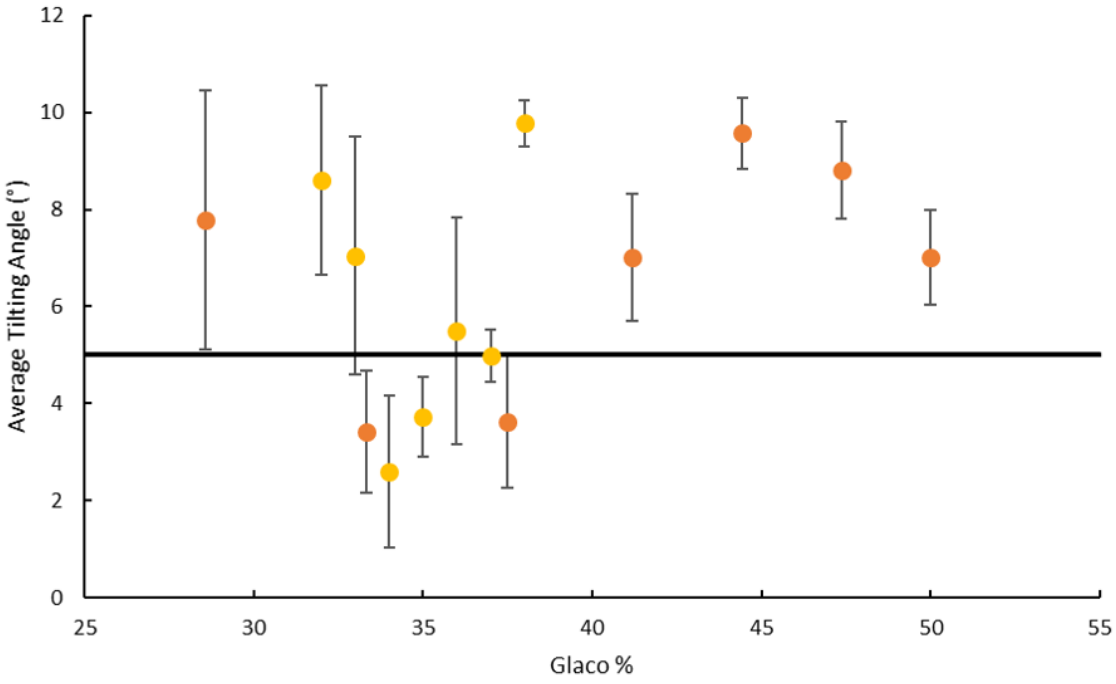

Figure 7.5.2: Comparison between percentage mixtures (orange circles) and ratio mixtures (yellow circles) showing that the 34% coating has the overall lowest sliding angle and error below 5°.

7.6 Solvent Evaporation

Once the 34% solution was determined to be the optimum SLIPS coating, an evaporation test was conducted. The aim of this was to confirm that the time chosen to leave the samples open (2 hours) and total time before testing (24 hours) was long enough for the IPA to fully evaporate from the coating leaving behind only SiO_2 particles and Silicone Oil on the sample. To do this the weight of a glass slide was measured prior to single coating application, once the solution had been applied and then at time

intervals after this until the weight began to plateau. The starting weight of the liquid was 1.720 g ± 0.005 g and decreased rapidly over the first 90 minutes to 1.227 g ± 0.005 g, culminating in an overall weight loss of 0.521 g ± 0.005 g. By closing the lid of the petri dish after 2 hours the likelihood of dust settling on the sample and therefore causing pinning points is considerably reduced. As can be seen from the evolution of the weights (Figure 7.6.1), at 2 hours the weight has reached 1.212 g which is only 0.013 g ± 0.005 g from the final value of 1.199 g measured at 3 hours after deposition. As the petri dish is vented the remainder of the IPA is assumed to continue to evaporate over the proceeding 22 hours.

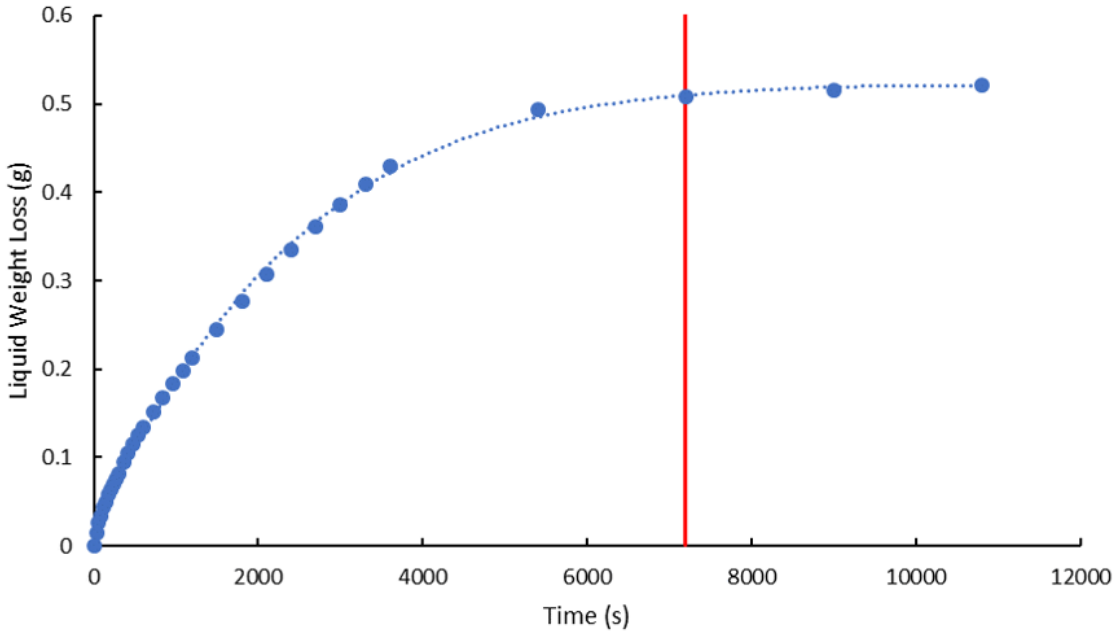

Figure 7.6.1: Sample weight loss due to solvent evaporation measured over 3 hours, with the red vertical line indicating the 2 hour petri dish lid covering point.

7.7 Péclet Number

The Péclet number is a measure of the balance between advection (evaporation driven transport) and diffusion (particle transport). Since the single coating mixture consists of both particles and liquid it could be an appropriate descriptor for the process occurring in the 24-hour sample production period and particularly in the first two evaporation hours. In the single coating case, a high Péclet number ($P_e >> 1$) would

indicate that it is the evaporation parameter that is dominating the movement with the particles aggregating at the water/air interface, in some cases creating a skin, with a non-uniform particle distribution[156, 157, 158, 159, 160]. A small Péclet number ($P_e << 1$) indicates that the diffusion parameter dominates, hence it is the SiO_2 particles themselves moving through the liquid, creating an evenly distributed mixture with uniform particle concentration[156, 157, 158, 159, 160].

As the SiO_2 particles are insoluble in the two liquids the solution can be said to be a colloid, hence the equation to calculate the Péclet number is

$$P_e = \frac{H_0 E}{D_o}, \tag{7.7.1}$$

where H_0 is the initial height of the film and E the evaporation rate. D_o is the Stokes – Einstein diffusion coefficient which is calculated following Equation 7.7.2,

$$D_o = \frac{k_B T}{(6\pi\eta R_o)}. \tag{7.7.2}$$

Combining Equation 7.7.9 and 7.7.2 produces

$$P_e = \frac{(6\pi\eta R_o H_0 E)}{k_B T}. \tag{7.7.3}$$

Equation 7.7.3 requires many values that can be determined experimentally. R_o is the radius of the spherical particles, which can be measured from SEM images in Figures 3.2.2 b and 3.2.3. E (evaporation rate) can be calculated from the solvent evaporation experiment conducted in Section 7.6. T is the temperature recorded at the time of experiment which varies between 20°C and 26°C. The initial film height, H_0, can be calculated from the dimensions of the sample and volume of liquid deposited. Both k_B (Boltzmann constant = 1.38 $\times 10^{-23}$ m^2 kg s_{-2} K_{-1})and η (viscosity) can be found in literature.

As the single coating mixture consists of two liquids, one of which is volatile and the other not, along with the particles it is difficult to calculate a combined viscosity for the mixture. Therefore, for the Péclet number calculation the components have been spilt into the two liquids, Si Oil and IPA. The viscosity for the Si Oil used in

this experiment is 20 cSt, which converts to 1.90 $\times 10^{-2}$ kg m^{-1} s^{-1}. The viscosity for the IPA is taken from an SDS and is found to be 2.27 $\times 10^{-3}$ kg m^{-1} s^{-1}. Splitting the liquids also renders the evaporation rate measured in Section 7.6 inaccurate, hence this parameter must also be calculated separately. On the time scales used for sample production the Si Oil does not evaporate and is given an evaporation rate of 0.0 g/hr. As with the viscosity the evaporation rate of pure IPA is taken again from the SDS which gives a value of 1.7 g/hr.

From SEM images it can be seen that the particles are spherical in shape, however the particle size is difficult to determine from these images as the resolution is poor at a view field of 5 μm for what is a very insulating sample. Therefore, the size measured could reasonably vary between R_o = 20 nm and R_o = 50 nm considering the blur on the edge of the spherical particles.

The dimensions of the glass slides are 25 mm by 75 mm, giving a total surface area of 1875 mm^2. 2 ml of single coating mixture fills a space equal to a volume of 2000 mm^3. Therefore, the height of the film can be calculated, H_0 = 2000 mm^3 / 1875 mm^2 = 1.07 mm.

With T at the lowest possible value (which in Kelvin equates to 293K) and R_o at the highest (50 nm), the subsequent Péclet number calculated is the largest possible value for the given initial conditions. Inputting these values into Equation 7.7.3 with 34% of the solution as IPA and 66% as Silicone oil produces the following calculations:

$$P_{eIPA} = \frac{0.34(6\pi(2.27 \times 10^{-2}) \times (50 \times 10^{-9}) \times (1.07 \times 10^{-3}) \times (4.72 \times 10^{-7}))}{(1.38 \times 10^{-23}) \times 293}. \tag{7.7.4}$$

$$P_{eSiOil} = \frac{0.66(6\pi(1.90 \times 10^{-2}) \times (50 \times 10^{-9}) \times (1.07 \times 10^{-3}) \times 0.0)}{(1.38 \times 10^{-23}) \times 293}. \tag{7.7.5}$$

$$P_e = P_{eIPA} + P_{eSiOil} = 90.62. \tag{7.7.6}$$

Taking T at its highest value (299K) and R_o at the lowest (20 nm) the calculated

Péclet number is the smallest possible value for the given initial conditions. Repeating the same calculations produces the following Péclet number:

$$P_{eIPA} = \frac{0.34(6\pi(2.27 \times 10^{-2}) \times (20 \times 10^{-9}) \times (1.07 \times 10^{-3}) \times (4.72 \times 10^{-7}))}{(1.38 \times 10^{-23}) \times 299}. \tag{7.7.7}$$

$$P_{eSiOil} = \frac{0.66(6\pi(1.90 \times 10^{-2}) \times (20 \times 10^{-9}) \times (1.07 \times 10^{-3}) \times 0.0)}{(1.38 \times 10^{-23}) \times 299}. \tag{7.7.8}$$

$$P_e = P_{eIPA} + P_{eSiOil} = 35.52. \tag{7.7.9}$$

The Péclet numbers calculated for both extremes are much larger than 1, therefore it is the advection rather than diffusion that is dominating the transport and movement of the particles. If the petri dish remained closed through the first 2 hours, the evaporation rate would be suppressed and the dominating transport method may switch from advection to diffusion, changing the structure of the surface. In this case there is a binary liquid mixture, therefore the Péclet number will decrease as the IPA evaporates, due to the evaporation rate decreasing and approaching 0 as the mixture tends towards 100% Si Oil. This means that towards the end of the process diffusion will dominate.

7.8 Different Liquid Mixing and Excess Oil Removal Methods

The average sliding angle for the single coating method at 34% Glaco content is 2.6° ± 1.6° which is still over 2° from the multiple coating method with samples dipped at a 0.1 mm/s withdrawal speed. Therefore, the next aim was to make the samples more reproducible, reducing the error whilst also lowering the sliding angle. Therefore, two stages to the single coating process were investigated further to see where improvements

could be made, these were the oil removal method and the Glaco/Silicone Oil mixing method. Until this point each mixture recipe had been mixed by hand by shaking the vial continuously for 5 minutes before application onto the cleaned glass substrates. Once the evaporation (2 hours) and particle settling time (24 hours) had elapsed the excess Silicone Oil was removed by a simple 50 ml DI water rinse. The new mixing method to be tested was sonication using a sonic bath (Ultrawave Sonic Cleaner), with the aim of breaking up particle aggregates and evenly dispersing the singular particles through the liquid for a more homogeneous mixture. The other oil removal methods apart from the DI water rinse were: a 24 hour drain time where the samples would be held vertically to allow gravity to remove any oil that was no held onto the surface via van der Waals forces and a second method where compressed air would be swept across the sample again removing any oil that was not held within the structure. Combining these led to 6 different amalgamations of solution mixing method and excess oil removal (Figure 7.8.1). For each combination, 5 different samples were produced to check for reproducibility and 8 droplets deposited on different areas of the samples to check for coating uniformity, giving 40 sliding angle repeats for each coating method. The single coating recipe used for these tests was optimum 34% mixture as this produced the lowest sliding angle of all, however the accompanying error bar is large indicating there is room for recipe improvement.

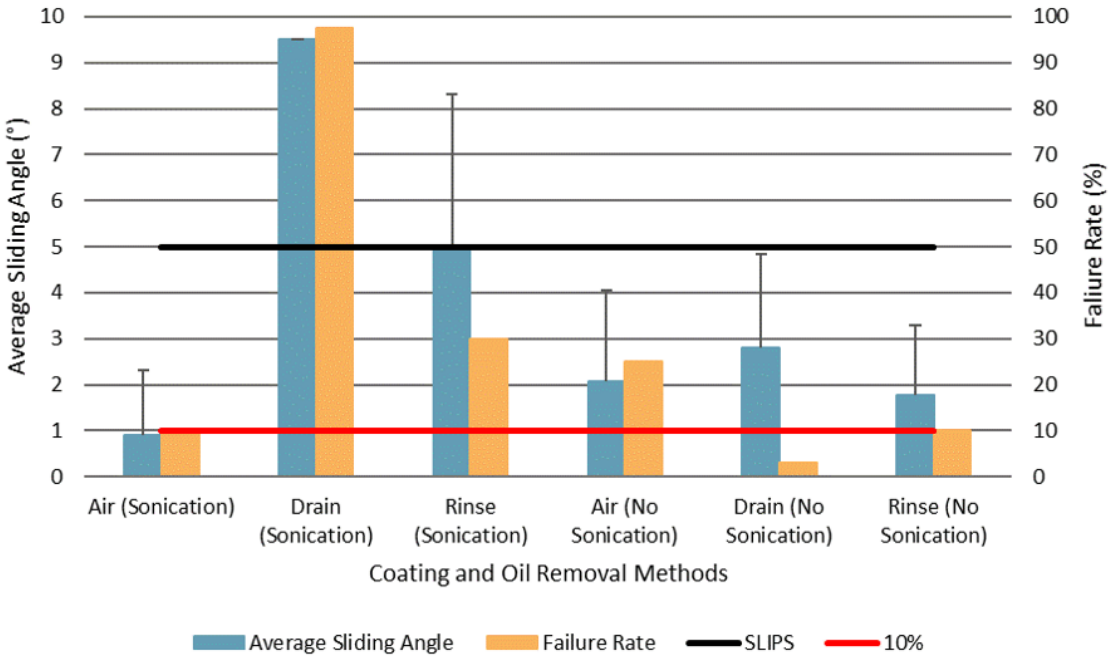

Figure 7.8.1: The six different mixing and excess oil removal methods failure rate (blue bar) and sliding angles (orange bar) along with the accepted upper limits (black and red lines).

Previously, when recording the sliding angles the stage was taken to 10° ± 0.2° (the criteria for superhydrophobicity), if the droplet did not move at this point it was recorded an angle >10°. For the new methods, the stage was taken to 20.0° ± 0.2°, if the droplet did not slide at this angle then it was deemed to be a failure and contributes to the orange column seen next to the sliding angle data in Figure 7.8.1 To take an average of the sliding angle it is only the droplets that were removed from the sample that contribute to the final value, any droplet in the orange column was excluded from the averaging, in the blue column. Therefore, it is the combination of sliding angle values along with the failure rate that indicates whether the mixing and oil removal method was producing a useable SLIPS coating.

In Figure 7.8.1 two guidelines have been added for the minimum single coating criteria. The first line (black) indicates the SLIPS value of 5°, anything above this did not produce a SLIPS coating. The second line (red) indicates a 10% failure rate. With the possibility of the droplets movement having been impeded by pinning points created by dust it was decided that a 10% failure rate would be an acceptable value. By just looking at the sliding angles measured, 2 methods can be immediately eliminated. Both

oil drainage and rinse removal method for sonication mixing have sliding angles above 5°. When taking into account the error bars, the failure rate for these two methods are also the highest of the 6 combinations. In fact, for the Drain with Sonication only one droplet was successful with a sliding angle below 20°, hence the large failure rate of >90%. The next method that is easy to omit from the potential single coating improvements is the air removal with no sonication due to its high failure rate of >20%. This leaves 3 combinations with appropriate values fitting the 2 criteria.

The second Draining method without the Sonication mixing step also exhibits a large siding angle, however it has the lowest accompanying failure rate. This high sliding angle is attributed to an accumulation of dust. Whilst every effort was made to reduce the samples contact with the air when draining the oil, in normal lab conditions, it is impossible to isolate the sample completely, therefore this method was also omitted from the potential recipes. As the aim of the single coating recipe was not only to produce a coating replicating the sliding angle seen for the multiple coating method, it is important to consider whether the recipe could be replicated by others. Out of the two remaining methods Air with Sonication provides the lowest sliding angle with a mixing method (Sonication) that could be repeated by others. The final method (Air removal with Sonication mixing) has a sliding angle of 0.9° ± 1.4° with an additional error of 10%.

Rinse with no Sonication produces a sliding angle of 1.8° ± 1.5° with a 10% error, which should be the same as the sliding angle seen previously for the 34% recipe, 2.6° ± 1.6° as the two methods are the same. The discrepancy between the two values is attributed to the addition of a failure rate parameter. This removes a proportion of the overall error, reducing this value, along with the sliding angle itself.

7.9 SEM Comparison

There is still a large discrepancy between the sliding angles measured for the 34% single coating mixture (0.9° ± 1.4°) and the 5 times coated multiple step method, when dipped at a withdrawal speed of 0.1 mm/s (0.46° ± 0.20°). The error associated with the single coating sample is also much larger than the value itself and much

larger than that associated with the multiple step method, indicating that there are significant heterogeneities still present in the single coating.

To investigate this, cross sections of both samples were taken and the height and uniformity of the coating measured. 4 nm of Platinum was used to coat the Glaco as the SiO_2 particles are insulating and will maintain the charge from the electrons creating bright patches on the images and eventually damage to the sample itself. With too much platinum, the particles become smothered and the porosity of the structure is impossible to examine. Analysing the cross section of the 5 times coated sample there is a very clear porous structure for the Silicone oil to imbibe into and there is overall a fairly flat, homogenous top layer with an average height of 1.93 μm $\pm$ 0.16 μm (Figure 7.9.1).

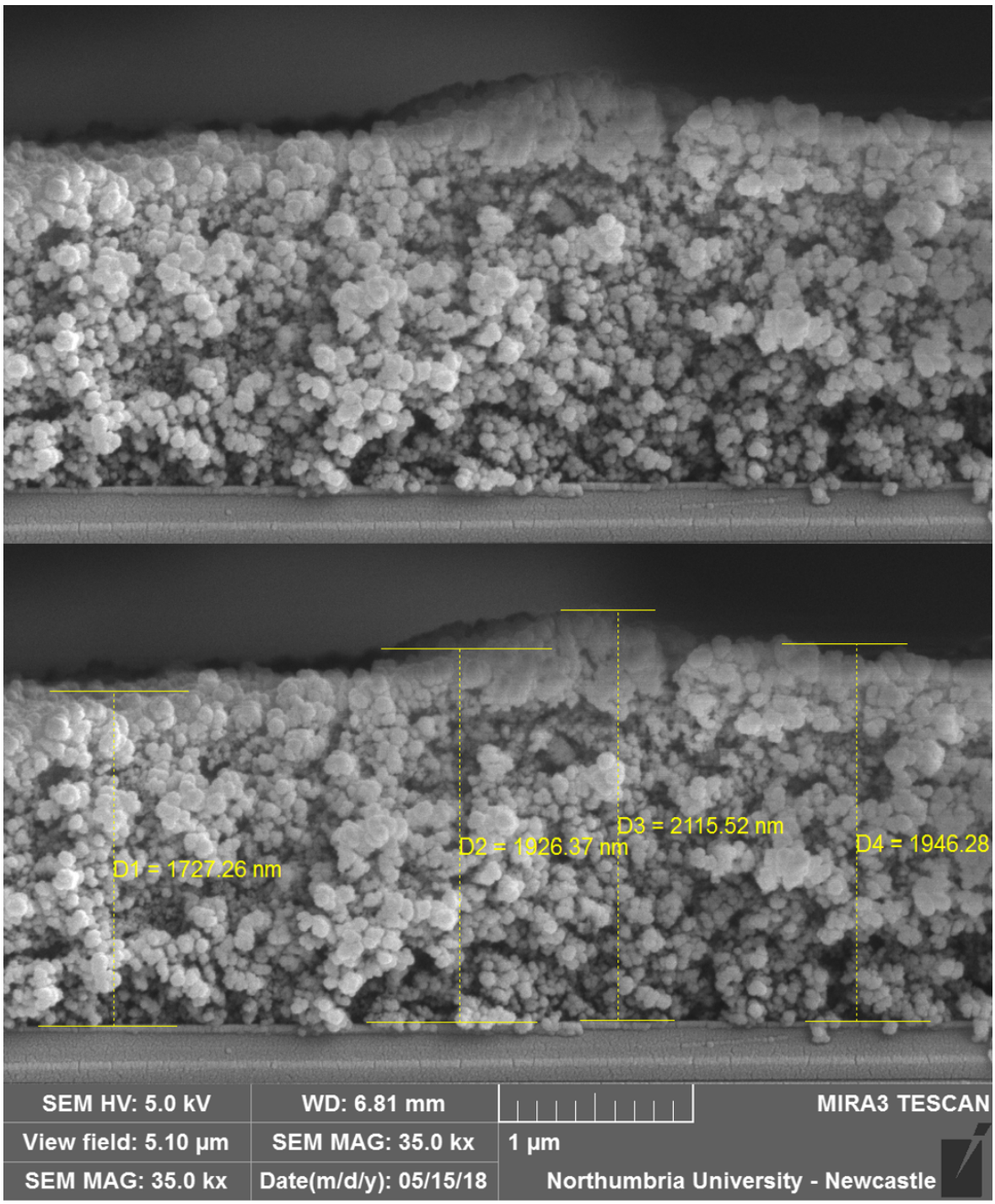

Figure 7.9.1: SEM cross section image of a) 5 times Glaco coated multiple coating sample with b) the height of the Glaco coating as measured using the SEM.

Normally the particulate structure would be examined prior to Silicone oil imbibition, however as the single coating method contains the oil to begin with the oil has to be removed from the sample before being placed into the vacuum of the SEM. As Toluene is miscible with Silicone oil this solvent was used to remove the Silicone oil imbibed into the single coating sample. This removal method was first tested on

a multiple coating sample to ensure that the use of Toluene would have no effect on the particle bed. It was found that the Toluene caused no damage to the number of particles or the porous network.

Taking a cross section of this sample and preparing it as before, the scans seen in Figure 7.9.2 can be produced. The SEM scans show a much smaller particle layer thickness of 0.43 μm $\pm$ 0.07 μm, which provides just enough of a porous network to retain the oil layer but may not produce a superhydrophobic coating, causing a difference between the two methods and therefore their corresponding sliding angles.

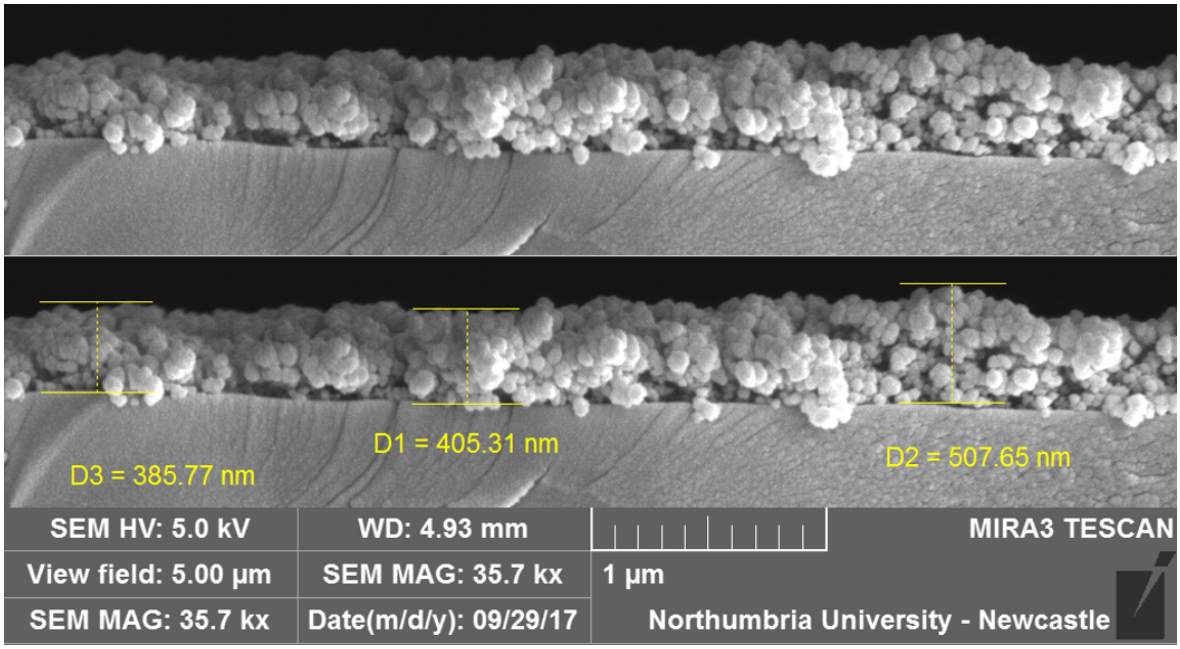

Figure 7.9.2: SEM cross section image of a) 34% single coating sample with b) the height of the Glaco coating as measured using the SEM.

Using top view scans of the two coatings side by side (Figure 7.9.3) provides more information on the coating uniformity. Figure 7.9.3 a is the top view scan of the multiple step method, confirming the evenness of the coating assumed from the cross section. This coating uniformity not only justifies the low sliding angle but also provides a reasonable explanation for the very small error associated with this sliding angle. Figure 7.9.3 b displays the opposite to what is seen for the multiple step process with a very clear non-uniformity across the sample. Over a small scan area approximately equal to 30 μm there are agglomerations of particles creating lumps that would act as pinning point as well as darker areas in the image which corresponds to areas with few,

or no, particles. The areas with few particles would also lead to pinning points where the droplets contact lines would become stuck, leading to the higher sliding angle and error associated with this value.

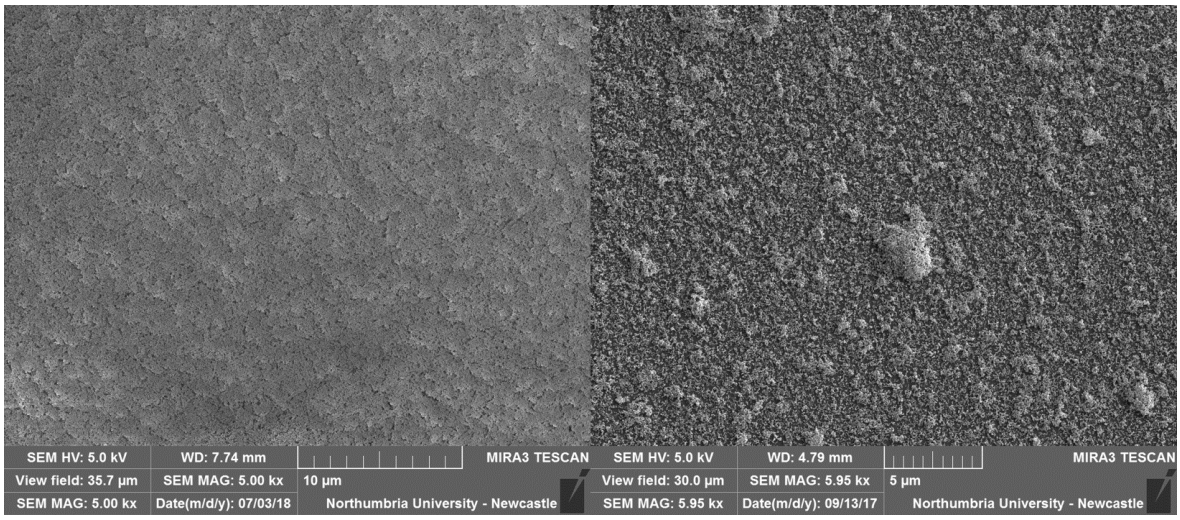

Figure 7.9.3: Comparison between top surface images of a) 5 times multiple coated surface and b) 34% single coating mixture sample.

The agglomerations and poorly dispersed particle structure indicated that the particles are being attracted to each other before reaching the surface boundary and therefore may require an improved mixing method.

7.10 Homogenisation

To obtain a better mixed solution, that would hopefully be stable for a longer period of time, one final mixing method, homogenisation, was tested. To do this, a standard batch of the single coating mixture (10 g of the 34% mixture) was weighed out into a large glass beaker. The mixing by either hand or sonication step was then replaced with mixing via homogenisation. The homogeniser (IKA Disperser T18) was operated at a rotational speed of 6000 rpm for a total of 2 minutes.

To test the stability of the solution 5 samples were made at different time intervals after homogenisation. Sample 1 was created at 0 minutes (time normally used for the single coating mixture), or just after the homogenisation had been completed. Sample 2 was created after a settling time of 10 minutes and Sample 3 after 20 minutes. Samples 4 and 5 were produced after settling times of 30 minutes and 1 hour. The samples were

each then left for the single coating setting time of 24 hours before any of the excess material was removed from the samples. At one hour after coating deposition, Sample 1 still had air bubbles generated by the homogenisation process present on the surface.

On first inspection each of the samples visually appear to be similar to those produced via the standard process. Placing a droplet by hand onto the samples and tilting the droplet gives a quick test of the surface's slipperiness. The droplet deposited onto Sample 1 remains stationary, indicating that there is an inherent stickiness to the surface and may not produce a SLIPS. When performing the same quick experiment on Samples 2 to 5 each of the droplets slide.

The sliding angle was again used as a characterisation measure of the surface's hysteresis. 5 DI droplets of volume 2 μl were placed onto each sample and the tilting table taken to a maximum angle of 10° (superhydrophobic criteria). On Sample 1 as was predicted none of the droplets moved. For Sample 2 there was clear movement from all 5 of the droplets sliding in the range of 0.5° to 2.3°, giving an average sliding angle of 1.40° ± 0.77°, which is only 0.49° above that seen for the 'best' coating but with a much smaller error (0.77° instead of 1.42°). Sample 3 performed even better than Sample 2, with most droplets moving on the surface without the tilt stage being moved and one droplet sliding at 0.2°, giving an average sliding angle of 0.05° ± 0.10°. One droplet however did encounter a pinning point on the surface (which was visible to the eye) with the droplet remaining stationary at a tilt angle of 10°, this droplet was taken as an anomalous point and was therefore not included in the subsequent data averaging. For Samples 4 and 5 the droplet acted in a similar manner to Sample 1 with the droplets remaining in a stationary position on the surface.

For a single coating surface to not exhibit SLIPS properties there is usually one of two things happening, either there are too few particles present on the surface to create a porous structure or there are agglomerations of particles creating pinning points. As on Sample 2 an agglomeration of particles could be seen visually, creating a significant pinning point, it can be assumed that it is agglomerations that are introducing a stickiness to the surface. By studying the SEM cross sections, the extent of the agglomerations can be measured. In Figure 7.10.1 there are two images of Sample 5. Figure

7.10.1 a is focused in on the edge of the sample with two clear agglomerations present on the surface surrounded by a fairly uniform layer of particles. The first, largest agglomeration is greater than 2 μm in height and 5 μm in length. In the background another two, larger agglomerations are visible. Focusing the beam at a distance of 0.03 mm from the edge these agglomerations come into focus (Figure 7.10.1 b), again, the agglomerations measured are greater than 5 μm and 2 μm in width and height and more particle agglomerations can be seen even further into the sample.

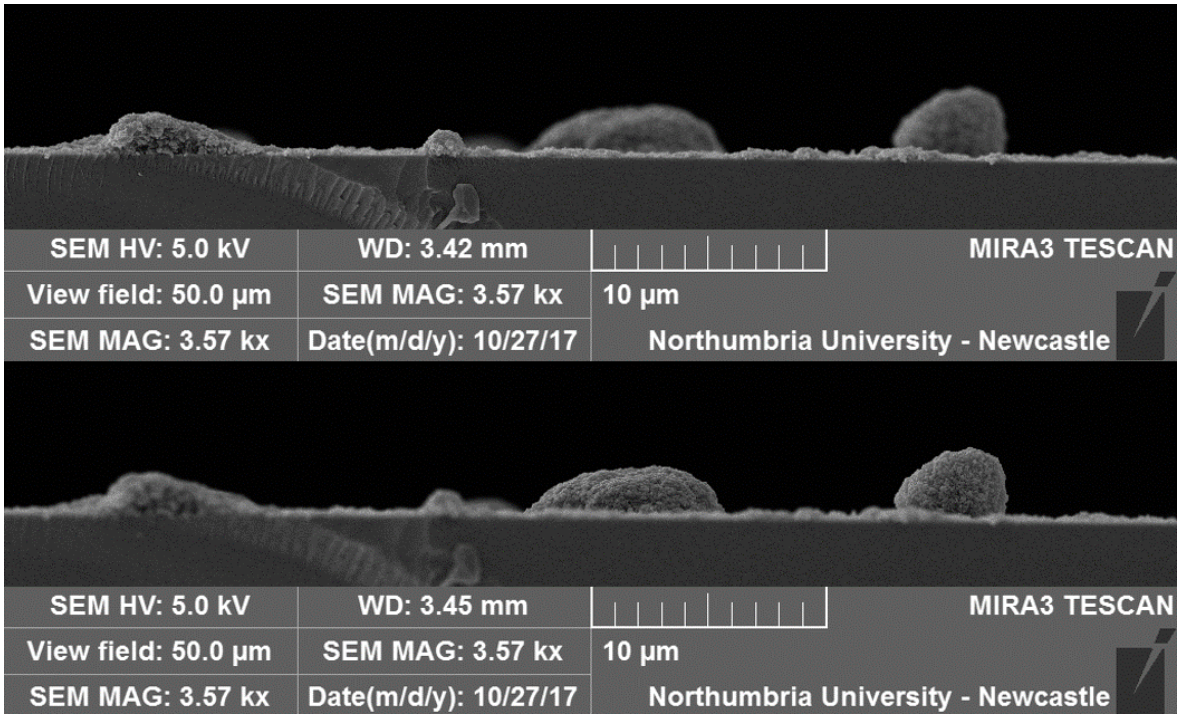

Figure 7.10.1: Cross sectional images of Sample 5 with a) the edge of the sample in focus and b) a cross sectional slice of the surface 0.03 mm in from the edge.

In addition to this, the homogenisation appears to have damaged the particles to some extent with the once well-defined spherical nanoparticles now appearing to be joined with its neighbours, losing the spherical shape that could be seen in Figures 7.9.1 and 7.9.2. Not only can the single particles not be distinguished from each other but they form large masses of particles that from the SEM cross sections (Figure 7.10.2) appear to have little porosity. The implication of this is the lifetime of the surface might be compromised, if the surface does not have a porous coating then the surface will not be able to retain the oil after extended use or storage time.

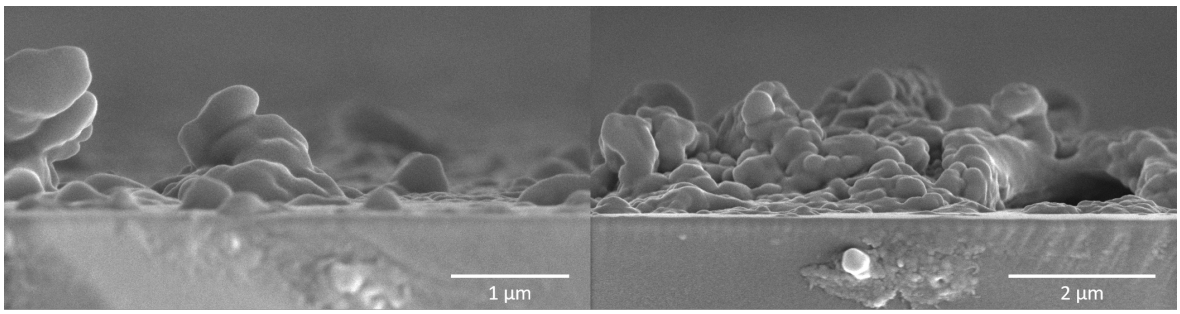

Figure 7.10.2: Damage to the nanoparticles, presumably cased by the homogenisation.

Consequently, despite the fact this mixing method produces an average sliding angle of 0.05° ± 0.10° the loss of porosity reduces the actual usability of the surface. Therefore, a compromise between the requirement of a low sliding angle and surface durability has to be made, hence the optimum mixture from Section 7.8 with the sonication mixing step is still the ideal coating, with the homogenisation mixing requiring further study.

7.11 Longevity Test

A coating lifetime test was carried out on 3 samples of 34% Glaco, 30 minutes sonication, compressed air excess oil removal (the optimum single coating solution). The samples were recharacterised as previously, via the sliding angle, 418 days after the samples were first produced and then a second test conducted 761 days after the production date. 5 DI water droplets of volume, 2 μl, were placed on to each sample giving an original averaged sliding angle of 2.6° ± 1.6°. The error on this value is much larger than would be expected (over 50% of the value itself) for a uniform coating meaning that there may be pinning points on the surface or the coating varies significantly between samples. Testing again at 418 days after production gave a higher sliding angle of 3.0° ± 0.6°, meaning a 0.4° difference, however this average value is still within the error of the original sliding angle. Repeating this test on the same set of samples, 761 days after production gives a sliding angle of 2.65° ± 0.31°, reducing the error by a further 50% (Figure 7.11.1).

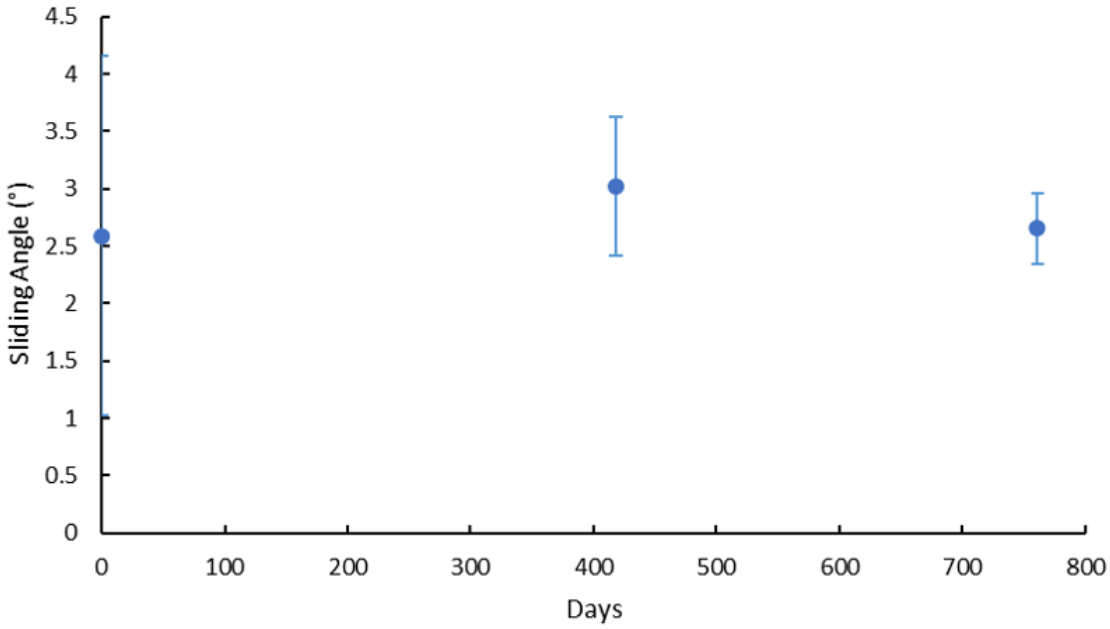

Figure 7.11.1: Evolution of the sliding angle and corresponding error measured on three samples as a function of days after original sample production date.

All of the above values are well within the SLIPS regime of siding angles $< 5.0°$. Furthermore, the final value of $2.65° \pm 0.31°$ is below that reported in McHale et al. 2019[41] ($3.40° \pm 0.20°$) for a conformal SLIPS coating fabricated using the method outlined in Chapter 3, Section 2. By simply comparing the two droplets side by side in Figure 7.11.2 it can be seen that the droplets form the same spherical cap shape but neither have a visible wetting ridge on the macro scale. By comparing the contact angles from conformal SLIPS (108.4°) to single coating (107.1°), there is only a 1.3° difference between the two figures, implying that sessile droplets have a similar interaction with each of the surfaces (Figure 7.11.2). The imperfections, such as dust, lumps of particles etc. are more visible on the single coating sample and would normally be attributed to surface pinning points, however with the single coating this appears to have very little effect on the overall surface performance.

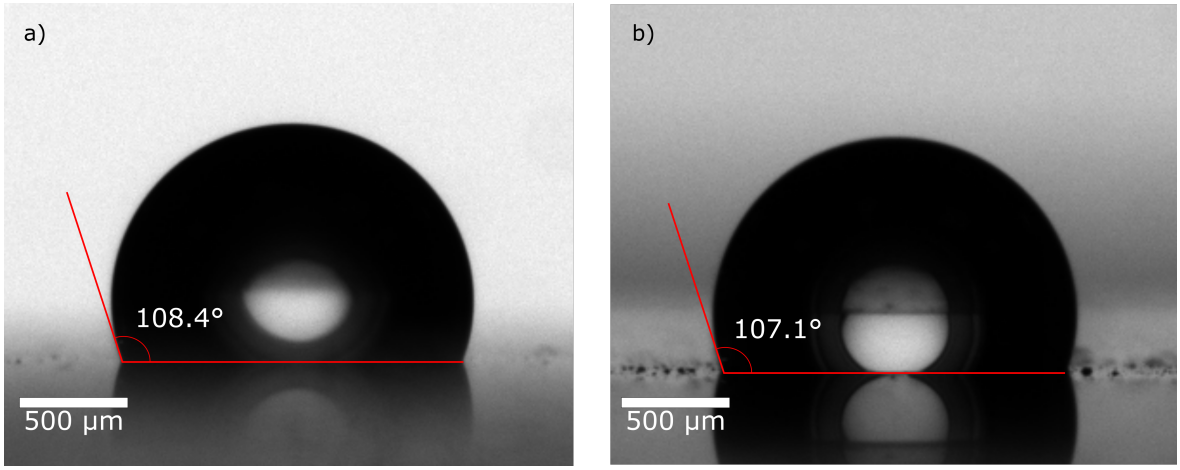

Figure 7.11.2: a) 2 μl droplet on conformal SLIPS, depicting the contact angle (taken from McHale et al. 2019). b) 2 μl droplet on single coating SLIPS, the red line shows the contact angle with the surface

7.12 Droplet Repeats

The single coating has been shown to exhibit remarkable longevity when not under continuous use (Section 7.11), however the durability of the surface also needs to be characterised before being able to say the coating would be applicable to many industrial applications. To do this, one sample of 34% single coating mixture (created using the optimum coating method) was placed onto the Krüss DSA30 and tilted to 1°. A 2 μl droplet was then placed onto the surface to slide down the sample, creating an oil depletion region behind it. A further five droplets were deposited in quick succession onto the same position, to travel down the same path as the previous droplets. After the 6th droplet the next droplet experiences pinning and will not slide. The sample was then tilted a further 1° and the same volume droplets placed onto the same deposition position. At an angle of 2° only two droplets managed to slide down the surface before pinning occurred. Again, the surface was tilted another 1° to take the angle to 3° and the experiment repeated. This time, all droplets remained stationary. At this point the surface was tilted back to a horizontal configuration and left for 5 minutes to allow for oil to reimbibe into the depleted section before again being tilted to 1°. Using the same deposition position a further five droplets were deposited onto and slid down the surface before pinning. The surface was again tilted back to its horizontal position and left for the same length of time. This full procedure was repeated five times, meaning

a total of 26 droplets slid down the surface at an angle of 1°.

7.13 Conclusion

From this series of experiments is has been possible to produce a reproducible, uniform SLIPS coating in a single step, exhibiting an average sliding angle below 1°. The actual process of particles structure formation is driven by advection rather than diffusion of the particles creating a thinner layer of nanoparticles than the multiple step spray coating method. This single coating method also has the potential for coating nonstandard samples, such as those with closed geometries due to the elimination of the need for an open area for the particles to be sprayed onto. When considering the potential for this coating to be used in industrial applications it has been shown that the coating itself will outlast many materials especially when considering the lifetime of biological substances. The coating will also withstand a number of droplets sliding down the same section of the surface without the requirement of silicone oil rejuvenation via a post process dipping procedure. There is still the potential to improve the coating, reducing the error on the sliding angle and creating a mixture that will remain stable for longer before sample production, possibly by investigating further the possibility of using homogenisation as the mixing method.

Chapter 8

Conclusion and Future Work

This thesis has explored how droplets interact with a solid substrate as well as a lubricating liquid layer. The experiments detailed in the results chapters have explored the ability to return droplet control to a very slippery surface as well as the ability of the surface itself to transport these droplets using no external energy input to the system, by utilising a very simple surface structure. Natural phenomena, such as evaporation, have been used to study more complex substrate topographies and how they influence droplet shaping and movement. The main experimental step that had to be overcome within this study was to produce coatings that had stable oil layer and nanoparticulate structure over both time and continuous use.

In the first experimental chapter, control has been returned to a highly mobile droplet on a slippery surface via the addition of a topographical structure to the flat substrate. The addition of this step creates a deformation in the imbibed liquid layer, similar to the deformations created by a droplet on the surface. The combination of these deformations is strong enough to produce a capillary force to retain a droplet in a stationary position on the step, given the right conditions, up to a tilting angle of 180°, holding the droplet upside down. The strength of this force is governed by the oil thickness, step height, tilting direction and initial position of the droplet. The force is only applicable in the direction normal to the step, not parallel (where the droplet will still slide at an angle $> 1°$), meaning that this form of SLIPS is bi-directional. By using the stationary point, a droplet could be held in place long enough to perform biological reactions before being removed with no contaminants left on the surface,

allowing the surface to be reused. The initial positioning effect could be exploited for droplet sorting, with the surface capable of maintaining two droplets on the surface until tilting to a threshold angle to remove just one of the droplets.

Using the pinning point again, but this time to transport the droplet, it has been shown that this simple structure is complex enough to induce both an attractive and repulsive force. The repulsive force, generated by a mismatch in surface deformation curvatures, is strong enough to transport the droplet over twice the droplet radius within the first 30 seconds on the surface, with the distance ultimately determined by the oil layer thickness. The region of the surface where the attractive regime should occur not only exhibits attractive behaviour but given the correct combination of conditions a repulsive force can also be seen in what is assumed to be a depletion region. The attractive regime has also been found to be time dependent. Areas that exhibit a repulsive interaction (within the depletion region) can be converted into attraction by simply leaving the droplet on the surface for a longer period of time before initialising the interaction. Both the attractive and repulsive movements of the droplets require no external force (such as gravity) to be inputted to the system to trigger any of the droplet interactions and in turn motion. Such surfaces could reasonably be used in applications such as inkjet printing where satellite droplets can cause printing errors. The satellite droplets on these surfaces could either be attracted to the area they were supposed to be deposited on or repelled to an area that would not subsequently be used.

Taking this idea further and creating more complex underlying topographies does not create a full pinning point as such, but instead produces a smooth surface capable of shaping a droplet. By increasing or decreasing the droplet volume and size (by condensation or evaporation) generates movement of the droplet which is purely governed by the underlying macro topography and not by surface pinning effects as the droplet maintains a constant contact angle with the surface. The macro structure governs what shape the droplet will adopt and as the droplet evaporates the size and shape of the droplet is highly predictable and reproducible. It is currently unknown whether the structures on the surface are creating positive/negative curvature deformations in the

liquid layer but this phenomenon my assist in the smooth droplet contact line motion through the surface troughs. Such surfaces are similar to the complex structures seen in nature, such as on a beetles back, which are used to gather liquid from water saturated vapour before transporting this, possibly for storage or drinking[79, 78]. Hence, these types of surface could be used for fog harvesting applications.

Microfluidic devices are commonly used with biological substances and therefore require a surface coating, such as SLIPS, that will inhibit contamination so the device can be used more than once as well as reducing the sample size required to perform chemical interactions. However, most microfluidic, lab-on-chip, cassettes are enclosed, meaning there is no open face onto which the nanoparticles could be sprayed (Chapter 3). Hence, the final experimental results chapter describes the procedure used to develop a now patented coating in a liquid form which could be followed through a device and applied in a single step. This coating achieves similar sliding angles to that seen with the multiple step coating method (Chapter 3) but with a more practical and universal coating method. The single coating will also remain stable for an extended storage time of over 2 years, producing a shelf life beyond many biological substances.

The work presented within this thesis could provide the preliminary work for further study of multiple droplet systems with particular focus on droplet control and prediction of how this system will interact not only with each other, but with the surface itself. It is expected that the experimental studies conducted in Chapters 4 and 5 could, in the future, be expanded to provide insight into the construction of future microfluidic devices. One main issue that is currently seen is that the channel structures inherently have corners which enhance liquid filling whilst also creating a point for any particles within a liquid to be trapped. Therefore, applying a SLIPS coating would appear to the logical step forward, however, as was seen with the stepped structure, a positive curvature next to the step or within the channel will attract the droplet more so that without any coating. Hence, the SLIPS coating will reduce the contamination but enhance the adhesion and corner filling. Thinking of this problem in another way, the best method to remove channel contamination is to remove the channel all together. Removing the channel would normally produce a flat substrate with no droplet con-

finement and hence very little droplet control. However, by inverting that channel and creating a large pillared structure (resembling the same path which the channel would have followed) and combining this with the repulsive force from the Cheerios effect (two negative curvatures should be produced on each edge of the macro topography) should create enough droplet confinement for a droplet to follow the path without coming into contact with the edges of the structure. This idea has been briefly explored as a proof of concept experiment in Figure 8.0.1.

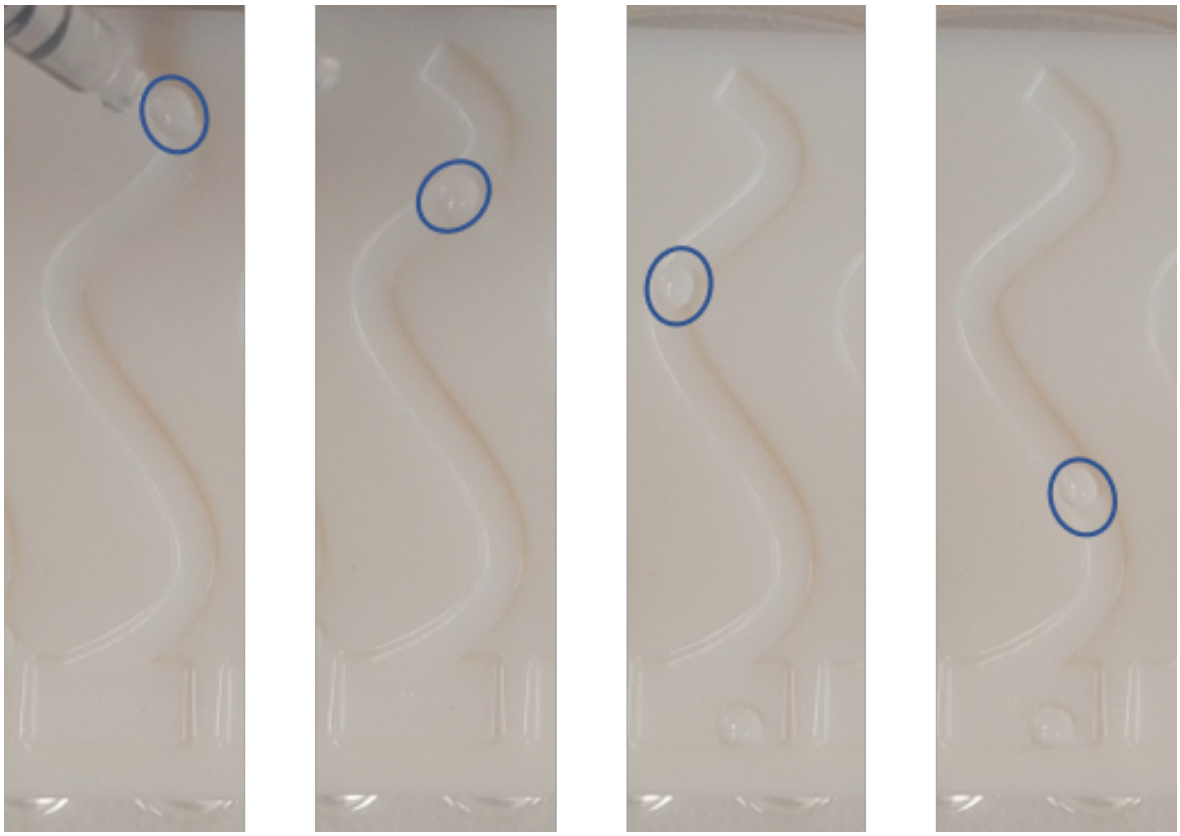

Figure 8.0.1: An image sequence showing the transportation of a droplet down a macro structured pillar placed at an approximate tilt angle of 10°.

Further investigation into this would provide additional insights and direction for future experimental set ups aimed at providing even more control to the droplets and accurate transport in more than one direction, with the Cheerios effect providing a unique opportunity to explore these further possibilities.

Bibliography

[1] C. Neinhuis and W. Barthlott. Characterization and distribution of water-repellent, self-cleaning plant surfaces. *Annals of Botany*, 79(6):667–677, 1997.

[2] Pierre-Gilles de Gennes, Françoise Brochard-Wyart, and David Quéré. *Capillarity and Wetting Phenomena*. Springer US, 2004.

[3] Alexander Otten and Stephan Herminghaus. How Plants Keep Dry: A Physicist's Point of View. *Langmuir*, 20(6):2405–2408, 2004.

[4] W Barthlott and C Neinhuis. Purity of the sacred lotus, or escape from contamination in biological surfaces. *Planta*, 202(1):1–8, 1997.

[5] Ulrike Bauer and Walter Federle. The insect-trapping rim of Nepenthes pitchers: surface structure and function. *Plant signaling & behavior*, 4(11):1019–1023, 2009.

[6] Holger F. Bohn and Walter Federle. Insect aquaplaning: Nepenthes pitcher plants capture prey with the peristome, a fully wettable water-lubricated anisotropic surface. *Proceedings of the National Academy of Sciences of the United States of America*, 101(39):14138–14143, 2004.

[7] Thomas Young. An essay on the cohesion of fluids. *Philosophical Transactions of the Royal Society of London*, pages 65–87, 1805.

[8] Pierre Simone de Laplace. Complete Works of Laplace: Volume 4. 4:1–548, 1805.

[9] Robert N Wenzel. Resistance of solid surfaces to wetting by water. *Industrial and Engineering Chemistry*, 28(8):988–994, 1936.

[10] Robert N Wenzel. Surface roughness and contact angle. *Journal of Physical & Colloid Chemistry*, 53(9):1466–1467, 1949.

[11] A B D Cassie and S Baxter. Wettability of porous surfaces. *Transactions of the Faraday Society*, 40(5):546–551, 1944.

[12] David Quéré. Non-sticking drops. *Reports on Progress in Physics*, 68(11):2495–2532, 2005.

[13] Tak-Sing Wong, Sung Hoon Kang, Sindy K Y Tang, Elizabeth J Smythe, Benjamin D Hatton, Alison Grinthal, and Joanna Aizenberg. Bioinspired self-repairing slippery surfaces with pressure-stable omniphobicity. *Nature*, 477(7365):443–447, 2011.

[14] A Lafuma and D Quéré. Slippery pre-suffused surfaces. *Epl*, 96(5), 2011.

[15] William D Harkins and Aaron Feldman. Films. The spreading of liquids and the spreading coefficient. *Journal of the American Chemical Society*, 44(12):2665–2685, 1922.

[16] A. B D Cassie. Contact angles. *Discussions of the Faraday Society*, 3:11–16, 1948.

[17] G. W.C. Kaye and T. H. Laby. *Tables of Physical and Chemical Constants*. 1995.

[18] Kock Yee Law. Definitions for hydrophilicity, hydrophobicity, and superhydrophobicity: Getting the basics right. *Journal of Physical Chemistry Letters*, 5(4):686–688, 2014.

[19] Lin Feng, Yanan Zhang, Jinming Xi, Ying Zhu, Nü Wang, Fan Xia, and Lei Jiang. Petal effect: A superhydrophobic state with high adhesive force. *Langmuir*, 24(8):4114–4119, 2008.

[20] Bharat Bhushan. Bioinspired structured surfaces. *Langmuir*, 28(3):1698–1714, 2012.

[21] Tak Sing Wong, Taolei Sun, Lin Feng, and Joanna Aizenberg. Interfacial materials with special wettability. *MRS Bulletin*, 38(5):366–371, 2013.

[22] Woo Lee, Mi Kyoung Jin, Won Cheol Yoo, and Jin Kyu Lee. Nanostructuring of a polymeric substrate with well-defined nanometer-scale topography and tailored surface wettability. *Langmuir*, 20(18):7665–7669, 2004.

[23] Taolei Sun, Lin Feng, Xuefeng Gao, and Lei Jiang. Bioinspired Surfaces with Special Wettability. *Accounts of Chemical Research*, 38(8):644–652, aug 2005.

[24] C W Extrand and Y Kumagai. Advancing and Receding Contant Angle of PTFE. *Journal of Colloid and Interface Science*, 191(191):378–383, 1997.

[25] Mingming Liu, Yuanyuan Hou, Jing Li, Lu Tie, and Zhiguang Guo. Transparent slippery liquid-infused nanoparticulate coatings. *Chemical Engineering Journal*, 337(December 2017):462–470, 2018.

[26] Neil J Shirtcliffe, Glen McHale, Shaun Atherton, and Michael I Newton. An introduction to superhydrophobicity. *Advances in Colloid and Interface Science*, 161(1-2):124–138, 2010.

[27] John T Simpson, Scott R Hunter, and Tolga Aytug. Superhydrophobic materials and coatings: A review. *Reports on Progress in Physics*, 78(8):86501, 2015.

[28] Yongjoo Kwon, Neelesh Patankar, Junkyu Choi, and Junghoon Lee. Design of surface hierarchy for extreme hydrophobicity. *Langmuir*, 25(11):6129–6136, 2009.

[29] Ferdinand Walther, Tanja Drobek, Alexander M. Gigler, Marc Hennemeyer, Michael Kaiser, Helmut Herberg, Tetsuji Shimitsu, Gregor E. Morfill, and Robert W. Stark. Surface hydrophilization of SU-8 by plasma and wet chemical processes. *Surface and Interface Analysis*, 42(12-13):1735–1744, 2010.

[30] Sung Jin Hwang, Dong Joon Oh, Phill Gu Jung, Sang Min Lee, Jeung Sang Go, Joon Ho Kim, Kyu Youn Hwang, and Jong Soo Ko. Dry etching of polydimethylsiloxane using microwave plasma. *Journal of Micromechanics and Microengineering*, 19(9), 2009.

[31] Harold F. Winters and J. W. Coburn. Surface science aspects of etching reactions. *Surface Science Reports*, 14(4-6):162–269, 1992.

[32] Neil J Shirtcliffe, Sanaa Aqil, Carl Evans, Glen McHale, Michael I Newton, Carole C Perry, and Paul Roach. The use of high aspect ratio photoresist (SU-8) for super-hydrophobic pattern prototyping. *Journal of Micromechanics and Microengineering*, 14(10):1384–1389, 2004.

[33] Vijay Kumar and Niti Nipun Sharma. Synthesis of hydrophilic to superhydrophobic SU8 surfaces. *Journal of Applied Polymer Science*, 132(18):1–10, 2015.

[34] Yinyong Li, Jacob John, Kristopher W Kolewe, Jessica D Schiffman, and Kenneth R Carter. Scaling Up Nature: Large Area Flexible Biomimetic Surfaces. *ACS Applied Materials and Interfaces*, 7(42):23439–23444, 2015.

[35] Lina Ejenstam, Agne Swerin, and Per M Claesson. Toward Superhydrophobic PolydimethylsiloxaneSilica Particle Coatings. *Journal of Dispersion Science and Technology*, 37(9):1375–1383, 2016.

[36] Junpeng Liu, Zaid Janjua, Martin Roe, Fang Xu, Barbara Turnbull, Kwing-So Choi, and Xianghui Hou. Super-Hydrophobic/Icephobic Coatings Based on Silica Nanoparticles Modified by Self-Assembled Monolayers. *Nanomaterials*, 6(12):232, 2016.

[37] Paul Roach, Neil J. Shirtcliffe, and Michael I. Newton. Progess in superhydrophobic surface development. *Soft Matter*, 4(2):224, 2008.

[38] T. Onda, S. Shibuichi, N. Satoh, and K. Tsujii. Super-water-repellent fractal surfaces. *Langmuir*, 12(9):5–7, 1996.

[39] Neil J. Shirtcliffe, Glen McHale, Michael I. Newton, Carole C. Perry, and Paul Roach. Porous materials show superhydrophobic to superhydrophilic switching. *Chemical Communications*, (25):3135–3137, 2005.

[40] G. McHale. All solids, including Teflon, are hydrophilic (to some extent), but some have roughness induced hydrophobic tendencies. *Langmuir*, 25(13):7185–7187, 2009.

[41] Glen McHale, Bethany V Orme, Gary George Wells, and Rodrigo Andres Ledesma-Aguilar. Apparent Contact Angles on Lubricant Impregnated Surfaces/SLIPS: From Superhydrophobicity to Electrowetting. *Langmuir*, 35:acs.langmuir.8b04136, 2019.

[42] ROBERT H. DETTRE and RULON E. JOHNSON. Contact Angle Hysteresis. *Advances in Chemistry*, pages 136–144, 1964.

[43] J F Joanny and P G De Gennes. A model for contact angle hysteresis. *The Journal of Chemical Physics*, 81(1):552–562, 1984.

[44] Lichao Gao and Thomas J. McCarthy. Contact angle hysteresis explained. *Langmuir*, 22(14):6234–6237, jul 2006.

[45] David Quéré. Wetting and Roughness. *Annual Review of Materials Research*, 38(1):71–99, 2008.

[46] H. B. Eral, D. J.C.M. 'T Mannetje, and J. M. Oh. Contact angle hysteresis: A review of fundamentals and applications. *Colloid and Polymer Science*, 291(2):247–260, 2013.

[47] Lichao Gao and Thomas J. McCarthy. How Wenzel and Cassie were wrong. *Langmuir*, 23(7):3762–3765, 2007.

[48] G. McHale. Cassie and Wenzel: Were they really so wrong? *Langmuir*, 23(15):8200–8205, 2007.

[49] D Bartolo, F Bouamrirene, É Verneuil, A Buguin, P Silberzan, and S Moulinet. Bouncing or sticky droplets: Impalement transitions on superhydrophobic micropatterned surfaces. *Europhysics Letters*, 74(2):299–305, 2006.

[50] Edward Bormashenko, Roman Pogreb, Gene Whyman, and Mordehai Erlich. Cassie-Wenzel wetting transition in vibrating drops deposited on rough surfaces: Is the dynamic Cassie-Wenzel wetting transition a 2D or 1D affair? *Langmuir*, 23(12):6501–6503, 2007.

[51] M. Reyssat, J. M. Yeomans, and D. Quéré. Impalement of fakir drops. *EPL (Europhysics Letters)*, 81(2):26006, jan 2008.

[52] Tao Deng, Kripa K Varanasi, Ming Hsu, Nitin Bhate, Chris Keimel, Judith Stein, and Margaret Blohm. Nonwetting of impinging droplets on textured surfaces. *Applied Physics Letters*, 94(13):13–16, 2009.

[53] Periklis Papadopoulos, Lena Mammen, Xu Deng, Doris Vollmer, and Hans-Jürgen Butt. How superhydrophobicity breaks down. *Proceedings of the National Academy of Sciences*, 110(9):3254–3258, 2013.

[54] J.F Oliver, Chun Huh, and S.G Mason. Resistance to spreading of liquids by sharp edges. *Journal of Colloid and Interface Science*, 59(3):568–581, may 1977.

[55] José Bico, Uwe Thiele, and David Quéré. Wetting of textured surfaces. *Colloids and Surfaces A: Physicochemical and Engineering Aspects*, 206(1-3):41–46, 2002.

[56] C Ishino, M Reyssat, E Reyssat, K Okumura, and D Quéré. Wicking within forests of micropillars. *Epl*, 79(5), 2007.

[57] Jiaqian Li, Xiaofeng Zhou, Jing Li, Lufeng Che, Jun Yao, Glen McHale, Manoj K Chaudhury, and Zuankai Wang. Topological liquid diode. *Science Advances*, 3(10):19–25, 2017.

[58] Daoai Wang, Xiaolong Wang, Xinjie Liu, and Feng Zhou. Engineering a titanium surface with controllable oleophobicity and switchable oil adhesion. *Journal of Physical Chemistry C*, 114(21):9938–9944, 2010.

[59] Michael Nosonovsky. Slippery when wetted. *Nature*, 477(7365):412–413, sep 2011.

[60] Arun K Kota, Yongxin Li, Joseph M Mabry, and Anish Tuteja. Hierarchically structured superoleophobic surfaces with ultralow contact angle hysteresis. *Advanced Materials*, 24(43):5838–5843, 2012.

[61] Mordechai Sokuler, Günter K. Auernhammer, Marcel Roth, Chuanjun Liu, Elmar Bonacurrso, and Hans Jürgen Butt. The softer the better: Fast condensation on soft surfaces. *Langmuir*, 26(3):1544–1547, 2010.

[62] Stefan Karpitschka, Anupam Pandey, Luuk A Lubbers, Joost H Weijs, Lorenzo Botto, Siddhartha Das, Bruno Andreotti, and Jacco H Snoeijer. Liquid drops attract or repel by the inverted Cheerios effect. *Proceedings of the National Academy of Sciences*, 113(27):7403–7407, 2016.

[63] Akshay Phadnis and Konrad Rykaczewski. Dropwise Condensation on Soft Hydrophobic Coatings. *Langmuir*, 33(43):12095–12101, 2017.

[64] Robert W. Style and Eric R. Dufresne. Static wetting on deformable substrates, from liquids to soft solids. *Soft Matter*, 8(27):7177–7184, 2012.

[65] José Bico, Étienne Reyssat, and Benoît Roman. Elastocapillarity: When Surface Tension Deforms Elastic Solids. *Annual Review of Fluid Mechanics*, 50(1):629–659, 2018.

[66] Antonin Marchand, Siddhartha Das, Jacco H. Snoeijer, and Bruno Andreotti. Contact angles on a soft solid: From young's law to neumann's law. *Physical Review Letters*, 109(23), 2012.

[67] Jian H Guan, Gary G Wells, Ben Xu, Glen McHale, David Wood, James Martin, and Simone Stuart-Cole. Evaporation of Sessile Droplets on Slippery Liquid-Infused Porous Surfaces (SLIPS). *Langmuir*, 31(43):11781–11789, 2015.

[68] Ciro Semprebon, Glen McHale, and Halim Kusumaatmaja. Apparent contact angle and contact angle hysteresis on liquid infused surfaces. *Soft Matter*, 13(1):101–110, 2017.

[69] Frank Schellenberger, Jing Xie, Noemí Encinas, Alexandre Hardy, Markus Klapper, Periklis Papadopoulos, Hans Jürgen Butt, and Doris Vollmer. Direct observation of drops on slippery lubricant-infused surfaces. *Soft Matter*, 11(38):7617–7626, 2015.

[70] Martin Villegas, Yuxi Zhang, Noor Abu Jarad, Leyla Soleymani, and Tohid F. Didar. Liquid-Infused Surfaces: A Review of Theory, Design, and Applications. *ACS Nano*, 13(8):8517–8536, 2019.

[71] J David Smith, Rajeev Dhiman, Sushant Anand, Ernesto Reza-Garduno, Robert E Cohen, Gareth H McKinley, and Kripa K Varanasi. Droplet mobility on lubricant-impregnated surfaces. *Soft Matter*, 9(6):1772–1780, 2013.

[72] Dan Daniel, Jaakko V I Timonen, Ruoping Li, Seneca J Velling, and Joanna Aizenberg. Oleoplaning droplets on lubricated surfaces. *Nature Physics*, 13(10):1020–1025, 2017.

[73] Jacopo Seiwert, Christophe Clanet, and David Quéré. Coating of a textured solid. *Journal of Fluid Mechanics*, 669:55–63, 2011.

[74] Robert D Deegan, Olgica Bakajin, Todd F Dupont, Greg Huber, Sidney R Nagel, and Thomas A Witten. Capillary flow as the cause of ring stains from dried liquid drops. *Nature*, 389(6653):827–829, 1997.

[75] Ronald G. Larson. Transport and deposition patterns in drying sessile droplets. *AIChE Journal*, 60(5):1538–1571, may 2014.

[76] Madhusudan Singh, Hanna M. Haverinen, Parul Dhagat, and Ghassan E. Jabbour. Inkjet printing-process and its applications. *Advanced Materials*, 22(6):673–685, 2010.

[77] George M Whitesides and Bartosz Grzybowski. Self-assembly at all scales. *Science*, 295(5564):2418–2421, 2002.

[78] Kyoo Chul Park, Philseok Kim, Alison Grinthal, Neil He, David Fox, James C Weaver, and Joanna Aizenberg. Condensation on slippery asymmetric bumps. *Nature*, 531(7592):78–82, 2016.

[79] Andrew R. Parker and Chris R. Lawrence. Water capture by a desert beetle. *Nature*, 414(6859):33–34, nov 2001.

[80] Sushant Anand, Konrad Rykaczewski, Srinivas Bengaluru Subramanyam, Daniel Beysens, and Kripa K. Varanasi. How droplets nucleate and grow on liquids and liquid impregnated surfaces. *Soft Matter*, 11(1):69–80, 2015.

[81] X. Q. Wang, C. D. Gu, L. Y. Wang, J. L. Zhang, and J. P. Tu. Ionic liquids-infused slippery surfaces for condensation and hot water repellency. *Chemical Engineering Journal*, 343(March):561–571, 2018.

[82] Hu Luo, Yao Lu, Shaohui Yin, Shuai Huang, Jinlong Song, Faze Chen, Fengjun Chen, Claire J. Carmalt, and Ivan P. Parkin. Robust platform for water harvesting and directional transport. *Journal of Materials Chemistry A*, 6(14):5635–5643, 2018.

[83] Philseok Kim, Tak-sing Wong, Jack Alvarenga, Michael J Kreder, Wilmer E Adorno-martinez, and K I M E T Al. Liquid-infused-nanostructured-surfaces-with-extreme-anti-ice-and-anti-frost-performance_2012_ACS-Nano.pdf. (8):6569–6577, 2012.

[84] Songnan Zhang, Jianying Huang, Yan Cheng, Hui Yang, Zhong Chen, and Yuekun Lai. Bioinspired Surfaces with Superwettability for Anti-Icing and Ice-Phobic Application: Concept, Mechanism, and Design. *Small*, 13(48):1–20, 2017.

[85] James A. Callow and Maureen E. Callow. Trends in the development of environmentally friendly fouling-resistant marine coatings. *Nature Communications*, 2(1), 2011.

[86] Andrew J Scardino and Rocky de Nys. Mini review: Biomimetic models and bioinspired surfaces for fouling control. *Biofouling*, 27(1):73–86, 2011.

[87] Brian R Solomon, Karim S Khalil, and Kripa K Varanasi. La5021143. 2014.

[88] A. K. Epstein, T.-S. Wong, R. A. Belisle, E. M. Boggs, and J. Aizenberg. Liquid-infused structured surfaces with exceptional anti-biofouling performance. *Proceedings of the National Academy of Sciences*, 109(33):13182–13187, aug 2012.

[89] Caitlin Howell, Alison Grinthal, Steffi Sunny, Michael Aizenberg, and Joanna Aizenberg. Designing Liquid-Infused Surfaces for Medical Applications: A Review. *Advanced Materials*, 30(50):1–26, 2018.

[90] Wenqing He, Peng Liu, Jianqiang Zhang, and Xi Yao. Emerging Applications of Bioinspired Slippery Surfaces in Biomedical Fields. *Chemistry - A European Journal*, 24(56):14864–14877, 2018.

[91] Nico Keller, Julia Bruchmann, Thomas Sollich, Christiane Richter, Richard Thelen, Frederik Kotz, Thomas Schwartz, Dorothea Helmer, and Bastian E. Rapp. Study of Biofilm Growth on Slippery Liquid-Infused Porous Surfaces Made from Fluoropor. *ACS Applied Materials and Interfaces*, 11(4):4480–4487, 2019.

[92] Junsheng Li, Erica Ueda, Dorothea Paulssen, and Pavel A. Levkin. Slippery Lubricant-Infused Surfaces: Properties and Emerging Applications. *Advanced Functional Materials*, 29(4):1–13, 2019.

[93] Cameron S Ware, Truis Smith-Palmer, Sam Peppou-Chapman, Liam R J Scarratt, Erin M Humphries, Daniel Balzer, and Chiara Neto. Marine Antifouling Behavior of Lubricant-Infused Nanowrinkled Polymeric Surfaces. *ACS Applied Materials and Interfaces*, 10(4):4173–4182, 2018.

[94] Nancy R Sottos and Chuck Extrand. B ioinspired Materials for Self-Cleaning and Self-Healing Self-Cleaning Surfaces. *MRS Bulletin*, 33(August):732–741, 2008.

[95] Shunsuke Nishimoto and Bharat Bhushan. Bioinspired self-cleaning surfaces with superhydrophobicity, superoleophobicity, and superhydrophilicity. *RSC Advances*, 3(3):671–690, 2013.

[96] Gary G Wells, Élfego Ruiz-Gutiérrez, Youen Le Lirzin, Anthony Nourry, Bethany V Orme, Marc Pradas, and Rodrigo Ledesma-Aguilar. Snap evaporation of droplets on smooth topographies. *Nature Communications*, 9(1):1–7, 2018.

[97] Zuzana Brabcova, Glen McHale, Gary G. Wells, Carl V. Brown, and Michael I. Newton. Electric field induced reversible spreading of droplets into films on lubricant impregnated surfaces. *Applied Physics Letters*, 110(12):121603, 2017.

[98] Longquan Chen, Andreas Geissler, Elmar Bonaccurso, and Kai Zhang. Transparent slippery surfaces made with sustainable porous cellulose lauroyl ester films. *ACS Applied Materials and Interfaces*, 6(9):6969–6976, 2014.

[99] F. Brochard. Motions of Droplets on Solid Surfaces Induced by Chemical or Thermal Gradients. *Langmuir*, 5(2):432–438, 1989.

[100] J. B. Brzoska, F. Brochard-Wyart, and F. Rondelez. Motions of Droplets on Hydrophobic Model Surfaces Induced by Thermal Gradients. *Langmuir*, 9(8):2220–2224, 1993.

[101] Vincent Miralles, Axel Huerre, Hannah Williams, Bastien Fournié, and Marie Caroline Jullien. A versatile technology for droplet-based microfluidics: Thermomechanical actuation. *Lab on a Chip*, 15(9):2133–2139, 2015.

[102] R. Shankar Subramanian, Nadjoua Moumen, and John B. McLaughlin. Motion of a drop on a solid surface due to a wettability gradient. *Langmuir*, 21(25):11844–11849, 2005.

[103] Sandra C. Hernández, Charlee J.C. Bennett, Chad E. Junkermeier, Stanislav D. Tsoi, Francisco J. Bezares, Rory Stine, Jeremy T. Robinson, Evgeniya H. Lock, David R. Boris, Brian D. Pate, Joshua D. Caldwell, Thomas L. Reinecke, Paul E. Sheehan, and Scott G. Walton. Chemical gradients on graphene to drive droplet motion. *ACS Nano*, 7(6):4746–4755, 2013.

[104] M. Reyssat, F. Pardo, and D. Quéré. Drops onto gradients of texture. *EPL (Europhysics Letters)*, 87(3):36003, aug 2009.

[105] Nikolaos T. Chamakos, George Karapetsas, and Athanasios G. Papathanasiou. How asymmetric surfaces induce directional droplet motion. *Colloids and Surfaces A: Physicochemical and Engineering Aspects*, 511:180–189, 2016.

[106] Dan Soto, Guillaume Lagubeau, Christophe Clanet, and David Quéré. Surfing on a herringbone. *Physical Review Fluids*, 1(1):1–10, 2016.

[107] M. G. Pollack, A. D. Shenderov, and R. B. Fair. Electrowetting-based actuation of droplets for integrated microfluidics. *Lab on a Chip*, 2(2):96–101, 2002.

[108] Zubin Wang, Liping Heng, and Lei Jiang. Effect of lubricant viscosity on the self-healing properties and electrically driven sliding of droplets on anisotropic slippery surfaces. *Journal of Materials Chemistry A*, 6(8):3414–3421, 2018.

[109] Daniel P. Regan and Caitlin Howell. Droplet manipulation with bioinspired liquid-infused surfaces: A review of recent progress and potential for integrated detection. *Current Opinion in Colloid and Interface Science*, 39:137–147, 2019.

[110] Saheli Biswas, Yves Pomeau, and Manoj K. Chaudhury. New Drop Fluidics Enabled by Magnetic-Field-Mediated Elastocapillary Transduction. *Langmuir*, 32(27):6860–6870, 2016.

[111] Pengda Che, Liping Heng, and Lei Jiang. Lubricant-Infused Anisotropic Porous Surface Design of Reduced Graphene Oxide Toward Electrically Driven Smart Control of Conductive Droplets' Motion. *Advanced Functional Materials*, 27(22):1–9, 2017.

[112] Biyu Jin, Mingzhu Liu, Qinghua Zhang, Xiaoli Zhan, and Fengqiu Chen. Silicone Oil Swelling Slippery Surfaces Based on Mussel-Inspired Magnetic Nanoparticles with Multiple Self-Healing Mechanisms. *Langmuir*, 33(39):10340–10350, 2017.

[113] Wendong Wang, Jaakko V.I. Timonen, Andreas Carlson, Dirk Michael Drotlef, Cathy T. Zhang, Stefan Kolle, Alison Grinthal, Tak Sing Wong, Benjamin Hatton, Sung Hoon Kang, Stephen Kennedy, Joshua Chi, Robert Thomas Blough, Metin Sitti, L. Mahadevan, and Joanna Aizenberg. Multifunctional ferrofluid-infused surfaces with reconfigurable multiscale topography. *Nature*, 559(7712):77–82, 2018.

[114] Uttam Manna and David M Lynn. Fabrication of liquid-infused surfaces using reactive polymer multilayers: Principles for manipulating the behaviors and

mobilities of aqueous fluids on slippery liquid interfaces. *Advanced Materials*, 27(19):3007–3012, 2015.

[115] Jian Hui Guan, Élfego Ruiz-Gutiérrez, Ben Bin Xu, David Wood, Glen McHale, Rodrigo Ledesma-Aguilar, and Gary George Wells. Drop transport and positioning on lubricant-impregnated surfaces. *Soft Matter*, 13(18):3404–3410, 2017.

[116] Élfego Ruiz-Gutiérrez, Jian H. Guan, Ben Xu, Glen McHale, Gary G. Wells, and Rodrigo Ledesma-Aguilar. Energy Invariance in Capillary Systems. *Physical Review Letters*, 118(21):1–12, 2017.

[117] By Lili Wang, Liping Heng, and Lei Jiang. Temperature-Responsive Anisotropic Slippery Surface for Smart Control of the Droplet Motion. *ACS Applied Materials and Interfaces*, 10(8):7442–7450, 2018.

[118] Finn Box, Chris Thorogood, and Jian Hui Guan. Guided droplet transport on synthetic slippery surfaces inspired by a pitcher plant. *Journal of The Royal Society Interface*, 16(158):20190323, 2019.

[119] Kuan Kai Tseng, Wei Hao Lu, Chih Wei Han, and Yu Min Yang. Highly-transparent slippery liquid-infused porous surfaces made with silica nanoparticulate thin films. *Thin Solid Films*, 653(March):67–72, 2018.

[120] N. R. Geraldi, J. H. Guan, G. McHale, Y. Q. Fu, G. G. Wells, and J. T. Luo. Slippery Liquid-Infused Porous Surfaces and Droplet Transportation by Surface Acoustic Waves. *Physical Review Applied*, 7(1), 2017.

[121] Nicasio R Geraldi, Jian H Guan, Linzi E Dodd, Pietro Maiello, Ben B Xu, David Wood, Michael I Newton, Gary G Wells, and Glen Mchale. Double-sided slippery liquid- infused porous materials using conformable mesh. *Scientific Reports*, pages 1–8, 2019.

[122] G McHale, N J Shirtcliffe, and M I Newton. Contact-angle hysteresis on superhydrophobic surfaces. *Langmuir*, 20(23):10146–10149, 2004.

[123] C. G.L. Furmidge. Studies at phase interfaces. I. The sliding of liquid drops on solid surfaces and a theory for spray retention. *Journal of Colloid Science*, 17(4):309–324, 1962.

[124] David Quéré, Marie José Azzopardi, and Laurent Delattre. Drops at rest on a tilted plane. *Langmuir*, 14(8):2213–2216, 1998.

[125] L. Landau and B. Levich. Dragging of a Liquid by a Moving Plate. *Acta Physicochim. URSS*, 17:42, 1942.

[126] Boris Vladimirovitch Derjaguin. Thickness of liquid layer adhering to walls of vessels on their emptying and theory of photo and motion picture film coating. *Comptes Rendus De L'Académie Des Sciences De L'URSS*, 39:13–16, 1943.

[127] Arun G Banpurkar, Kevin P Nichols, and Frieder Mugele. Electrowetting-based microdrop tensiometer. *Langmuir*, 24(19):10549–10551, 2008.

[128] Martin Tress, Stefan Karpitschka, Periklis Papadopoulos, Jacco H Snoeijer, Doris Vollmer, and Hans Jürgen Butt. Shape of a sessile drop on a flat surface covered with a liquid film. *Soft Matter*, 13(20):3760–3767, 2017.

[129] Antonin Marchand, Siddhartha Das, Jacco H. Snoeijer, and Bruno Andreotti. Capillary pressure and contact line force on a soft solid. *Physical Review Letters*, 108(9):1–5, 2012.

[130] Bethany Orme, Glen McHale, Rodrigo Andres Ledesma-Aguilar, and Gary George Wells. Droplet Retention and Shedding on Slippery Substrates. *Langmuir*, 35:9146–9151, 2019.

[131] Matthew J Hancock, Koray Sekeroglu, and Melik C Demirel. Bioinspired directional surfaces for adhesion, wetting, and transport. *Advanced Functional Materials*, 22(11):2223–2234, 2012.

[132] Dominic Vella and L Mahadevan. The 'Cheerios effect'. *American Journal of Physics*, 73(9):817–825, 2004.

[133] Xuefeng Gao and Lei Jiang. Water-repellent legs of water striders. *Nature*, 432(7013):36, 2004.

[134] David L. Hu and John W.M. Bush. Meniscus-climbing insects. *Nature*, 437(7059):733–736, 2005.

[135] Yu En Liang, Inggit Kresna Maharsih, Yu Jane Sheng, and Heng Kwong Tsao. Capillary interactions between droplets and ideal roughness: Attractive protrusion and repulsive trench. *Experimental Thermal and Fluid Science*, 105(March):216–222, 2019.

[136] M A Hack, M Costalonga, T Segers, S Karpitschka, H Wijshoff, and J H Snoeijer. Printing wet-on-wet: Attraction and repulsion of drops on a viscous film. *Applied Physics Letters*, 113(18), 2018.

[137] S. Karpitschka, S. Das, M. Van Gorcum, H. Perrin, B. Andreotti, and J. H. Snoeijer. Droplets move over viscoelastic substrates by surfing a ridge. *Nature Communications*, 6:1–7, 2015.

[138] Patricia B. Weisensee, Yunbo Wang, Hongliang Qiang, Daniel Schultz, William P. King, and Nenad Miljkovic. Condensate droplet size distribution on lubricant-infused surfaces. *International Journal of Heat and Mass Transfer*, 109:187–199, 2017.

[139] Philseok Kim, Michael J Kreder, Jack Alvarenga, and Joanna Aizenberg. Hierarchical or not? Effect of the length scale and hierarchy of the surface roughness on omniphobicity of lubricant-infused substrates. *Nano Letters*, 13(4):1793–1799, 2013.

[140] R G Picknett and R Bexon. The Evaporation of Sessile or Pendant Drops in Still Air. 1977.

[141] H. Yildirim Erbil. Evaporation of pure liquid sessile and spherical suspended drops: A review. *Advances in Colloid and Interface Science*, 170(1-2):67–86, 2012.

[142] D. Brutin and V. Starov. Recent advances in droplet wetting and evaporation. *Chemical Society Reviews*, 47(2):558–585, 2018.

[143] G. McHale, S. Aqil, N. J. Shirtcliffe, M. I. Newton, and H. Y. Erbil. Analysis of droplet evaporation on a superhydrophobic surface. *Langmuir*, 21(24):11053–11060, 2005.

[144] Martin E.R. Shanahan. Simple Theory of "Stick-Slip" Wetting Hysteresis. *Langmuir*, 11(3):1041–1043, 1995.

[145] H Yildirim Erbil, G McHale, and M I Newton. Drop evaporation on solid surfaces: Constant contact angle mode. *Langmuir*, 18(7):2636–2641, 2002.

[146] Tugba Ozturk and H Yildirim Erbil. Evaporation of water-ethanol binary sessile drop on fluoropolymer surfaces: Influence of relative humidity. *Colloids and Surfaces A: Physicochemical and Engineering Aspects*, 553(May):327–336, 2018.

[147] Liming Wang and Thomas J McCarthy. Covalently Attached Liquids: Instant Omniphobic Surfaces with Unprecedented Repellency. *Angewandte Chemie - International Edition*, 55(1):244–248, 2016.

[148] Steven Armstrong, Glen McHale, Rodrigo Ledesma-Aguilar, and Gary G Wells. Pinning-Free Evaporation of Sessile Droplets of Water from Solid Surfaces. *Langmuir*, 35(8):2989–2996, 2019.

[149] Sam Peppou-Chapman and Chiara Neto. Mapping Depletion of Lubricant Films on Antibiofouling Wrinkled Slippery Surfaces. *ACS Applied Materials and Interfaces*, 10(39):33669–33677, 2018.

[150] Pritam Kumar Roy, Reeta Pant, Arun Kumar Nagarajan, and Krishnacharya Khare. Mechanically Tunable Slippery Behavior on Soft Poly(dimethylsiloxane)-Based Anisotropic Wrinkles Infused with Lubricating Fluid. *Langmuir*, 32(23):5738–5743, 2016.

[151] Peter J Yunker, Tim Still, Matthew A Lohr, and A G Yodh. Suppression of the coffee-ring effect by shape-dependent capillary interactions. *Nature*, 476(7360):308–311, 2011.

[152] Shiquan Ling, Yong Luo, Lin Luan, Zhiwei Wang, and Tianzhun Wu. Inkjet printing of patterned ultra-slippery surfaces for planar droplet manipulation. *Sensors and Actuators, B: Chemical*, 235:732–738, 2016.

[153] Xu Hou, Jianyu Li, Alexander B Tesler, Yuxing Yao, Miao Wang, Lingli Min, Zhizhi Sheng, and Joanna Aizenberg. Dynamic air/liquid pockets for guiding microscale flow. *Nature Communications*, 9(1):1–7, 2018.

[154] Ned Bowden, Francisco Arias, Tao Deng, and George M Whitesides. Self-assembly of microscale objects at a liquid/liquid interface through lateral capillary forces. *Langmuir*, 17(5):1757–1765, 2001.

[155] Yizhi Zhuo, Feng Wang, Senbo Xiao, Jianying He, and Zhiliang Zhang. One-Step Fabrication of Bioinspired Lubricant-Regenerable Icephobic Slippery Liquid-Infused Porous Surfaces. *ACS Omega*, 3(8):10139–10144, 2018.

[156] Alexander F Routh and William B Zimmerman. Distribution of particles during solvent evaporation from films. *Chemical Engineering Science*, 59(14):2961–2968, 2004.

[157] Stergios G Yiantsios and Brian G Higgins. Marangoni flows during drying of colloidal films. *Physics of Fluids*, 18(8), 2006.

[158] Reinhard Vehring, Willard R Foss, and David Lechuga-Ballesteros. Particle formation in spray drying. *Journal of Aerosol Science*, 38(7):728–746, 2007.

[159] Ervina Widjaja and Michael T Harris. Particle deposition study during sessile drop evaporation. *AIChE Journal*, 54(9):2250–2260, sep 2008.

[160] Christine M Cardinal, Yoon Dong Jung, Kyung Hyun Ahn, and L F Francis. Drying regime maps for particulate coatings. *AIChE Journal*, 56(11):2769–2780, nov 2010.

Published Work

1. Gary G Wells, Elfego Ruiz-Gutierrez, Youen Le Lirzin, Anthony Noury, Bethany V Orme, Marc Pradas and Rodrigo Ledesma-Aguilar. Snap Evaporation of Droplets on Smooth Topographies. *Nature Communications*, 9(1):1-7, 2018.

2. Glen McHale, Bethany V Orme, Gary G Wells and Rodrigo Ledesma-Aguilar. Apparent Contact Angles on Lubricant Impregnated Surfaces/SLIPS: From Superhydrophobicity to Electrowetting. *Langmuir*, 35:4197-4204, 2019.

3. Bethany V Orme, Glen McHale, Rodrigo Ledesma-Aguilar and Gary G Wells. Droplet Retention and Shedding on Slippery Substrates, *Langmuir*, 35:91464-9151, 2019.

nature COMMUNICATIONS

ARTICLE

DOI: 10.1038/s41467-018-03840-6 OPEN

Snap evaporation of droplets on smooth topographies

Gary G. Wells[1], Élfego Ruiz-Gutiérrez[1], Youen Le Lirzin[1,2], Anthony Nourry[1,2], Bethany V. Orme[1], Marc Pradas[3] & Rodrigo Ledesma-Aguilar[1]

Droplet evaporation on solid surfaces is important in many applications including printing, micro-patterning and cooling. While seemingly simple, the configuration of evaporating droplets on solids is difficult to predict and control. This is because evaporation typically proceeds as a "stick-slip" sequence—a combination of pinning and de-pinning events dominated by static friction or "pinning", caused by microscopic surface roughness. Here we show how smooth, pinning-free, solid surfaces of non-planar topography promote a different process called snap evaporation. During snap evaporation a droplet follows a reproducible sequence of configurations, consisting of a quasi-static phase-change controlled by mass diffusion interrupted by out-of-equilibrium snaps. Snaps are triggered by bifurcations of the equilibrium droplet shape mediated by the underlying non-planar solid. Because the evolution of droplets during snap evaporation is controlled by a smooth topography, and not by surface roughness, our ideas can inspire programmable surfaces that manage liquids in heat- and mass-transfer applications.

[1] Smart Materials & Surfaces Laboratory, Faculty of Engineering and Environment, Northumbria University, Ellison Place, Newcastle upon, Tyne NE1 8ST, UK. [2] Institut Universitaire de Technologie de Lannion, Rue Édouard Branly, 22300 Lannion, France. [3] School of Mathematics and Statistics, The Open University, Milton, Keynes MK7 6AA, UK. These authors contributed equally: Gary G. Wells, Élfego Ruiz-Gutiérrez. Correspondence and requests for materials should be addressed to R.L.-A. (email: rodrigo.ledesma@northumbria.ac.uk)

The configuration of evaporating droplets on a solid topography—e.g., their shape and location—is important for a broad range of applications. For example, in microcontact printing (a soft-lithography etching technique), an "ink" made of a polymer-solvent mixture is applied to a surface of designed topography and allowed to evaporate; the dry polymer residue is then printed onto a target surface, leaving a negative pattern of the original topography that can be used to replicate structures en masse from a single master template[1]. In immersion lithography (a widely used technique for integrated circuits manufacturing), a liquid water bridge is used to increase the precision of a UV light source for curing a target resin; an undesired side effect is the formation of droplets on the cured resin, which, upon evaporation, leave "water marks" that can spoil pattern features[2]. Spatio-temporal control of evaporating liquids is also attractive, as in edge lithography, where an ink droplet is left to evaporate on a hydrophobic patch; here, the low surface energy of the patch induces a transient dewetting process, which guides the ink residue to form edge patterns[3]. Finally, droplet evaporation is very important in heat-transfer applications[4]. For instance, a recently reported jumping-drop technique exploits super-hydrophic surfaces to induce the motion of evaporating-condensing droplets for "hotspot cooling", and is a promising heat-management technique in microelectronics[5]. These applications, however, depend on the control over the position and shape of the liquid, and this is often limited by solid–liquid–gas interactions occurring at the droplet's edge.

Since it was first proposed by Picknett and Bexon in the 1970s[6], the so-called stick-slip model has remained a canonical framework to explain the evaporation of droplets on solid surfaces. During stick-slip, a droplet alternates between two ideal "modes" as its volume is reduced: a slip mode, where the droplet edge smoothly retracts from the solid, and a stick mode, where the edge remains pinned to it. The slip mode (also called constant-contact-angle mode) is a diffusion-dominated process, where small gradients in the humidity over the surface of the droplet only drive weak hydrodynamic flows. As a consequence, the liquid and gas phases remain at rest while the interface smoothly reduces in size following the law $R(t)^2 \sim t_e - t$, where R is the base radius of the droplet, t is time and t_e is the time at which the droplet completely evaporates[7]. The stick mode, on the other hand, involves a static contact line, i.e., $R(t) = \text{const}$. Because of this geometrical constraint a radial flow develops to make up for the mass lost at the pinned edge upon evaporation[8]; any solid particles suspended in the liquid drift to the edge, and this is the mechanism responsible for the familiar ring-like stains left behind by coffee drops[9,10].

It is widely accepted that transitions from stick to slip, called de-pinning events, are activation processes[11]. Microscopically, a solid surface has chemical[12] or topographical[13] defects that impose a static energy barrier, hampering the translational motion of the contact line. As a consequence, an evaporating droplet with a pinned contact line stores surface energy as its volume is reduced. This proceeds until the energy barrier due to pinning is overcome, the contact line depins, and the motion of the interface is restored[14–17].

So far, the widespread conception has been that contact-line pinning caused by microscopic surface roughness dominates the evolution of evaporating droplets. Such a fundamental aspect poses severe limitations to predict and control the configuration of a droplet upon evaporation.

Here we show that droplets evaporating on a smooth—but non-flat—solid surface exhibit a different mode of evaporation: instead of pinning the droplet in an uncontrolled manner, the underlying smooth topography promotes a reproducible sequence of well-defined droplet configurations paced by dynamic "snap" events. Such a snap mode of evaporation has the unique advantages of precise predictability and controllability over the shape and location of the droplet as it evaporates, making it useful for applications that need efficient mass and heat transfer at sub-millimetre scales.

Results

Evaporation on ultra-smooth liquid-impregnated rough surfaces. We investigated the response of evaporating water droplets to a smooth topography using Lubricant-Impregnated Rough surfaces (LIRs). LIRs are solid surfaces of arbitrary shape that are first treated with a super-hydrophobic nano-coating to create a rough, water-repellant, surface, and then impregnated by a lubricant oil (see Supplementary Notes 1–3 for fabrication details). The oil creates a thin lubricating layer, of thickness $\ell \sim 10\,\mu m$, that covers the solid roughness, creating an ultra-smooth surface (for instance, on a tilted flat LIRs, a water droplet has a sliding angle below 1°).

We first tested the evaporation of a water droplet on a flat LIR surface (Fig. 1a). We found that the squared-base radius of the droplet decreases linearly with time, while the apparent contact angle, θ_a (measured relative to the horizontal), decreases smoothly due to the effect of a wetting lubricant ridge located at the base of the droplet[18,19] (Fig. 1b). Such kinematics, which persists for up to ~80% of the evaporation time, indicate that contact-line pinning effects are negligible[20].

We then carried out experiments of droplets evaporating on a wavy LIR surface (Fig. 1c). We placed an 80–μL droplet on a surface of wavelength $\lambda = 2$ mm and amplitude $\epsilon = 0.2$ mm, and left it to evaporate under room temperature and humidity conditions. The droplet quickly settled to adopt a symmetric shape (on a plane parallel to the wave) with its left and right edges lying close to the peaks of the topography (see panel 1 in Fig. 1c). As evaporation took place, we tracked the base radius of the droplet (a measure of the droplet's contact area) and the apparent contact angle (measured relative to the horizontal and at the intersection of the droplet's surface with the sinusoidal LIR surface (inset of Fig. 1d)). Contrary to the smooth evaporation observed on a flat surface, we found that the non-flat topography promotes a different evaporation kinematics. Initially, evaporation results in a slow retraction of the contact lines from the peaks of the topography, as shown by the continuous decrease of the base radius observed in Fig. 1d. Such kinematics is interrupted when, suddenly, one of the edges of the drop "snaps" by retracting to the adjacent peak (see images 2–3 in Fig. 1 and Supplementary Movie 1). The duration of a snap event is very short compared to the evaporation time of the droplet. Therefore, a snap appears as a discontinuous change in the lateral base radius and the apparent contact angle in the timescale of our experiments (Figs. 1d and 1e). Once a snap has occurred, the droplet continues to evaporate in a smooth manner (again, with the contact lines slowly retracting from the peaks of the wave) until another snap event is triggered. We found that sequential snaps undergone by the same droplet can be triggered at either of its edges (compare, e.g., images 3–4 and 4–5 in Fig. 1c). In addition, we found that the apparent contact angles of the left and right edges remain remarkably close to each other during the whole evaporation process. These features suggest that the smooth surface provided by the lubricant layer of the LIR surfaces eliminates contact-line pinning, and, therefore, that snaps are not de-pinning events. This contrasts with the stick-jump dynamics observed for droplets evaporating on periodic micro-patterned super-hydrophobic surfaces, where pinning effects dominate[21–23].

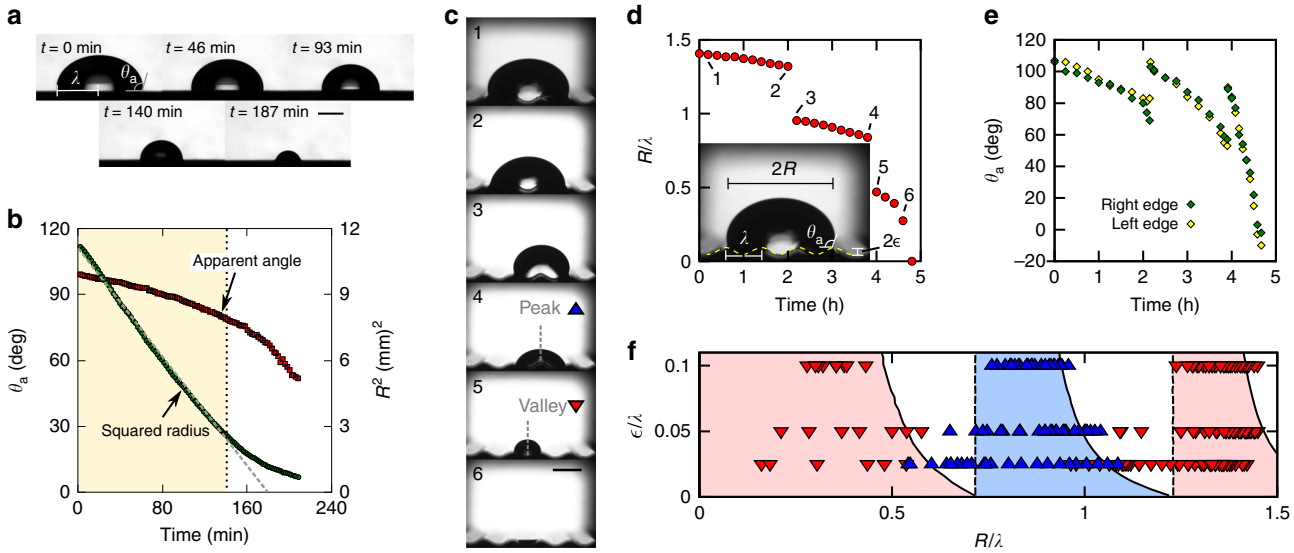

Fig. 1 Snap evaporation on a smooth wavy surface. **a** Time-lapsed images of an 80-μL water droplet evaporating on a flat LIR surface. **b** Evaporation kinematics on a flat surface, characterised by the squared-base radius (R^2) and apparent contact angle (θ_a) as functions of time. The diffusion-dominated, pinning-free regime is indicated by the yellow-shaded region. **c** Time-lapsed images of an 80-μL water droplet evaporating on a wavy LIR surface of wavelength $\lambda = 2$ mm and amplitude $\epsilon = 200$ μm (inset). The dashed lines in images 4 and 5 indicate the droplet's mid-plane. **d**, **e** Evaporation kinematics on a wavy LIR surface, characterised by the base radius (**d**) and apparent contact angle (**e**) as functions of time. **f** Observed droplet configurations (peak in blue or valley in red) for different surface aspect ratios and droplet sizes. The dashed and continuous lines that bound the shaded regions correspond to the boundary lines of each configuration predicted by the bifurcation theory model (see text). The scale bars in (**a**, **c**) are equivalent to 2 mm

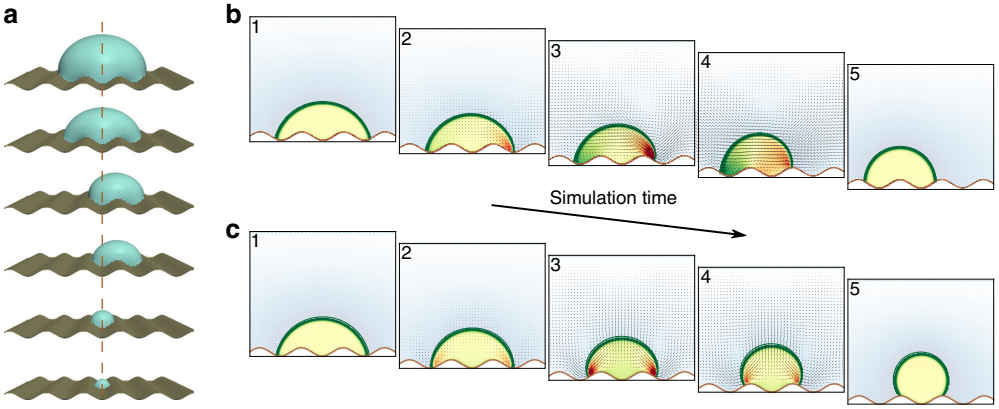

Fig. 2 Mechanism of snap evaporation. **a** 3D Lattice-Boltzmann simulation of a droplet undergoing snap evaporation on a wavy surface. The simulation parameters match the experimental conditions of Fig. 1c. The reference midline indicates the plane of symmetry of the surface. **b**, **c** 2D simulations showing the dynamics of a snap event with broken (**b**) and conserved (**c**) plane symmetry. The arrows indicate the direction of the local flow pattern. The colour map outside the droplet indicates the magnitude of the local chemical potential. The colour map within the droplet indicates the magnitude of the pressure field

Between snaps, the interface shape is always symmetric about a vertical line (Fig. 1c). This symmetry is lost momentarily during a snap, while the droplet undergoes a lateral motion. As a result, the symmetry line alternates between two positions: it is either aligned with a peak of the topography or with a valley (see images 4 and 5 in Fig. 1c). Therefore, the alternation between the two configurations induces a periodic variation in the droplet's position and shape. We repeated the experiments using surfaces of different amplitude-to-wavelength ratio, ϵ/λ, and found a highly reproducible emerging pattern: the position of the drop always alternates between peak and valley configurations, and there is a clear correlation between these configurations and the droplet base radius which becomes increasingly marked for larger amplitudes of the topography. As illustrated in Fig. 1f, for a given droplet size and wave amplitude, it is possible to anticipate the shape of the droplet and its position relative to the solid surface.

Lattice–Boltzmann simulations. To better understand the mechanism of snap evaporation, we carried out numerical simulations of the coupled diffusion and hydrodynamics equations using a lattice–Boltzmann algorithm (see Supplementary Note 4 for details). In the simulations, we modelled the smooth LIR surface as a solid boundary with a small static noise in its

wettability; this allows the droplets to break the plane symmetry, but does not introduce any pinning effects. To validate our numerical model, we first considered full 3D simulations of evaporating droplets including the effect of gravity (Fig. 2a), which are in very good agreement with the sequence of droplet configurations observed in the experiments (cf. Fig. 1c). Normalising the simulation and experimental time sequences by the total evaporation time, confirms that peak and valley states always occur over the same specific ranges in the droplet base radius, and implies that the effect of the evaporation rate is purely kinematic (see Supplementary Movie 2).

Next, we carried out simulations of gravity-free 2D droplets; we found the same evaporation sequences, ruling out gravitational and 3D effects on the snap events (Fig. 2b and Supplementary Movie 3). Instead, a closer examination of the flow profiles, characterised by the velocity and pressure fields, reveals that the slow evolution of the droplets (when on a peak or a valley) is controlled by mass diffusion in the gas due to evaporation (images 1 and 5 in Fig. 2b). This situation changes when the contact lines approach the valleys of the topography. At such points, the Laplace pressure inside the droplet builds up near one of the contact lines and drives a capillary flow towards the opposite edge, triggering a snap (image sequence 2–4 in Fig. 2b). We then removed the noise from the simulations, which forces the droplet to keep the plane symmetry. Surprisingly, the droplets still undergo snaps, albeit with no translational motion (Fig. 2c and Supplementary Movie 4).

Snap sequences and shape bifurcations. Our numerical simulations indicate that the slow evolutions of peak and valley configurations correspond to quasi-static processes, and that during snaps the interface is out-of-equilibrium.

We expect that the 2D quasi-static droplet shapes are circular sections that intersect the solid surface with an equilibrium contact angle, θ_e (measured relative to the local surface tangent). Such interfacial shapes are indeed valid solutions of the Young–Laplace equation subject to Young's condition[13], which are the equilibrium equations for a liquid–gas interface in contact with a solid boundary[24]. On a flat surface, fixing the contact angle and the cross-sectional area of the droplet, A, yields a single equilibrium solution which remains invariant upon a continuous translation over the surface. On a wavy surface, corresponding to $\epsilon/\lambda > 0$, the translational invariance becomes discrete (with periodicity λ) as two symmetric equilibrium solutions appear—the peak and valley configurations. These states can be distinguished by their lateral base radius, R, and lateral coordinate, say $x = x_P = 0, \pm\lambda, \pm2\lambda, \ldots$, for a peak, and $x = x_V = \pm\frac{1}{2}\lambda, \pm\frac{3}{2}\lambda, \ldots$ for a valley. This situation is maintained upon increasing the wave amplitude further, up to a critical value $(\epsilon/\lambda)^*$ where multiple circular-arc shaped equilibrium solutions (of different base radius R) emerge (see Supplementary Note 5). The critical amplitude thus corresponds to the onset of a cusp bifurcation[25,26]. For example, for $\epsilon/\lambda = 0.1$ and $A/\lambda^2 = 4$ there is one valley configuration and three distinct peak configurations (Fig. 3a). In addition to symmetric states, one also finds asymmetric solutions; for instance, in Fig. 3a there are four non-symmetric solutions formed by two pairs of mirror images located at intermediate positions between peaks and valleys.

The multiplicity of symmetric solutions above the critical amplitude is clearly manifested in the functional relation between R and A, which is not bijective (see Fig. 3b). In fact, the structure of $R(A)$ curves for peak and valley states implies that reducing A (e.g., due to evaporation) eventually leads to a fold where available equilibrium solutions of equivalent cross-sectional area have a smaller radius (Fig. 3b). At first sight, one might expect that such a geometrical constraint dictates the fate of the droplets, and that snaps are triggered whenever A reaches the value at the fold of the curve, A_f.

However, an analysis of the stability of the equilibrium solutions reveals a subtler picture. In the stability analysis, we compute the surface energy $F(R, x)$ of droplets of circular shape and prescribed cross-sectional area as a function of the base radius R and the lateral coordinate x (see Supplementary Note 5). Consider Fig. 3c–e, which show the evolution of the energy landscape as the area is decreased from an initial value $A/\lambda^2 = 4$, falling below the value at the fold $A_f/\lambda^2 \approx 3.11$ (see Fig. 3b). Initially, there are three sinks (the valley and the two peak configurations marked with solid lines in Fig. 3a), one source (the peak configuration marked with a dashed line) and four saddles (the asymmetric configurations). Now consider a droplet in the stable peak configuration of largest radius. As A decreases and reaches a value $A_p/\lambda^2 \approx 3.26$, such a stable point merges with the two adjacent saddles, leaving a single saddle as a remnant. The area A_p thus corresponds to the critical point of an inverted pitchfork bifurcation[25]. The structure of the energy landscape at $A = A_p$ explains the lateral migration of the droplet during snaps: at the bifurcation point, the remaining source prevents the droplet from migrating towards the remaining stable peak state; instead, the surface energy is always reduced upon a migration to the adjacent valley state. This sequence is repeated as the area is reduced further, and explains the clear alternation of experimental interface configurations.

The pitchfork bifurcation always occurs at a cross-sectional area A_p larger than the area of the fold, A_f. As A is reduced further from A_p, the saddle produced by the pitchfork bifurcation annihilates with the source at $A = A_f$, leaving a single sink in the peak branch (see Fig. 3e). Such a situation corresponds to a 2D saddle-node (or fold) bifurcation[25]. Indeed, one can remove the pitchfork bifurcation to observe the fold bifurcation by forcing the droplets to keep the plane symmetry at all times, explaining the symmetric snap events observed in the simulations (Fig. 2c). In the presence of lateral fluctuations, however, the effect of the pitchfork bifurcation is to "weaken" the fold bifurcation, producing only a remnant of the lost saddle-node.

A bifurcation diagram in x-A space, shown in Fig. 3f, summarises the hierarchy of the pitchfork and saddle-node bifurcations governing the snapping behaviour of the droplets triggered by the sinusoidal topography. The pitchfork bifurcation always occurs when the contact lines approach the valleys of the topography, and thus the critical radius R_p is independent of the amplitude of the surface pattern. However, the range of stable equilibria on a given branch becomes smaller on surfaces of a larger wave amplitude. This leads to the collapse of states at larger ϵ/λ observed in Fig. 1f. Despite overlooking the details of the 3D interface configuration, the 2D model gives a good prediction of the corresponding separatrices, which we present as overlays in Fig. 1f.

Discussion

It is reasonable to expect that similar mechanisms underpin the stability of evaporating droplets on more complex topographies. Indeed, an "egg-box" surface leads to the alternation between well-defined "diamond" and "rectangle" droplet shapes (Fig. 4a). Here, again, the contact line tends to avoid the valleys of the topography, and thus the droplet adopts a shape whose typical width, W, and length, L, are multiples of the underlying wavelength of the surface pattern, λ. Snap events now involve a stepwise reduction of one of the droplet length scales, and thus the

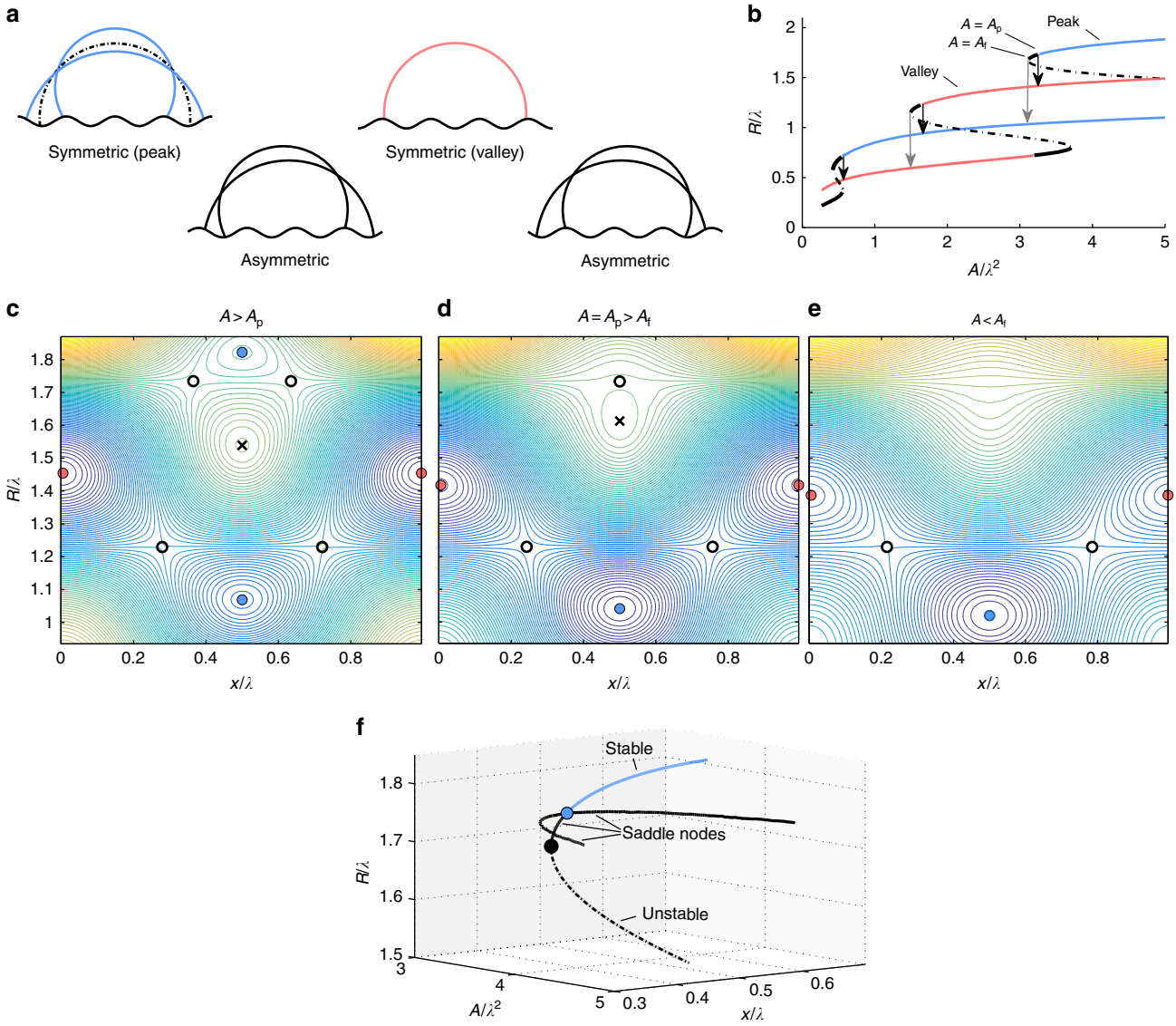

Fig. 3 Bifurcation diagrams of equilibrium shapes of 2D droplets on a wavy surface. **a** Equilibrium droplet configurations of identical cross-sectional area $A/\lambda^2 = 4$ and intersection angle $\theta_e = 105°$ on a wavy surface of amplitude $\epsilon/\lambda = 0.1$. There are four plane-symmetric configurations: three centred at a peak and one centred at a valley. There are also four asymmetric configurations that apperar as mirror-image pairs. **b** Functional relation between the lateral radius, R and cross-sectional area, A of plane-symmetric droplets. The blue and red branches correspond to stable equilibria on peak and valley configurations, respectively. The dashed branches correspond to unstable solutions. The solid black branches correspond to saddles, where the droplet is stable to axisymmetric perturbations, but unstable against lateral displacements along the solid surface. **c**–**e** Evolution of the energy landscape in R–x space for decreasing droplet cross-sectional area. The contour lines indicate levels of the surface energy, increasing from blue to yellow. Blue and red circles correspond to stable peak and valley configurations, crosses to unstable configurations and black empty circles to saddle nodes. **c** For a $A > A_p$, a droplet in a peak state with large radius is stable to both radial and lateral displacements. **d** At $A = A_p$ the stable state merges with the two adjacent saddles (asymmetric droplet configurations), leaving a single saddle point. **e** At $A = A_f$, the saddle annihilates with the symmetric unstable state. **f** Bifurcation diagram showing stable, unstable and saddle branches for a droplet in a peak configuration. The blue point corresponds to a subcritical pitchfork bifurcation, which triggers the lateral motion of the droplet to a valley configuration (not shown). The black point corresponds to the onset of a saddle-node bifurcation, which occurs only if the droplet cannot break the plane symmetry

droplet evolves following a sequence $W \times L \approx 5\lambda \times 5\lambda \to 4\lambda \times 5\lambda \to 4\lambda \times 4\lambda \ldots$, which can be exploited to control the aspect ratio of the droplet (Fig. 4b).

Therefore, snap evaporation is a distinct mode of droplet evaporation on smooth—but topographically patterned—solid surfaces. Unlike stick-slip evaporation, the alternation of well-defined quasi-static states observed in snap evaporation is controlled by shape bifurcations of the liquid–gas interface dictated by the interplay between the underlying surface topography and the droplet volume, and not by contact-line pinning.

In our experiments, the timescale of snap events is very short compared to the evaporation time of the droplet (see Fig. 1d). The regime where the evaporation and snap timescales compete poses fundamental questions in relation to the dynamics of bifurcations (for which our experimental setup provides a useful test bed), but can also find application in situations where evaporation happens in a short timescale, such as in micro-fluidics. Our ideas can also be applied to other methods of variation of the droplet volume on smooth surfaces, such as condensation[27], mass transfer via flow rate[28], or by exploiting external fields (e.g., temperature or

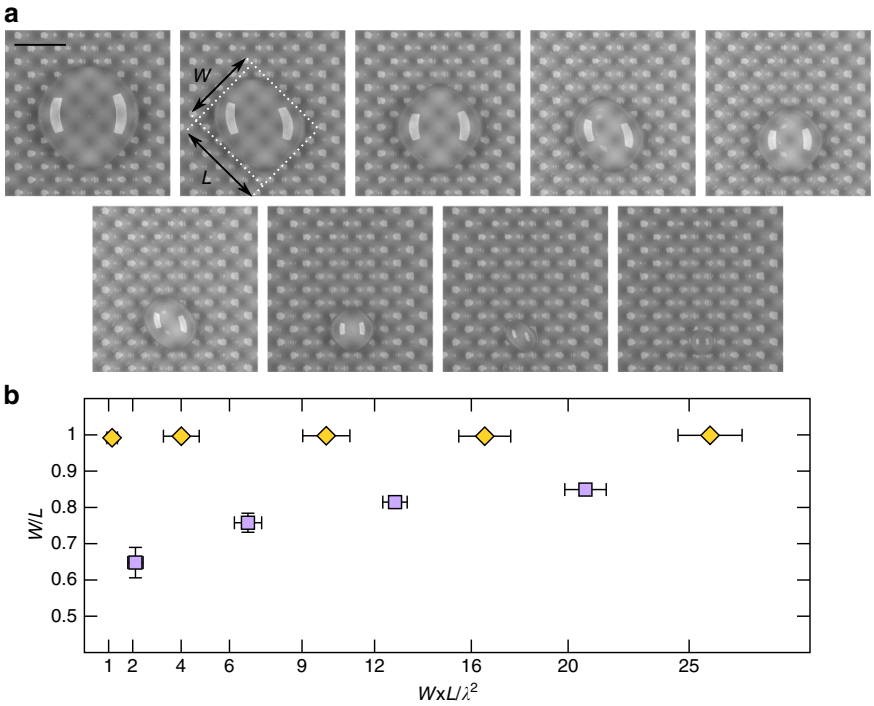

Fig. 4 Droplet shape alternation during snap evaporation on an egg-box topography. **a** Time-lapsed sequence of an 80-µL droplet evaporating on a surface of wavelength $\lambda = 4$ mm and amplitude $\epsilon = 200$ µm. At any given time, the shape of the droplet is characterised by its width, W, and length, L. **b** Width-to-length aspect ratio as a function of the apparent contact area of the of the droplet, $W \times L$. The droplet shape alternates between 'diamond' (yellow diamonds) and 'rectangle' (purple squares) configurations with droplet size (the ticks in the x-axis correspond to contact areas that are multiples of the underlying grid). The scale bar in (**a**) is equivalent to 1 cm

pressure). Finally, the variation of the surface topography, either spatially through designed patterns, or dynamically via forced droplet motion[29] or actuation of flexible solids, can be used to extend these principles to achieve a better control of droplet localisation and transport mediated by snaps.

Data availability. The data that support the findings of this study are available from R.L.A. upon reasonable request.

Received: 4 December 2017 Accepted: 16 March 2018
Published online: 11 April 2018

References

1. Perl, A., Reinhoudt, D. N. & Huskens, J. Microcontact printing: limitations and achievements. *Adv. Mater.* **21**, 2257–2268 (2009).
2. Kawamura, D. et al. Influence of the watermark in immersion lithography process. In *Proc. SPIE 5753, Advances in Resist Technology and Processing XXII, Microlithography 2005,* 818–826 (International Society for Optics and Photonics, San Jose, CA, US, 2005).
3. Lee, K.-H., Kim, S.-M., Jeong, H. & Jung, G.-Y. Spontaneous nanoscale polymer solution patterning using solvent evaporation driven double-dewetting edge lithography. *Soft Matter* **8**, 465–471 (2012).
4. Grissom, W. M. & Wierum, F. Liquid spray cooling of a heated surface. *Int. J. Heat. Mass Trans.* **24**, 261–271 (1981).
5. Wiedenheft, K. F. et al. Hotspot cooling with jumping-drop vapor chambers. *Appl. Phys. Lett.* **110**, 141601 (2017).
6. Picknett, R. & Bexon, R. The evaporation of sessile or pendant drops in still air. *J. Colloid Interface Sci.* **61**, 336–350 (1977).
7. Cazabat, A.-M. & Guéna, G. Evaporation of macroscopic sessile droplets. *Soft Matter* **6**, 2591–2612 (2010).
8. Hu, H. & Larson, R. G. Evaporation of a sessile droplet on a substrate. *J. Phys. Chem. B.* **106**, 1334–1344 (2002).
9. Deegan, R. D. et al. Capillary flow as the cause of ring stains from dried liquid drops. *Nature* **389**, 827–829 (1997).
10. Sáenz, P. et al. Dynamics and universal scaling law in geometrically-controlled sessile drop evaporation. *Nat. Commun.* **8**, 14783 (2017).
11. de Gennes, P. G. Wetting: statics and dynamics. *Rev. Mod. Phys.* **57**, 827–863 (1985).
12. Johnson Jr, R. E. & Dettre, R. H. *Contact Angle Hysteresis* (ACS Publications, Washington, 1964).
13. Huh, C. & Mason, S. Effects of surface roughness on wetting (theoretical). *J. Colloid Interface Sci.* **60**, 11–38 (1977).
14. Savva, N., Kalliadasis, S. & Pavliotis, G. A. Two-dimensional droplet spreading over random topographical substrates. *Phys. Rev. Lett.* **104**, 084501 (2010).
15. Stauber, J. M., Wilson, S. K., Duffy, B. R. & Sefiane, K. On the lifetimes of evaporating droplets. *J. Fluid. Mech.* **744**, R2 (2014).
16. Dietrich, E., Kooij, E. S., Zhang, X., Zandvliet, H. J. & Lohse, D. Stick-jump mode in surface droplet dissolution. *Langmuir* **31**, 4696–4703 (2016).
17. Pham, T. & Kumar, S. Drying of droplets of colloidal suspensions on rough substrates. *Langmuir* **33**, 10061–10076 (2017).
18. Smith, J. D. et al. Droplet mobility on lubricant-impregnated surfaces. *Soft Matter* **9**, 1772–1780 (2013).
19. Semprebon, C., McHale, G. & Kusumaatmaja, H. Apparent contact angle and contact angle hysteresis on liquid infused surfaces. *Soft Matter* **13**, 101–110 (2017).
20. Guan, J. H. et al. Evaporation of sessile droplets on slippery liquid-infused porous surfaces (slips). *Langmuir* **31**, 11781–11789 (2015).
21. McHale, G., Aqil, S., Shirtcliffe, N., Newton, M. & Erbil, H. Y. Analysis of droplet evaporation on a superhydrophobic surface. *Langmuir* **21**, 11053–11060 (2005).
22. do Nascimento, R. M., Cottin-Bizonne, C., Pirat, C. & Ramos, S. M. Water drop evaporation on mushroom-like superhydrophobic surfaces: temperature effects. *Langmuir* **32**, 2005–2009 (2016).
23. Debuisson, D., Merlen, A., Senez, V. & Arscott, S. Stick–Jump (SJ) evaporation of strongly pinned nanoliter volume sessile water droplets on quick drying, micropatterned surfaces. *Langmuir* **32**, 2679–2686 (2016).
24. de Gennes, P.-G., Brochard-Wyart, F. & Quéré, D. *Capillarity And Wetting Phenomena: Drops, Bubbles, Pearls, Waves* (Springer Science & Business Media, Germany, 2013).

25. Strogatz, S. H. *Nonlinear Dynamics And Chaos: With Applications To Physics, Biology, Chemistry, And Engineering. Studies in Nonlinearity,* 1st edn (Westview Press, Colorado, 2001).
26. Arnol'd, V. I. Singularities, bifurcations, and catastrophes. *Sov. Phys. Uspekhi* **26**, 1025 (1983).
27. Park, K.-C. et al. Condensation on slippery asymmetric bumps. *Nature* **531**, 78–82 (2016).
28. Pradas, M., Savva, N., Benziger, J. B., Kevrekidis, I. G. & Kalliadasis, S. Dynamics of fattening and thinning 2D sessile droplets. *Langmuir* **32**, 4736–4745 (2016).
29. Herde, D., Thiele, U., Herminghaus, S. & Brinkmann, M. Driven large contact angle droplets on chemically heterogeneous substrates. *Europhys. Lett.* **100**, 16002 (2012).

Acknowledgements

We would like to thank J. Sardanyés and M. Sommacal for useful discussions. E.R.G. and B.V.O. acknowledge financial support from Northumbria University via a PhD Studentship. R.L.A. and G.G.W. thank the Royal Society Research Grant Scheme for financial support (grant no. RG150470); E.R.G. and R.L.A. acknowledge support from EPSRC (grant no. EP/P024408/1). R.L.A. acknowledges support from EPSRC as a member of the UK Consortium on Mesoscale Engineering Sciences (grant no. EP/L00030X/1).

Author contributions

M.P. and R.L.A. conceived the research. M.P., R.L.A. and G.G.W. supervised the research. G.G.W. designed the experiments. G.G.W., Y.L.L. and A.N. carried out the experiments of drop evaporation on flat and plane-wave surfaces. B.V.O. and G.G.W. carried out the experiments of drop evaporation on egg-box surfaces. G.G.W., R.L.A., Y. L.L., A.N. and B.V.O. analysed the experimental data. E.R.G. developed and carried out the simulations. M.P., R.L.A. and E.R.G. developed the theoretical model. R.L.A. and M. P. wrote the paper. E.R.G. and G.G.W. contributed equally to this work.

Additional information

Supplementary Information accompanies this paper at https://doi.org/10.1038/s41467-018-03840-6.

Competing interests: The authors declare no competing interests.

Reprints and permission information is available online at http://npg.nature.com/reprintsandpermissions/

Publisher's note: Springer Nature remains neutral with regard to jurisdictional claims in published maps and institutional affiliations.

LANGMUIR
Cite This: *Langmuir* 2019, 35, 4197−4204
Article
pubs.acs.org/Langmuir

Apparent Contact Angles on Lubricant-Impregnated Surfaces/SLIPS: From Superhydrophobicity to Electrowetting

Glen McHale,* Bethany V. Orme, Gary G. Wells, and Rodrigo Ledesma-Aguilar

Smart Materials & Surfaces Laboratory, Faculty of Engineering & Environment, Northumbria University, Newcastle upon Tyne NE1 8ST, U.K.

ABSTRACT: A fundamental limitation of liquids on many surfaces is their contact line pinning. This limitation can be overcome by infusing a nonvolatile and immiscible liquid or lubricant into the texture or roughness created in or applied onto the solid substrate so that the liquid of interest no longer directly contacts the underlying surface. Such slippery liquid-infused porous surfaces (SLIPS), also known as lubricant-impregnated surfaces, completely remove contact line pinning and contact angle hysteresis. However, although a sessile droplet may rest on such a surface, its contact angle can be only an apparent contact angle because its contact is now with a second liquid and not a solid. Close to the solid, the droplet has a wetting ridge with a force balance of the liquid−liquid and liquid−vapor interfacial tensions described by Neumann's triangle rather than Young's law. Here, we show how, provided the lubricant coating is thin and the wetting ridge is small, a surface free energy approach can be used to obtain an apparent contact angle equation analogous to Young's law using interfacial tensions for the lubricant−vapor and liquid−lubricant and an effective interfacial tension for the combined liquid−lubricant−vapor interfaces. This effective interfacial tension is the sum of the liquid−lubricant and the lubricant−vapor interfacial tensions or the liquid−vapor interfacial tension for a positive and negative spreading power of the lubricant on the liquid, respectively. Using this approach, we then show how Cassie−Baxter, Wenzel, hemiwicking, and other equations for rough, textured or complex geometry surfaces and for electrowetting and dielectrowetting can be used with the Young's law contact angle replaced by the apparent contact angle from the equivalent smooth lubricant-impregnated surface. The resulting equations are consistent with the literature data. These results enable equilibrium contact angle theory for sessile droplets on surfaces to be used widely for surfaces that retain a thin and conformal SLIPS coating.

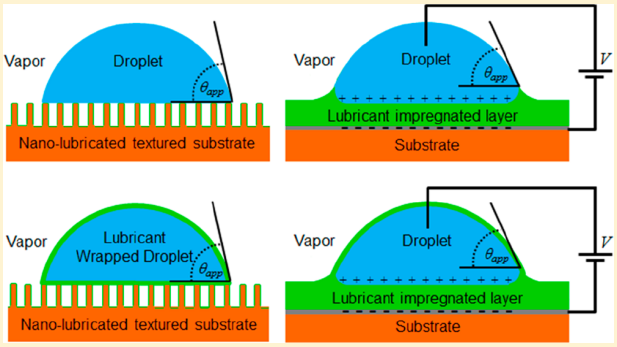

1. INTRODUCTION

A fundamental underpinning concept when dealing with droplets on surfaces is the Young's law contact angle (θ_Y) defined by

$$\cos\theta_Y = \frac{(\gamma_{SV} - \gamma_{SL})}{\gamma_{LV}} \quad (1)$$

where the γ_{IJ} represents the interfacial tensions for the solid−vapor, solid−liquid, and liquid−vapor interfaces.[1] However, in experiments, the measured angles are the static contact angle (θ_S), advancing contact angle (θ_A), receding contact angle (θ_R), and dynamic contact angle (θ_D), none of which match the contact angle given by Young's law.[2−4] This reflects the contact line pinning and contact angle hysteresis, $\Delta\theta_{CAH} = (\theta_A - \theta_R)$, arising from the intrinsically heterogeneous nature of substrates due to small-scale roughness and surface chemistry. In a typical sessile droplet measurement, the observed static contact angle has a value intermediate between the advancing and receding contact angles, whose range defines the contact angle hysteresis. The existence of contact line pinning has multiple consequences, from the need to provide sufficient force to overcome the contact line pinning before droplet (or contact line) motion can occur in a microfluidic system to the formation of ring stains during the drying of droplets.[5,6]

Recently, the concept of slippery liquid-infused porous surfaces (SLIPS), or equivalently lubricant-impregnated surfaces, has been introduced to overcome contact line pinning.[7−9] On these surfaces, sessile-type droplets are observed and apparent contact angles can be defined despite the paradox that the droplet rests on a lubricant and never actually contacts the underlying solid surface.[10] Thus, contact line pinning causing contact angle hysteresis is removed, but so is the concept of a Young's law contact angle. Conceptually, the system becomes the limit of a liquid lens (droplet) on a shallow pool of (lubricant) liquid with the concept of the contact angle replaced by the balance among three interfacial tensions for the liquid−lubricant−liquid system in a Neumann triangle.[11,12] Moreover, if the spreading power for the lubricant liquid on the liquid of the droplet is positive, then the droplet

Received: December 13, 2018
Revised: February 9, 2019
Published: February 13, 2019

DOI: 10.1021/acs.langmuir.8b04136
Langmuir 2019, 35, 4197−4204

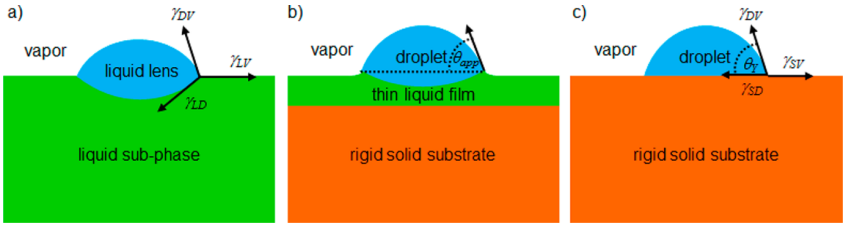

Figure 1. (a) Liquid lens on a deep liquid subphase with a Neumann triangle of forces, (b) a droplet on a thin liquid film on a rigid solid substrate, and (c) a droplet obeying Young's law on a rigid solid substrate.

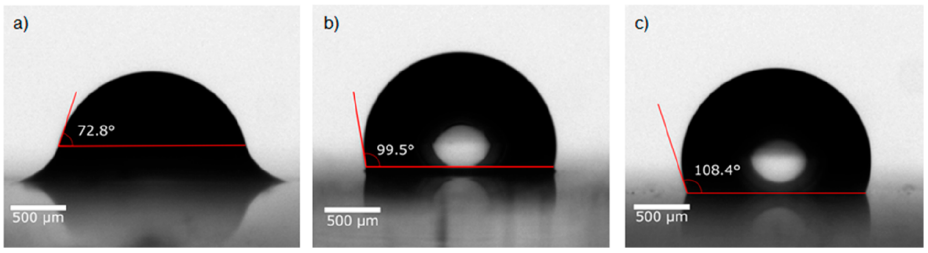

Figure 2. Experimental side-profile views of small droplets of water on SLIP surfaces with (a) a visible wetting ridge, (b) a small wetting ridge, and (c) no visibly obvious wetting ridge.

may be fully coated in a thin layer of the lubricant,[8] further complicating any interpretation arising from contact angle approaches.

From the perspective of droplets on soft substrates, Young's law and Neumann's triangle are the two extremes in the wetting behavior in the limits of an infinitely hard substrate (i.e., solid) and an infinitely soft (i.e., liquid) substrate.[13] It is possible to imagine a transition from a liquid lens on a liquid subphase to a sessile droplet on a solid surface as the liquid subphase becomes ever thinner and which in the extreme limit has vanishing thickness (Figure 1). Experimentally, lubricant coatings on a solid substrate can be created, which are extremely thin (typically <1 μm), so a question arises about how concepts arising from contact angle theory can be applied in this limit. In contact angle theory, the interfacial tensions can be regarded as either forces per unit length or surface free energies per unit area. The use of a surface free energy approach enables simple derivations of Young's law on a smooth surface, Wenzel and Cassie–Baxter equations on topographical rough and textured surfaces,[3,14] the Young–Lippmann electrowetting-on-dielectric contact angle,[15] and the effect on the contact angles of interface-localized dielectrophoresis (dielectrowetting).[16] Because SLIPS coatings have been used experimentally with topographically structured surfaces (e.g., SLIPS Wenzel[17] and SLIPS Cassie–Baxter[17,18] states) and with both electrowetting[19−22] and dielectrowetting,[21] it would be extremely useful if a similar simple approach could be applied to SLIP surfaces in the limit of thin film coatings.

In this work, we show how a surface free energy approach can be used to derive the apparent equilibrium contact angle for droplets on SLIP surfaces with thin conformal lubricant films. We show how this argument can be applied to topographically structured surfaces, such as those used in superhydrophobicity, roughness-induced wetting, and hemiwicking, to surfaces with complex geometry or shape, and to electrowetting and dielectrowetting. We also show that the results are consistent with literature data. Our work therefore provides a conceptual framework for apparent equilibrium contact angles for droplets and contact lines, which is widely applicable to surfaces with thin conformal SLIPS, lubricant-impregnated coatings, or lubricant coatings.

2. SLIP SURFACES

Lubricant-impregnated surfaces can be created using a wide variety of material techniques. These include using porous layers,[7] electrospinning,[23] membranes,[24] lithographically fabricated textures,[8,10] particle coatings,[25,26] sand-blasting and boehimite,[27] etching,[28] electrodeposition,[29] and roll-to-roll nanoimprint lithography[30] of surfaces. The principle is to increase the solid surface area through roughness/texture or other means and ensure it is either intrinsically hydrophobic or has a hydrophobic surface coating; if the droplet of interest is not water, then the surface chemistry is chosen to be repellent to that liquid. A lubricant is chosen to be nonvolatile, to completely and preferentially wet the solid and be locked into the surface structure by the balance of interfacial tensions, and to be immiscible to the liquid in the droplet. The hydrophobicity (or liquid repellence) of the solid surface ensures that the lubricant is not displaced by the water (liquid) in the droplet. Under these circumstances, a droplet rests entirely on the lubricant and never contacts the underlying solid (similar to Figure 1b). The motion of a droplet contact line then always occurs on the lubricant whether it is advancing or receding, and this leads to complete mobility of the contact line and, hence, the droplet. Smith et al. provide an overview of the possible states of droplets on lubricant-impregnated surfaces, including ones in which partial contact with the underlying solid occurs.[8] From one perspective, a surface suitable for impregnation, prior to lubricant being infused, can be considered to be a Wenzel (e.g., hemiwicking) or a Cassie–Baxter (e.g., superhydrophobic)-type surface interpreted in the most general sense.[14] The process of infusing a lubricant often uses withdrawal from a lubricant bath, which leaves a film of thickness determined by the withdrawal speed and lubricant properties that can be estimated using the Landau–Levich–Derjaguin (LLD) equation.[31] Such films can be ∼1−100 μm thick, and this can be reduced by applying shear stress (e.g., by rinsing with water or spinning) until a thin thermodynamically

DOI: 10.1021/acs.langmuir.8b04136
Langmuir 2019, 35, 4197−4204

stable film is obtained. One complication in the choice of a lubricant (referred to here as "oil" to avoid notational confusion with liquid for the droplet) is whether its interfacial tensions favor it spreading on the liquid−vapor interface of the droplet. Thus, if the interfacial energy for the combined droplet−oil and oil−vapor interfaces is less than the interfacial energy for the droplet−vapor interface, $\gamma_{DO} + \gamma_{OV} < \gamma_{DV}$, then a film of oil will coat (wrap) the droplet. This is simply a statement that a positive (or zero) spreading power for oil on the liquid droplet in the presence of vapor

$$S^{V}_{OD} = \gamma_{DV} - \gamma_{DO} - \gamma_{OV} \geq 0 \quad (2)$$

favors an oil-film-coated droplet. Conversely, lubricant oils where the spreading power is negative will not self-coat in a film of the lubricant.

Figure 2 shows three examples of small droplets of water, viewed in a side profile, on SLIP surfaces, and in each case, it is possible to define an apparent contact angle, θ_{app}, from the profile; for a discussion of its definition, see Guan et al.[10] The size of the droplets is much less than the capillary length of water, $\kappa^{-1} = (\gamma_{LV}/\rho g)^{1/2}$, where ρ is the density and g = 9.81 ms^{-2} is the acceleration due to gravity, so the majority of their profile conforms to spherical caps. In Figure 2a, there is an obvious distortion close to the surface caused by a wetting ridge, whereas in Figure 2b a wetting ridge exists but at a significantly smaller length scale due to the thinness of the lubricant. In Figure 2c, there is no visibly obvious wetting ridge. The SLIP surfaces in Figure 2 were created using a superhydrophobic nanoparticle coating (Glaco Mirror Coat, Nippon Shine) on glass, which gives a static contact angle of 160° with contact angle hysteresis <10°. The surface in Figure 2a had 20 cSt viscosity silicone oil infused by withdrawal from a bath at 2 mm s^{-1}. This gave an oil thickness of (21.1 ± 0.1) μm measured by reflectometry and consistent with the LLD equation. This surface has an apparent contact angle of θ_{app} = 72.8° and a sliding angle of (0.1 ± 0.2)°, but a thick layer of excess oil is evidenced by the visibly significant wetting ridge. Reducing the withdrawal speed to 0.1 mm s^{-1} gives the thinnest controllable layer of oil (with our equipment for fabricating these surfaces) of (3.1 ± 0.4) μm with an apparent contact angle of θ_{app} = 99.5° and a sliding angle of (0.5 ± 0.2)° and with a significantly reduced wetting ridge (Figure 2b). Removing all excess oil by rinsing decreases the oil thickness to (1.9 ± 0.2) μm and increases the apparent contact angle to θ_{app} = 108.4° with an increase in the sliding angle to (3.4 ± 0.2)°.

The wetting ridge (lubricant skirt) for a droplet on a SLIP surface is caused by the balance of interfacial tensions at the droplet liquid−lubricant−vapor "contact line" close to the solid surface and is described by Neumann's triangle. In this interpretation, there is an effective interfacial force, γ_{eff}, given by

$$\gamma_{eff} = \begin{cases} \gamma_{DV} & S^{V}_{OD} < 0 \\ \gamma_{DO} + \gamma_{OV} & S^{V}_{OD} \geq 0 \end{cases} \quad (3)$$

For a thin lubricating film and droplet with a vanishingly small wetting ridge, it can be shown that the apparent contact angle can be approximated as[32] (also see ref 33)

$$\cos\theta_{app} = \frac{(\gamma_{OV} - \gamma_{OD})}{\gamma_{eff}} \quad (4)$$

This can be interpreted as Young's law for the apparent contact angle using the horizontal component of a net force balance per unit length of the apparent contact line but using an effective interfacial tension for the droplet−vapor interface (Figure 3; also see refs 32 and 33). Equation 4 no longer has

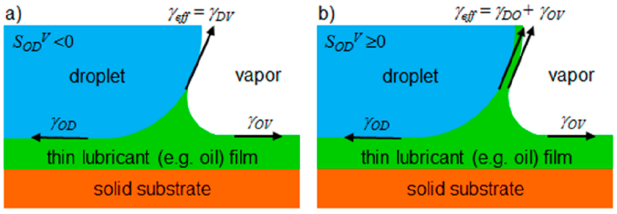

Figure 3. Schematic of a wetting ridge (a) without lubricant wrapping ($S^{V}_{OD} < 0$) and (b) with lubricant wrapping ($S^{V}_{OD} \geq 0$). Small-scale texture within which the lubricant is impregnated is omitted for clarity.

an explicit dependence on the interfacial tensions of the solid. For the surfaces in Figure 2, using γ_{DV} = 72.8 mN m^{-1}, γ_{OV} = 19.8 mN m^{-1} (measured), and γ_{OD} = 38 mN m^{-1} (data from Banpurkar et al.[34]) gives a positive spreading power of S^{V}_{OD} = 15.8 mN m^{-1}, and eq 4 predicts θ_{app} = 108.4°, which is the measured angle in Figure 2c; reducing γ_{OD} to 35 mN m^{-1} (data from Peters and Arabali[35]) reduces the prediction to θ_{app} = 106.1°. Literature data cited by Kreder et al.[33] in their Table 3 and Figure 1c, and from Rykaczewski et al.[36] suggests that eq 4 is a reasonable description of the observed apparent contact angles.

The work of Semprebon et al.[32] included an expression for the apparent contact angle of a droplet in contact with a wetting ridge that only partially wets the droplet. In the limit of small ridges relative to the size of the droplet, the apparent contact angle reaches a limiting upper-bound value. They showed that this can be understood in terms of the higher capillary pressure within smaller ridges, which effectively acts as line tension and leads to an increase in the apparent contact angle. Extrapolating this idea implies that eq 4 gives an upper bound to the value of the observed apparent contact angle for larger wetting ridges, consistent with the data in Figure 2.

3. SURFACE FREE ENERGY APPROACH

3.1. Apparent Equilibrium Contact Angle. The Young's law contact angle can be viewed as arising from a local equilibrium given by a local minimum in a surface free energy landscape close to the contact line and does not depend on the global shape of a droplet. Thus, the contact angle for a large gravitationally flattened droplet is, in principle, the same as for a small spherical cap-shaped droplet, although experimentally a difference may be observed as a result of the contact angle hysteresis. We therefore consider the droplet profile close to a solid surface having a thin lubricant-impregnated layer and consider small translational perturbations, ΔA, of the droplet edge along the lubricant interface, where we consider both $S^{V}_{OD} < 0$ and $S^{V}_{OD} \geq 0$ (Figure 4). In considering this translation, we assume the changes to the detail of the wetting ridge are small for a thin lubricating layer so that there is no net energy difference between its final and initial positions. The net surface free energy change is therefore due to the replacement of the oil−vapor interfacial area, ΔA, by an oil−water interface and the increase in the water−vapor or water−oil and oil−

DOI: 10.1021/acs.langmuir.8b04136
Langmuir 2019, 35, 4197−4204

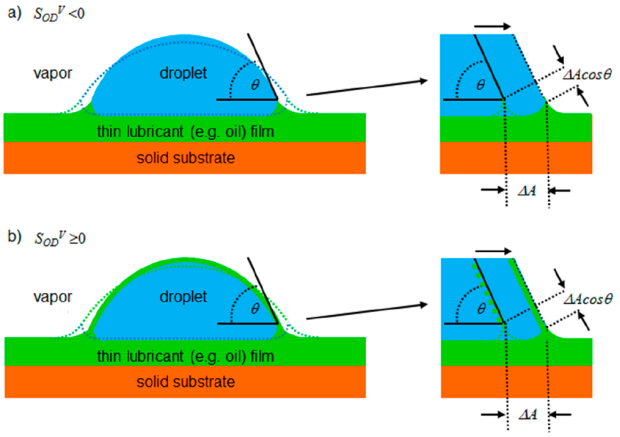

Figure 4. Surface free energy changes due to the small advance, ΔA, of the droplet edge on a smooth SLIP surface (a) without lubricant wrapping ($S_{OD}^{V} < 0$) and (b) with lubricant wrapping ($S_{OD}^{V} \geq 0$). Small-scale texture within which the lubricant is impregnated is omitted for clarity.

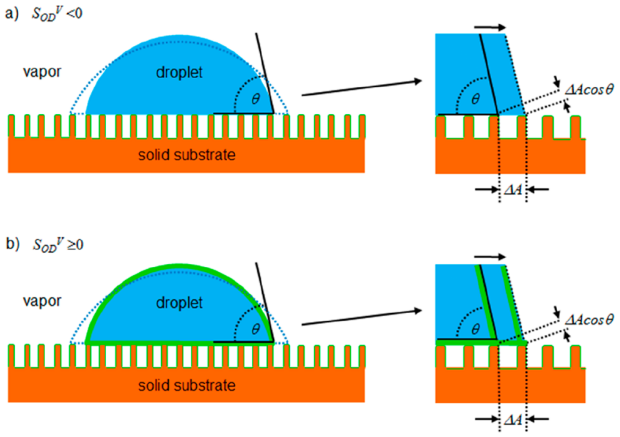

Figure 5. Surface free energy changes due to a one-period advance, $\Delta A(x)$, of the droplet edge on a macrotextured surface possessing a thin conformal SLIPS coating. Cassie–Baxter state (a) without lubricant wrapping ($S_{OD}^{V} < 0$) and (b) with lubricant wrapping ($S_{OD}^{V} \geq 0$). In the latter case, the droplet surface is entirely coated in a thin lubricant layer, including on its underneath surface.

vapor interfacial areas, $\cos\theta\,\Delta A$, depending on whether $S_{OD}^{V} < 0$ or $S_{OD}^{V} \geq 0$. This latter dependence on the spreading power implies that the $\cos\theta\,\Delta A$ change in interfacial area is scaled by either γ_{DV} or by $(\gamma_{DO} + \gamma_{OV})$ (i.e., by γ_{eff}). The first-order change in the surface free energy, ΔF, is therefore

$$\Delta F = (\gamma_{OD} - \gamma_{OV})\Delta A + \gamma_{eff}\Delta A \cos\theta \quad (5)$$

Since this change vanishes when the system is in local equilibrium, $\Delta F = 0$ gives eq 4, which defines the apparent contact angle where θ_{app} is tangent to the profile close to the lubricant surface but is away from any distortion in the droplet profile due to the (small) wetting ridge. Kreder et al.[33] also commented in their work that eq 4 could be obtained by minimizing the energy as well as by balancing forces due to the interfacial tension at the ridge or using a purely geometrical argument. This surface free energy derivation depends on the assumption that at equilibrium a small translational perturbation of the wetting ridge position does not significantly alter the structure of the wetting ridge.

3.2. SLIPS-Modified Cassie–Baxter and Wenzel Equations. The creation of a SLIP surface is achieved using lubricant impregnation of the hydrophobic surface roughness or texture, but this can be part of a multilevel hierarchy of roughness or texture.[17,18,27] For example, a microscale or nanoscale SLIP surface could be part of a macroscale roughness or texture which remains on a length scale much shorter than the capillary length, κ^{-1}, of a droplet. In this case, the SLIP surface becomes a conformal low-pinning lubricant surface of the larger-scale rough or textured macrostructure provided the lubricant does not fill the macrotexture.

Figure 5 shows a small displacement of a droplet edge by one period of pillar-type structure with the same assumptions on the wetting ridge as in section 3.1. The use of a one-period perturbation is an averaging assumption around a droplet perimeter that should be valid when the droplet size is much large than the macrotexture.[37] This perturbation, $\Delta A(x)$, is based on a starting position, x, for the perimeter and so samples whether that position is a local minimum of the surface free energy landscape. Consequently, various parameters are local averages in the vicinity of the perimeter at position x and are not global averages taken across the droplet footprint. If global averages are used for the Cassie solid surface fraction or the Wenzel roughness when the surface has local variations and the Cassie–Baxter and Wenzel equations are applied, inaccurate estimates of the contact angle will occur.[37,38] However, provided parameters local to the perimeter are used, consistent with the surface energy minimization to determine the local equilibrium, the methodology will be valid. This approach is then able to deal with contact angles on surfaces with gradients in topography; for a further discussion, see refs 39 and 40.

The surface free energy changes are composed of three parts: (i) the advance over the tops of microposts, which causes an energy change $(\gamma_{OD} - \gamma_{OV})\varphi_S(x)\,\Delta A(x)$, where $\varphi_S(x)$ is the macrotexture Cassie solid surface fraction local to the droplet perimeter, (ii) the advance over the spaces between microposts, which causes an energy change $\gamma_{eff}(1 - \varphi_S(x))\cdot\Delta A(x)$, where γ_{eff} is due to the water from the droplet bridging the space between microposts, which may or may not be covered in a film oil depending on the spreading power (Figure 5a,b), and (iii) the extended droplet surface, which has an additional surface energy of $\gamma_{eff}\cos\theta(x)\,\Delta A(x)$. The total surface free energy change is

$$\Delta F(x) = (\gamma_{OD} - \gamma_{OV})\varphi_S(x)\,\Delta A(x) + \gamma_{eff}(1 - \varphi_S(x))\,\Delta A(x) + \gamma_{eff}\Delta A(x)\cos\theta(x) \quad (6)$$

and setting this change equal to zero gives

$$\cos\theta_{app}^{CB}(x) = \varphi_S(x)\cos\theta_{app} - (1 - \varphi_S(x)) \quad (7)$$

where θ_{app} is defined by eq 4. This is the analogue of the usual simplified form of the Cassie–Baxter equation in which the contact angle has been replaced by the interfacial-tension-defined apparent contact angle, taking into account whether the spreading power of the lubricant on the droplet is positive (or zero) or negative via the effective droplet–vapor interfacial tension, γ_{eff}.

Equation 7 can be applied to the data from Dong et al., who created a doubly re-entrant micropillar-based superoleophobic surface with nanorough pillar tops infused with Krytox-103.[18] These surfaces were tested with droplets of water, ethanol, and

DOI: 10.1021/acs.langmuir.8b04136
Langmuir 2019, 35, 4197–4204

n-octane, giving apparent advancing and receding contact angles of θ_A/θ_R = 160.7°/148.6°, 160.0°/134.3°, and 160.5°/133.0°, respectively, which are similar to the values measured on the non-lubricant-infused structures. We note that Krytox has positive spreading power on water but not on ethanol, so these liquids should include both oil-wrapped and nonwrapped droplets. Their Supporting Information gives apparent advancing and receding angles on a flat nonstructured Krytox-103-infused surface of θ_A/θ_R = 109.9°/107.4°, 56.0°/54.7°, and 47.2°/46.1°. Because they estimated a Cassie fraction φ_S for the macrotexture of between 5 and 8%, eq 4 predicts θ_{app}^{CB} = 161−165, 151−157, and 150−156°, respectively, using the average of the apparent advancing and receding angles on the nonstructured infused surface (i.e., θ_{ave} = 108.7, 55.4, and 46.7°); we believe the use of this average is justified by the low hysteresis on the nonstructured infused surface. The energy minimization approach provides only equilibrium results. On non-SLIPS Cassie−Baxter surfaces, experiments show that droplets adopt contact angles between the advancing and receding contact angles and typically closer to the advancing angle; the range of hysteresis can be large or small depending on the specific surface. The Cassie−Baxter approach therefore predicts an apparent angle between these two. The SLIPS Cassie−Baxter equation gives predictions here that are slightly (∼0−4°) above the measured advancing apparent angle for water and below the apparent advancing but above the apparent receding angle for ethanol and *n*-octane. In the latter two cases, the predicted apparent angles are closer to the measured apparent advancing angles (within ∼3−9 and ∼5−11°, respectively). Thus, eq 7 gives values broadly consistent with the measured advancing apparent contact angles based on the measured average apparent contact angle on the flat nonstructured Krytox-103-infused surfaces. It also illustrates the (usual) insensitivity of the dependence on the precise value of those values, providing a Cassie−Baxter state is achieved. The continued existence of hysteresis in the apparent advancing and receding contact angles on this superoleophobic surface reflects the discrete micropillar texture of the surface. The contact line must still move from the top of one micropillar to another to advance or recede.

A similar approach can be used for the Wenzel case (Figure 6) and gives

$$\cos\theta_{app}^{W}(x) = r_W(x)\cos\theta_{app} \tag{8}$$

where the Wenzel roughness, $r_W(x)$, is the macroscale surface area compared to its horizontal projection at the location of the drop edge. Dai et al. reported apparent contact angle measurements of droplets of water, ethylene glycol, hexadecane, and heptane on Krytox-oil-infused low-aspect-ratio micropillar surfaces with a macrotexture Wenzel roughness of up to r_W = 1.52.[17] They noted that the Wenzel equation using the apparent contact angle was in good agreement with measurements in the high-contact-angle range (i.e., 101.6° < θ_{app} < 121.3°) and at moderate roughness (i.e., r_W < 1.6) but started to deviate at the mid-to-low apparent contact angle range (i.e., 50.9° < θ_{app} < 70.5°) for their data. Their Supporting Information has top-view images (Figure S3) for heptane droplets that show faceted droplets when the roughness is greater than unity. No comments were provided on the faceting of droplets, so it is unclear whether this also applied to droplets of other liquids. This limits the extent to which our model, which assumes axisymmetry, can be applied to the data. It also limits the confidence in reported contact angles, which may depend on the viewing direction.

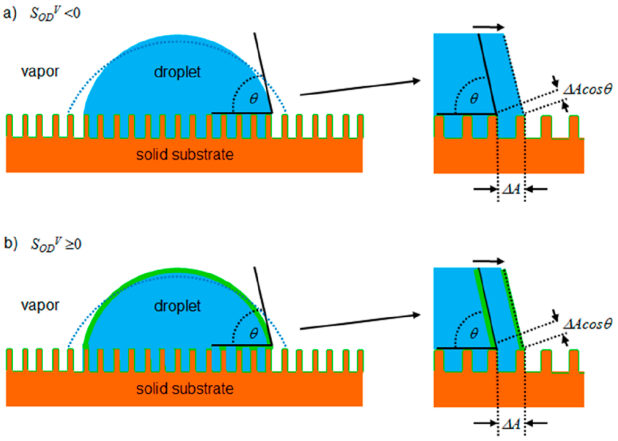

Figure 6. Surface free energy changes due to a one-period advance, $\Delta A(x)$, of the droplet edge on a macrotextured surface possessing a thin conformal SLIPS coating. Wenzel state (a) without lubricant wrapping (S_{OD}^{V} < 0) and (b) with lubricant wrapping (S_{OD}^{V} ≥ 0).

3.3. SLIPS-Modified Hemiwicking and Cassie-to-Wenzel Stability Equations. These ideas can also be applied to other wetting problems involving topography, including hemiwicking and the criteria for the stability of the Cassie−Baxter state and the transition to a Wenzel state.[14] For example, for hemiwicking into a textured surface, the surface free energy change for a liquid (with a liquid labeled D here for consistency with previous sections) to propagate along the texture by one period Δx is $\Delta F(x) = (\gamma_{DO} - \gamma_{OV})(r_W(x) - \varphi_S(x))\Delta A + \gamma_{eff}(1 - \varphi_S(x))\Delta A$ (Figure 7). If this reduces the surface free energy, then liquid will hemiwick into the structure, providing the apparent contact angle, $\theta_{app}(x)$, is smaller than the critical angle, $\theta_c(x)$, defined by

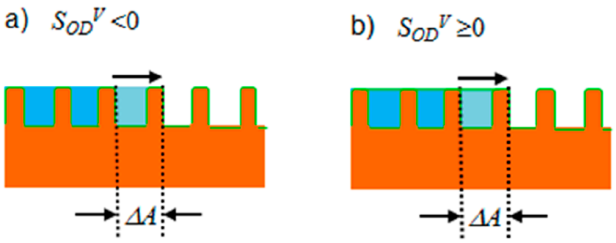

Figure 7. Surface free energy changes for hemiwicking (a) without lubricant wrapping (S_{OD}^{V} < 0) and (b) with lubricant wrapping (S_{OD}^{V} ≥ 0). In the former case, the liquid surface between the pillars does not have a lubricant coating, whereas in the latter case the liquid surface is entirely coated in a thin layer of the lubricant.

$$\cos\theta_c(x) = \frac{1 - \varphi_S(x)}{r_W(x) - \varphi_S(x)} \tag{9}$$

Interestingly, the critical angle defined by eq 9 is the same as for a nonlubricated solid texture and remains at a value determined by its design.

Similarly, the Cassie−Baxter state is energetically preferred over the Wenzel state, provided the apparent contact angle is larger than a critical angle given by $\theta_{st}(x)$, defined by

DOI: 10.1021/acs.langmuir.8b04136
Langmuir 2019, 35, 4197−4204

$$\cos\theta_{st}(x) = -\left(\frac{1-\varphi_S(x)}{r_W(x)-\varphi_S(x)}\right) \tag{10}$$

which gives a critical angle of 180° minus the critical angle for which hemiwicking occurs. Thus, the equations familiar from prior contact angle theory on textured surfaces should apply, provided the contact angle is replaced by the apparent contact angle defined by eq 4.

3.4. SLIPS-Modified Electric-Field-Controlled Apparent Contact Angles. The surface free energy approach taken for understanding apparent contact angles on thin SLIPS-coated topographically structured/textured surfaces can be extended to equilibrium contact angle considerations in other physical systems. In electrowetting on a dielectric, a conducting droplet (typically water with a small concentration of KCl) is used to define one electrical contact on a solid (typically hydrophobic) dielectric surface whose reverse surface is in contact with an electrical conductor.[15,41,42] This forms a capacitive structure, but with the droplet's solid−liquid interfacial contact area forming an electrode with a voltage-dependent area. To determine the equilibrium contact angle changes, the combination of the surface free energy and the capacitive energy changes is minimized, and this leads to a reduction in contact angle with the surface effectively becoming more hydrophilic. A thin SLIPS coating on top of the solid dielectric removes all droplet liquid−solid contacts, but an apparent contact angle still occurs and electrowetting can be performed by applying an external voltage, V.[21] The surface free energy change for a small change in the droplet apparent contact area is given by eq 5, where $\Delta A = 2\pi r\Delta r$ and r is the apparent contact radius. Assuming that any double-layer effects can be ignored, the energy change in charging due to the creation of the additional capacitor area is

$$\Delta U = \frac{-\varepsilon_o\varepsilon_r V^2}{2d} \tag{11}$$

where ε_o is the permittivity of free space, ε_r is the effective relative permittivity of the solid dielectric with the SLIPS coating, and d is total dielectric thickness. Setting the total energy change equal to zero gives the equilibrium condition

$$\cos\theta_{app}(V) = \cos\theta_{app}(0) + \frac{\varepsilon_o\varepsilon_r V^2}{2d\gamma_{eff}} \tag{12}$$

where $\cos\theta_{app}(0)$ is given by eq 4.

An alternative method to controlling a contact angle is to use an applied electric potential of form $V_0e^{-2z/\delta}$, where z is the vertical coordinate normal to the surface and δ is a penetration depth, to create a nonuniform electric field which decays with distance above a substrate and to use a dielectric liquid droplet of relative permittivity ε_l. When the droplet thickness is much larger than δ, changes in the applied voltage V cause the droplet to spread due to the storage of dielectrophoretic energy in the interfacial layer of the dielectric liquid of the droplet.[16,43] Assuming the system is in air, the change in interface-localized liquid dielectrophoretic energy is

$$\Delta U = \frac{-\varepsilon_o(\varepsilon_l - 1)V^2}{2\delta} \tag{13}$$

and the voltage-dependent apparent contact angle for this dielectrowetting becomes

$$\cos\theta_{app}(V) = \cos\theta_{app}(0) + \frac{\varepsilon_o(\varepsilon_l - 1)V^2}{2\delta\gamma_{eff}} \tag{14}$$

In this case, the dielectric properties of the lubricant liquid have been neglected due to the assumption of a sufficiently thin SLIPS coating. Equations 12 and 14 can be written in common notation for electric-field-controlled wetting as

$$\cos\theta_{app}(V) = \cos\theta_{app}(0) + [1-\cos\theta_{app}(0)]\left(\frac{V}{V_{Th}}\right)^2 \tag{15}$$

where V_{Th} is the voltage that would be needed to first create a film (i.e., $\theta_{app}(V_{Th}) \to 0$.[44] These formulas are consistent with the electrowetting and dielectrowetting experimental data presented by Brabcova et al.[21] Their data used a silicone-oil-infused hydrophobic nanoparticle SLIP coating with glycerol as the droplet and demonstrated both significantly reduced hysteresis in the apparent contact angle and linearity of cos $\theta_{app}(V)$ with voltage squared. In this work, a small hysteresis in the apparent contact angle of 3−4° was observed during dielectrowetting but not during electrowetting, which suggests the applied nonuniform electric field caused small changes in the SLIP surface used in the experiment.

4. COMPLEX SURFACE GEOMETRIES AND SHAPES

The ability to predict the apparent contact angle on a thin SLIPS or lubricant-coated surface using eq 4 also allows the equilibrium configuration for a droplet in contact with multiple surfaces or on a complex surface geometry to be predicted.

As an example of the first situation, consider a droplet between and in contact with two planar surfaces which form a wedge of opening angle 2β (inset to Figure 8). For perfectly smooth solid wedges formed by ordinary (non-SLIPS) surfaces, it is well known that when the contact angle of the droplet is between 90° + β and 180° the minimum surface free energy configuration of the droplet is a "liquid-barrel" shape: a spherical segment that intersects the two planes with the

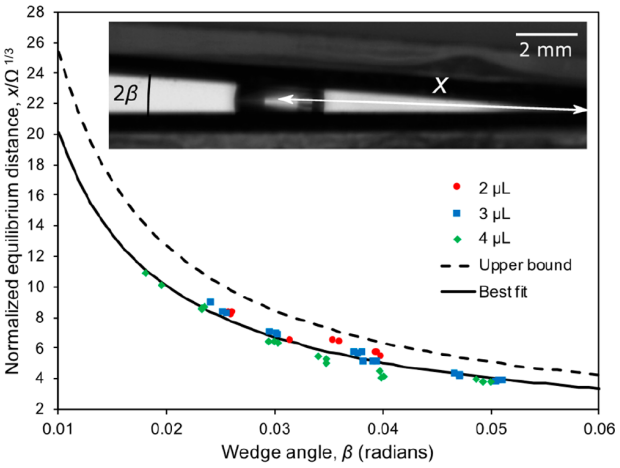

Figure 8. Normalized equilibrium position for a droplet inside a SLIPS wedge. The symbols correspond to experimental measurements; the dashed line corresponds to eq 16 using the upper-bound prediction of eq 4, θ_{app} = 108.4°. The solid line corresponds to a best fit to eq 16 which yields θ_{app} = 103°. Data taken from Ruiz-Gutiérrez et al.[45]

DOI: 10.1021/acs.langmuir.8b04136
Langmuir 2019, 35, 4197−4204

equilibrium contact angle, θ_e.[45,46] The droplet's equilibrium configuration can be described in terms of its radius and its equilibrium distance from the apex of the wedge, both of which are determined by the wedge angle, β, the contact angle, θ_e, and the droplet volume, Ω. This configuration was recently reported by Ruiz-Gutiérrez et al.,[45] who observed liquid-barrel shapes for water droplets, but in their experiment, the implementation used SLIPS wedges (inset to Figure 8). Because eq 4 allows the apparent contact angle to be calculated, the equilibrium position of the droplet in the wedge geometry, x, can now be predicted as a function of the apparent contact angle and the droplet volume using geometry:

$$x(\theta_{app}, \Omega) = -\frac{\cos\theta_{app}}{\sin\beta}\left[\frac{6\Omega}{\pi(\cos(3\theta_{app}) - 9\cos\theta_{app})}\right]^{1/3} \quad (16)$$

In their experiments, Ruiz-Gutiérrez et al.[45] used water droplets on micropatterned SLIP surfaces created via photolithography and infused with silicone oil. Figure 8 shows a comparison of the prediction of eq 16 with the experimental data using the upper-bound apparent contact angle predicted by eq 4, $\theta_{app} = 108.4°$, and a value arising from a best fit of eq 16 to the experimental data, $\theta_{app} = 103°$. This lower value of the apparent angle is reasonable, as the SLIP surfaces in their experiments were infused by dip-coating at relatively low speeds (of about 1 mm s^{-1}) and thus are expected to leave a relatively thick lubricant film similar to the surface shown in Figure 2b.

As an example of the second situation of a complex surface geometry, Wells et al. studied the response of a droplet on a smooth but regularly sinusoidal corrugated SLIP surface.[47] The surfaces were created using a 3D-printer resin and subsequently treated using the nanocoating method reported in Figure 2. On such surfaces, a droplet sits in equilibrium, adopting a shape that intersects the local tangent to the solid with an apparent contact angle $\theta_{app} = 109°$ (cf. Supporting Information in ref 47), which the authors used to successfully predict the stability of the droplet upon evaporation. Remarkably, the experimentally observed apparent angle is almost identical to the angle reported in Figure 2 for SLIPS on a glass substrate ($\theta_{app} = 108.4°$), which further supports the prediction of eq 4 that the apparent contact angle on SLIPS is independent of the underlying solid surface.

5. CONCLUSIONS

In this work, we have considered theoretically how apparent contact angles can be predicted in the thin-layer limit of liquid-infused or lubricant-impregnated surfaces defined by a small wetting ridge. We have argued that equilibrium can be defined for a wide variety of situations by using small surface free energy changes dominated by changes in the lubricant–droplet, lubricant–vapor, and droplet–vapor interfacial areas and that changes in the wetting ridges cause higher-order corrections. On a smooth nontextured surface, this results in an equation analogous to Young's law involving the lubricant–droplet and lubricant–vapor interfacial tensions and an effective interfacial tension for the droplet–lubricant–vapor or droplet–vapor interface depending on whether the oil has a positive spreading power on the droplet. We have shown how this view can justify the use of Cassie–Baxter, Wenzel, hemiwicking, and other topographic contact angle equations using the apparent contact angle based on macroscopic textures that retain a conformal thin SLIP surface coating. We have also argued that the same approach can be applied more widely to contact angle situations, such as electrowetting and dielectrowetting, and to complex surface shapes. Our work provides a conceptual framework which enables results from equilibrium contact angle theory to be applied to a wide variety of surfaces possessing thin lubricant layers for which there is no direct droplet contact with the underlying solid.

AUTHOR INFORMATION

Corresponding Author

*E-mail: glen.mchale@northumbria.ac.uk.

ORCID

Glen McHale: 0000-0002-8519-7986

Rodrigo Ledesma-Aguilar: 0000-0001-8714-0556

Notes

The authors declare no competing financial interest.

ACKNOWLEDGMENTS

G.G.W. acknowledges the financial support of the UK Engineering & Physical Sciences Research Council (EP/P026613/1).

REFERENCES

(1) Young, T. An Essay on the Cohesion of Fluids. *Philos. Trans. R. Soc. London* **1805**, *95*, 65–87.

(2) de Gennes, P. G. Statics and Dynamics: Wetting. *Rev. Mod. Phys.* **1985**, *57* (3), 827–863.

(3) Shirtcliffe, N. J. N. J.; McHale, G.; Atherton, S.; Newton, M. I. M. I. An Introduction to Superhydrophobicity. *Adv. Colloid Interface Sci.* **2010**, *161* (1–2), 124–138.

(4) Bonn, D.; Eggers, J.; Meunier, J.; Rolley, E. Wetting and Spreading. *Surfaces, Interfaces, and Colloids*; John Wiley & Sons, Inc.: New York; pp 415–447.

(5) Deegan, R. D.; Bakajin, O.; Dupont, T. F.; Huber, G.; Nagel, S. R.; Witten, T. A. Capillary Flow as the Cause of Ring Stains from Dried Liquid Drops. *Nature* **1997**, *389* (6653), 827–829.

(6) Erbil, H. Y. Y. Evaporation of Pure Liquid Sessile and Spherical Suspended Drops: A Review. *Adv. Colloid Interface Sci.* **2012**, *170* (1–2), 67–86.

(7) Wong, T.-S.; Kang, S. H.; Tang, S. K. Y.; Smythe, E. J.; Hatton, B. D.; Grinthal, A.; Aizenberg, J. Bioinspired Self-Repairing Slippery Surfaces with Pressure-Stable Omniphobicity. *Nature* **2011**, *477* (7365), 443–447.

(8) Smith, J. D.; Dhiman, R.; Anand, S.; Reza-Garduno, E.; Cohen, R. E.; McKinley, G. H.; Varanasi, K. K. Droplet Mobility on Lubricant-Impregnated Surfaces. *Soft Matter* **2013**, *9* (6), 1772–1780.

(9) Lafuma, A.; Quéré, D. Slippery Pre-Suffused Surfaces. *EPL (Europhysics Lett.* **2011**, *96* (5), 56001.

(10) Guan, J. H.; Wells, G. G.; Xu, B.; Bin; McHale, G.; Wood, D.; Martin, J.; Stuart-Cole, S. Evaporation of Sessile Droplets on Slippery Liquid-Infused Porous Surfaces (SLIPS). *Langmuir* **2015**, *31* (43), 11781–11789.

(11) Harkins, W. D.; Feldman, A. Films. The Spreading of Liquids and the Spreading Coefficient. *J. Am. Chem. Soc.* **1922**, *44* (12), 2665–2685.

(12) Bico, J.; Reyssat, É.; Roman, B. Elastocapillarity: When Surface Tension Deforms Elastic Solids. *Annu. Rev. Fluid Mech.* **2018**, *50* (1), 629–659.

(13) Style, R. W.; Dufresne, E. R. Static Wetting on Deformable Substrates, from Liquids to Soft Solids. *Soft Matter* **2012**, *8* (27), 7177.

(14) Quéré, D. Wetting and Roughness. *Annu. Rev. Mater. Res.* **2008**, *38* (1), 71–99.

DOI: 10.1021/acs.langmuir.8b04136
Langmuir 2019, 35, 4197–4204

(15) Mugele, F.; Baret, J.-C. Electrowetting: From Basics to Applications. *J. Phys.: Condens. Matter* **2005**, *17* (28), R705−R774.
(16) Edwards, A. M. J.; Brown, C. V.; Newton, M. I.; McHale, G. Dielectrowetting: The Past, Present and Future. *Curr. Opin. Colloid Interface Sci.* **2018**, *36*, 28−36.
(17) Dai, X.; Stogin, B. B.; Yang, S.; Wong, T.-S. Slippery Wenzel State. *ACS Nano* **2015**, *9* (9), 9260−9267.
(18) Dong, Z.; Schumann, M. F.; Hokkanen, M. J.; Chang, B.; Welle, A.; Zhou, Q.; Ras, R. H. A.; Xu, Z.; Wegener, M.; Levkin, P. A. Superoleophobic Slippery Lubricant-Infused Surfaces: Combining Two Extremes in the Same Surface. *Adv. Mater.* **2018**, *30* (45), 1803890.
(19) Hao, C.; Liu, Y.; Chen, X.; He, Y.; Li, Q.; Li, K. Y.; Wang, Z. Electrowetting on Liquid-Infused Film (EWOLF): Complete Reversibility and Controlled Droplet Oscillation Suppression for Fast Optical Imaging. *Sci. Rep.* **2015**, *4* (1), 6846.
(20) Bormashenko, E.; Pogreb, R.; Bormashenko, Y.; Aharoni, H.; Shulzinger, E.; Grinev, R.; Rozenman, D.; Rozenman, Z. Progress in Low Voltage Reversible Electrowetting with Lubricated Polymer Honeycomb Substrates. *RSC Adv.* **2015**, *5* (41), 32491−32496.
(21) Brabcova, Z.; McHale, G.; Wells, G. G.; Brown, C. V.; Newton, M. I. Electric Field Induced Reversible Spreading of Droplets into Films on Lubricant Impregnated Surfaces. *Appl. Phys. Lett.* **2017**, *110* (12), 121603.
(22) He, X.; Qiang, W.; Du, C.; Shao, Q.; Zhang, X.; Deng, Y. Modification of Lubricant Infused Porous Surface for Low-Voltage Reversible Electrowetting. *J. Mater. Chem. A* **2017**, *5* (36), 19159−19167.
(23) Abe, J.; Tenjimbayashi, M.; Shiratori, S. Electrospun Nanofiber SLIPS Exhibiting High Total Transparency and Scattering. *RSC Adv.* **2016**, *6* (44), 38018−38023.
(24) Bazyar, H.; Lv, P.; Wood, J. A.; Porada, S.; Lohse, D.; Lammertink, R. G. H. Liquid-Liquid Displacement in Slippery Liquid-Infused Membranes (SLIMs). *Soft Matter* **2018**, *14* (10), 1780−1788.
(25) Luo, J. T. T.; Geraldi, N. R. R.; Guan, J. H.; McHale, G.; Wells, G. G.; Fu, Y. Q. Q. Slippery Liquid-Infused Porous Surfaces and Droplet Transportation by Surface Acoustic Waves. *Phys. Rev. Appl.* **2017**, *7* (1), 014017.
(26) Hui Guan, J.; Ruiz-Gutiérrez, É.; Xu, B.; Bin; Wood, D.; McHale, G.; Ledesma-Aguilar, R.; George Wells, G. Drop Transport and Positioning on Lubricant-Impregnated Surfaces. *Soft Matter* **2017**, *13* (18), 3404−3410.
(27) Kim, P.; Kreder, M. J.; Alvarenga, J.; Aizenberg, J. Hierarchical or Not? Effect of the Length Scale and Hierarchy of the Surface Roughness on Omniphobicity of Lubricant-Infused Substrates. *Nano Lett.* **2013**, *13* (4), 1793−1799.
(28) Zhang, P.; Chen, H.; Zhang, L.; Zhang, D. Anti-Adhesion Effects of Liquid-Infused Textured Surfaces on High-Temperature Stainless Steel for Soft Tissue. *Appl. Surf. Sci.* **2016**, *385*, 249−256.
(29) Kim, P.; Wong, T. S.; Alvarenga, J.; Kreder, M. J.; Adorno-Martinez, W. E.; Aizenberg, J. Liquid-Infused Nanostructured Surfaces with Extreme Anti-Ice and Anti-Frost Performance. *ACS Nano* **2012**, *6* (8), 6569−6577.
(30) Li, Y.; John, J.; Kolewe, K. W.; Schiffman, J. D.; Carter, K. R. Scaling Up Nature: Large Area Flexible Biomimetic Surfaces. *ACS Appl. Mater. Interfaces* **2015**, *7* (42), 23439−23444.
(31) Seiwert, J.; Clanet, C.; Quéré, D. Coating of a Textured Solid. *J. Fluid Mech.* **2011**, *669*, 55−63.
(32) Semprebon, C.; McHale, G.; Kusumaatmaja, H. Apparent Contact Angle and Contact Angle Hysteresis on Liquid Infused Surfaces. *Soft Matter* **2017**, *13* (1), 101−110.
(33) Kreder, M. J.; Daniel, D.; Tetreault, A.; Cao, Z.; Lemaire, B.; Timonen, J. V. I.; Aizenberg, J. Film Dynamics and Lubricant Depletion by Droplets Moving on Lubricated Surfaces. *Phys. Rev. X* **2018**, *8* (3), 31053.
(34) Banpurkar, A. G.; Nichols, K. P.; Mugele, F. Electrowetting-Based Microdrop Tensiometer. *Langmuir* **2008**, *24* (19), 10549−10551.
(35) Peters, F.; Arabali, D. Interfacial Tension between Oil and Water Measured with a Modified Contour Method. *Colloids Surf., A* **2013**, *426*, 1−5.
(36) Rykaczewski, K.; Paxson, A. T.; Staymates, M.; Walker, M. L.; Sun, X.; Anand, S.; Srinivasan, S.; McKinley, G. H.; Chinn, J.; Scott, J. H. J.; et al. Dropwise Condensation of Low Surface Tension Fluids on Omniphobic Surfaces. *Sci. Rep.* **2015**, *4*, 4158.
(37) McHale, G. Cassie and Wenzel: Were They Really so Wrong? *Langmuir* **2007**, *23* (15), 8200−8205.
(38) Gao, L.; McCarthy, T. J. How Wenzel and Cassie Were Wrong. *Langmuir* **2007**, *23* (7), 3762−3765.
(39) Newton, M. I.; Elliott, S. J.; Shirtcliffe, N. J.; McHale, G. Superhydrophobicity: Localized Parameters and Gradient Surfaces. *Contact Angle, Wettability and Adhesion*; Brill Academic Publishers, 2009; Vol. 6, pp 217−234.
(40) McHale, G.; Newton, M. I. M. I.; Shirtcliffe, N. J. N. J. Dynamic Wetting and Spreading and the Role of Topography. *J. Phys.: Condens. Matter* **2009**, *21* (46), 464122.
(41) Berge, B. Electrocapillarity and Wetting of Insulator Films by Water. *C. R. Acad. Des Sci. Ser. II* **1993**, *317* (2), 157−163.
(42) Vallet, M.; Berge, B.; Vovelle, L. Electrowetting of Water and Aqueous Solutions on Poly(Ethylene Terephthalate) Insulating Films. *Polymer* **1996**, *37* (12), 2465−2470.
(43) McHale, G.; Brown, C. V.; Newton, M. I.; Wells, G. G.; Sampara, N. Dielectrowetting Driven Spreading of Droplets. *Phys. Rev. Lett.* **2011**, *107* (18), 186101.
(44) McHale, G.; Brown, C. V.; Sampara, N. Voltage-Induced Spreading and Superspreading of Liquids. *Nat. Commun.* **2013**, *4*, 1605.
(45) Ruiz-Gutiérrez, É.; Guan, J. H.; Xu, B.; McHale, G.; Wells, G. G.; Ledesma-Aguilar, R. Energy Invariance in Capillary Systems. *Phys. Rev. Lett.* **2017**, *118* (21), 218003.
(46) Ruiz-Gutiérrez, É.; Semprebon, C.; McHale, G.; Ledesma-Aguilar, R. Statics and Dynamics of Liquid Barrels in Wedge Geometries. *J. Fluid Mech.* **2018**, *842*, 26−57.
(47) Wells, G. G.; Ruiz-Gutiérrez, É.; Le Lirzin, Y.; Nourry, A.; Orme, B. V.; Pradas, M.; Ledesma-Aguilar, R. Snap Evaporation of Droplets on Smooth Topographies. *Nat. Commun.* **2018**, *9* (1), 1380.

DOI: 10.1021/acs.langmuir.8b04136
Langmuir 2019, 35, 4197−4204

LANGMUIR
Cite This: *Langmuir* 2019, 35, 9146–9151
Article
pubs.acs.org/Langmuir

Droplet Retention and Shedding on Slippery Substrates

Bethany V. Orme, Glen McHale, Rodrigo Ledesma-Aguilar, and Gary G. Wells*

Smart Materials & Surfaces Laboratory, Faculty of Engineering & Environment, Northumbria University, Newcastle upon Tyne NE1 8ST, U.K.

ABSTRACT: A significant limitation for droplet mobility on solid surfaces is to overcome the inherent pinning of the droplet's contact line that occurs because of chemical/physical heterogeneities. A recent innovation is to use surface texture or porosity to create a stabilized lubricant surface. Droplets on such slippery liquid-infused porous surfaces (SLIPS)/lubricant-impregnated surfaces (LIS) are highly mobile because of the lubricant layer. Low pinning of the contact line reduces the energy required to move a droplet; however, it makes it difficult to accurately position the droplet or to stop its motion altogether. In this paper, a simple structure (step), as small as a few microns in height, is used to introduce controlled droplet pinning on a slippery substrate. The key effect is identified as the capillary force, arising from the interaction between the lubricant menisci created by the step and droplet. The effect of changing step height, lubricant thickness, and initial position on step–droplet interactions has been investigated, showing that droplets can both be repelled from and attracted to the step. To measure the adhesion strength, we report droplet detachment angle measurements under gravity and scaling of force with the lubricant thickness/step height ratio. Under certain conditions, the interaction strength is sufficient to ensure droplet–step attachment even when the surface is rotated to an upside-down orientation. These findings can motivate the design of SLIPS structures, capable of shedding or retaining droplets preferentially, for example, according to the size or wettability, relevant to applications from microfluidics to fog harvesting.

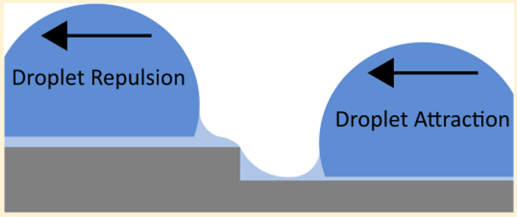

INTRODUCTION

The ability to accurately position a droplet on a surface has relevance in a variety of industrial and practical applications, such as inkjet printing,[1] self-cleaning surfaces,[2] precise deposition of particles,[3,4] microfluidics,[5] drug delivery,[6] and cell analysis.[7]

Recent research into the surface design has focused on suppressing,[8,9] and in some cases eliminating, droplet pinning to create freely moving contact lines.[10,11] This increases the ease with which a droplet can be transported by reducing the frictional force created by the droplet's direct contact with the underlying substrate.[12] The reduction of this frictional force has previously been achieved using superhydrophobic surfaces which reduce the solid–liquid contact area,[13−15] creating a Cassie–Baxter[16,17] condition or by chemical treatments such as Teflon.[18] Low pinning has been most successfully achieved by producing slippery liquid-infused porous surfaces or lubricant-impregnated surfaces (SLIPS/LIS) which are inspired by the Nepenthes pitcher plant[19] and based on an imbibed lubricant layer.[20]

However, SLIPS/LIS lack the ability to accurately control the position of a droplet. Previous attempts to overcome this barrier include introducing an "on/off switch" to the SLIPS properties via thermal actuation,[21] but controlling the droplet in the SLIPS phase is difficult.

Accidental surface defects on a SLIPS/LIS can pin droplets into fixed, stationary positions and can be attributed to large increases in droplet sliding angles. Drawing inspiration from this idea, the forces created by tailor-made small-scale structures on an otherwise slippery surface could be implemented as a method for droplet positioning and control. Because any surface defect, or any droplet on a SLIP surface, creates deformation in the meniscus of the lubricating liquid, it is expected that capillary forces arise between a droplet and a surface defect even in the absence of direct droplet/solid contact.[22] This is similar to the Cheerios effect[23] and responsible for the attractive interactions between floating solid objects or bubbles mediated by liquid–gas menisci. A similar effect has also been seen for droplets on soft, elastic solids where the thickness of the layer and conservation of volume determines whether the force is attractive or repulsive.[24]

Recently, Guan et al. showed aspects of the Cheerios effect on a SLIPS-coated macrostructure, in the form of a V-shaped channel. This was used to accurately guide and position a droplet.[25] In this case, the lubricating liquid layer was mobile and able to fully cloak the droplet because of a positive spreading coefficient.[10,22] The wetting ridge at the channel wall and the wetting ridge around the base of the droplet both have the same sign of curvature, leading to an overall attractive capillary force.[23] However, the Cheerios effect for particles on liquid surfaces can also create repulsive capillary forces using menisci, or wetting ridges, with curvature of opposite signs.[24]

Received: March 29, 2019
Revised: June 11, 2019
Published: June 19, 2019

DOI: 10.1021/acs.langmuir.9b00931
Langmuir 2019, 35, 9146–9151

Despite these previous attempts to introduce accurate droplet positioning to surfaces, controlling the droplet on a SLIPS/LIS remains an open challenge. In this paper, experiments are reported that show how a structure, a step as small as 7 μm in height, treated with an easy-to-apply SLIPS coating[26] is capable of producing attractive and repulsive forces on a droplet in a reproducible manner. The mechanism is controlled purely by capillary forces arising from the combination of the droplets meniscus, which forms wetting ridges with positive curvature (where the meniscus rises above the plane of the interface)[27] and the positive meniscus created by the solid step. The strength of the attractive interaction is characterized by measuring the detachment angle of droplets as a function of step height, oil thickness, and initial droplet deposition position relative to the step. A scaling relation for this force in terms of the ratio of height of the step to oil thickness is reported.

METHOD

Figure 1a,b shows the step sample preparation method. Glass slides/wafers were used as a substrate base onto which a step was attached via two different methods. In method 1, a rectangular glass cover slip was attached to the top of a 25 mm × 75 mm borosilicate, glass microscope slide. This method created a sharp, vertical step with a fixed height of 140 μm.

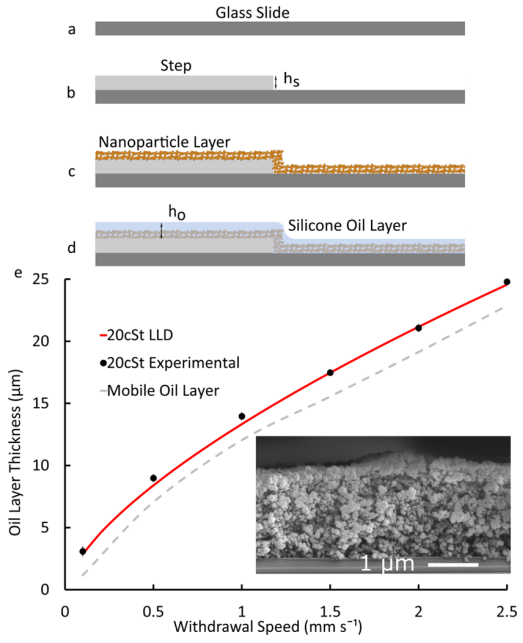

Figure 1. Sample production and characterization. (a–d) Schematic of the production of the step from, a glass cover slip and SU-8 (via simple photolithography), where h_s is varied and measured by white-light optical profilometry. The nanoparticle coating consists of a commercial product (Glaco) and applied via spray coating. Silicone oil imbibition is performed by a dip-coating method where the withdrawal speed can be varied to produce different oil layer thicknesses. (e) Oil thickness for different withdrawal speeds. Black dots are the experimental layer thickness measured using a reflectometer. Red solid line is a fit to the LLD equation. The grey dashed line indicates the estimated oil layer thickness.(e-inset) SEM image of a typical sample cross section, indicating the uniformity of the coating and nanoparticle layer height..

Method 2 was used to create steps of variable heights. Standard photolithographic techniques were used to apply at a layer of negative photoresist, SU-8 (MicroChem, SU-8 2010, 2050 and 2100). The thickness of the layer was varied in the range of 7–150 μm by changing the viscosity and spin speed. The exposure time was varied in accordance with the SU-8 thickness. The heights of the resulting SU-8 steps were measured using white-light optical profilometry (Bruker Contour GT).

Figure 1c,d depicts the process of coating the steps with a thin SLIPS layer. First, a nanoparticle- and solvent-based coating (Glaco Mirror Coat) was sprayed onto the samples to create a uniform thickness, porous hydrophobic coating[26] (Figure 1c). The nanoparticle-layered samples were then infused with a lubricating layer of silicone oil (surface tension, γ = 19.8 mN m^{-1} and viscosity, η = 19 mPa s) by automated dip coating (Fisnar F4200N). The automation allowed for controllable sample withdrawal from a silicone oil bath, with the withdrawal speed, V, varied within the range of 0.1–2.5 mm s^{-1}. This corresponds to the thickness of the oil layer, h_o, shown in Figure 1d.

To calibrate the relationship between the thickness of the oil layer, h_o, and the withdrawal speed, the apparent thickness of the oil layer was measured using reflectometry (Filmetrics F20) and the refractive index of silicone oil, 1.403. The experimental results are reported in Figure 1e (black circles) and are well fitted by the Landau–Levich–Derjaguin (LLD)[28,29] equation (Figure 1e, solid red line), $h_o \approx 0.94aCa^{2/3}$, where a is the capillary length of the oil (≈1.46 mm) and Ca is the capillary number ($Ca = \eta V/\gamma$).

During the dip coating procedure, the oil fully coats the particles to create index-matched layers and renders the porous nanoparticle layer transparent; therefore, the value measured by reflectometry is the combination of the two layers. The uniformity and thickness of the dry nanoparticle layer was measured via cross-sectional scanning electron microscopy (SEM) scans of several samples (Tescan MIRA3). Figure 1e inset shows a typical SEM scan of the nanoparticle layer. The average thickness of the nanoparticle layer was determined to be 1.93 ± 0.16 μm. The thickness of the mobile oil layer was determined by subtracting the thickness of the nanoparticle layer from the apparent thickness measured by reflectometry (shown as the gray dotted line in Figure 1e). Whilst it is expected there will be some oil drainage of the mobile oil layer, on the experimental timescale, the greatest oil weight loss percentage (from the thickest oil sample, h_o = 24.79 μm) is only 2.72%.

The thickness of the mobile layer is the determining factor when considering the angle formed when the droplet is in contact with the surface. For the SLIP surfaces produced in these experiments, it is assumed there is no direct solid/droplet contact bcause of the reduction in contact-angle hysteresis between a dry surface and one that has been infused with an oil layer. For the dry surface, the hysteresis is measured to be 7.5° ± 0.5° and when lubricated, it is measured to be 0.56° ± 0.20°. Even for a surface with a thermodynamically stable lubricating layer of thickness equivalent to the particle layer, the contact-angle hysteresis is still lower than the dry surface at 3.4° ± 0.2°. Despite the lack of direct contact, the water droplet and oil layer still form an angle determined by the interfacial tension and is given by the Neumann triangle.[30] For a thin oil layer, there is only a small availability of oil, creating a small wetting ridge and apparent contact angle ≈100°. As the oil layer is

DOI: 10.1021/acs.langmuir.9b00931
Langmuir 2019, 35, 9146–9151

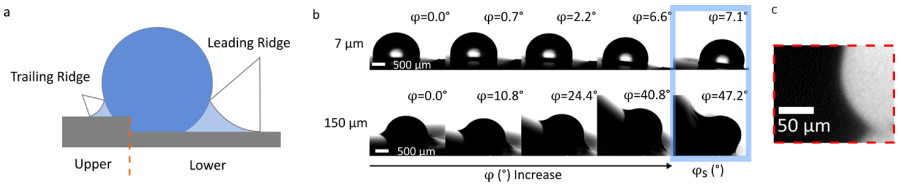

Figure 2. Changes in position and configuration of droplets by varying step height (h_s) and the effect this has on the detachment angle (φ_s). (a) Schematic showing how a water droplet interacts with the system with the upper and lower sections designated on the sample and the asymmetry between trailing and leading wetting ridges defined. (b) Sequence of images showing droplet shape evolution during sample tilting, step detachment, and finally droplet motion as h_s increases. (c) In the dashed red box, there is an image zoomed 10 times to depict more clearly the smallest wetting ridge achievable on the thinnest oil layer (h_o = 3.09 μm).

increased, the wetting ridge grows and the apparent contact angle decreases.[31]

To determine whether it is more energetically favorable to have a water droplet that will be fully cloaked with the lubricating liquid or an uncloaked water droplet, a simple spreading coefficient calculation can be completed for the combination of liquids used within this system. To be cloaked, the interfacial tension for water/vapor ($\gamma_{w,v}$) must be greater than the combination of the water/oil and oil/vapor interfaces ($\gamma_{w,o} + \gamma_{o,v}$), meaning the spreading parameter must be positive

$$S^{v}_{w,o} = \gamma_{w,v} - \gamma_{w,o} - \gamma_{o,v} \geq 0 \quad (1)$$

By using $\gamma_{w,v}$ = 72.8 mN m^{-1}, $\gamma_{w,o}$ = 38 mN m^{-1},[32] and $\gamma_{o,v}$ = 19.8 mN m^{-1},[31] the spreading parameter is calculated to be 15.8 mN m^{-1}; therefore, the water droplet will be fully cloaked by the oil.

To characterize the static friction acting on a droplet on the slippery surfaces, the sliding angle of multiple droplets has been measured. In this instance, the sliding angle, φ_s, is defined as the threshold angle for which the surface must be inclined to induce the onset of constant droplet motion. Water droplets of 2 μL were used to ensure that the droplet diameter was below the capillary length, thus maintaining a spherical cap and ruling out gravitational effects on the droplet shape. Each sample was placed on the tilting stage of a Kruss DSA30 contact-angle meter and a droplet placed was onto the step. The sample was then tilted in a direction parallel to the step until motion was observed. The average sliding angle was measured to be 0.56° ± 0.20°.

RESULTS AND DISCUSSION

Step Adhesion Force. To measure the adhesion force of the step, droplets of volume 2 μL were placed below a step coated in a layer of silicone oil. The initial inclination of the sample was 0°, with the sample being horizontal, so no external forces acted on the droplets. The droplets were immediately attracted to the step, suggesting an unbalanced capillary force created by the interaction between the wetting ridges produced by both the step and the droplet. Figure 2a shows a schematic of the system and the positioning of the water droplet in relation to the step. Once the droplet had settled in a static position, the sample was tilted in a direction normal to the step where gravity pulled the droplet away from the step. The angle of tilt was changed in increments of 0.20°. Figure 2b shows the side profiles of the droplets throughout the tilting process. The last image in the sequence shows the droplet at the point of detachment. On a 7 μm SU-8 step coated in a 3.09 μm layer of silicone oil, the sliding or detachment angle, φ_s, occurred at φ_s = 7.10° ± 0.20°, which is 1 order of magnitude larger than the sliding angle measured on a flat surface. The experiment was repeated across several samples, with five droplets deposited onto each separate sample to ensure the adhesion force was only being governed by the step. The average detachment angle obtained was 7.18° ± 0.31°.

Changing the step height to a maximum of 150 μm leads to similar observations, albeit with a substantially larger average detachment angle of 46.22° ± 1.63°. The droplet itself maintains a spherical cap, however, it can be seen that there is now a very clear asymmetry between the right-hand side wetting ridge (leading ridge) and the left-hand side (trailing ridge) (Figure 2b, bottom row), indicating the presence of capillary force balancing the driving force of gravity. When comparing the top and bottom row images in Figure 2b as well the enlarged image of the wetting ridge for the 7 μm step height (Figure 2c), it is clear that the larger step height (150 μm) produces larger wetting ridge, indicating greater oil availability. This is likely due to the droplet drawing oil into the ridge along the filled corner of the step and not from the thin film of oil. Because the curvature of the wetting ridge is weaker at the leading droplet edge than that of the trailing droplet edge, higher pressure is expected at the front of the droplet. This disparity enables the droplet to remain stuck to the step with a flow of lubricating liquid through the ridge from leading to trailing, balancing the gravitational force. Hence, stronger capillary force (due to the larger difference in ridge curvature) explains the significantly higher detachment angle.

Figure 3a shows the variation of the detachment angle as a function of the step height, h_s on substrates coated with different thicknesses of the oil layer. The data show a linear increase of φ_s with h_s, which holds good regardless of the material used to create the step (glass or SU-8). For a given step height, however, increasing the thickness of the oil layer has the effect of reducing the detachment angle (Figure 3a—black and red markers). To examine the effect of increasing the thickness of the oil layer in more detail, experiments in the range of $h_o \approx 3-25$ μm were carried out. The data for h_s = 140 μm confirms a decrease in the detachment angle with increasing oil layer thickness (colored triangles in Figure 3a). Such a reduction on the adhesion force is likely due to a reduction in the difference in curvature of the leading and trailing ridges caused by the restriction to the shape of the wetting ridge imposed by the thickness of the oil layer. This concept was examined by Semprebon et al.[33] where the droplet is seen to deform more as the wetting ridge pressure increases, which is equivalent to decreasing the oil layer thickness. The combination of the two length scales, oil thickness and step height, used in this experiment appears to show an approach to saturation at ≈12° for the largest values of oil thickness (h_o = 21.07 and 24.79 μm). Therefore, the adhesion force at the detachment angle, (φ_s), is expected to be the capillary force,

DOI: 10.1021/acs.langmuir.9b00931
Langmuir 2019, 35, 9146−9151

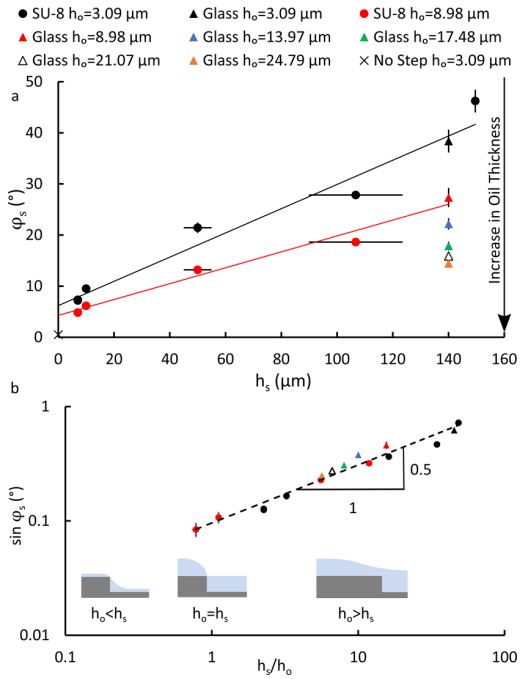

Figure 3. Effect on the detachment angle (φ_s) as the step height (h_s) increases. (a) Detachment angle (φ_s) data for increasing step heights (black circles and black triangle) for the thinnest oil layer (3.09 μm). Red circles and red triangle show the reduction of φ_s for a thicker oil layer. All triangles indicate the evolution of φ_s from minimum to maximum oil thickness. Each of the data points corresponds to an average of five experimental results. (b) Data from (a) plotted on a log–log scale with accompanying oil layer schematics. sin φ_s scales as the square root of the ratio of step height to oil thickness.

F_{cap}, balanced by the gravitational force, F_g, acting on the droplet. Because of the fact that the droplet is stationary, any viscous drag effects are ignored. Because $F_g \approx \sin \varphi_s$, $F_{cap} \approx \sin \varphi_s$. The dependence of sin φ_s on the step height and the thickness of the oil layer is shown in Figure 3b. As h_s controls the geometry of the step and h_o the length scale of the oil meniscus, it is reasonable to assume that the force is dependent on the ratio h_s/h_o. As shown in Figure 3b, a plot of sin φ_s versus (h_s/h_o) leads to a collapse of the data onto a single curve, which appears to fit a power law in the form $F_{cap} \approx (h_s/h_o)^{1/2}$.

Effect of the Initial Position of the Droplet Relative to the Step. By splitting the step into two distinct sample sections, upper and lower, the initial droplet deposition position was investigated. The upper section is that seen at the top of the step and the lower section is the portion of the sample below the step (Figure 2a).

Droplets (2 μL) were placed onto the upper section of a 140 μm step for different oil thicknesses. On deposition, droplet repulsion from the step can be seen. As the lubricant layer is expected to be pinned to the step corner,[34] a meniscus of negative curvature is formed at the corner (where the meniscus curves below the interface).[27] Therefore, there is a combination of menisci of opposite curvatures, and hence, the repulsion can be explained.

Tilting the sample clockwise so that gravity forces the droplet toward the step leads to a two-stage process before the droplet is finally detached and slides down the surface. First, for a range of tilting angles, the droplet remains above the step because of the repulsive force. During this stage, the leading-edge wetting ridge continues to grow until a tilting angle where the drop overcomes the corner and moves to the lower section of the step. At this point, the attractive force acts, adhering the droplet to the step and retaining the droplet on the surface in a stationary position. Further tilting is required until the droplet fully detaches and slides down. As shown in Figure 4a, this final

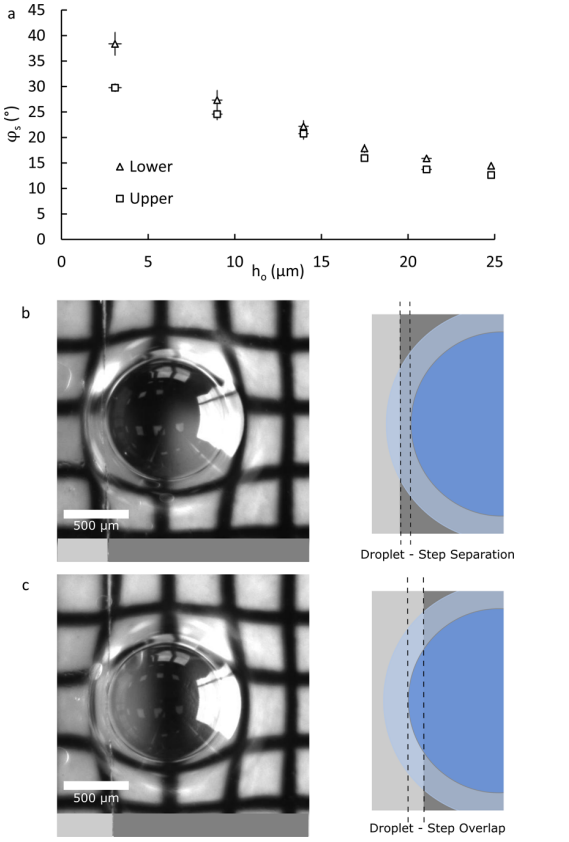

Figure 4. Exact droplet positions when the droplet has arrived at its final stationary point on the stepped samples, close to the point of detachment, given differing initial positions. (a) Detachment angles for 140 μm hs with increasing oil layer thickness. Squares initial position on the step's upper portion, triangles on the lower, both tilted in a clockwise direction (away from the step). (b) Top view of 2 μL droplet close to step detachment, with its initial position having been on the upper portion of the step, along with a schematic to show droplet separation from the step. (c) Droplet (2 μL) close to step detachment where the droplet initial position was on the lower portion of the stepped sample. The accompanying schematic indicates the droplet overlap with the step.

detachment angle is consistently below the values measured for droplets initially placed on the lower sample section; this becomes more prominent for thinner oil layers. Therefore, the droplets exhibit a different behavior depending on the initial conditions of the experiment.

A possible mechanism for this effect is the relaxation that the droplets undergo in two different initial positions. A droplet initially placed on the lower section is only subject to the capillary force formed by the droplet and step wetting ridges, pulling the droplet into a stationary position, adhered to the step. However, for a droplet initially placed on the upper section, the transition to the lower stationary position occurs

DOI: 10.1021/acs.langmuir.9b00931
Langmuir 2019, 35, 9146–9151

under two opposing forces of gravity and capillary force. Therefore, the difference between these forces reduces the step adhesion force. Indeed, the top-view images of the droplets presented in Figure 4b,c confirm that the contact between the step and droplet changes, depending on the initial droplet deposition position. When arriving from the upper section (Figure 4b), the droplet is deformed slightly by the step, with the trailing edge becoming flattened. However, the droplet itself does not appear to be in contact with the step and has, in fact, a droplet−step separation of 54.45 μm ± 1.66 μm. When arriving to the step from the lower section (Figure 4c), both the wetting ridge and droplet are attached to the step giving an average droplet−step overlap of 88.34 μm ± 1.66 μm. This difference in configuration is most likely the cause for the observed difference in the detachment angles between the two initial conditions.

What is also noticeable is the reduction in the difference between the detachment angle in the two configurations as h_o is increased. This can be attributed to the difference in the droplet/wetting ridge contact area on the step. For thin oil layers, the difference between having both the droplet and wetting ridge attached to the step and just the wetting ridge is large because of the small size of the wetting ridge and equates to a large difference in the force required to detach the droplets. However, with a larger wetting ridge changing between purely wetting ridge attachment and both droplet and wetting ridge attachment leads to a small overall change in the contact area and therefore a small change in force required to detach the droplet.

Effect of the Tilting Direction. To investigate the full range, the interactions between droplets and steps, a set of experiments was conducted where the substrate was tilted in the opposite, negative direction (clockwise), and the droplets start on the same upper/lower sample sections previously defined. In these experiments, a droplet initially on the lower surface must now climb the step before being detached from the surface and a droplet on the upper surface must simply move away from the step. Figure 5 shows measurements for all four possible configurations. Figure 4a,b above the 0° axis show the data we have previously discussed.

Remarkably, for droplets that must climb the step coated in thin oil layers, the sample can undergo a full 180° rotation whilst still retaining the droplet (indicated by the crosses in Figure 5a). The final sample position results in an upside-down orientation of the droplet. If the rotation was to continue, the droplet will transition from its original configuration (droplet deposited below the step and tilted anticlockwise) to the configuration seen on the upper, positive axis of Figure 5a.

As previously mentioned, a droplet placed above the step is initially repelled from the step before again becoming stationary away from the effects of the oil curvatures. Hence, it is expected that the angle required for droplets to move away from the top of the step matches the sliding angle on a perfectly flat SLIPS (in this case 0.56° ± 0.20°). This is indeed the case, as shown by filled triangles in Figure 5b.

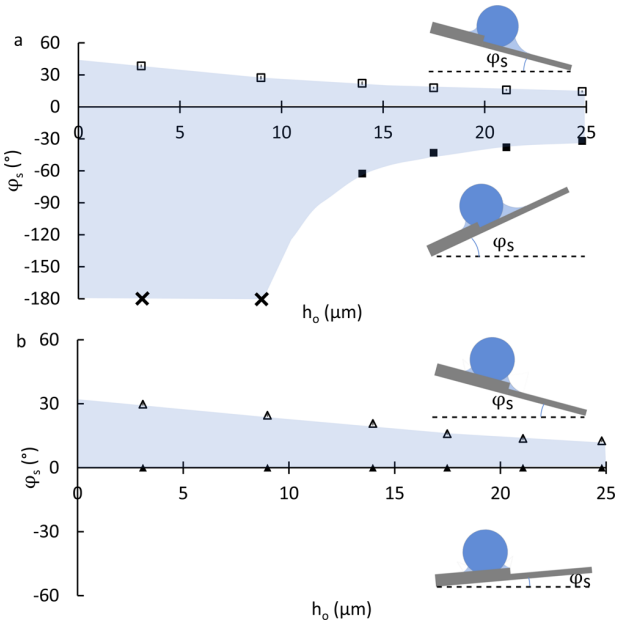

Figure 5. Changes in the droplet initial position and the direction of tilt (clockwise/anticlockwise). (a) Comparison between 2 μL droplets placed on the lower portion of the step and tilted both clockwise and anticlockwise for increasing oil thickness. The shaded area indicates where the droplet is stationary on the surface and stuck to the step. The (crosses) indicate droplets that did not slide at all on the surface and remained there even at 180°. (b) Droplet (2 μL) placed on the upper portion of the step and the same procedure as seen applied. The error bars on both graphs are equivalent to the size of the symbols and each data point corresponds to an average of results from five experiments.

CONCLUSIONS

In this study, the interaction between water droplets and a SLIPS/LIS-coated macroscopic, linear step has been investigated, with a view to improving control in droplet retention and shedding. The effect of the step is to induce the formation of a meniscus of the SLIPS/LIS lubricant layer, which leads to capillary interactions with the meniscus of the lubricant layer induced by a droplet. Droplets are attracted to the lower face of a step whilst they are repelled from the top edge of the step in a manner consistent with the Cheerios effect. The capillary force exerted on a droplet by the lower side of a step has been characterized by measuring the detachment angle in the presence of gravity for different step heights/oil layers and found that, for the range of measurements considered in our experiments, this force scales as $F_{cap} \approx (h_s/h_o)^{1/2}$. Whilst the theoretical model for why F_{cap} scales to half power is still unclear, it is a subject that requires further investigation. It has also been shown that the capillary force depends on the initial position of the droplet relative to the step. A droplet approaching from the upper section of a step experiences lower adhesion force because of the effect of gravity, creating a lower detachment angle and a "memory" of the initial conditions. Finally, we have shown that droplets forced against a step because of gravity can sustain tilting angles up to 180° without detaching from the surface. The simple step configuration reported in this paper is an illustration of how capillary interactions mediated by the lubricant layer of SLIPS/LIS can provide a means for droplet retention and shedding. We believe that our results can motivate the study of more complex features as a means to achieve better control on the transport and location of droplets on low-friction surfaces by exploiting the capillary interactions presented here.

AUTHOR INFORMATION

Corresponding Author

*E-mail: gary.wells@northumbria.ac.uk.

DOI: 10.1021/acs.langmuir.9b00931
Langmuir 2019, 35, 9146−9151

ORCID

Bethany V. Orme: 0000-0003-4280-7702
Glen McHale: 0000-0002-8519-7986
Rodrigo Ledesma-Aguilar: 0000-0001-8714-0556

Notes

The authors declare no competing financial interest.

■ ACKNOWLEDGMENTS

B.V.O. acknowledges the University of Northumbria at Newcastle for its support via a postgraduate research studentship. The authors would like to thank Dr. Andrew Edwards for assistance during sample production.

■ REFERENCES

(1) Singh, M.; Haverinen, H. M.; Dhagat, P.; Jabbour, G. E. Inkjet Printing-Process and Its Applications. *Adv. Mater.* **2010**, *22*, 673−685.
(2) Quéré, D. Wetting and Roughness. *Annu. Rev. Mater. Res.* **2008**, *38*, 71−99.
(3) Deegan, R. D.; Bakajin, O.; Dupont, T. F.; Huber, G.; Nagel, S. R.; Witten, T. A. Capillary Flow as the Cause of Ring Stains from Dried Liquid Drops. *Nature* **1997**, *389*, 827−829.
(4) Yunker, P. J.; Still, T.; Lohr, M. A.; Yodh, A. G. Suppression of the Coffee-Ring Effect by Shape-Dependent Capillary Interactions. *Nature* **2011**, *476*, 308−311.
(5) Baroud, C. N.; Gallaire, F.; Dangla, R. Dynamics of Microfluidic Droplets. *Lab Chip* **2010**, *10*, 2032−2045.
(6) Leslie, D. C.; Waterhouse, A.; Berthet, J. B.; Valentin, T. M.; Watters, A. L.; Jain, A.; Kim, P.; Hatton, B. D.; Nedder, A.; Donovan, K.; et al. A Bioinspired Omniphobic Surface Coating on Medical Devices Prevents Thrombosis and Biofouling. *Nat. Biotechnol.* **2014**, *32*, 1134−1140.
(7) Ling, S.; Luo, Y.; Luan, L.; Wang, Z.; Wu, T. Inkjet Printing of Patterned Ultra-Slippery Surfaces for Planar Droplet Manipulation. *Sens. Actuators, B* **2016**, *235*, 732−738.
(8) McHale, G.; Shirtcliffe, N. J.; Newton, M. I. Contact-Angle Hysteresis on Super-Hydrophobic Surfaces. *Langmuir* **2004**, *20*, 10146−10149.
(9) Wu, C.-J.; Li, Y.-F.; Woon, W.-Y.; Sheng, Y.-J.; Tsao, H.-K. Contact Angle Hysteresis on Graphene Surfaces and Hysteresis-Free Behavior on Oil-Infused Graphite Surfaces. *Appl. Surf. Sci.* **2016**, *385*, 153−161.
(10) Guan, J. H.; Wells, G. G.; Xu, B.; McHale, G.; Wood, D.; Martin, J.; Stuart-Cole, S. Evaporation of Sessile Droplets on Slippery Liquid-Infused Porous Surfaces (SLIPS). *Langmuir* **2015**, *31*, 11781−11789.
(11) Wang, L.; McCarthy, T. J. Covalently Attached Liquids: Instant Omniphobic Surfaces with Unprecedented Repellency. *Angew. Chem. Int. Ed.* **2016**, *55*, 244−248.
(12) Hancock, M. J.; Sekeroglu, K.; Demirel, M. C. Bioinspired Directional Surfaces for Adhesion, Wetting, and Transport. *Adv. Funct. Mater.* **2012**, *22*, 2223−2234.
(13) Kota, A. K.; Li, Y.; Mabry, J. M.; Tuteja, A. Hierarchically Structured Superoleophobic Surfaces with Ultralow Contact Angle Hysteresis. *Adv. Mater.* **2012**, *24*, 5838−5843.
(14) Shirtcliffe, N. J.; Aqil, S.; Evans, C.; McHale, G.; Newton, M. I.; Perry, C. C.; Roach, P. The Use of High Aspect Ratio Photoresist (SU-8) for Super-Hydrophobic Pattern Prototyping. *J. Micromech. Microeng.* **2004**, *14*, 1384−1389.
(15) Shirtcliffe, N. J.; McHale, G.; Atherton, S.; Newton, M. I. An Introduction to Superhydrophobicity. *Adv. Colloid Interface Sci.* **2010**, *161*, 124−138.
(16) Cassie, A. B. D.; Baxter, S. Wettability of Porous Surfaces. *Trans. Faraday Soc.* **1944**, *40*, 546−551.
(17) Barthlott, W.; Neinhuis, C. Purity of the Sacred Lotus, or Escape from Contamination in Biological Surfaces. *Planta* **1997**, *202*, 1−8.
(18) Simpson, J. T.; Hunter, S. R.; Aytug, T. Superhydrophobic Materials and Coatings: A Review. *Rep. Prog. Phys.* **2015**, *78*, 086501.
(19) Bauer, U.; Federle, W. The insect-trapping rim of Nepenthes pitchers. *Plant Signal. Behav.* **2009**, *4*, 1019−1023.
(20) Wong, T.-S.; Kang, S. H.; Tang, S. K. Y.; Smythe, E. J.; Hatton, B. D.; Grinthal, A.; Aizenberg, J. Bioinspired Self-Repairing Slippery Surfaces with Pressure-Stable Omniphobicity. *Nature* **2011**, *477*, 443−447.
(21) Wang, B. L.; Heng, L.; Jiang, L. Temperature-Responsive Anisotropic Slippery Surface for Smart Control of the Droplet Motion. *ACS Appl. Mater. Interfaces* **2018**, *10*, 7442−7450.
(22) Smith, J. D.; Dhiman, R.; Anand, S.; Reza-Garduno, E.; Cohen, R. E.; McKinley, G. H.; Varanasi, K. K. Droplet Mobility on Lubricant-Impregnated Surfaces. *Soft Matter* **2013**, *9*, 1772−1780.
(23) Vella, D.; Mahadevan, L. The "Cheerios Effect". *Am. J. Phys.* **2004**, *73*, 817−825.
(24) Karpitschka, S.; Pandey, A.; Lubbers, L. A.; Weijs, J. H.; Botto, L.; Das, S.; Andreotti, B.; Snoeijer, J. H. Liquid Drops Attract or Repel by the Inverted Cheerios Effect. *Proc. Natl. Acad. Sci. U.S.A.* **2016**, *113*, 7403−7407.
(25) Guan, J. H.; Ruiz-Gutiérrez, É.; Xu, B. B.; Wood, D.; McHale, G.; Ledesma-Aguilar, R.; Wells, G. G. Drop Transport and Positioning on Lubricant-Impregnated Surfaces. *Soft Matter* **2017**, *13*, 3404−3410.
(26) Luo, J. T.; Geraldi, N. R.; Guan, J. H.; McHale, G.; Fu, Y. Q.; Wells, G. G. Slippery Liquid-Infused Porous Surfaces and Droplet Transportation by Surface Acoustic Waves. *Phys. Rev. Appl.* **2017**, *7*, 014017.
(27) Bowden, N.; Arias, F.; Deng, T.; Whitesides, G. M. Self-Assembly of Microscale Objects at a Liquid/Liquid Interface through Lateral Capillary Forces. *Langmuir* **2001**, *17*, 1757−1765.
(28) Landau, L.; Levich, B. Dragging of a Liquid by a Moving Plate. In *Dynamics of Curved Fronts*; Pelcé, P., Ed.; Academic Press: San Diego, 1988; pp 141−153.
(29) Seiwert, J.; Clanet, C.; Quéré, D. Coating of a Textured Solid. *J. Fluid Mech.* **2011**, *669*, 55−63.
(30) Harkins, W. D.; Feldman, A. Films. The Spreading of Liquids and the Spreading Coefficient. *J. Am. Chem. Soc.* **1922**, *44*, 2665−2685.
(31) McHale, G.; Orme, B. V.; Wells, G. G.; Ledesma-Aguilar, R. A. Apparent Contact Angles on Lubricant Impregnated Surfaces/SLIPS: From Superhydrophobicity to Electrowetting. *Langmuir* **2019**, *35*, 4197.
(32) Banpurkar, A. G.; Nichols, K. P.; Mugele, F. Electrowetting-Based Microdrop Tensiometer. *Langmuir* **2008**, *24*, 10549−10551.
(33) Semprebon, C.; McHale, G.; Kusumaatmaja, H. Apparent Contact Angle and Contact Angle Hysteresis on Liquid Infused Surfaces. *Soft Matter* **2017**, *13*, 101−110.
(34) Whittaker, E. T.; Gibbs, J. W. The Scientific Papers of J Willard Gibbs. *Math. Gaz.* **1907**, *64*, 87.

DOI: 10.1021/acs.langmuir.9b00931
Langmuir 2019, 35, 9146−9151